

Quantum Monte Carlo studies of a metallic spin-density wave transition

Inaugural-Dissertation

zur

Erlangung des Doktorgrades

der Mathematisch-Naturwissenschaftlichen Fakultät

der Universität zu Köln

vorgelegt von

Max Henner Gerlach

aus Köln



Köln 2017

Berichterstatter: Prof. Dr. Simon Trebst

Prof. Dr. Achim Rosch

Tag der mündlichen Prüfung: 20.01.2017

Abstract

Plenty experimental evidence indicates that quantum critical phenomena give rise to much of the rich physics observed in strongly correlated itinerant electron systems such as the high temperature superconductors. A quantum critical point of particular interest is found at the zero-temperature onset of spin-density wave order in two-dimensional metals. The appropriate low-energy theory poses an exceptionally hard problem to analytic theory, therefore the unbiased and controlled numerical approach pursued in this thesis provides important contributions on the road to comprehensive understanding. After discussing the phenomenology of quantum criticality, a sign-problem-free determinantal quantum Monte Carlo approach is introduced and an extensive toolbox of numerical methods is described in a self-contained way. By the means of largeßscale computer simulations we have solved a lattice realization of the universal effective theory of interest. The finite-temperature phase diagram, showing both a quasi-long-range spin-density wave ordered phase and a d -wave superconducting dome, is discussed in its entirety. Close to the quantum phase transition we find evidence for unusual scaling of the order parameter correlations and for non-Fermi liquid behavior at isolated hot spots on the Fermi surface.

Kurzzusammenfassung

Zahlreiche experimentelle Ergebnisse deuten darauf hin, dass quantenkritische Phänomene der Auslöser für einen Großteil der reichhaltigen Physik sind, die man in Hochtemperatursupraleitern und anderen stark korrelierten Systemen beweglicher Elektronen beobachtet. Ein besonders interessanter quantenkritischeser Punkt findet sich in zweidimensionalen Metallen am Übergang zu antiferromagnetischer Spindichtewellen-Ordnung am absoluten Temperatur-Nullpunkt. Die zugehörige Niedrigenergie-Theorie ist mit analytischen, theoretischen Methoden sehr schwer zu lösen, so dass ein umfassendes Verständnis bisher nicht erreicht werden konnte. In dieser Dissertation wird als komplementärer Zugang ein numerischer Ansatz verfolgt, mit dem wichtige Beiträge geliefert werden können, weil alle Rechnungen gut unter Kontrolle zu halten sind und keine händisch gesetzten Ansätze die Ergebnisse in bestimmte Richtungen drängen. Nach der Besprechung der Phänomenologie von Quantenkritikalität wird ein vorzeichenproblemfreies Determinanten-Quanten-Monte-Carlo-Verfahren eingeführt und ein umfassender Satz numerischer Methoden beschrieben. Dieser Methodenteil kann weitgehend für sich stehen. Mittels groß angelegter Computersimulationen haben wir eine Gitterrealisierung der universellen effektiven Theorie dieses Problems gelöst. Das Phasendiagramm bei endlicher Temperatur beschreiben wir in seiner Gänze. Es weist sowohl eine quasi-langreichweitig geordnete Spindichtewellen-Phase als auch eine d -Wellen-supraleitende Phase auf. In der Nähe des Quantenphasenübergangs können wir Nachweise für ein ungewöhnliches Skalenverhalten der Ordnungsparameterkorrelationen und für fermionische Eigenschaften, die an isolierten Punkten der Fermi-Fläche nicht den Erwartungen nach Landaus Theorie der Fermi-Flüssigkeiten entsprechen, finden.

Contents

1	Introduction	1
I	Quantum phase transitions and unconventional superconductivity	5
2	Modeling quantum phase transitions	7
2.1	Introduction to quantum phase transitions	7
2.1.1	Phase transitions, criticality, and universality	7
2.1.2	Interplay of thermal and quantum fluctuations	9
2.1.3	Scaling at quantum phase transitions	11
2.1.4	Effective theories	12
2.2	Quantum phase transitions in systems of itinerant electrons	14
2.2.1	Motivation of the spin-fermion model	14
2.2.2	Metal close to the onset of spin-density wave order	19
2.2.3	Analytical approaches beyond mean field	21
3	Unconventional superconductivity on the verge of antiferromagnetism	25
II	Numerically exact solution by quantum Monte Carlo	29
4	Quantum Monte Carlo approach	31
4.1	Determinantal quantum Monte Carlo (DQMC)	32
4.1.1	Basic formalism	33
4.1.2	Markov chain Monte Carlo sampling	35
4.1.3	Observable expectation values	39
4.2	Fermion sign problem	44
4.2.1	Absence of the sign problem	46
4.2.2	Determinant factorization	47
4.2.3	Generalized time reversal symmetry	50
4.2.4	More sign-problem-free formulations	54
4.3	Sign-problem-free two-flavor model	54
4.3.1	Mean field	56
4.3.2	Single-fermion matrix structure and antiunitary symmetry . .	58
4.3.3	Fermion determinant and $O(N)$ symmetric variations	59

4.3.4	Other types of Fermi surfaces	62
5	Numerical methodology	63
5.1	Numerical stabilization	63
5.1.1	Matrix decomposition for the equal-time Green's function . .	65
5.1.2	Efficient and stable DQMC sweep	68
5.2	Monte Carlo updating schemes	72
5.2.1	Local updates	73
5.2.2	Global updates	79
5.2.3	Replica exchange	82
5.3	Efficient linear algebra	91
5.3.1	Checkerboard break up	91
5.3.2	Delayed updates	96
5.4	Finite-size effects	101
5.4.1	Perpendicular magnetic field	101
5.4.2	Fictitious “magnetic” field for the SDW model	104
5.4.3	Twisted boundary conditions	106
5.5	Aspects of data analysis	107
5.5.1	Multiple histogram reweighting	108
5.5.2	Correlation functions via fast Fourier transform (FFT)	110
III	Numerical results	113
6	Phase diagrams and competing orders	115
6.1	Analysis of the spin-density wave (SDW) transition	116
6.2	Phase diagram for $\lambda = 1 = c$	119
6.3	Identification of the superconducting transition	120
6.4	Phase diagram for $\lambda = 3, c = 2$	125
6.4.1	Competition and coexistence of magnetic and superconducting order	127
6.4.2	Charge-density wave (CDW) and pair-density wave (PDW) susceptibilities	132
6.5	Phase diagrams for several values of λ and $c = 3$	136
6.6	Discussion	139
7	Manifestations of quantum critical behavior	143
7.1	Magnetic correlations	143
7.1.1	Bosonic SDW susceptibility	144

7.1.2	Fermion bilinear SDW susceptibility	149
7.1.3	Temperature dependence	151
7.2	Single-fermion correlations	155
7.3	Superconducting state	160
7.4	Discussion	162
8	Concluding remarks and outlook	165
A	Identities for fermionic many-particle states	169
B	Promoting charge-density wave order	175
C	Hybrid Monte Carlo	179
	Bibliography	183
	Acknowledgments	197

1 Introduction

To this day various classes of highly correlated itinerant electron systems such as the high temperature superconductors elude full physical understanding. It is widely believed that the key to the solution of many open problems concerning these materials can be found in quantum critical phenomena, i.e. continuous phase transitions at zero temperature, driven by quantum fluctuations and tuned by a non-thermal control parameter [1–3]. Quantum phase transitions are particularly hard to reason about in metallic systems, where fermionic quasiparticles at low energies close to the Fermi surface strongly interact with critical order parameter fluctuations [4, 5]. As a consequence it is often not sufficient to deal with effective theories of an order parameter field alone with the fermions integrated out. A viable approach can rather be found in low energy theories that incorporate both a collective bosonic order parameter and fermions which are free apart from the coupling to the bosons [6]. Since there are no obvious small parameters, the solution of these theories is very hard by purely analytic approaches.

The topic of this thesis is one important type of metallic quantum phase transitions, namely the transition between an itinerant, but antiferromagnetic spin-density wave (SDW) ordered state and a quantum-disordered paramagnetic state. The magnetic quantum critical point at the zero-temperature boundary between these two phases is believed to be prototypical for the physics of the cuprates, certain iron-based and heavy fermion superconductors, and other materials [7].

We pursue an alternative route to solving a low-energy theory realizing this quantum phase transition that is complementary to analytic theory. Our method of choice is a flavor of quantum Monte Carlo (QMC) adapted to the simulation of coupled fermion-boson many-particle lattice models at finite temperature [8]. At this time QMC is the only established numerically exact, unbiased method capable of providing solutions for such systems in two spatial dimensions on moderately large lattices in polynomial time. Its applicability is unfortunately limited to models free of the “fermion sign problem” [9], which has hindered progress for long, but fortunately a sign-problem-free realization of a metallic SDW model has been found recently [10, 11].

This thesis is structured into three parts. In Part I we start with a short introduction to the phenomenology of quantum phase transitions with a special emphasis put on the quantum critical regime at finite temperatures above a quantum critical point. The concept of effective order parameter field theories is discussed with its shortcomings for systems with Fermi surfaces. The spin-fermion model is carefully

introduced as an adequate model to analyze a metallic spin-density wave quantum phase transition and analytical approaches to its solution are summarized. Three classes of strongly correlated materials at the focus of experimental research are the subject of the subsequent Chapter 3: the cuprates, the iron-based superconductors, and the heavy fermion systems. They have in common that their phase diagrams feature an antiferromagnetic phase in vicinity of an unconventional superconducting phase whose existence can be linked to quantum critical phenomena.

The goal of Part II is to give a mostly self contained account of the numerical methods we have used to study the metallic SDW model. In Chapter 4 the versatile and numerically exact method of determinantal quantum Monte Carlo (DQMC) is introduced in its finite-temperature formulation. The largest limit to its applicability is the fermion sign problem plaguing most simulations of interacting electron systems. Here we show how to circumvent it for our model by moving to a two-band variation, carefully constructed to be symmetric under a generalized time-reversal transformation. The nature of Chapter 5 is very technical. While the aspects of the method that we discuss here may appear to be mere implementation details, their attentive consideration is a prerequisite for obtaining correct numerical results in limited computing time.

Finally, Part III presents the rich physics found in the numerically exact results obtained in the simulations of our variation of the spin-fermion model. Detailed finite-temperature phase diagrams for several sets of parameters are discussed in their entirety in Chapter 6. In the vicinity of an SDW quantum phase transition we do not only find a quasi-long-range ordered SDW phase, but also an emergent d -wave superconducting phase. The susceptibilities of various potentially competing orders are also investigated. Chapter 7 then focuses on manifestations of quantum critical behavior associated with a putative quantum critical point underlying the superconducting phase. At temperatures above T_c order parameter correlations are found to agree surprisingly well to Hertz-Millis theory, but show intriguing deviations in their temperature dependence. Moreover, in an apparently quantum critical regime non-Fermi liquid behavior is induced for momenta close to the “hot spots” of the Fermi surfaces. Here we also give a closer look at properties of the superconducting state close to the quantum phase transition.

We close in Chapter 8 with concluding remarks and an outlook on the prospects of future continuations of this work.

This thesis is the outcome of an intensive collaboration with Yoni Schattner and Erez Berg of the Weizmann Institute of Science. Two independent software codes for simulation and evaluation have been used in combination. At the beginning of Chapters 6 and 7 it is pointed out which parts have not been evaluated by the author of this thesis, but have been obtained by the Weizmann group.

The C++ software developed by the author, implementing efficient algorithms for DQMC simulations, will be made available to the public under an open source license.

The results presented in this thesis have been published previously in these papers:

- Y. Schattner, M. H. Gerlach, S. Trebst, and E. Berg, *Competing Orders in a Nearly Antiferromagnetic Metal*, Phys. Rev. Lett. **117**, 097002 (2016).
- M. H. Gerlach, Y. Schattner, E. Berg, and S. Trebst, *Quantum critical properties of a metallic spin-density-wave transition*, Phys. Rev. B **95**, 035124 (2017).

During the time frame of the author's doctoral research work two additional papers have been published, which are not covered in this thesis:

- E. Sela, H.-C. Jiang, M. H. Gerlach, and S. Trebst, *Order-by-disorder and spin-orbital liquids in a distorted Heisenberg-Kitaev model*, Phys. Rev. B **90**, 035113 (2014).
- M. H. Gerlach and W. Janke, *First-order directional ordering transition in the three-dimensional compass model*, Phys. Rev. B **91**, 045119 (2015).

These address problems of frustrated spin systems, which have been tackled by extensive classical Monte Carlo simulations. The second of these papers is mainly based on data obtained during the author's diploma thesis work.

Part I

Quantum phase transitions and unconventional superconductivity

2 Modeling quantum phase transitions

Phase transitions are ubiquitous in various complex systems in nature, including the freezing of water, the spontaneous magnetization of a ferromagnetic material, or the transition of a metal into a superconducting state. These example phase transitions all take place at finite temperatures. At the transition temperature a macroscopic type of order is destroyed by thermal fluctuations. Conversely, quantum phase transitions occur at zero temperature, where a control parameter other than temperature such as pressure, chemical composition, or an external field is varied across a transition point. Only quantum fluctuations, ultimately a manifestation of Heisenberg's uncertainty principle, destroy order in this case. Even though the third law of thermodynamics precludes experiments at absolute zero, zero temperature quantum critical points (QCPs) have attracted considerable interest in condensed matter physics. The reason for this is that the special excitation spectrum of the ground state at a QCP gives rise to quantum critical behavior also at finite temperatures in a regime above the transition point. This influences physical observables over a wide range of the phase diagram. Understanding quantum criticality is a key objective on the road to uncovering the mechanisms behind phenomena such as high-temperature superconductivity.

In this Chapter, Sec. 2.1 first introduces quantum phase transitions in general, then Sec. 2.2 proceeds to discuss the modeling of quantum phase transitions in systems of itinerant electrons, focusing on a spin-density wave (SDW) transition.

2.1 Introduction to quantum phase transitions

In this Section we briefly introduce the general phenomenology of quantum phase transitions [4, 12, 13]. The presentation mostly follows M. Vojta's review [12].

2.1.1 Phase transitions, criticality, and universality

Generally, we distinguish between first-order phase transitions and continuous phase transitions. First-order transitions are characterized by the coexistence of two phases at the transition point, while phases do not coexist at a continuous transition. A conventionally ordered phase is described by a local order parameter, which is zero outside of the ordered phase and takes up a non-unique, non-zero value in the

ordered phase. At the **critical point** of a continuous transition the value of the order parameter vanishes continuously as it is crossed from the ordered phase.

In the disordered phase the expectation value of the order parameter is zero, but it has non-zero fluctuations. As the critical point is approached, spatial correlations of these fluctuations become long-ranged and the correlation length ξ , which is their typical length scale, diverges as

$$\xi \sim |t|^{-\nu}, \quad (2.1)$$

where ν is the correlation length critical exponent and t measures the distance to the critical point. For a thermal phase transition at a temperature $T = T_c$ one can set $t = (T - T_c)/T_c$. Similarly, there are also long-range correlations of order parameter fluctuations in time. The typical time scale for their decay is the correlation time τ_c , which in the vicinity of the critical point diverges as

$$\tau_c \sim \xi^z \sim |t|^{-z\nu} \quad (2.2)$$

with the dynamical critical exponent z . Close to the critical point, ξ is the only characteristic length scale and τ_c is the only characteristic time scale of the system.

By Eqs. (2.1) and (2.2) correlation length and time are infinite at the transition point. Since there fluctuations occur on all length and time scales, the system must be scale invariant. Consequently, all measurable quantities depend via power laws on the external parameters; one speaks of critical phenomena. Near the critical point the exponents of these power laws, the critical exponents, fully characterize the behavior of the system.

To illustrate the concept of **scaling** let us consider a classical ferromagnet, where the magnetization $M(\mathbf{r})$ is the order parameter and external parameters are the reduced temperature $t = (T - T_c)/T_c$ and an applied magnetic field B , which couples to M . Close to the critical point all physical properties must be invariant under rescaling of all lengths in the system by a common factor if we simultaneously adjust the external parameters such that the correlation length, which is the only important length scale, remains unchanged. By requiring this we obtain a homogeneity relation for the singular part of the free-energy density

$$f(t, B) = b^{-d} f(tb^{1/\nu}, Bb^{y_B}), \quad (2.3)$$

where $b > 0$ is arbitrary, d is the spatial dimension, and y_B is a second critical exponent. Differentiating f gives rise to similar expressions for other thermodynamic quantities. This is the scaling hypothesis [14], which can be derived in renormalization group theory [15, 16].

An intriguing feature of critical phenomena at continuous phase transitions is their **universality**. The critical exponents are robust features that take the same values for entire classes of phase transitions occurring in very different physical systems. Such universality classes are determined only by the spatial dimension of the system, the range of the interaction, and the symmetry of the order parameter. Consequently, the critical behavior of an experimental system close to a phase transition can be determined fully by solving a minimal model system of the same universality class. This universality is rooted in the divergence of the correlation length close to a critical point, where the physics is effectively averaged over large length scales such that microscopic details of the model lose their importance.

2.1.2 Interplay of thermal and quantum fluctuations

So far our discussion of continuous phase transitions can equally be applied to classical and quantum mechanical systems. Quantum mechanics is often already essential to understand the existence of an ordered phase. But besides that quantum mechanics can influence the asymptotic behavior at criticality. To understand this we compare two energy scales: the typical energy of long-distance order parameter fluctuations $\hbar\omega_c$ and the thermal energy $k_B T$. By Eq. (2.2) the typical time scale of order parameter fluctuations τ_c diverges as a continuous transition is approached. This is tantamount to the typical frequency scale ω_c going to zero. Hence we have for the typical energy scale

$$\hbar\omega_c \propto \tau_c^{-1} \sim |t|^{\nu_z} \quad (2.4)$$

with t close to zero. Close to a continuous phase transition at a finite temperature T_c this typical energy scale separates two regimes: If it is larger than the thermal energy, $\hbar\omega_c \gg k_B T$, quantum mechanics will be important, while order parameter fluctuations can be understood in a purely classical description for $\hbar\omega_c \ll k_B T$. In between we have a crossover of the character of fluctuations from quantum to classical. Consequently, quantum mechanics is unimportant for $|t| \ll T_c^{1/\nu_z}$. In effect there is a regime, which shrinks as the temperature is lowered, asymptotically close to the transition where the critical behavior is entirely classical. While the quantum mechanical description remains important on microscopic scales, classical thermal fluctuations dominate on the macroscopic scales of critical behavior.

On the other hand, the behavior at a continuous transition at zero temperature, which is controlled by a non-thermal control parameter r , is dominated by purely quantum fluctuations. Hence, we speak of a quantum phase transition (QPT).

The interplay of thermal and quantum fluctuations can give rise to interesting

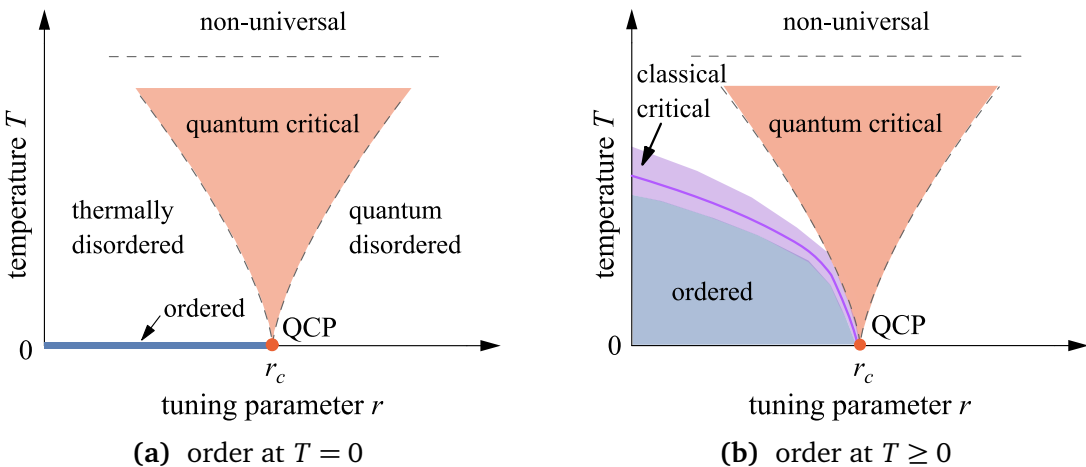


Figure 2.1: Schematic finite-temperature phase diagrams close to a quantum critical point (QCP) at $r = r_c$. Dashed lines indicate crossovers. (a) Long-range order only at zero temperature. (b) An ordered phase extends to finite temperature, with the solid line marking the phase transition. In panel (b) the thermally disordered and quantum disordered regimes are still present, although not labeled. Figure based on Ref. [12].

phase diagrams in the vicinity of a quantum critical point. We can distinguish two cases, depending on whether finite-temperature long-range order can exist.

In two-dimensional systems with an order parameter of continuous symmetry the Mermin-Wagner theorem [17] forbids long-range order at finite temperature. Such a situation can lead to the phase diagram in Fig. 2.1a, where order only exists at $T = 0$ and no finite-temperature phase transitions occur. Nevertheless, the finite-temperature behavior is characterized by three distinct regimes, separated by crossovers. The **quantum disordered** region is dominated by quantum fluctuations with the system resembling the quantum disordered ground state for $r > r_c$. The elementary excitations on top of this ground state are typically well defined quasiparticles with a finite energy gap Δ , such that their density at low temperatures is exceptionally small. We have a **thermally disordered** region, where primarily thermal fluctuations destroy the zero temperature order and the density of thermally excited quasiparticles is again small. In an intermediate **quantum critical** regime both quantum and thermal fluctuations are important. It is located above the quantum critical point at $r = r_c$ and its boundaries are determined by crossover lines $k_B T \sim \hbar\omega_c \sim |r - r_c|^{\nu_z}$. Here the picture of dilute quasiparticle excitations does not apply. Physics in this region is controlled by thermal excitations of the quantum critical ground state, typically characterized by the absence of conventional quasiparticle excitations, which are replaced by a quantum critical continuum of

excitations. This leads to unusual features of the finite-temperature quantum critical region, including unconventional power laws and non-Fermi liquid behavior with uncommon transport properties. The behavior in this region is universal, but far away from the quantum critical point microscopic length scales begin to exceed the correlation length. Therefore quantum critical behavior is cut off at high temperatures where $k_B T$ is larger than characteristic microscopic energy scales such as a typical exchange energy. Here the physics is **non-universal**.

If order can also exist at finite temperatures, the richer phase diagram of Fig. 2.1b with a phase transition at low finite temperatures is established. Here the quantum critical point can be seen as the end point of a finite temperature transition line. This line is surrounded by a **classical critical** regime, which becomes narrower as the quantum critical point is approached.

2.1.3 Scaling at quantum phase transitions

Thermodynamic properties can be derived from the partition function $\mathcal{Z} = \text{Tr } e^{-\mathcal{H}/k_B T}$ with the Hamiltonian $\mathcal{H} = \mathcal{H}_{\text{kin}} + \mathcal{H}_{\text{pot}}$. In a classical system both parts of \mathcal{H} commute and \mathcal{Z} factorizes, $\mathcal{Z} = \mathcal{Z}_{\text{kin}} \mathcal{Z}_{\text{pot}}$, such that statics and dynamics decouple. Usually singularities only occur in the static interacting part \mathcal{Z}_{pot} . This allows us to study classical phase transitions with effective time-independent theories in d spatial dimensions.

For a quantum mechanical system, on the other hand, \mathcal{H}_{kin} and \mathcal{H}_{pot} generally do not commute and \mathcal{Z} does not factorize. Consequently, statics and dynamics are coupled and the order parameter field theory must be formulated in terms of space- and time-dependent fields. To do so, one introduces an imaginary time direction to the system, formally by applying the path integral representation of the partition function. At zero temperature the extent in this direction is infinite such that imaginary time acts as an additional spatial dimension, which by Eq. (2.2) scales with the z th power of a length. Therefore the homogeneity law (2.3) at $T = 0$ for a quantum phase transition reads

$$f(t, B) = b^{-(d+z)} f(t b^{1/\nu}, B b^{y_B}), \quad (2.5)$$

with $t = (r - r_c)/r_c$. In this way a quantum phase transition in d spatial dimensions is related to a classical transition in $(d+z)$ dimensions. A generalization of Eq. (2.5) to finite temperature, where we recognize that we can approach the quantum critical singularity both by tuning r to r_c at $T = 0$ and by lowering T to zero at $r = r_c$, is

$$f(t, B) = b^{-(d+z)} f(t b^{1/\nu}, B b^{y_B}, T b^z). \quad (2.6)$$

From the homogeneity law one can derive scaling relations for static and dynamic observables. For a correlation function $C(\mathbf{k}, \omega)$ at momentum \mathbf{k} , measured relative to the ordering wavevector, and frequency ω we find for instance the following scaling relation at the quantum critical point:

$$C(t = 0, \mathbf{k}, \omega, T = 0) = |\mathbf{k}|^{-\dim C} C_1(|\mathbf{k}|^z / \omega), \quad (2.7)$$

where $\dim C$ is the scaling dimension of C . Similarly, at finite temperatures above the quantum critical point we obtain for $\mathbf{k} = \mathbf{0}$:

$$C(t = 0, \mathbf{k} = \mathbf{0}, \omega, T) = T^{-\dim C/z} C_2(\omega/T). \quad (2.8)$$

These naive scaling relations (2.7) and (2.8) are, however, only expected to be valid if the quantum critical point satisfies hyperscaling, which need not be true above the upper-critical dimension.

The value of the quantum-classical analogy can be seen by considering a correlation function G directly at a critical point. In a classical system of d dimensions critical correlations fall off with a power law in momentum space $G(\mathbf{k}) \sim |\mathbf{k}|^{-2+\eta_d}$. For a quantum phase transition with dynamical critical exponent $z = 1$ we can conclude from the mapping at $T = 0$ that $G(\mathbf{k}, i\omega_n) \sim [\mathbf{k}^2 + \omega_n^2]^{(-2+\eta_{d+1})/2}$ where the Matsubara frequency ω_n acts as an extra component to \mathbf{k} .¹ By analytic continuation this translates to the retarded Green's function at real frequencies $G^R(\mathbf{k}, \omega) \sim [\mathbf{k}^2 - (\omega + i0^+)^2]^{(-2+\eta_{d+1})/2}$. This illustrates the excitation spectrum at a quantum critical point: G^R does not have a quasiparticle pole, but a branch cut at $\omega > |\mathbf{k}|$, corresponding to a continuum of excitations [4, Sec. 7.2].

2.1.4 Effective theories

Since the important physics at criticality is described by long-wavelength order parameter fluctuations, it can be appropriate to work with an effective theory of only these order parameter fluctuations that disregards microscopic details. Such a theory can formally be obtained by integrating out suitably decoupled interaction terms from a microscopic model. Since the correlation length is sufficiently large near a continuous transition, the effective action can be formulated in the continuum limit and will typically consist of powers of the order parameter field and of gradient terms. Its form will only depend on the symmetry and dimension of the underlying system and on the symmetry of the order parameter, consistent with the expectations

¹Here we assume the theory to be Lorentz invariant. Generally, additional terms of the form $f(\omega/|\mathbf{k}|)$ would be allowed.

for universal critical behavior. As an example consider a quantum rotor model

$$\mathcal{H}_{\text{rot}} = \frac{Jg}{2} \sum_i \vec{L}_i^2 - J \sum_{\langle i,j \rangle} \vec{n}_i \cdot \vec{n}_j, \quad (2.9)$$

with N -component operators \vec{n}_i , $\vec{n}_i^2 = 1$ on the sites i of a d -dimensional lattice representing orientations and with the corresponding angular momenta \vec{L}_i . Minimizing the energy of the nearest-neighbor term favors an ordered ferromagnetic state, while the kinetic term prefers quantum-disordered delocalization. The parameter g tunes through a quantum phase transition.

A suitable order parameter for that transition is the ferromagnetic magnetization. From the lattice model (2.9) a continuum theory is obtained in a spatial coarse graining procedure where the \vec{n}_i are averaged over microscopic length scales. This yields the order parameter field $\vec{\varphi}$, which is no longer of fixed length. An expansion to lowest order in gradients of $\vec{\varphi}$ produces a $\vec{\varphi}^4$ quantum field theory $\mathcal{Z} = \int D\vec{\varphi} \exp(-S)$ with action

$$S = \int d^d x \int_0^{\hbar/k_B T} d\tau \left[\frac{1}{2c^2} (\partial_\tau \vec{\varphi})^2 + \frac{1}{2} (\nabla_x \vec{\varphi})^2 + \frac{r}{2} \vec{\varphi}^2 + \frac{u}{4} (\vec{\varphi}^2)^2 \right]. \quad (2.10)$$

Here r tunes the system across the quantum phase transition, c is a velocity, and u contains self-interactions of the fluctuations of $\vec{\varphi}$. The dynamical critical exponent is $z = 1$.

Eq. (2.10) provides a theory for quantum criticality that is appropriate for more models than just Eq. (2.9), with some non-conserved density as the order parameter field $\vec{\varphi}(x, \tau)$. The approach of effective field theories of this kind has been very successful in treating quantum phase transitions in bosonic and insulating systems. Suitable models can be solved exactly or are, more often, understood very well in the framework of renormalization group theory with controlled expansions [4]. Moreover, efficient unbiased numerical methods such as sign-problem-free quantum Monte Carlo simulations are often available. These results confirm the general phenomenology that we have outlined qualitatively in this Section. However, models of itinerant electrons, adequate for the description of strongly correlated metals, can frequently not be treated safely in effective theories of only local order parameter fluctuations. Rather, low-lying fermionic excitations must be included explicitly in a critical theory.

2.2 Quantum phase transitions in systems of itinerant electrons

Various quantum phase transitions in metals can be studied via effective models of itinerant electrons coupled to an order parameter field. Since in a metal there is an interplay between low energy fermionic quasiparticles at the top of the Fermi sea and the quantum fluctuations of this order parameter, the fermions cannot in general be safely integrated out without introducing divergences. Consequently such problems are intrinsically more complicated than quantum critical points in gapped insulators, which are captured by purely bosonic effective theories such as Eq. (2.10) that can be largely understood by mapping them to a classical theory.

The focus of this thesis is the quantum phase transition to antiferromagnetic order in a two-dimensional metal. To investigate the universal physics near such a quantum critical point we introduce in this Chapter a carefully motivated generic model of itinerant fermions coupled to a Néel spin-density wave order parameter at wavevector $\mathbf{Q} = (\pi, \pi)^T$. Magnetic quantum phase transitions in Fermi liquids are of considerable interest due to the rich physics that emerges from the quantum critical regime [5].

Beyond the scope of this work lie various other interesting quantum phase transitions in Fermi liquids, including the (Mott) metal-insulator transition [18], charge-density wave quantum critical points [19], or Ising-nematic quantum criticality [20, 21].

2.2.1 Motivation of the spin-fermion model

In the momentum representation a microscopic Hamiltonian for a single band of itinerant $S = 1/2$ fermions subject to two-body interactions is given by

$$\mathcal{H}_{\text{gen}} = \mathcal{H}_{\text{kin}} + \mathcal{H}_{\text{int}} = \sum_{\mathbf{k}, s} \varepsilon_{\mathbf{k}} c_{\mathbf{k}, s}^\dagger c_{\mathbf{k}, s} + \sum_{\mathbf{k}_i, s_i} U_{\mathbf{k}_1, \mathbf{k}_2, \mathbf{k}_3, \mathbf{k}_4}^{s_1, s_2, s_3, s_4} c_{\mathbf{k}_1, s_1}^\dagger c_{\mathbf{k}_2, s_2}^\dagger c_{\mathbf{k}_3, s_3} c_{\mathbf{k}_4, s_4}. \quad (2.11)$$

Here $c_{\mathbf{k}, s}^\dagger$ creates and $c_{\mathbf{k}, s}$ annihilates a fermion with momentum \mathbf{k} and spin $s = \uparrow, \downarrow$. On its own \mathcal{H}_{kin} would describe a tight-binding model with band-structure dispersion $\varepsilon_{\mathbf{k}}$. In the additional \mathcal{H}_{int} we allow for a generic four-fermion interaction $U_{\mathbf{k}_1, \mathbf{k}_2, \mathbf{k}_3, \mathbf{k}_4}^{s_1, s_2, s_3, s_4}$.

For a generalized one-band Hubbard model [22] with local repulsion $U > 0$ the interaction term would be given by [23, Chapt. 3]

$$U_{\mathbf{k}_1, \mathbf{k}_2, \mathbf{k}_3, \mathbf{k}_4}^{s_1, s_2, s_3, s_4} = U \delta_{\mathbf{0}, \mathbf{k}_1 + \mathbf{k}_2 - \mathbf{k}_3 - \mathbf{k}_4} \delta_{s_1, s_3} \delta_{s_2, s_4} \delta_{s_1, \uparrow} \delta_{s_2, \downarrow}. \quad (2.12)$$

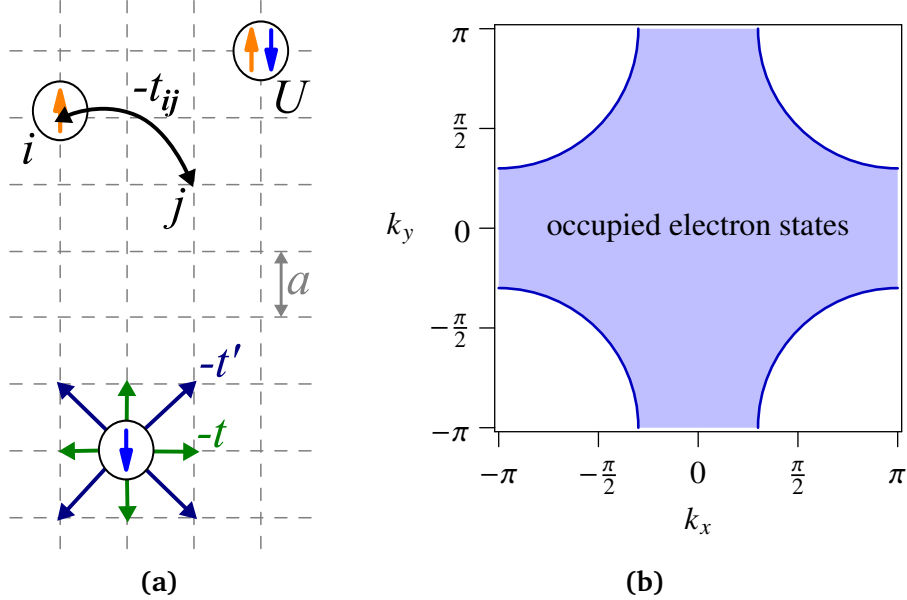


Figure 2.2: (a) Illustration of the Hubbard model on a two-dimensional square lattice and visualization of nearest neighbor hopping t and next-nearest neighbor hopping t' . (b) Sketch of the first Brillouin zone with a Fermi surface typical for a cuprate-like dispersion.

In real space with $c_{i,s}^\dagger = \frac{1}{\sqrt{N_s}} \sum_{\mathbf{k}} e^{-i\mathbf{k}\cdot\mathbf{r}_i} c_{\mathbf{k},s}^\dagger$ the Hubbard Hamiltonian reads

$$\mathcal{H}_{\text{Hub}} = - \sum_{ij,s} (t_{ij} + \mu \delta_{ij}) c_{i,s}^\dagger c_{j,s} + U \sum_i n_{i,\uparrow} n_{i,\downarrow}, \quad (2.13)$$

where $i, j \in \{1, \dots, N_s\}$ label lattice sites, t_{ij} are hopping constants, μ is the chemical potential, and $n_{i,s} = c_{i,s}^\dagger c_{i,s}$ are occupation number operators for spin $s = \uparrow, \downarrow$ at site i . In the following we will consider models of this type mainly on two-dimensional square lattices with unit lattice spacing a as sketched in Fig. 2.2a. Often we are interested in dispersion relations that yield Fermi surfaces akin to the sketch in Fig. 2.2b. These are appropriate for the electronic band structure of the cuprate superconductors, which can be well fitted by [24]

$$\epsilon_{\mathbf{k}} = -2t(\cos(k_x) + \cos(k_y)) - 2t'(\cos(k_x + k_y) + \cos(k_x - k_y)) - \mu, \quad (2.14)$$

where $t > 0$ is the hopping element for nearest neighbor sites and $t' < 0$ the hopping element for next-nearest neighbor site. The other t_{ij} are zero.

To study the effects of magnetic order it is beneficial to rewrite the Hubbard

Hamiltonian in terms of local spin operators

$$\vec{S}_i = \frac{1}{2} \sum_{ss'} c_{is}^\dagger (\vec{s})_{ss'} c_{is'}, \quad \vec{s} = \left[\begin{pmatrix} 0 & 1 \\ 1 & 0 \end{pmatrix}, \begin{pmatrix} 0 & -i \\ i & 0 \end{pmatrix}, \begin{pmatrix} 1 & 0 \\ 0 & -1 \end{pmatrix} \right]^\top, \quad (2.15)$$

where \vec{s} are the Pauli matrices. Explicitly we have $\vec{S}_i = (S_i^x, S_i^y, S_i^z)^\top$ with

$$S_i^x = \frac{1}{2} (c_{i\uparrow}^\dagger c_{i\downarrow} + c_{i\downarrow}^\dagger c_{i\uparrow}), \quad (2.16a)$$

$$S_i^y = -\frac{i}{2} (c_{i\uparrow}^\dagger c_{i\downarrow} - c_{i\downarrow}^\dagger c_{i\uparrow}), \quad (2.16b)$$

$$S_i^z = \frac{1}{2} (n_{i\uparrow} - n_{i\downarrow}). \quad (2.16c)$$

As in, for example, [23, Chapt. 2] we find

$$\begin{aligned} \mathcal{H}_{\text{Hub}} &= \sum_{\mathbf{k}, s} \varepsilon_{\mathbf{k}} c_{\mathbf{k}, s}^\dagger c_{\mathbf{k}, s} - \frac{2U}{3} \sum_i \vec{S}_i^2 + \frac{U}{2} \sum_{i, s} n_{i, s} \\ &= \sum_{\mathbf{k}, s} \tilde{\varepsilon}_{\mathbf{k}} c_{\mathbf{k}, s}^\dagger c_{\mathbf{k}, s} - \frac{U}{6N_s} \sum_{\substack{a, b, c, d \\ = \uparrow, \downarrow}} \sum_{\substack{\mathbf{k}_1, \mathbf{k}_2, \mathbf{q} \\ \mathbf{q}}} c_{\mathbf{k}_1 + \mathbf{q}, a}^\dagger (\vec{s})_{ab} c_{\mathbf{k}_1, b} \cdot c_{\mathbf{k}_2 - \mathbf{q}, c}^\dagger (\vec{s})_{cd} c_{\mathbf{k}_2, d}. \end{aligned} \quad (2.17)$$

Since the term in $n_{i, s}$ only renormalizes the chemical potential, we let $\tilde{\varepsilon}_{\mathbf{k}}$ absorb it in the second line and will drop the tilde in the following. From this transformed form of the Hubbard Hamiltonian we can now easily move to a slightly more general specification of the generic Hamiltonian in Eq. (2.17):

$$\mathcal{H} = \sum_{\mathbf{k}, s} \varepsilon_{\mathbf{k}} c_{\mathbf{k}, s}^\dagger c_{\mathbf{k}, s} - \frac{1}{4N_s} \sum_{\substack{\mathbf{k}_1, \mathbf{k}_2, \mathbf{q}, \\ a, b, c, d}} V(\mathbf{q}) c_{\mathbf{k}_1 + \mathbf{q}, a}^\dagger (\vec{s})_{ab} c_{\mathbf{k}_1, b} \cdot c_{\mathbf{k}_2 - \mathbf{q}, c}^\dagger (\vec{s})_{cd} c_{\mathbf{k}_2, d}, \quad (2.18)$$

where we now allow for an arbitrary interaction with momentum transfer \mathbf{q} in the spin channel, $V(\mathbf{q}) = V(-\mathbf{q})$. We would recover \mathcal{H}_{Hub} by setting $V(\mathbf{q}) = \frac{2U}{3}$. The remaining quartic term in Eq. (2.18) needs to be treated with some care. First, we write the grand-canonical partition function of a system governed by \mathcal{H} at temperature $T = 1/\beta$ as a functional field integral [25, Sect. 4.2]

$$\mathcal{Z} = \text{Tr } e^{-\beta \mathcal{H}} = \int D(c^\dagger, c) e^{-S[c^\dagger, c]} \quad (2.19)$$

with the action $S[c^\dagger, c] = S_{\text{kin}} + S_{\text{int}}$ and

$$S_{\text{kin}} = \int_0^\beta d\tau \sum_{\mathbf{k}, s} c_{\mathbf{k}, s}^\dagger(\tau) [\partial_\tau + \varepsilon_{\mathbf{k}}] c_{\mathbf{k}, s}(\tau), \quad (2.20\text{a})$$

$$S_{\text{int}} = -\frac{1}{4} \int_0^\beta d\tau \sum_{\substack{\mathbf{k}_1, \mathbf{k}_2, \mathbf{q}, \\ a, b, c, d}} V(\mathbf{q}) c_{\mathbf{k}_1 + \mathbf{q}, a}^\dagger(\tau) [\vec{s}]_{ab} c_{\mathbf{k}_1, b}(\tau) \cdot c_{\mathbf{k}_2 - \mathbf{q}, c}^\dagger(\tau) [\vec{s}]_{cd} c_{\mathbf{k}_2, d}(\tau). \quad (2.20\text{b})$$

We use the same symbols c^\dagger, c interchangeably for Grassmann variables and fermionic operators in Fock space. With this change of language from Hamiltonian to action it is straightforward to decouple the interaction via a Hubbard-Stratonovich transformation, see [26, Chapt. 3] and [25, Sect. 6.2]. Formally, this amounts to the application of a standard identity for real Gaussian integrals

$$\int d\mathbf{v} e^{-\frac{1}{2}\mathbf{v}^\top \mathbf{A}\mathbf{v} + \mathbf{j}^\top \mathbf{v}} = (2\pi)^{N/2} \det \mathbf{A}^{-1/2} e^{\frac{1}{2}\mathbf{j}^\top \mathbf{A}^{-1}\mathbf{j}}, \quad (2.21)$$

where \mathbf{v} is a real N -component vector, \mathbf{A} is a real symmetric $N \times N$ matrix, and \mathbf{j} is an arbitrary N -component vector.

To apply (2.21) we set $\vec{\varrho}_{\mathbf{q}}(\tau) = \sum_{\mathbf{k}, a, b} c_{\mathbf{k} + \mathbf{q}, a}^\dagger(\tau) [\vec{s}]_{ab} c_{\mathbf{k}, b}(\tau)$ and for each τ form a vector $\underline{\varrho}(\tau)$ containing $\vec{\varrho}_{\mathbf{q}}$ for each distinct momentum \mathbf{q} . From the values $V(\mathbf{q})$ we construct an antidiagonal symmetric matrix \mathbf{V} , which allows us to write S_{int} in a shortened notation:

$$e^{-S_{\text{int}}} = \exp \left\{ \int_0^\beta d\tau \frac{1}{4} \sum_{\mathbf{q}} \vec{\varrho}_{\mathbf{q}}(\tau) V(\mathbf{q}) \vec{\varrho}_{-\mathbf{q}}(\tau) \right\} \quad (2.22)$$

$$= \exp \left\{ \int_0^\beta d\tau \frac{1}{4} \underline{\varrho}(\tau)^\top \cdot \mathbf{V} \cdot \underline{\varrho}(\tau) \right\}. \quad (2.23)$$

Now we can put Eq. (2.21) to use at each τ and find (dropping arguments τ):

$$\begin{aligned} \exp \left\{ \frac{1}{4} \underline{\varrho}^\top \cdot \mathbf{V} \cdot \underline{\varrho} \right\} &= \text{const} \cdot \int d\underline{\varphi} \exp \left\{ -\underline{\varphi}^\top \cdot \mathbf{V}^{-1} \cdot \underline{\varphi} + \underline{\varrho}^\top \cdot \underline{\varphi} \right\} \\ &= \text{const} \cdot \int d\underline{\varphi} \exp \left\{ -\underline{\varphi}^\top \cdot \mathbf{V} \cdot \underline{\varphi} + \underline{\varrho}^\top \cdot \mathbf{V} \cdot \underline{\varphi} \right\}. \end{aligned} \quad (2.24)$$

Here the integration variable $\vec{\varphi}$ is a vector built from three real numbers $\vec{\varphi}_q$ for each distinct momentum q . The constant factors in front of the integrals are irrelevant for expectation values computed from \mathcal{Z} and for the functional integrals we will include them in the integration measure. In the second line of Eq. (2.24) we have transformed the integration variable $\vec{\varphi} \rightarrow V\vec{\varphi}$. Both forms are equivalent.

In this way we have effectively traded the four-fermion interaction in for an auxiliary bosonic field $\vec{\varphi}$. The partition function is now given by the functional integral over fermionic and bosonic fields with a coupled action:

$$\mathcal{Z} = \int D(c^\dagger, c, \vec{\varphi}) e^{-(S_{\text{kin}}[c^\dagger, c] + S_{\text{FB}}[c^\dagger, c, \vec{\varphi}] + S_B[\vec{\varphi}])}, \quad (2.25a)$$

$$S_{\text{kin}} = \int_0^\beta d\tau \sum_{k,s} c_{k,s}^\dagger [\partial_\tau + \varepsilon_k] c_{k,s}, \quad (2.25b)$$

$$S_{\text{FB}} = \int_0^\beta d\tau \sum_{k,q,a,b} V(q) c_{k+q,a}^\dagger [\vec{s}]_{ab} c_{k,b} \cdot \vec{\varphi}_{-q}, \quad (2.25c)$$

$$S_B = - \int_0^\beta d\tau \sum_q \vec{\varphi}_q V(q) \vec{\varphi}_{-q}. \quad (2.25d)$$

Eq. (2.25) constitutes the spin-fermion model [6, 27, 28]. The spin-fermion model is to be thought of as having arisen from a microscopic Hamiltonian, from which high-energy degrees of freedom, i.e. behavior at energies comparable to the fermionic bandwidth W , have been integrated out. Thus it can serve as an effective theory at energies smaller than a cutoff $\Lambda < W$. We can understand the spin-fermion model as describing low-energy fermions which interact with their own spin fluctuations. Due to the separation of energy scales these collective modes appear as autonomous bosonic spins $\vec{\varphi}_q$. The spin-fermion model is often stated as a Hamiltonian of itinerant electrons c and spins $\vec{\varphi}$

$$\mathcal{H}_{\text{sf}} = \sum'_{k,s} \mathbf{v}_F(\mathbf{k} - \mathbf{k}_F) c_{k,s}^\dagger c_{k,s} + \sum'_q \chi_0^{-1}(\mathbf{q}) \vec{\varphi}_q \vec{\varphi}_{-q} + g \sum'_{k,q,a,b} c_{k+q,a}^\dagger [\vec{s}]_{ab} c_{k,b} \cdot \vec{\varphi}_{-q}, \quad (2.26)$$

where the primed sums limit momenta below Λ . Here the low-energy fermion propagator retains Fermi-liquid form, but note that the electronic dispersion ε_k has been linearized for momenta k close to the Fermi surface at \mathbf{k}_F with the Fermi velocity $\mathbf{v}_F = \partial_k \varepsilon_k|_{\mathbf{k}_F}$. The bare boson susceptibility is taken as $\chi_0^{-1}(\mathbf{q}) = \chi_0 / [\xi_0^{-2} + (\mathbf{q} - \mathbf{Q})^2]$

with a bare magnetic correlation length ξ_0 and the ordering wavevector \mathbf{Q} . g is introduced as a coupling constant, which must be small compared to W . The value of \mathbf{Q} has been determined by higher energy interactions and, like the other parameters, should be considered as input to the theory; for commensurate antiferromagnetic Néel order in two dimensions it is $\mathbf{Q} = (\pi, \pi)^\top$.

The action (2.25) should be thought of as an effective theory on its own right for the underlying strongly correlated microscopic system. We will use a variation of this model to study a metal close to a spin-density wave quantum critical point where it will capture the universal physics. While we have sketched the derivation from a microscopic Hamiltonian, this Hamiltonian may actually not be known for certain and the resulting action (2.25) stands independent of its formal derivation.

2.2.2 Metal close to the onset of spin-density wave order

Having outlined how the spin-fermion model (2.25) can be obtained from a Hubbard-like Hamiltonian, we now specify the formulation we shall use to study a two-dimensional metal close to a spin density wave (SDW) quantum critical point (QCP). Our choice follows [4, Chapt. 18]. In a slight extension to the derivation in the last Section we allow the bare bosonic susceptibility to depend on frequency. We define the real bosonic field $\vec{\varphi}_\mathbf{q}$ to represent long-wavelength fluctuations with small momentum \mathbf{q} around collinear SDW order at wavevector $\mathbf{Q} = (\pi, \pi)^\top$, such that $\vec{\varphi}_\mathbf{q}$ corresponds to the electron spin density at $\mathbf{Q} + \mathbf{q}$.² The bosonic action is given by a Ginzburg-Landau φ^4 theory similar to Eq. (2.10), which can be thought to have been generated by integrating out high-energy electrons. The complete model has the action $S = S_F + S_{FB} + S_B$ with

$$S_F = \int_0^\beta d\tau \sum_{\mathbf{k}, s} c_{\mathbf{k}, s}^\dagger [\partial_\tau + \varepsilon_{\mathbf{k}}] c_{\mathbf{k}, s}, \quad (2.27a)$$

$$S_{FB} = \lambda \int_0^\beta d\tau \sum_{\mathbf{k}, \mathbf{q}, s, s'} c_{\mathbf{k} + \mathbf{Q} + \mathbf{q}, s}^\dagger [\vec{s} \cdot \vec{\varphi}_\mathbf{q}]_{ss'} c_{\mathbf{k}, s'} = \lambda \int_0^\beta d\tau \sum_{i, s, s'} e^{i\mathbf{Q} \cdot \mathbf{r}_i} c_{i, s}^\dagger [\vec{s} \cdot \vec{\varphi}_i]_{ss'} c_{i, s'}, \quad (2.27b)$$

$$S_B = \int_0^\beta d\tau \sum_i \left[\frac{1}{2c^2} (\partial_\tau \vec{\varphi}_i)^2 + \frac{1}{2} (\nabla \vec{\varphi}_i)^2 + \frac{r}{2} \vec{\varphi}_i^2 + \frac{u}{4} (\vec{\varphi}_i^2)^2 \right]. \quad (2.27c)$$

²Compared to the action (2.25) this is a shift $\vec{\varphi}_\mathbf{q} \rightarrow \vec{\varphi}_{\mathbf{Q} + \mathbf{q}}$.

Here, λ is the “Yukawa coupling” constant between fermionic and bosonic fields, c is the bare bosonic velocity, and the parameters r and u control the magnitude of the SDW fluctuations. In a mean-field theory for S_B alone long-range SDW order is present for $r \leq 0$, but this transition point is shifted by interactions. The derivatives in Eq. (2.27) need to be discretized appropriately for the actual space-time lattice. A first understanding of the physics of the combined model (2.27) can be found in mean-field theory. We can distinguish two phases: a Fermi liquid with $\langle \vec{\varphi} \rangle = 0$ and an ordered SDW phase with $\langle \vec{\varphi} \rangle \neq 0$. To describe them on mean-field level we replace in S_{FB} the field $\vec{\varphi}_q$ by its uniform expectation value $\langle \vec{\varphi}_q \rangle_{MF} = \delta_{q,0} \vec{\varphi}_0$, corresponding to perfect Néel order, and drop the action S_B for the now constant field. This procedure can be motivated by a saddle point approximation of S . Since rotational symmetry is broken spontaneously in the ordered phase, different directions of $\vec{\varphi}_0$ are equivalent and only its magnitude is important. Returning from the functional integral formalism, we obtain the mean-field Hamiltonian

$$\mathcal{H}_{MF} = \sum_{\mathbf{k},s} \varepsilon_{\mathbf{k}} c_{\mathbf{k},s}^\dagger c_{\mathbf{k},s} + \lambda \sum_{\mathbf{k},\mathbf{s},\mathbf{s}'} c_{\mathbf{k}+\mathbf{Q},s}^\dagger [\vec{s} \cdot \vec{\varphi}_0]_{ss'} c_{\mathbf{k},s'}. \quad (2.28)$$

In mean field the SDW order $\vec{\varphi}_0$ mixes only fermionic states at momenta \mathbf{k} and $\mathbf{k} + \mathbf{Q}$. Consequently, there is only a restricted set of zero-energy states (measured relatively to the chemical potential) on the Fermi surface that interact in \mathcal{H}_{MF} . They are found by taking the intersection of the Fermi surface and the Fermi surface shifted by \mathbf{Q} . If there is no intersection, e.g. if the Fermi surface for a cuprate-like dispersion (2.14) is too small, there is no SDW interaction at low energies. Otherwise in two dimensions we typically find a discrete set of intersection points. These are the “hot spots” illustrated in rows I and II of Fig. 2.4. As far as the low-energy physics of the action (2.27) is concerned, the close vicinities of the hot spots will remain the most important regions of the Brillouin zone also beyond mean field. There an electron at \mathbf{k} may scatter into a state at $\mathbf{k} + \mathbf{Q} + \mathbf{q}$, but \mathbf{q} will generally be small compared to the size of the Brillouin zone for the predominating $\vec{\varphi}_q$.

With the help of spinors $d_{\mathbf{k}}^\dagger = (c_{\mathbf{k},\uparrow}^\dagger, c_{\mathbf{k},\downarrow}^\dagger, c_{\mathbf{k}+\mathbf{Q},\uparrow}^\dagger, c_{\mathbf{k}+\mathbf{Q},\downarrow}^\dagger)$ we can write the Hamiltonian in the form $\mathcal{H}_{MF} = \sum'_{\mathbf{k}} d_{\mathbf{k}}^\dagger h_{\mathbf{k}} d_{\mathbf{k}}$, where the primed sum indicates that the summation now runs over a smaller set of momenta \mathbf{k} and $h_{\mathbf{k}}$ is a 4×4 -matrix

$$h_{\mathbf{k}} = \begin{bmatrix} \varepsilon_{\mathbf{k}} & & & \\ & \varepsilon_{\mathbf{k}} & & \lambda \vec{\varphi}_0 \cdot \vec{s} \\ \hline & & \varepsilon_{\mathbf{k}+\mathbf{Q}} & \\ \lambda \vec{\varphi}_0 \cdot \vec{s} & & & \varepsilon_{\mathbf{k}+\mathbf{Q}} \end{bmatrix}. \quad (2.29)$$

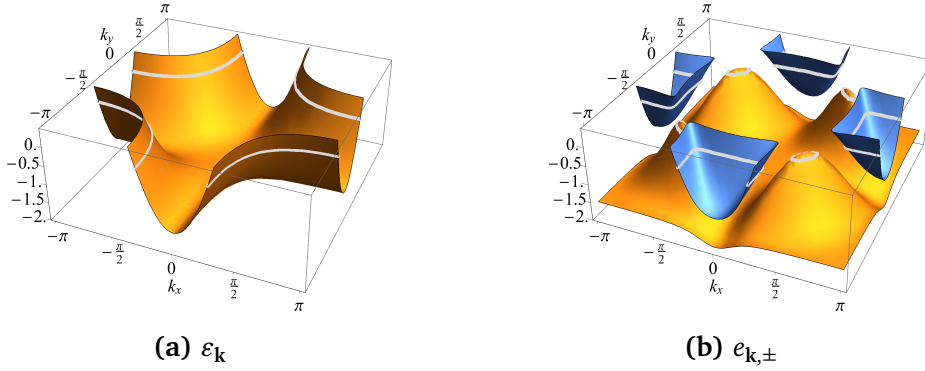


Figure 2.3: 3D plots of (a) the original dispersion ε_k from Eq. (2.14) with $t = 1$, $t' = -0.5$, $\mu = -0.5$, and of (b) the hybridized mean-field dispersion $e_{k,\pm}$ from Eq. (2.30) for SDW order $|\vec{\varphi}_0| = 0.4$. The Fermi surfaces are marked by gray lines, compare Fig. 2.4c.

This matrix is easily diagonalized and we find two-fold degenerate single-electron energy eigenvalues

$$e_{k,\pm} = \frac{\varepsilon_k + \varepsilon_{k+Q}}{2} \pm \sqrt{\left(\frac{\varepsilon_k - \varepsilon_{k+Q}}{2}\right)^2 + (\lambda\vec{\varphi}_0)^2}. \quad (2.30)$$

In the presence of SDW order, $e_{k,\pm}$ give the dispersion for two electronic bands. Filling up the lowest-energy states both bands we find the new Fermi surface as illustrated in Fig. 2.3. For $|\vec{\varphi}_0| > 0$ gaps open at the hot spots and the originally “large” Fermi surface is reconstructed into “small” Fermi pockets, see row III in Fig. 2.4. As $|\vec{\varphi}_0|$ increases, these pockets shrink. For the half-filled system they vanish simultaneously, in the hole-doped case the electron pockets disappear first, while in the electron-doped case the hole pockets disappear first, see row IV in Fig. 2.4. A configuration of small Fermi pockets is a generic feature of an SDW-ordered Fermi liquid.

2.2.3 Analytical approaches beyond mean field

The pioneering work on quantum criticality in Fermi liquids was presented by Hertz [29], who studied magnetic transitions by a renormalization group method. Millis later extended this work and added the evaluation of finite-temperature crossovers [30]. In Hertz-Millis theory the fermions are integrated out and only low-energy order parameter fluctuations are kept in the action. While this step is formally exact, in the presence of gapless fermionic excitations the resulting coefficients can be highly non local. A priori it is not clear that such an action can be expanded in $\vec{\varphi}$

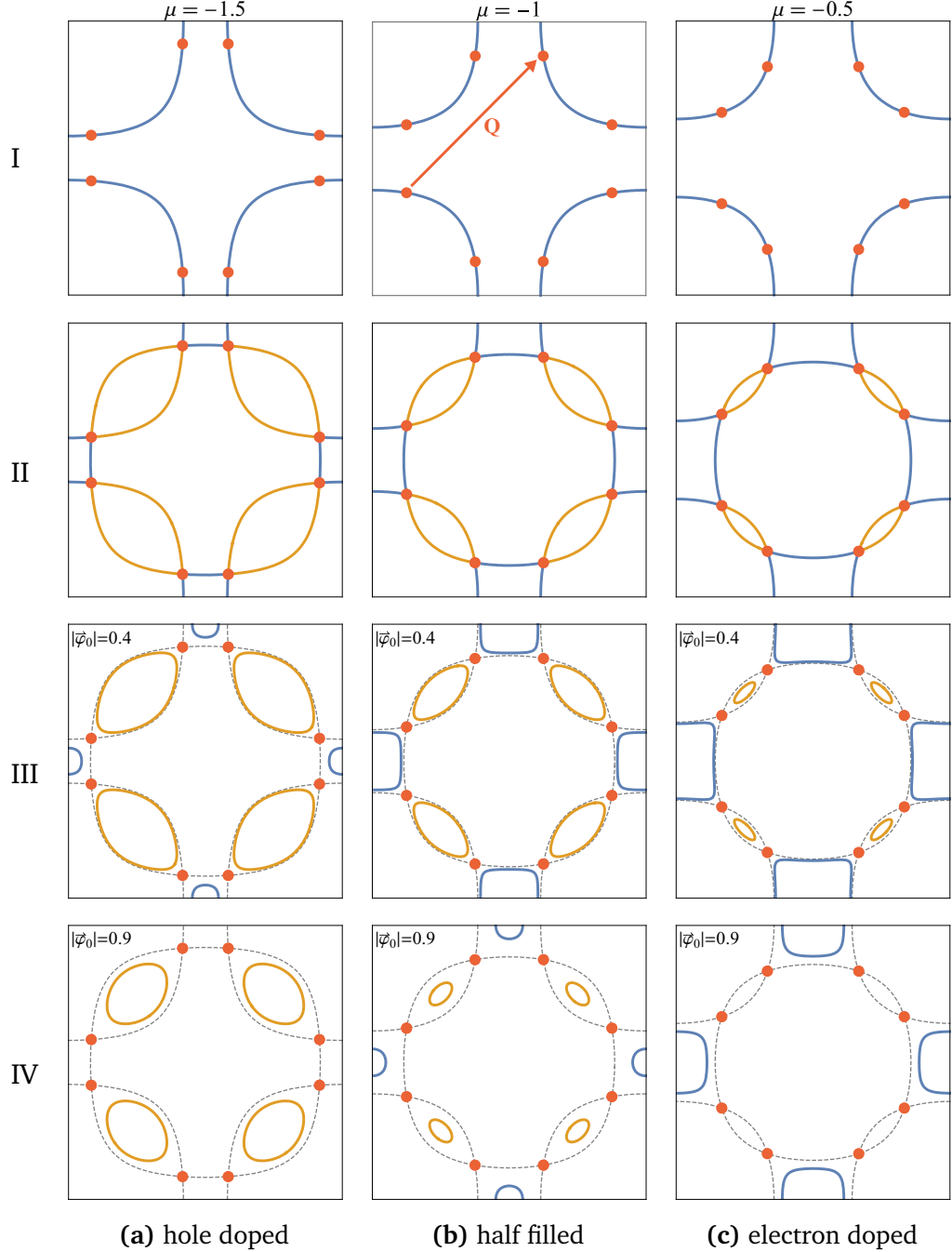


Figure 2.4: Mean-field transformation of the Fermi surface due to SDW order for Eq. (2.14) with $t = 1$, $t' = -0.5$, and (a) $\mu = -1.5$, (b) $\mu = -1$, (c) $\mu = -0.5$. The momentum $\mathbf{k} = (0, 0)^T$ is at the center of each plot, as in Fig. 2.2b. Row I: Fermi surface without SDW order with hot spots separated by $\mathbf{Q} = (\pi, \pi)^T$. Row II: Original Fermi surface together with surface shifted by \mathbf{Q} ; hot spots are at the intersection points. Row III: Small Fermi surfaces with SDW order $|\vec{\varphi}_0| = 0.4$, computed from Eq. (2.30). Row IV: With $|\vec{\varphi}_0| = 0.9$ electron pockets have shrunk to zero in case (a), while both pockets disappear simultaneously in case (b) and hole pockets have vanished in case (c).

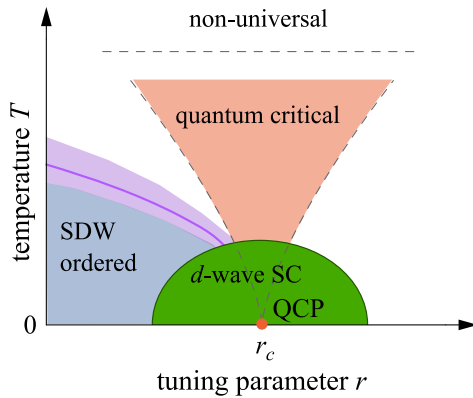


Figure 2.5: Proposed schematic phase diagram in the vicinity of an antiferromagnetic metallic quantum critical point. Next to a spin-density wave (SDW) ordered phase a d -wave superconducting (SC) dome emerges atop the quantum critical point (QCP). Compare to Fig. 2.1.

and that a controlled truncation of this expansion is possible. Assuming that one can proceed in this way, the resulting action for the case of the ordering wave vector \mathbf{Q} connecting a $(d - 2)$ -dimensional hot manifold is

$$S = \int \frac{d^d k}{(2\pi)^d} T \sum_{\omega_n} \frac{1}{2} [\mathbf{k}^2 + \gamma |\omega_n| + r] |\vec{\varphi}(\mathbf{k}, \omega_n)|^2 + \frac{u}{4} \int d^d x d\tau (\vec{\varphi}(\mathbf{x}, \tau)^2)^2. \quad (2.31)$$

In contrast to a conventional $\vec{\varphi}^4$ theory, the dynamical term is replaced by $|\omega_n|$. This describes Landau damping, the possibility for order parameter fluctuations to decay into particle-hole pairs. Therefore the dynamical critical exponent in this theory is $z = 2$.

Subsequent theoretical analysis of the spin-fermion model has shown that in spatial dimension $d = 2$ the quantum critical theory of metallic antiferromagnetism is generically strongly coupled and that the Hertz-Millis approach is invalid in this case [27, 31–33]. It appears to be very important to keep the low energy fermions as active parts of the theory, as in the proposed action (2.27).

Alternative popular approaches include a $1/N$ expansion in the inverse number of fermion flavors N [6]. But this method is uncontrolled in $d = 2$, too [32, 34]. Alternative expansion have been introduced [35, 36] or have been found to emerge from an exact calculation [37]. Despite this and further work on antiferromagnetic quantum criticality in metals [38–45], a fully controlled analytical treatment remains a major challenge and basic characteristics of this quantum critical point are continuously under debate.

It has long been known that strong order parameter fluctuations at a spin-density

wave instability in a metal can mediate unconventional singlet electron pairing with a d -wave form factor [46]. Building on this, several studies have proposed an anomalous enhancement of superconductivity at a spin-density wave quantum critical point [47–50]. The generic phase diagram of Fig. 2.1b would then be extended by a superconducting phase close to the critical point, leading to a phase diagram similar to Fig. 2.5.

Hyperscaling is violated at this antiferromagnetic quantum critical point and at $d \geq 2$ the quantum critical theory is above its upper critical dimension. Concomitant with this, more microscopic details matter than for the simpler bosonic effective theories discussed above in Sec. 2.1.4 and simple scaling relations such as Eqs. (2.7) and (2.8) are broken. Nevertheless, from the theoretical analysis of the low-energy theory (2.27) [27, 31–33] it is widely believed that, while details of the Fermi surface matter, fermionic excitations near the hot spots are by far the most important, such that only the structure of these hot spots matters for the universal physics near the quantum critical point. Details and topology of the Fermi surface away from these hot spots are expected to be irrelevant.

In this spirit Metlitski and Sachdev have developed a theory focusing on the vicinity of the hot spots with a *linearized* Fermi surface [32]. They find spin-density wave fluctuations to give rise to a d -wave superconducting instability and that, in this linearized theory, an additional pseudospin symmetry emerges, relating the superconducting order to a charge-density wave (CDW) order with the same form factor at an ordering wavevector collinear with \mathbf{Q} . From this, one would expect also tendencies towards CDW order close to the quantum critical regime. Strong fluctuations of the resulting multi-component order parameter have also been proposed as the origin of the pseudogap in the cuprates [39, 51–53]. It has not been established, however, if this fluctuation regime is important beyond the linearized theory.

Spin-density wave interactions at the quantum critical point may also enhance other types of CDW order [54] or further types of subsidiary order such as pair-density waves (PDW) [55, 56].

In summary, the lack of a controlled solution of the spin-fermion model combined with the great physical interest in the properties of the SDW quantum critical point make it highly desirable to add the additional perspective provided by an unbiased numerically-exact method such as quantum Monte Carlo. While also this approach has long been thwarted by the presence of the Fermi surface, leading to the infamous fermion sign problem, we will see in Part II how such simulations can be made viable. But before we move on to more technical discussions, the next Chapter will briefly introduce some of the experimental systems where the SDW quantum critical point is thought to be important.

3 Unconventional superconductivity on the verge of antiferromagnetism

The discovery of unconventional high-temperature superconductivity in the cuprates [57] is frequently counted as one of major scientific breakthroughs of the twentieth century. The question of the mechanism behind superconductivity in these systems and the understanding of their normal state physics, however, is far from settled [58]. Unconventional superconductivity, that contradicted the expectations from classic Bardeen-Cooper-Schrieffer (BCS) theory [59], had already been found earlier in heavy fermion systems [60] and in organic salts [61], albeit at lower transition temperatures. In the mean time other classes of unconventional superconductors such as the iron based superconductors [62] have been discovered.

While there is quite a variation in the chemical composition of these strongly correlated materials, a group of them, namely the cuprates, the iron based superconductors, and some of the heavy fermion materials, share a wealth of common features in their phase diagrams, which ultimately suggests that spin-fluctuation mediated electron pairing is involved in the formation of the superconducting phase [7]. The crystal structure for all these materials is built from quasi-two-dimensional layers containing square arrays of d - or f -electron cations. Their phase diagrams as function of temperature and doping all show an antiferromagnetic or spin-density wave ordered phase in close proximity to an unconventional superconducting phase. In some cases there is coexistence between these two types of order. Several experiments, employing for instance NMR or neutron scattering measurements, show a strong coupling between superconductivity and antiferromagnetism.

In these cases the superconductors are *unconventional* in the sense that their momentum resolved superconducting gap function Δ changes sign between parts of the Fermi surface that are linked by the spin-density wave ordering wavevector \mathbf{Q} : $\text{sgn } \Delta(\mathbf{k} + \mathbf{Q}) = -\text{sgn } \Delta(\mathbf{k})$. These include anisotropic d -wave symmetry, where the gap changes sign under a $\pi/2$ rotation, or isotropic s -wave symmetry in combination with a sign change under \mathbf{Q} . In contrast to this, conventional BCS superconductors have s -wave symmetry without sign change.

The phase diagrams for two Ce-based heavy fermion materials are shown in Fig. 3.1. With material (a) there is a superconducting phase whose transition temperature T_c decreases with increasing concentration x of Cd until superconductivity

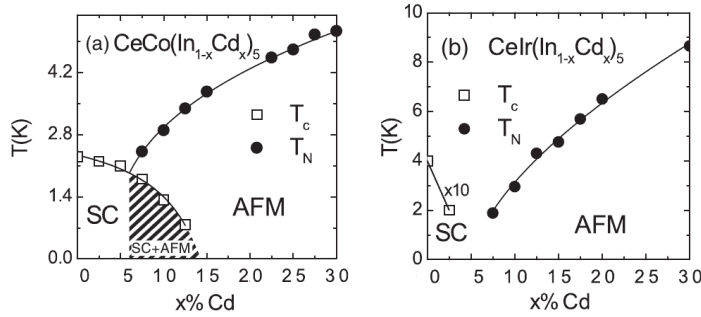


Figure 3.1: Finite-temperature phase diagrams as function of Cd-doping for two heavy-fermion Ce-115 systems: (a) $\text{CeCo}(\text{In}_{1-x}\text{Cd}_x)_5$ [63], (b) $\text{CeIr}(\text{In}_{1-x}\text{Cd}_x)_5$ with T_c multiplied by a factor of 10 [64]. Both display superconducting (SC) and antiferromagnetic (AFM) order. In case (a) there is a region of coexistence of both orders. Reprinted figure with permission from D.J. Scalapino, Rev. Mod. Phys. **84**, 1383 (2012). © 2012 by the American Physical Society [7].

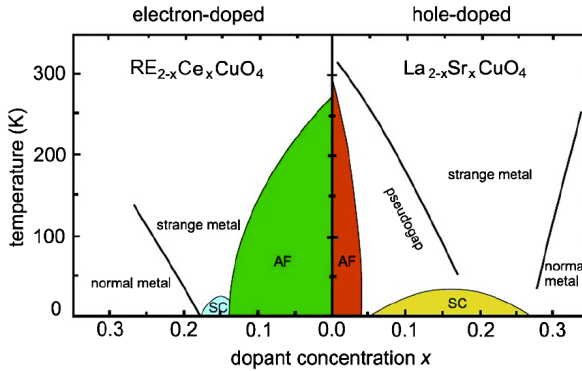


Figure 3.2: Schematic phase diagrams for hole-doped $\text{La}_{2-x}\text{Sr}_x\text{CuO}_4$ and electron-doped $\text{RE}_{2-x}\text{Ce}_x\text{CuO}_4$ ($\text{RE} = \text{La}, \text{Pr}, \text{Nd}$) cuprates [65]. Reprinted figure with permission from D.J. Scalapino, Rev. Mod. Phys. **84**, 1383 (2012). © 2012 by the American Physical Society [7].

appears to be absent at $x \approx 0.15$. For $x \gtrsim 0.05$ an antiferromagnetic phase emerges with a transition temperature T_N that increases with doping. There is an intermediate doping regime where both types of order coexist. The phase diagram of material (b), where Co is replaced by Ir, is similar, although the maximum T_c is lower and with increasing doping superconductivity vanishes before antiferromagnetism sets in.

Fig. 3.2 displays the schematic phase diagrams for two cuprate compounds. The undoped materials are insulators that undergo an antiferromagnetic Néel transition as the temperature is lowered. When La is replaced by Sr, the copper oxide layers are hole doped, while the introduction of Ce leads to electron doping. With increasing

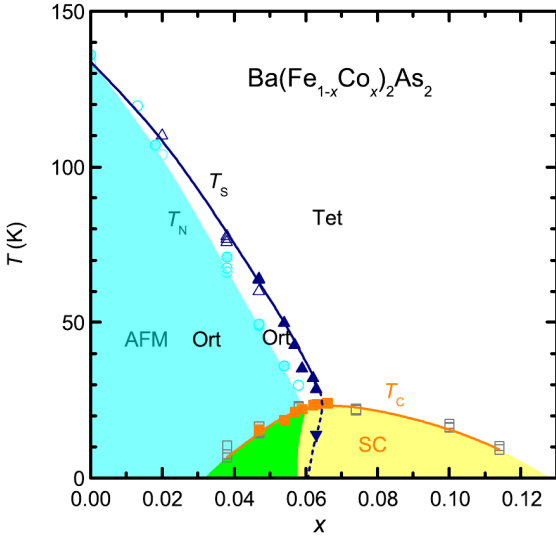


Figure 3.3: Temperature-doping phase diagram for the iron-arsenide superconductor $\text{Ba}(\text{Fe}_{1-x}\text{Co}_x)\text{As}_2$ showing a region of coexistence of antiferromagnetism (AF) and superconductivity (SC) [66]. T_s is the structural transition temperature, T_N is the Néel temperature, and T_c is the onset temperature of superconductivity. Reprinted figure with permission from D.J. Scalapino, Rev. Mod. Phys. **84**, 1383 (2012). © 2012 by the American Physical Society [7].

doping the Néel temperature is first reduced, then a superconducting phase emerges. In the electron-doped case the optimal doping leading to maximal T_c is close to the onset of antiferromagnetism, while there is a clear separation in the hole-doped case.

In Fig. 3.3 we have the phase diagram for an iron-based superconductor. The undoped ($x = 0$) material is metallic and is subject to a structural transition from a tetragonal to an orthorombic lattice, which is linked to an electronic nematic transition. At the same temperature it undergoes an antiferromagnetic SDW transition. With increased concentration of Co the system is electron doped, which suppresses the structural and magnetic transition temperatures. At finite doping the structural transition temperature T_s is slightly higher than the magnetic Néel temperature T_N . For $x \gtrsim 0.07$ both T_s and T_N collapse to zero and superconductivity sets in. The maximum T_c of the superconducting dome is located close to this point. Similarly to the heavy fermion phase diagram of Fig. 3.1a there is an intermediate doping region $0.03 \lesssim x \lesssim 0.06$, where superconductivity and spin-density wave order coexist. Here also orthorombic order is present.

Especially the phase diagrams of the heavy fermion compound $\text{CeCo}(\text{In}_{1-x}\text{Cd}_x)_5$, the electron-doped cuprates, and the iron-based superconductor $\text{Ba}(\text{Fe}_{1-x}\text{Co}_x)\text{As}_2$

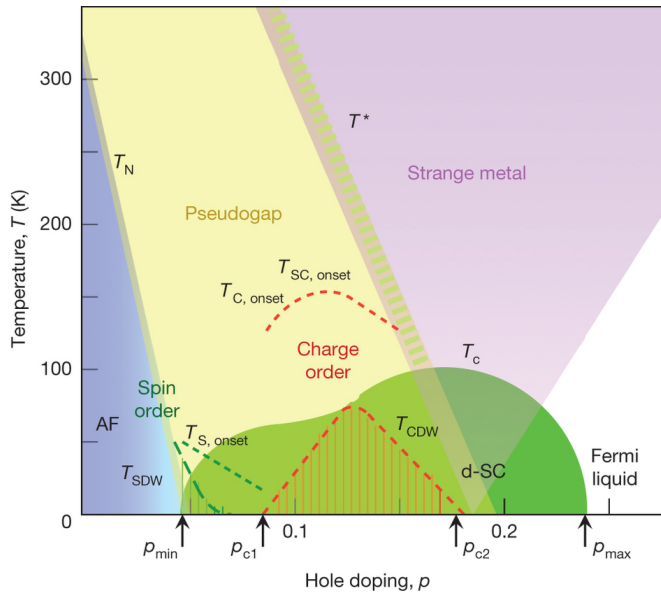


Figure 3.4: Schematic detailed phase diagram for hole-doped cuprates as function of doping and temperature. Reprinted by permission from Macmillan Publishers Ltd: *Nature*. B. Keimer et al., *Nature* **518**, 179 (2015), © 2015 [69].

suggest that the magnetic fluctuations close to a spin-density wave quantum critical point may give rise to the dome-shaped superconducting phase that appears near the endpoint of an antiferromagnetic phase. This interpretation is supported by the observation of *strange metal* behavior in many of these materials, see Ref. [67] for a review. In a region of the phase diagram above the superconducting phase the electrical resistivity ρ is found to be linear in the temperature T . This stands in stark contrast to the regular characteristics of a standard Fermi liquid with $\rho \sim T^2$ at low temperatures. This non-Fermi liquid behavior of transport quantities can be related to the quantum critical regime of a zero temperature critical point underlying the superconducting dome. Similar features have also been seen in an organic superconductor close to a magnetic quantum critical point [68].

The physics of the hole-doped cuprates appear to be particularly rich and complicated [69]. Their phase diagram, schematically shown in Fig. 3.4, contains the unique and puzzling *pseudogap* regime below a crossover temperature T^* , where the electronic density of states is substantially suppressed at low energies without a simple relation to a broken symmetry. There are also tendencies towards multiple competing or “intertwined” orders [70] including charge-density wave (CDW) order. Most likely there are multiple quantum critical points underneath this superconducting dome.

Part II

**Numerically exact solution by
quantum Monte Carlo**

4 Quantum Monte Carlo approach

The objects of interest of research in condensed matter physics are the rich collective phenomena that arise in many-particle systems. Still, to a surprisingly high degree, our understanding of physics is based on single-particle theories, which are successful as long as interactions between the constituents of a system can be handled perturbatively. Starting with Landau's Fermi liquid theory, much of solid state theory, for example, has been developed in terms of weakly interacting quasiparticles as elementary excitations. Once systems become more complex or interactions strong, however, these theories reach their limits. Understanding the intricate, emergent behavior of systems composed of a macroscopic number of strongly correlated fermions, that gives rise to novel, distinctly quantum phases of matter such as high-temperature superconductors, non-Fermi liquid metals, or quantum spin liquids, requires to fully take into account interactions. Exact solutions of the relevant microscopic models are extraordinary feats, but to a large extent analytical theory fails at describing systems of this kind. Mean-field theory and effective field theories can provide guiding insight and lead to physical understanding, but they often rely on severe approximations which are not well controlled. Underlying assumptions are frequently under debate and can lead to conflicting predictions. Therefore, unbiased numerical simulations are an essential tool to address these problems. Not only do they allow to verify and test the extend of validity of basic assumptions, putting analytical theories on solid ground and providing the means to discriminate between multiple candidates, but they also serve as an instrument of quantitative guidance, for instance when numerically exact phase diagrams are mapped out. The complexity of the problems in quantum many-body physics has lead to the development of a great variety of sophisticated numerical techniques that take advantage of today's large-scale computing facilities [71, 72].

Principally, a quantum many-body system on a finite-size lattice can be solved by diagonalizing the Hamiltonian operator. However, since the Hilbert space grows exponentially with system size, exact diagonalization is limited to only very small systems. While sophisticated sparse methods to compute low-lying eigenstates have been pushed to reach up to dozens of sites in problems of frustrated magnetism [73, 74], in most cases these methods are mostly of use as benchmarks and when no other numerically exact technique is available.

In recent years the density matrix renormalization group (DMRG) [75–77] has been developed into a very powerful technique. Fundamentally, it is a variational method that minimizes entanglement. DMRG is the most versatile method available

in one spatial dimension. Despite considerable advances, two and higher dimensions, however, remain problematic [78]. Here the numerical cost scales exponentially with the circumference of two-dimensional systems when the boundary or “area” law of quantum information theory governs the entanglement entropy for gapped systems [79]. Nevertheless, first results for such systems have been obtained by DMRG. These famously include the identification of the spin-liquid ground state of the antiferromagnetic Heisenberg model on the kagome lattice [80], but also itinerant systems in two dimensions such as a weakly interacting Hubbard model at and off half-filling are studied by DMRG [81].

Stochastic Monte Carlo techniques arguably provide the most general toolbox for, within controlled error bars, numerically exact simulations of statistical systems in equilibrium with polynomially scaling computational effort. The simulation of quantum mechanical many-body systems requires mapping the problem to a classical system, which will generally introduce an extra dimension of “imaginary time”. The methods that realize such a mapping in simulations are collected under the umbrella term of quantum Monte Carlo (QMC) [82]. For quantum problems formulated on lattices of at least moderate size in two or three dimensions, QMC simulations are often the only viable choice for numerically exact studies. The major limitation of QMC is the fermion sign problem, discussed below in Sec. 4.2, which can be inherent to the quantum-classical mapping. It amplifies statistical uncertainties exponentially in system size and inverse temperature, often rendering simulations infeasible. But in the absence of a sign problem QMC is very powerful. This is the case for bosonic systems and spin systems without frustration from lattice or interaction, for which advanced world line [83] and stochastic series expansion [84] methods are available. For systems of itinerant fermions on lattices, which are the subject matter of this thesis, the sign problem is prevalent unless one finds a way to set up an action for the problem at hand that features a remedial symmetry. The discovery of such a formulation can be the breakthrough that paves the way towards the first controlled numerically exact solution of a problem. For a two-dimensional metal in the vicinity of an antiferromagnetic quantum critical point such a recipe for sign-problem-free QMC simulations was presented in Ref. [11], which we review in Sec. 4.3. In the following we first discuss the general standard approach to QMC simulations for fermions on lattices.

4.1 Determinantal quantum Monte Carlo (DQMC)

A Hamiltonian of interacting fermions contains terms that are at least quartic in creation and annihilation operators. While such terms cannot readily be integrated,

an auxiliary field can be introduced via a Hubbard-Stratonovich transformation, producing an action that is only quadratic in fermions at the expense of a bosonic extra degree of freedom. The action (2.27) of a metal coupled to an SDW order parameter, that has been introduced in Sec. 2.2, can be understood in this way. For each configuration of this bosonic field only a quadratic fermion Hamiltonian needs to be considered, which reduces the problem to a simple Gaussian integral, solving which involves the computation of a determinant. In all practical cases it remains impossible to enumerate all such bosonic configurations; hence, it is favorable to apply a Monte Carlo importance sampling scheme. In the following we describe the Blankenbecler-Scalapino-Sugar (BSS) algorithm for the simulation of coupled boson-fermion systems [8], which was published in 1981 and to this day remains the standard algorithm for fermionic lattice systems at finite temperature. The aim of this Chapter is to give a self-contained introduction to the algorithm, while further important, but more technical, aspects are discussed in Chap. 5. This presentation is based on several pedagogical texts introducing the method [83, 85–87]. A helpful introduction is also provided in the recently published textbook by Gubernatis, Kawashima, and Werner [82].

4.1.1 Basic formalism

Our starting point is the partition function \mathcal{Z} at temperature $T = 1/\beta$ expressed as a functional integral over a fermionic field c , c^\dagger and a bosonic field φ with an action $S = S_F + S_{FB} + S_B$:

$$\mathcal{Z} = \int D(c, c^\dagger, \varphi) e^{-S}, \quad (4.1)$$

where

$$S_F = S_F[c, c^\dagger] = \int_0^\beta d\tau \underline{c}^\dagger(K + \partial_\tau)\underline{c}, \quad (4.2a)$$

$$S_{FB} = S_{FB}[c, c^\dagger, \varphi] = \int_0^\beta d\tau \underline{c}^\dagger V[\underline{\varphi}] \underline{c}, \quad (4.2b)$$

and $S_B = S_B[\varphi]$ is a functional of the bosonic field only. Here we think of a finite system of N_s single-particle states distributed over a d -dimensional lattice, $\underline{c}^\dagger = (c_1^\dagger, \dots, c_{N_s}^\dagger)$ is a fermionic vector at imaginary time τ , and $\underline{\varphi} = (\varphi_1(\tau), \dots, \varphi_{N_s}(\tau))^\top$ is the bosonic configuration at τ . The matrix K contains “kinetic” terms without

interactions, while the interactions mediated by the field φ are encoded in the matrix $V[\varphi]$. Generally, K and V do not commute. With the path integral formulation of the action a $d+1$ -dimensional spacetime has already been introduced.

The structure of the fermionic part of the action (4.2) allows us to express it in terms of a single-particle Hamiltonian matrix $\mathcal{H} = K + V[\varphi]$. To prepare for numeric evaluation we write the partition function as a trace in Fock space integrated over all possible bosonic configurations,

$$\mathcal{Z} = \int D\varphi e^{-S_B[\varphi]} \text{Tr} \left[e^{-\int_0^\beta d\tau \underline{c}^\dagger [K + V[\varphi]] \underline{c}} \right], \quad (4.3)$$

and discretize imaginary time, $\tau = \ell \Delta\tau$, $\beta = m \Delta\tau$:

$$\mathcal{Z} = \int D\varphi e^{-S_B[\varphi]} \text{Tr} \left[\exp \left(-\sum_{\ell=1}^m \Delta\tau \underline{c}^\dagger [K + V[\varphi(\ell \Delta\tau)]] \underline{c} \right) \right]. \quad (4.4)$$

This is tantamount to thinking of a model defined on a finite spacetime lattice, although we will generally be interested in the extrapolated limits $N_s \rightarrow \infty$ and $m \rightarrow \infty$, the latter being equivalent to the imaginary time continuum limit $\Delta\tau \rightarrow 0$.

Accepting a controlled systematic error, we can split the exponential of a linear combination of noncommuting operators K, V via a symmetric Suzuki-Trotter decomposition [88]:

$$e^{-\Delta\tau(K+V)} = e^{-\frac{\Delta\tau}{2}K} e^{-\Delta\tau V} e^{-\frac{\Delta\tau}{2}K} + O(\Delta\tau^3). \quad (4.5)$$

Having discretized imaginary time, we can repeatedly apply Eq. (4.5) to split the exponential under the trace in Eq. (4.3) and, from now on dropping the underlines, find:

$$\exp \left(-\sum_{\ell=1}^m \Delta\tau \underline{c}^\dagger [K + V[\varphi(\ell \Delta\tau)]] \underline{c} \right) = \prod_{\ell=m}^1 U_\ell + O(\Delta\tau^2), \quad (4.6)$$

where we observe $m \cdot O(\Delta\tau^3) = O(\beta \Delta\tau^2) = O(\Delta\tau^2)$ and have introduced the φ -dependent operators U_ℓ given by

$$U_\ell = e^{-\frac{\Delta\tau}{2} \underline{c}^\dagger K \underline{c}} e^{-\Delta\tau \underline{c}^\dagger V[\varphi(\ell \Delta\tau)] \underline{c}} e^{-\frac{\Delta\tau}{2} \underline{c}^\dagger K \underline{c}}. \quad (4.7)$$

For notational convenience in the further development of the formalism the order of the operators U_ℓ in the product in Eq. (4.6) is descending: $\prod_{\ell=m}^1 U_\ell = U_m U_{m-1} \cdots U_1$.

Note that, if K and $V[\varphi]$ were simultaneously real representable, we could use a lower order Trotter decomposition and still achieve an overall systematic error of $O(\Delta\tau^2)$ in Eq. (4.6) [89].

Finally, making use of property A.3 shown in Appendix A, we can evaluate the trace:

$$\begin{aligned} \mathcal{Z} &= \int D\varphi e^{-S_B[\varphi]} \text{Tr} \left[\prod_{\ell=m}^1 U_\ell \right] + O(\Delta\tau^2) \\ &= \int D\varphi e^{-S_B[\varphi]} \det \left[\mathbb{I} + \prod_{\ell=m}^1 B_\ell \right] + O(\Delta\tau^2) \end{aligned} \quad (4.8)$$

with φ -dependent matrices

$$B_\ell = e^{-\frac{\Delta\tau}{2}K} e^{-\Delta\tau V[\varphi(\ell\Delta\tau)]} e^{-\frac{\Delta\tau}{2}K}. \quad (4.9)$$

Under the condition that S_B is real and that the determinant always evaluates to a positive real number the formulation (4.8) of the partition function is very advantageous: The strictly positive integrand can be interpreted as a probability measure, enabling sampling by Monte Carlo techniques. In every other case we have a sign (or complex phase) problem, which we discuss in detail in Sec. 4.2 below. For the time being we will assume this problem to be absent and give an overview over how determinantal quantum Monte Carlo (DQMC) simulations based on Eq. (4.8) are set up in the following sections.

4.1.2 Markov chain Monte Carlo sampling

There is vast body of high-quality literature discussing Monte Carlo simulations in statistical physics, so here we only give a cursory introduction and point to textbooks [90–94] and lecture notes [95–98] for details.

With Eq. (4.8) we have transformed the partition function into the form

$$\mathcal{Z} = \int D\varphi p[\varphi], \quad (4.10)$$

where we assume $p[\varphi] > 0$ for all configurations φ . We are mainly interested in

computing expectation values of physical observables \mathcal{O} , which are given by

$$\langle \mathcal{O} \rangle = \frac{1}{\mathcal{Z}} \int D\varphi p[\varphi] \langle \mathcal{O} \rangle_\varphi. \quad (4.11)$$

Therefore $p[\varphi]/\mathcal{Z}$ can be seen as the probability density associated to a configuration φ , which in this high-dimensional integral appropriately weights the various contributions $\langle \mathcal{O} \rangle_\varphi$ to $\langle \mathcal{O} \rangle$. When we do a Monte Carlo computation of $\langle \mathcal{O} \rangle$, we estimate its value statistically. We sample a high number M of configurations φ_i according to a probability distribution ρ , then compute an estimate $\widehat{\mathcal{O}}$ of $\langle \mathcal{O} \rangle$:

$$\langle \mathcal{O} \rangle \approx \widehat{\mathcal{O}} = \frac{\sum_{i=1}^M \langle \mathcal{O} \rangle_{\varphi_i} p[\varphi] \rho[\varphi]^{-1}}{\sum_{i=1}^M p[\varphi] \rho[\varphi]^{-1}}. \quad (4.12)$$

The best choice of ρ is proportional to the physical probability density p/\mathcal{Z} , leading to optimal importance sampling. Then Eq. (4.12) reduces to the sample mean $\overline{\mathcal{O}}$:

$$\widehat{\mathcal{O}} = \overline{\mathcal{O}} = \frac{1}{M} \sum_{i=1}^M \langle \mathcal{O} \rangle_{\varphi_i}. \quad (4.13)$$

The central limit theorem tells us that if we sample sufficiently many statistically independent configurations the estimate (4.13) will be normally distributed around the exact $\langle \mathcal{O} \rangle$ with variance

$$\sigma_{\overline{\mathcal{O}}}^2 = \left\langle [\overline{\mathcal{O}} - \langle \overline{\mathcal{O}} \rangle]^2 \right\rangle = \frac{\sigma_{\mathcal{O}}^2}{M}. \quad (4.14)$$

Integrals like Eq. (4.11) with a general distribution that is only known up to the normalization constant are best sampled by generating configurations iteratively in a **Markov process**. Such a process is specified by the transition probability $W_{mn} = W(\varphi_m \rightarrow \varphi_n)$ to go from a state φ_m to a state φ_n in one step. History older than φ_m does not influence this probability. The W_{mn} form a stochastic matrix if $W_{mn} > 0$ for all m, n and if $\sum_n W_{mn} = 1$ for all m . Starting from an arbitrary initial state φ_0 the distribution of the generated states φ_n will converge to a stationary distribution ρ if two conditions are met:

Ergodicity: Every state φ_n can eventually be reached from any φ_m in a finite number of steps: $(W^k)_{mn} > 0$ for all $k < K$ for some $K < \infty$.

Detailed balance: The transition probabilities have the following relation to the

target distribution:

$$\frac{W(\varphi_m \rightarrow \varphi_n)}{W(\varphi_n \rightarrow \varphi_m)} = \frac{\rho[\varphi_n]}{\rho[\varphi_m]}. \quad (4.15)$$

This is a sufficient condition for **balance**

$$\sum_m \rho[\varphi_m] W(\varphi_m \rightarrow \varphi_n) = \rho[\varphi_n], \quad (4.16)$$

but detailed balance is easier to verify and a process satisfying only balance and not detailed balance may have weaker convergence properties.

The first algorithm that has been presented to satisfy detailed balance is the **Metropolis** algorithm [99], which is still the most widely used. Here the transition probability is expressed as $W(\varphi_m \rightarrow \varphi_n) = g(\varphi_m \rightarrow \varphi_n)A(\varphi_m \rightarrow \varphi_n)$, where g is the probability the new state φ is proposed with and A is the probability that this newly proposed state is accepted. The proposal probabilities are chosen symmetric

$$\frac{g(\varphi_m \rightarrow \varphi_n)}{g(\varphi_n \rightarrow \varphi_m)} = 1 \quad (4.17)$$

and detailed balance is satisfied through the Metropolis acceptance probability

$$A(\varphi_m \rightarrow \varphi_n) = \min \left\{ 1, \frac{\rho[\varphi_n]}{\rho[\varphi_m]} \right\}. \quad (4.18)$$

Two additional general considerations need to be taken into account in practical Monte Carlo simulations: First, the generated states of the Markov chain are not statistically independent. In consequence the variance of the observable mean $\bar{\mathcal{O}}$ is modified from Eq. (4.14) and reads [100, 101]

$$\sigma_{\bar{\mathcal{O}}}^2 = (1 + 2\tau_{\mathcal{O},\text{int}}) \frac{\sigma_{\mathcal{O}}^2}{M} \quad (4.19)$$

with an integrated autocorrelation time $\tau_{\mathcal{O},\text{int}} \geq 0$. While the standard error $\delta \bar{\mathcal{O}} = \sqrt{\sigma_{\bar{\mathcal{O}}}^2}$ of a Monte Carlo estimate still goes to zero like $1/\sqrt{M}$ with increasing number of samples M , we see that it is crucial for efficient sampling to choose proposal probabilities that reduce statistical correlations in the Metropolis algorithm or to devise more advanced problem adapted sampling schemes. This is a bit of an art and will be discussed in Chap. 5. The second point to keep in mind is that, while

the Markov process will converge towards a stationary probability distribution, this will generally take a number of steps characterized by a relaxation time when we start from a random initial configuration. It is then necessary to allow for a phase of thermalization at the beginning of a simulation during which samples are not included in observable measurements.

At this point it is easy to see how the Markov chain for a DQMC algorithm can be set up. We start with a random initial spacetime configuration of the auxiliary field φ and successively propose small changes $\varphi \rightarrow \varphi'$ of this configuration, which we accept or reject according to Eq. (4.18) with ρ chosen to be the integrand of Eq. (4.8). The Metropolis acceptance probability is then given by

$$A(\varphi \rightarrow \varphi') = \min \left\{ 1, e^{-(S_B[\varphi'] - S_B[\varphi])} \frac{\det[\mathbb{1} + \prod_{l=m}^1 B'_l]}{\det[\mathbb{1} + \prod_{l=m}^1 B_l]} \right\}. \quad (4.20)$$

For the process of sampling as well as the evaluation of observables it is useful to introduce the equal-time **Green's function** for a constant field configuration φ :

$$G_\varphi(\tau = \ell \Delta\tau) \equiv G_\ell = (\mathbb{1} + B_\ell B_{\ell-1} \cdots B_1 B_m B_{m-1} \cdots B_{\ell+1})^{-1}. \quad (4.21)$$

Then the ratio of determinants in Eq. (4.20) can be written as¹

$$\begin{aligned} \frac{\det[\mathbb{1} + \prod_{k=m}^1 B'_k]}{\det[\mathbb{1} + \prod_{k=m}^1 B_k]} &= \frac{\det[\mathbb{1} + B'_m \cdots B'_1]}{\det[\mathbb{1} + B_m \cdots B_1]} \\ &= \frac{\det[\mathbb{1} + B'_\ell B'_{\ell-1} \cdots B'_1 B'_m B'_{m-1} \cdots B'_{\ell+1}]}{\det[\mathbb{1} + B_\ell B_{\ell-1} \cdots B_1 B_m B_{m-1} \cdots B_{\ell+1}]} = \frac{\det G_\ell}{\det G'_\ell} \end{aligned} \quad (4.22)$$

for any imaginary time slice ℓ .

In practice the evaluation of the long chains of matrix products in G_ℓ and of the ratio of determinants in Eq. (4.22) poses a numerical challenge because accumulated rounding errors can lead to severe instabilities. How these are handled in an efficient way will be discussed in Chap. 5.

¹Here we use that $\det(\mathbb{1} + AB) = \det(\mathbb{1} + BA)$ for square matrices A and B .

4.1.3 Observable expectation values

It remains to be discussed how physical observables \mathcal{O} are to be evaluated from a given configuration of the field φ to provide $\langle \mathcal{O} \rangle_\varphi$ for the estimate (4.13). In general, the expectation value of an observable is given by

$$\begin{aligned}\langle \mathcal{O} \rangle &= \frac{1}{\mathcal{Z}} \int D\varphi e^{-S_B} \text{Tr} \left[\mathcal{O} \exp \left(- \sum_{\ell=1}^m \Delta\tau c^\dagger [K + V[\varphi(\ell\Delta\tau)]] c \right) \right] \\ &= \frac{1}{\mathcal{Z}} \int D\varphi e^{-S_B} \text{Tr} \left[\mathcal{O} \prod_{\ell=m}^1 U_\ell \right] + O(\Delta\tau^2).\end{aligned}\quad (4.23)$$

This needs to be brought into the form (4.11) to determine $\langle \mathcal{O} \rangle_\varphi$.

4.1.3.1 Bosonic observables

Purely bosonic observables enter the integral as a c-number function of the field φ without influence of the fermions, so we directly have

$$\langle \mathcal{O}_{\text{bos}} \rangle = \frac{1}{\mathcal{Z}} \int D\varphi \mathcal{O}_{\text{bos}} e^{-S_B} \text{Tr} \left[\prod_{\ell=m}^1 U_\ell \right] + O(\Delta\tau^2)\quad (4.24)$$

and hence $\langle \mathcal{O} \rangle_\varphi = \mathcal{O}_{\text{bos}}[\varphi]$.

4.1.3.2 Fermionic equal time observables

A major advantage of the DQMC algorithm is that we have the freedom to compute the expectation value of arbitrary fermionic correlation functions. Let us first define the expectation value of an observable at imaginary time $\tau = \ell\Delta\tau$ for a fixed configuration of the field φ :

$$\langle \mathcal{O} \rangle_\varphi(\tau) = \frac{\text{Tr}[U_m \cdots U_{\ell+1} \mathcal{O} U_1 \cdots U_\ell]}{\text{Tr}[U_m \cdots U_1]}. \quad (4.25)$$

This can be understood in the imaginary time Heisenberg picture with a τ -dependent Hamiltonian $\mathcal{H} = K + V[\varphi]$. Eq. (4.25) is the discretized time version of

$$\langle \mathcal{O} \rangle_\varphi^{\text{cont}}(\tau) = \frac{\text{Tr} \left[\mathcal{O}(\tau) e^{-\int_0^\beta d\tau \mathcal{H}} \right]}{\text{Tr} \left[e^{-\int_0^\beta d\tau \mathcal{H}} \right]}, \quad \mathcal{O}(\tau) = e^{\int_0^\beta d\tau \mathcal{H}} \mathcal{O} e^{-\int_0^\beta d\tau \mathcal{H}}. \quad (4.26)$$

With Eq. (4.25) and

$$p[\varphi] = e^{-S_B[\varphi]} \det \left[\mathbb{1} + \prod_{\ell=m}^1 B_\ell \right] \quad (4.27)$$

we have

$$\langle \mathcal{O} \rangle(\tau) = \frac{1}{Z} \int D\varphi p[\varphi] \langle \mathcal{O} \rangle_\varphi(\tau). \quad (4.28)$$

Due to translational invariance in imaginary time all τ are equivalent and $\langle \mathcal{O} \rangle(\tau) \equiv \langle \mathcal{O} \rangle$. This also holds for the corresponding Monte Carlo estimate $\widehat{\mathcal{O}}(\tau)$, but the expectation values $\langle \mathcal{O} \rangle_\varphi(\tau)$ at different τ for one fixed φ are not necessarily equal. To improve effective statistics in simulations we generally average over imaginary time and compute $\widehat{\mathcal{O}} = \frac{1}{m} \sum_{\ell=1}^m \widehat{\mathcal{O}}(\ell \Delta \tau)$.

For single-particle observables $\mathcal{O} = \underline{c}^\dagger A \underline{c}$, that are bilinear in fermionic operators, Eq. (4.25) can be evaluated by introducing a source term and by applying property A.3:

$$\begin{aligned} \langle \mathcal{O} \rangle_\varphi(\tau) &= \frac{\partial \ln \text{Tr} [U_m \cdots U_{\ell+1} e^{\eta \mathcal{O}} U_\ell \cdots U_1]}{\partial \eta} \Bigg|_{\eta=0} \\ &= \frac{\partial \ln \det [\mathbb{1} + B_m \cdots B_{\ell+1} e^{\eta \mathcal{A}} B_\ell \cdots B_1]}{\partial \eta} \Bigg|_{\eta=0}. \end{aligned} \quad (4.29)$$

Since the relation $\ln \det X = \text{Tr} \ln X$ holds for any non-singular square matrix X , we have

$$\begin{aligned} \langle \mathcal{O} \rangle_\varphi(\tau) &= \text{Tr} \frac{\partial \ln [\mathbb{1} + B_m \cdots B_{\ell+1} e^{\eta \mathcal{A}} B_\ell \cdots B_1]}{\partial \eta} \Bigg|_{\eta=0} \\ &= \text{Tr} \left[(\mathbb{1} + B_m \cdots B_{\ell+1} e^{\eta \mathcal{A}} B_\ell \cdots B_1)^{-1} B_m \cdots B_{\ell+1} A e^{\eta \mathcal{A}} B_\ell \cdots B_1 \right] \Bigg|_{\eta=0} \\ &= \text{Tr} [B_\ell \cdots B_1 (\mathbb{1} + B_m \cdots B_1)^{-1} B_m \cdots B_{\ell+1} A] \end{aligned} \quad (4.30)$$

and with the help of a matrix identity, $X(\mathbb{1} + YX)^{-1}Y = \mathbb{1} - (\mathbb{1} + XY)^{-1}$, [102] we

obtain

$$\begin{aligned}\langle \mathcal{O} \rangle_\varphi(\tau) &= \text{Tr} \left[(\mathbb{1} - [\mathbb{1} + B_\ell \cdots B_1 B_m \cdots B_{\ell+1}]^{-1}) A \right] \\ &= \text{Tr} \left[(\mathbb{1} - G_\varphi(\tau)) A \right]\end{aligned}\quad (4.31)$$

with the equal time Green's function $G_\varphi(\tau)$ as defined in Eq. (4.21). We can, for example, evaluate $\langle c_b^\dagger c_a \rangle_\varphi$ with the matrix A given by $A_{c,d} = \delta_{c,a} \delta_{d,b}$ and find $\langle c_b^\dagger c_a \rangle_\varphi = \delta_{a,b} - G_\varphi(\tau)_{a,b}$. Therefore $\langle c_a c_b^\dagger \rangle_\varphi = G_\varphi(\tau)_{a,b}$ and we see that the Green's function is indeed defined sensibly.

In the DQMC algorithm we solve fermionic single-particle problems for fixed auxiliary field configurations. Therefore Wick's theorem applies, allowing us to reduce any multipoint correlation function to a sum of products of single-particle Green's functions. To see how this is done for products of operators $\mathcal{O}_i = \underline{c}^\dagger A^{(i)} \underline{c}$ we first define the cumulants

$$C_\varphi(\mathcal{O}_n, \dots, \mathcal{O}_1) = \frac{\partial^n \ln \text{Tr} [U_m \cdots U_{\ell+1} e^{\eta_n \mathcal{O}} \cdots e^{\eta_1 \mathcal{O}} U_\ell \cdots U_1]}{\partial \eta_n \cdots \partial \eta_1} \Bigg|_{\eta_n, \dots, \eta_1=0}. \quad (4.32)$$

By carrying out the derivatives we relate these cumulants to expectation values of products of the \mathcal{O}_i . For $n = 1$ and $n = 2$ we obtain

$$C_\varphi(\mathcal{O}_1) = \langle \mathcal{O}_1 \rangle_\varphi, \quad (4.33a)$$

$$C_\varphi(\mathcal{O}_2, \mathcal{O}_1) = \langle \mathcal{O}_2 \mathcal{O}_1 \rangle_\varphi - \langle \mathcal{O}_2 \rangle_\varphi \langle \mathcal{O}_1 \rangle_\varphi. \quad (4.33b)$$

Higher order cumulants arise as increasingly complex combinations of lower order cumulants. The cumulants can be computed in a similar way to Eqs. (4.29)–(4.31). For $\mathcal{O}_2 = c_\alpha^\dagger c_\beta$, $\mathcal{O}_1 = c_\gamma^\dagger c_\delta$ one finds for example [83]

$$C_\varphi(c_\alpha^\dagger c_\beta, c_\gamma^\dagger c_\delta) = \langle c_\alpha^\dagger c_\delta \rangle_\varphi \langle c_\beta c_\gamma^\dagger \rangle_\varphi \quad (4.34)$$

and with Eq. (4.33b) we have the relation

$$\langle c_\alpha^\dagger c_\beta c_\gamma^\dagger c_\delta \rangle_\varphi = \langle c_\alpha^\dagger c_\delta \rangle_\varphi \langle c_\beta c_\gamma^\dagger \rangle_\varphi + \langle c_\alpha^\dagger c_\beta \rangle_\varphi \langle c_\gamma^\dagger c_\delta \rangle_\varphi. \quad (4.35)$$

By (anti)commuting operators appropriately most physical correlation functions can be brought into the form of linear combinations of Eq. (4.35). Since the resulting expressions can become very lengthy it is advisable to use computer algebra software to help with this process [103]. Should higher-order correlation functions be necessary, recursive relations that give the $(n+1)$ th cumulant in terms of n th

cumulants can be derived.

4.1.3.3 Imaginary time displaced correlation functions

We can extend Eq. (4.25) to compute imaginary time displaced correlation functions in the presence of one auxiliary field configuration φ . For $\tau_1 = \ell_1 \Delta\tau$, $\tau_2 = \ell_2 \Delta\tau$, and $\tau_1 \geq \tau_2$ we have

$$\langle \mathcal{O}_1(\tau_1) \mathcal{O}_2(\tau_2) \rangle_\varphi = \frac{\text{Tr} [U_m \cdots U_{\ell_1+1} \mathcal{O} U_{\ell_1} \cdots U_{\ell_2} \mathcal{O} U_{\ell_2} \cdots U_1]}{\text{Tr} [U_m \cdots U_1]}. \quad (4.36)$$

After a Fourier transform this will allow us to compute susceptibilities at Matsubara frequencies $\omega_n = (2n + 1)\pi\beta$. For dynamic quantities at real frequencies ω it would be necessary to perform an analytic continuation of the Monte Carlo data, which in view of the statistical uncertainties is difficult to do in a controlled way.

By Wick's theorem correlation functions like Eq. (4.36) can again be reduced to linear combinations of single-particle Green's functions. The imaginary time displaced Green's function is

$$G_\varphi(\tau_1, \tau_2)_{\alpha, \beta} = \begin{cases} \langle c_\alpha(\tau_1) c_\beta^\dagger(\tau_2) \rangle_\varphi, & \text{if } \tau_1 \geq \tau_2, \\ -\langle c_\beta^\dagger(\tau_2) c_\alpha(\tau_1) \rangle_\varphi, & \text{if } \tau_2 > \tau_1, \end{cases} \quad (4.37)$$

and to evaluate it for the case $\tau_1 \geq \tau_2$ we write

$$G_\varphi(\tau_1, \tau_2)_{\alpha, \beta} = \frac{\text{Tr} [U_m \cdots U_{\ell_2+1} (U_{\ell_1} \cdots U_{\ell_{2+1}})^{-1} c_\alpha U_{\ell_1} \cdots U_{\ell_2} c_\beta^\dagger U_{\ell_2} \cdots U_1]}{\text{Tr} [U_m \cdots U_1]}. \quad (4.38)$$

When calculating this we encounter terms of the form $U_\ell^{-1} c_\alpha U_\ell$, which require the computation of $e^{\lambda \underline{c}^\dagger A \underline{c}} c_\alpha e^{-\lambda \underline{c}^\dagger A \underline{c}}$ for a Hermitian matrix A and some value of λ . By differentiating that term we obtain a differential equation in λ :

$$\begin{aligned} \frac{\partial}{\partial \lambda} \left[e^{\lambda \underline{c}^\dagger A \underline{c}} \underline{c} e^{-\lambda \underline{c}^\dagger A \underline{c}} \right]_\alpha &= \underline{c}^\dagger A \underline{c} e^{\lambda \underline{c}^\dagger A \underline{c}} c_\alpha e^{-\lambda \underline{c}^\dagger A \underline{c}} - e^{\lambda \underline{c}^\dagger A \underline{c}} c_\alpha \underline{c}^\dagger A \underline{c} e^{-\lambda \underline{c}^\dagger A \underline{c}} \\ &= e^{\lambda \underline{c}^\dagger A \underline{c}} \underbrace{\left[\underline{c}^\dagger A_{\gamma, \delta} c_\delta, c_\alpha \right]}_{-A_{\alpha, \delta} c_\delta} e^{-\lambda \underline{c}^\dagger A \underline{c}} \\ &= \left(A \cdot \left[e^{\lambda \underline{c}^\dagger A \underline{c}} \underline{c} e^{-\lambda \underline{c}^\dagger A \underline{c}} \right] \right)_\alpha, \end{aligned} \quad (4.39)$$

and see

$$e^{\lambda \underline{c}^\dagger A \underline{c}} c_\alpha e^{-\lambda \underline{c}^\dagger A \underline{c}} = [\underline{c}^\dagger \cdot \underline{c}]_\alpha. \quad (4.40)$$

Repeated application to Eq. (4.38) yields

$$\begin{aligned} G_\varphi(\tau_1, \tau_2)_{\alpha,\beta} &= \frac{\text{Tr} \left[U_m \cdots U_{\ell_2+1} (B_{\ell_1} \cdots B_{\ell_{2+1}} \cdot \underline{c})_\alpha c_\beta^\dagger U_{\ell_2} \cdots U_1 \right]}{\text{Tr} [U_m \cdots U_1]} \\ &= (B_{\ell_1} \cdots B_{\ell_{2+1}})_{\alpha,\gamma} \frac{\text{Tr} \left[U_m \cdots U_{\ell_2+1} c_\gamma c_\beta^\dagger U_{\ell_2} \cdots U_1 \right]}{\text{Tr} [U_m \cdots U_1]} \\ &= (B_{\ell_1} \cdots B_{\ell_{2+1}})_{\alpha,\gamma} \langle c_\gamma c_\beta^\dagger \rangle_\varphi(\tau_2) \\ &= [B_{\ell_1} \cdots B_{\ell_{2+1}} \cdot G_\varphi(\tau_2)]_{\alpha,\beta}, \end{aligned} \quad \tau_1 \geq \tau_2, \quad (4.41)$$

where we have pulled the matrices B_ℓ out of the trace in Fock space to finally see that the imaginary time displaced Green's function is obtained from the equal time Green's function by the application of these matrices B_ℓ .

The calculation for $\tau_2 > \tau_1$ proceeds in an equivalent way. Since c_α and c_β^\dagger change places in Eq. (4.38), we need the Hermitian conjugate of Eq. (4.40),

$$e^{\lambda \underline{c}^\dagger A \underline{c}} c_\beta e^{-\lambda \underline{c}^\dagger A \underline{c}} = [\underline{c}^\dagger \cdot e^{\lambda A}]_\beta, \quad (4.42)$$

and find

$$\begin{aligned} G_\varphi(\tau_1, \tau_2)_{\alpha,\beta} &= -\langle c_\gamma^\dagger c_\alpha \rangle_\varphi(\tau_1) (B_{\ell_1+1}^{-1} \cdots B_{\ell_2}^{-1})_{\gamma,\beta} \\ &= -[(\mathbb{1} - G_\varphi(\tau_1)) \cdot B_{\ell_1+1}^{-1} \cdots B_{\ell_2}^{-1}]_{\alpha,\beta}, \end{aligned} \quad \tau_2 > \tau_1. \quad (4.43)$$

With Wick's theorem we can obtain expressions for imaginary time displaced multi-point correlation functions that relate them to the single-particle Green's function. A useful relation for $\tau_1 \geq \tau_2$ is [83]

$$\begin{aligned} \langle c_\alpha^\dagger(\tau_1) c_\alpha(\tau_1) c_\beta^\dagger(\tau_2) c_\beta(\tau_2) \rangle_\varphi &= \\ &= [\mathbb{1} - G_\varphi(\tau_1)]_{\alpha,\alpha} [\mathbb{1} - G_\varphi(\tau_2)]_{\beta,\beta} - G_\varphi(\tau_2, \tau_1)_{b,a} G_\varphi(\tau_1, \tau_2)_{a,b}. \end{aligned} \quad (4.44)$$

4.2 Fermion sign problem

In Sec. 4.1.1 we have seen how the partition function for a model of fermions interacting via a bosonic field in Eq. (4.2) can be brought into the form

$$\mathcal{Z} = \int D\varphi p[\varphi], \quad p[\varphi] = e^{-S_B[\varphi]} \det \left[\mathbb{1} + \prod_{\ell=m}^1 B_\ell \right]. \quad (4.45)$$

As long as $p[\varphi]$ is strictly real and positive, $p[\varphi]/\mathcal{Z}$ can be interpreted as a probability density, directly allowing Monte Carlo sampling as described in Sec. 4.1.2. If $p[\varphi]$ can be negative or even have a nonzero complex phase, we have to resort to a workaround [8]: First, we define expectation values in an ensemble where we simply ignore the negative signs:

$$\langle \mathcal{O} \rangle^{|p|} = \frac{\int D\varphi |p[\varphi]| \langle \mathcal{O} \rangle_\varphi}{\int D\varphi |p[\varphi]|}, \quad (4.46)$$

and introduce the actual sign as an observable, $s[\varphi] = p[\varphi]/|p[\varphi]|$. Then we can recover the regular expectation value of an observable by setting

$$\langle \mathcal{O} \rangle_\varphi \equiv \frac{\int D\varphi p[\varphi] \langle \mathcal{O} \rangle_\varphi}{\int D\varphi p[\varphi]} = \frac{\int D\varphi s[\varphi] |p[\varphi]| \langle \mathcal{O} \rangle_\varphi}{\int D\varphi s[\varphi] |p[\varphi]|} = \frac{\langle \mathcal{O}s \rangle^{|p|}}{\langle s \rangle^{|p|}}. \quad (4.47)$$

Principally, both the numerator and the denominator can now be sampled in a Monte Carlo simulation. However, this is only feasible if the average sign $\langle s \rangle^{|p|}$ is close to $+1$ or -1 . Otherwise there are large cancellations in the terms that are averaged to estimate $\langle \mathcal{O}s \rangle^{|p|}$ and $\langle s \rangle^{|p|}$. Hence, we need to compute the quotient of two strongly fluctuating quantities. If $\langle s \rangle^{|p|} \approx 0$ as an average over ± 1 , its variance is $\text{Var}^{|p|}[s] \approx 1$, leading to a large relative uncertainty. Consequently, the quotient (4.47) of two such strongly fluctuating quantities will have a very large statistical uncertainty $\sim [\langle s \rangle^{|p|}]^{-2}$.

Unfortunately, the general expectation for the average sign in a lattice model is to decay exponentially with the system size L^d and inverse temperature $\beta = 1/T$:

$$\langle s \rangle^{|p|} \sim e^{-\Delta\beta L^d}, \quad (4.48)$$

where Δ is an intensive quantity corresponding to the difference of the free-energy densities for the ensembles with unnormalized probability density functions p and $|p|$ [9]. This transforms the favorable polynomial scaling of the computational effort

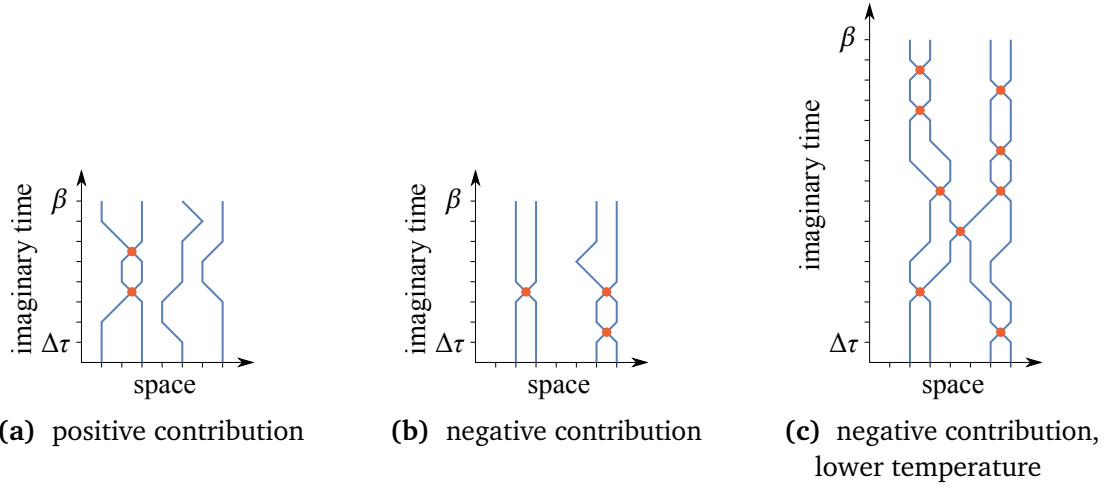


Figure 4.1: World line picture of contributions to the fermion determinant in Eq. (4.49).

in QMC methods to an exponentially hard problem – the sign problem. Practically, this restricts affected QMC studies to very small systems at high temperatures.

The behavior (4.48) can be understood qualitatively by interpreting the fermion determinant in $p[\varphi]$ in the path integral picture [9]:

$$\det \left[\mathbb{1} + \prod_{\ell=m}^1 B_\ell \right] = \text{Tr} \left[e^{- \int_0^\beta d\tau c^\dagger [K + V[\varphi]] c} \right] + O(\Delta\tau^2). \quad (4.49)$$

The trace corresponds to a sum over all possible world lines of fermions propagating in the background of a bosonic field configuration φ . Since we compute a trace, the sets of initial and final single-fermion states are equal, but fermions can exchange position, leading to world lines winding around each other. Each exchange contributes a negative sign, so the overall contribution of one set of world lines is positive if the total winding number is even, cf. Figs. 4.1a and 4.1b. At least for kinetic Hamiltonians that are restricted to local hopping with not too high densities, at low β exchanges will be rather rare leading to a weak sign problem. At larger β the number of available imaginary time slices grows as in Fig. 4.1c and we can expect the formation of world lines to depend only weakly on the initial states. Then we can expect the number of exchanges Δx per imaginary time interval $\Delta\tau$ to approach a constant, which will be proportional to the spatial system size,

$$\frac{dx}{d\tau} = CL^d, \quad x \propto e^{CL^d \int_0^\beta d\tau} = e^{CL^d \beta}, \quad (4.50)$$

leading to both the frequency of positive and negative determinants to grow exponentially and Eq. (4.48) for the average sign. More formal arguments have been made and, most importantly, the exponential decay with β has been confirmed numerically in DQMC studies of the Hubbard model [9].

4.2.1 Absence of the sign problem

The discussion above illustrates why we generally have to expect a sign problem in QMC simulations of fermions in formalisms that are ultimately based on a world line interpretation of quantum mechanics. The negative signs that emanate from antisymmetry under particle exchange are inherent to the nature of fermionic particles. A major advantage of the DQMC method is, however, that this nature is already accounted for to a certain degree when the fermionic determinant is evaluated exactly for one bosonic field configuration, which is equivalent to a sum over all possible fermion world lines. In spatial dimension $d = 1$, where fermion lattices are isomorphic to quantum spin chains via a Jordan-Wigner transformation, QMC methods that directly sample the sum over fermion world lines stochastically without a sign problem are available [104, 105], but in $d \geq 2$ one generally has to deal with configurations that carry negative weight. Conversely, with DQMC there are cases where symmetries guarantee that negative contributions to the weight (4.49) are canceled out and, hence, one can prove the absence of any sign problem. In the following two subsections we discuss two classes of problems that become treatable with DQMC for this reason.

As we can see, the sign problem is not fully a property of the physical system that it afflicts, but its appearance depends on the formulation of a specific flavor of QMC. For instance, a different choice of basis may remove a specific sign problem [106]. After all, at least the eigenbasis of a Hamiltonian always exists as a sign-problem-free basis. It has been shown, however, that the identification of a general procedure to find a sign-problem-free basis for any Hamiltonian is a nondeterministic polynomial (NP) hard problem [107]. Unless – against general expectations – the conjecture “ $NP \neq P$ ”, of which the proof is one of the millennium problems promising a million dollar reward, turns out to be false, this means that there is no general solution of the sign problem in polynomially scaling time that would work around Eq. (4.48) [108]. Nevertheless, as pointed out in Ref. [109], one should keep in mind that the authors of Ref. [107] chose a particularly challenging model to show that the generic removal of the sign problem is NP hard. In essence they demonstrated that the search for the ground state of a three-dimensional quantum spin glass is not easier than the case of the corresponding classical Ising spin glass, which is known to be an NP complete problem [110]. It remains to be seen whether generic procedures exist

to remove the sign problem for more restricted, but physically important, classes of problems such as translationally invariant fermion lattice models that are not covered by the special symmetries discussed below.

In the mean time the most promising path seems to be to study “designer Hamiltonians”, which are conceived as prototypes for some quantum mechanical many-body problem that cannot be understood without bias by other means, but are constructed in a way that avoids the sign problem in QMC simulations.

4.2.2 Determinant factorization

The Hubbard model is among the models that are amenable to sign-problem-free DQMC simulations in important special cases. It is convenient to define it in the form

$$\mathcal{H}_{\text{Hub}} = -t \sum_{\langle i,j \rangle, s} c_{i,s}^\dagger c_{j,s} + \text{h.c.} + \mu \sum_{i,s} n_{i,s} + U \sum_i \left(n_{i,\uparrow} - \frac{1}{2} \right) \cdot \left(n_{i,\downarrow} - \frac{1}{2} \right) \quad (4.51)$$

with nearest-neighbor sites $\langle i,j \rangle$, $i,j = 1, \dots, N_s$, spin indices $s = \uparrow, \downarrow$, occupation numbers $n_{i,s} = c_{i,s}^\dagger c_{i,s}$, and the chemical potential μ . In this form $\mu = 0$ at half filling $\langle n_{i,\uparrow} \rangle = \langle n_{i,\downarrow} \rangle = 1/2$. If the local interaction is repulsive, $U > 0$, it is beneficial to decouple the four-fermion term via a Hubbard-Stratonovich decomposition similar to the one applied in Chap. 2 after Eq. (2.21), where we now choose the spin- z channel. To do so we write Eq. (4.51) in the form

$$\mathcal{H}_{\text{Hub}} = \underbrace{-t \sum_{\langle i,j \rangle, s} c_{i,s}^\dagger c_{j,s} + \text{h.c.} + \mu \sum_{i,s} n_{i,s} + \frac{UN_s}{4}}_{\underline{c}^\dagger K \underline{c}} - 2U \sum_i (S_i^z)^2 \quad (4.52)$$

with the usual definition of S_i^z as in Eq. (2.16). After the Hubbard-Stratonovich transformation² we obtain the partition function

$$\mathcal{Z}_{\text{Hub}} = \text{Tr } e^{-\beta \mathcal{H}_{\text{Hub}}} = \int D\varphi e^{-S_B} \text{Tr} \exp \left\{ - \int_0^\beta d\tau \left[\underbrace{\underline{c}^\dagger K \underline{c}}_{\underline{c}^\dagger V[\varphi(\tau)] \underline{c}} - 4U \sum_i S_i^z \cdot \varphi_i(\tau) \right] \right\}, \quad (4.53)$$

²It is helpful to remember the Gaussian integral $\exp\left(\frac{1}{2}\alpha A^2\right) \propto \exp\left(-\frac{1}{2}\alpha x^2 + \alpha x A\right)$ for $\alpha > 0$.

where $\varphi_i(\tau)$ is a real scalar field and the bosonic action is $S_B = 2U \int_0^\beta d\tau \sum_i \varphi_i(\tau)^2$. Note that, if we index the fermionic operators as in $\underline{c}^\dagger = (c_{1,\uparrow}^\dagger, \dots, c_{N_s,\uparrow}^\dagger, c_{1,\downarrow}^\dagger, \dots, c_{N_s,\downarrow}^\dagger)$, the $2N_s \times 2N_s$ matrices K and $V[\varphi(\tau)]$ are block diagonal and have the form

$$K = \begin{bmatrix} K^\uparrow & | \\ \hline & K^\downarrow \end{bmatrix}, \quad V[\varphi(\tau)] = \begin{bmatrix} V^\uparrow[\varphi(\tau)] & | \\ \hline & V^\downarrow[\varphi(\tau)] \end{bmatrix}, \quad (4.54)$$

where $K^\uparrow = K^\downarrow$, while $V^s[\varphi(\tau)]$ are diagonal matrices that differ by an overall sign:

$$V^\uparrow[\varphi(\tau)]_{i,j} = -2U\delta_{ij}\varphi_i(\tau), \quad V^\downarrow[\varphi(\tau)]_{i,j} = 2U\delta_{ij}\varphi_i(\tau). \quad (4.55)$$

Consequently, after integrating out the fermions as in Eq. (4.8), the fermion matrix will have the same block diagonal structure and its determinant factorizes:

$$\det \left[\mathbb{1} + \prod_{\ell=m}^1 B_\ell \right] = \underbrace{\det \left[\mathbb{1} + \prod_{\ell=m}^1 B_\ell^\uparrow \right]}_{\det O^\uparrow} \cdot \underbrace{\det \left[\mathbb{1} + \prod_{\ell=m}^1 B_\ell^\downarrow \right]}_{\det O^\downarrow}, \quad (4.56)$$

where B_ℓ are defined in Eq. (4.9) and B_ℓ^\uparrow and B_ℓ^\downarrow are the corresponding matrices restricted to one spin sector:

$$B_\ell^s = e^{-\frac{\Delta\tau}{2}K^s} e^{-\Delta\tau V^s[\varphi(\ell\Delta\tau)]} e^{-\frac{\Delta\tau}{2}K^s}. \quad (4.57)$$

The factorization in Eq. (4.56) is advantageous if there are relations between the two determinant factors that force the product to be positive. In the case of the $U > 0$ Hubbard model **particle-hole symmetry** provides such a relation. Defining a particle-hole transformation with site-dependent sign [111]

$$c_{is}^\dagger \rightarrow \tilde{c}_{is} = (-1)^i c_{is}^\dagger, \quad c_{is} \rightarrow \tilde{c}_{is}^\dagger = (-1)^i c_{is}, \quad (4.58)$$

we see that particle occupation numbers transform into hole occupation numbers,

$$n_{is} \equiv c_{is}^\dagger c_{is} = \tilde{c}_{is} \tilde{c}_{is}^\dagger = 1 - \tilde{c}_{is}^\dagger \tilde{c}_{is} = 1 - \tilde{n}_{is}, \quad (4.59)$$

while hopping terms between the two sublattices of a bipartite lattice are invariant (see Fig. 4.2a):

$$-t c_{is}^\dagger c_{js} + \text{h.c.} = -t \underbrace{(-1)^i (-1)^j}_{\substack{-1 \text{ for } i,j \\ \text{nearest} \\ \text{neighbors}}} \underbrace{\tilde{c}_{is} \tilde{c}_{js}^\dagger}_{-\tilde{c}_{js}^\dagger \tilde{c}_{is}} + \text{h.c.} = -t \tilde{c}_{is}^\dagger \tilde{c}_{js} + \text{h.c.} \quad (4.60)$$

The interaction in Eq. (4.51) is always invariant:

$$\left(n_{i,\uparrow} - \frac{1}{2} \right) \cdot \left(n_{i,\downarrow} - \frac{1}{2} \right) = \left(\tilde{n}_{i,\uparrow} - \frac{1}{2} \right) \cdot \left(\tilde{n}_{i,\downarrow} - \frac{1}{2} \right), \quad (4.61)$$

while the chemical potential term changes under the transformation, except at half filling where $\mu = 0$:

$$\mu n_{is} = \mu (1 - \tilde{n}_{is}). \quad (4.62)$$

In summary we have particle-hole symmetry for half filling on a bipartite lattice with nearest neighbor hopping. In this case we find after the Hubbard-Stratonovich transformation:

$$\underline{c}_\uparrow^\dagger K^\uparrow \underline{c}_\uparrow = \tilde{\underline{c}}_\uparrow^\dagger K^\uparrow \tilde{\underline{c}}_\uparrow, \quad (4.63a)$$

$$\underline{c}_\uparrow^\dagger V^\uparrow[\varphi(\tau)] \underline{c}_\uparrow \equiv -2U \underline{\varphi}(\tau) \cdot \underline{n}_\uparrow = -2U \underline{\varphi}(\tau) \cdot (\underline{1} - \underline{\tilde{n}}_\uparrow) \quad (4.63b)$$

$$\equiv -2U \sum_i \varphi_i(\tau) + \tilde{\underline{c}}_\uparrow^\dagger V^\downarrow[\varphi(\tau)] \tilde{\underline{c}}_\uparrow, \quad (4.63c)$$

i.e., V^\uparrow and V^\downarrow are exchanged and an extra bosonic term is introduced. Defining operators U_ℓ^s as in Eq. (4.7) but for only one spin sector, we then find for one of the determinants in Eq. (4.56):

$$\begin{aligned} \det O^\uparrow &= \text{Tr}_{c_\uparrow} \prod_{\ell=m}^1 U_\ell^\uparrow = \text{Tr}_{c_\uparrow} \prod_{\ell=m}^1 e^{-\frac{\Delta\tau}{2} c_\uparrow^\dagger K^\uparrow c_\uparrow} e^{-\Delta\tau c_\uparrow^\dagger V^\uparrow[\varphi(\ell\Delta\tau)] c_\uparrow} e^{-\frac{\Delta\tau}{2} c_\uparrow^\dagger K^\uparrow c_\uparrow} \\ &= \text{Tr}_{\tilde{c}_\uparrow} \prod_{\ell=m}^1 e^{-\frac{\Delta\tau}{2} \tilde{c}_\uparrow^\dagger K^\downarrow \tilde{c}_\uparrow} e^{-\Delta\tau \tilde{c}_\uparrow^\dagger V^\downarrow[\varphi(\ell\Delta\tau)] \tilde{c}_\uparrow} e^{-\frac{\Delta\tau}{2} \tilde{c}_\uparrow^\dagger K^\downarrow \tilde{c}_\uparrow} e^{\Delta\tau 2U \sum_i \varphi_i(\ell\Delta\tau)} \\ &= e^{-\Delta\tau 2U \sum_{\ell,i} \varphi_i(\ell\Delta\tau)} \text{Tr}_{c_\downarrow} \prod_{\ell=m}^1 e^{\frac{\Delta\tau}{2} c_\downarrow^\dagger K^\downarrow c_\downarrow} e^{-\Delta\tau c_\downarrow^\dagger V^\downarrow[\varphi(\ell\Delta\tau)] c_\downarrow} e^{-\frac{\Delta\tau}{2} c_\downarrow^\dagger K^\downarrow c_\downarrow} \\ &= e^{\Delta\tau 2U \sum_{\ell,i} \varphi_i(\ell\Delta\tau)} \det O^\downarrow, \end{aligned} \quad (4.64)$$

where we have used $K^\dagger = K^\downarrow$ and we have changed the labeling of the operators under the trace in the third line. Returning to Eq. (4.56), we find that this forces the fermion determinant to be non-negative:

$$\det \left[\mathbb{1} + \prod_{\ell=m}^1 B_\ell \right] = e^{\Delta\tau 2U \sum_{\ell,i} \varphi_i(\ell\Delta\tau)} [\det O^\downarrow]^2 \geq 0. \quad (4.65)$$

The half-filled square-lattice $U > 0$ Hubbard model has been studied intensively in sign-problem-free DQMC simulations [112–114], where usually a discrete alternative to the Hubbard-Stratonovich transformation is applied [115]. Since the honeycomb lattice is also bipartite, the Hubbard model can be simulated without a sign problem due to the same symmetry on this lattice. Recently, it has been studied in very large scale DQMC simulations to clarify the nature of the transition between its semimetallic and antiferromagnetic Mott insulating phases, where the possible existence of an intermediate spin liquid phase was subject of controversy [116–118]. A similar particle-hole symmetry also enables sign-problem-free simulations of other two-dimensional models, such as the half filled Kondo lattice model [119, 120], SU(2N) symmetric generalizations of the Hubbard model [121–123], or the Kane-Mele-Hubbard model of interacting topological insulators [124, 125].

Note, however, that we cannot directly use a model of the type discussed in this Section to study the spin-density wave transition in a metal. First, the next-nearest neighbor hopping terms required to model a cuprate-like dispersion with a Fermi surface like the one in Fig. 2.2b break particle-hole symmetry, see Fig. 4.2a. Second, a half filled model with only nearest neighbor hopping on the square lattice has a Fermi surface that is perfectly nested by the Néel ordering wave vector $\mathbf{Q} = (\pi, \pi)^\top$, see Fig. 4.2b, which is a very particular special case compared to having just a discrete set of hot spots.

4.2.3 Generalized time reversal symmetry

To study the Hubbard model with attractive interactions, $U < 0$, it is more convenient to apply the Hubbard-Stratonovich transformation in the density channel [113]. To do so we first bring the Hamiltonian (4.51) into the following form:

$$\mathcal{H}_{\text{Hub}} = -t \underbrace{\sum_{\langle i,j \rangle, s} c_{i,s}^\dagger c_{j,s} + \text{h.c.}}_{\underline{c}^\dagger K \underline{c}} + \mu \sum_{i,s} n_{i,s} + \frac{|U|N_s}{4} - \frac{|U|}{2} \sum_i (n_{i,\uparrow} + n_{i,\downarrow} - 1)^2. \quad (4.66)$$

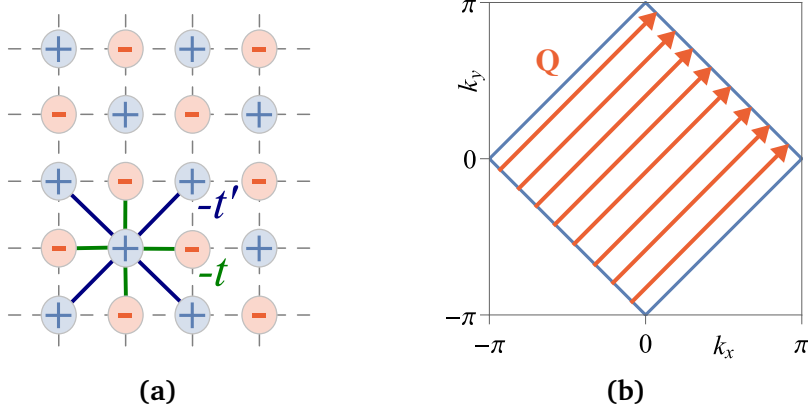


Figure 4.2: (a) The square lattice as an example for a bipartite lattice. Indicated is hopping between nearest ($-t$) and next-nearest neighbors ($-t'$). (b) Non-interacting Fermi surface of the half-filled Hubbard model on the square lattice. There is perfect nesting by the wave vector $\mathbf{Q} = (\pi, \pi)^T$.

Now we perform the Hubbard-Stratonovich transformation for the squared operator $(n_{i,\uparrow} + n_{i,\downarrow} - 1)^2$ and retrieve the following expression for the partition function:

$$\mathcal{Z}_{\text{Hub}} = \text{Tr } e^{-\beta \mathcal{H}_{\text{Hub}}} = \int D\varphi e^{-S_B} \text{Tr} \exp \left\{ - \int_0^\beta d\tau \underbrace{\left[\underline{c}^\dagger K \underline{c} - |U| \sum_i (n_{i,\uparrow} + n_{i,\downarrow}) \cdot \varphi_i(\tau) \right]}_{\underline{c}^\dagger V[\varphi(\tau)] \underline{c}} \right\}, \quad (4.67)$$

where $\varphi_i(\tau)$ is a real scalar field and $S_B = \frac{|U|}{2} \int_0^\beta d\tau \sum_i [\varphi_i(\tau)^2 + 2\varphi_i(\tau)]$. The matrices K and $V[\varphi(\tau)]$ again have the block diagonal structure of Eq. (4.54), but this time both the kinetic and the interaction matrices have equal blocks for both spin indices:

$$K_{i,j}^\uparrow \equiv K_{i,j}^\downarrow, \quad V^\uparrow[\varphi(\tau)]_{i,j} \equiv V^\downarrow[\varphi(\tau)]_{i,j} = -|U|\delta_{ij}\varphi_i(\tau). \quad (4.68)$$

Hence, the fermion determinant will factorize as in Eq. (4.56), but with two equal factors:

$$\det \left[\mathbb{1} + \prod_{\ell=m}^1 B_\ell \right] = [\det O^\uparrow]^2 \geq 0, \quad (4.69)$$

where $\det O^\uparrow$ is real. As we can see, the attractive Hubbard model never has a sign problem, while the repulsive Hubbard model needs to be tuned to very specific

parameters to be free of the sign problem. There is a deeper reason for this difference: Only in the attractive case the Hubbard-Stratonovich transformed action of the Hubbard model has **time-reversal symmetry** [10].

The time-reversal operator for a spin- $\frac{1}{2}$ particle in real space is [126, Chapt. XV18]

$$T = -is_2 C = \begin{pmatrix} 0 & -1 \\ 1 & 0 \end{pmatrix} C, \quad (4.70)$$

where the matrix flips spin and adds a minus sign for spin down, while C denotes the complex conjugation of scalars. T is an antiunitary operator³ with the property $T^2 = -\mathbb{1}$.

The kinetic part $\underline{c}^\dagger K \underline{c}$ of the Hubbard Hamiltonian is symmetric under time reversal since we have

$$T \sum_s c_{is}^\dagger c_{js} T^{-1} = T \left[c_{i\uparrow}^\dagger c_{j\uparrow} + c_{i\downarrow}^\dagger c_{j\downarrow} \right] T^{-1} = c_{i\downarrow}^\dagger c_{j\downarrow} + (-1)^2 c_{i\uparrow}^\dagger c_{j\uparrow} = \sum_s c_{is}^\dagger c_{js} \quad (4.71)$$

and all coefficients are real. Likewise the interaction part $\underline{c}^\dagger V[\varphi(\tau)] \underline{c}$ after the Hubbard-Stratonovich transformation in Eq. (4.67) is time-reversal symmetric, since $T[n_{i\uparrow} + n_{i\downarrow}]T^{-1} = n_{i\uparrow} + n_{i\downarrow}$ and the field φ is real. On the other hand, in Eq. (4.53) we have decoupled the repulsive Hubbard model in the spin- z -density channel and S_i^z is odd under time reversal:

$$TS_i^z T^{-1} = \frac{1}{2} T \left[n_{i\uparrow} - n_{i\downarrow} \right] T^{-1} = \frac{1}{2} \left[n_{i\downarrow} - n_{i\uparrow} \right] = -S_i^z. \quad (4.72)$$

If we also used a Hubbard-Stratonovich decomposition in the density channel for the $U > 0$ model, an extra imaginary factor of i would have been introduced in $\underline{c}^\dagger V[\varphi(\tau)] \underline{c}$, which would also break the symmetry under T .

As Wu and Zhang have realized [10] the coincidence of time-reversal symmetry and a positive definite fermion determinant is explained by a more general theorem.

Theorem 4.1. If an antiunitary operator T exists such that

$$TKT^{-1} = K, \quad TV[\varphi]T^{-1} = V[\varphi], \quad \text{and} \quad T^2 = -\mathbb{1}, \quad (4.73)$$

then all eigenvalues of the matrix $M = \mathbb{1} + \prod_{\ell=m}^1 B_\ell \equiv \mathbb{1} + \prod_{\ell=m}^1 e^{-\frac{\Delta\tau}{2} K} e^{-\Delta\tau V[\varphi(\ell\Delta\tau)]} e^{-\frac{\Delta\tau}{2} K}$

³An antiunitary operator U is an antilinear operator acting on a Hilbert space H , $U : H \rightarrow H$, with $\langle Ux|Uy\rangle = \langle x|y\rangle^*$ for all $|x\rangle, |y\rangle \in H$. Antilinearity signifies that $U[a|x\rangle + b|y\rangle] = a^*U|x\rangle + b^*U|y\rangle$ for all $a, b \in \mathbb{C}$ and all $|x\rangle, |y\rangle \in H$.

appear in complex conjugate pairs: If λ_i is an eigenvalue, also λ_i^* is an eigenvalue. If λ_i is real, it is twofold degenerate. Consequently, the fermion determinant is positive definite:

$$\det M = \prod_i |\lambda_i|^2 \geq 0. \quad (4.74)$$

Proof. Since K and, for any φ , $V[\varphi]$ are symmetric under T , also M is symmetric under T : $TMT^{-1} = M$. Assume \underline{v} to be an eigenvector of M with eigenvalue λ , $M\underline{v} = \lambda\underline{v}$. Then we have by symmetry under T :

$$MT\underline{v} = TM\underline{v} = \underbrace{T\underline{v}}_{\mathbb{1}} T^{-1}T\underline{v} = T\lambda\underline{v} = \lambda^*T\underline{v},$$

where we have used the antilinearity of T in the last step. Therefore, to every eigenvector \underline{v} with eigenvalue λ also $T\underline{v}$ is an eigenvector with eigenvalue λ^* . Moreover, \underline{v} and $T\underline{v}$ are orthogonal vectors, since we have

$$\langle \underline{v}, T\underline{v} \rangle = \langle T\underline{v}, T^2\underline{v} \rangle^* = -\langle T\underline{v}, \underline{v} \rangle^* = -\langle \underline{v}, T\underline{v} \rangle,$$

where we have used the antiunitarity of T in the first step and its property $T^2 = -\mathbb{1}$ in the second step. \square

A few remarks concerning this proof are in order:

1. The existence of a T -symmetry for the matrix kernels K and $V[\varphi]$ is equivalent to the existence of such a symmetry for the operators in second quantization $\underline{c}^\dagger K \underline{c}$ and $\underline{c}^\dagger V[\varphi] \underline{c}$.
2. We have assumed the matrix M to be diagonalizable such that the vector space it operates on has a basis formed by linear independent eigenvectors of M . By transforming M into the Jordan normal form the theorem can also be proved on more general grounds [10].
3. If the matrix M is Hermitian, this theorem is equivalent to Kramers theorem [126, Chapt. XV.21]: Since all eigenvalues are real, they are all twofold degenerate.

The theorem captures models for which no Hubbard-Stratonovich transformation is known which would lead to fermion determinants that are positive definite by factorization. We make use of this in Sec. 4.3 to introduce a sign-problem-free model to study the spin-density wave transition in a metal. Some other models

that are sign-problem-free by the theorem include multi-layer and multi-component Hubbard models with spin dependent interactions [127, 128] and an attractive Hubbard model with spin-orbit coupling [129].

4.2.4 More sign-problem-free formulations

In recent years encouraging progress in the identification of further models that admit the formulation of sign-problem-free QMC simulations has been made. Besides the models that have been found to fall into one of the categories explained in the previous two subsections, complementary approaches such as the meron cluster method [130] and the fermion bag method [131, 132] have emerged, which are based on continuous-time QMC approaches. Another recent development lies in the application of Hubbard-Stratonovich transformations in Majorana fermion hopping channels, which allows sign-problem-free DQMC simulations of spinless and, more generally, $SU(N)$ symmetric fermion models with odd N [133]. The discovery of this Majorana decomposition has also enabled a more sophisticated mathematical understanding of the classification of known sign-problem-free models and the identification of previously unknown models that fall into these classes [134–136].

4.3 Sign-problem-free two-flavor model

In Sec. 2.2.2 we have motivated the action (2.27) describing a system of itinerant electrons coupled to a bosonic spin-density wave (SDW) order parameter. As it stands this model cannot be simulated without a sign problem in DQMC simulations. Similarly to the repulsive Hubbard model decomposed in the spin- z channel, the action (2.27) is not invariant under time reversal. However, as Berg, Metlitski, and Sachdev realized [11], it is possible to write down a model with *two bands* of electrons, describing the same universal physics in the vicinity of an SDW QCP, that is symmetric under a generalized antiunitary transformation \hat{T} that fulfills the conditions of Theorem 4.1.

If our starting point is a single-band model with a Fermi surface like the one in Fig. 4.3a, where the universal physics near the QCP are generally believed to be determined by those regions in proximity to the hot spots linked by $\mathbf{Q} = (\pi, \pi)^T$, we can equally well study a modified model with the Fermi surface deformed far away from these hot spots. We are also free to split the Fermi surface at appropriate distances to the hot spots such that, by introducing an extra “flavor” or “orbital” label for the fermions, we arrive at the situation with two electronic bands and separate Fermi surfaces shown in Fig. 4.3b. Here we have distributed the hot spots into two

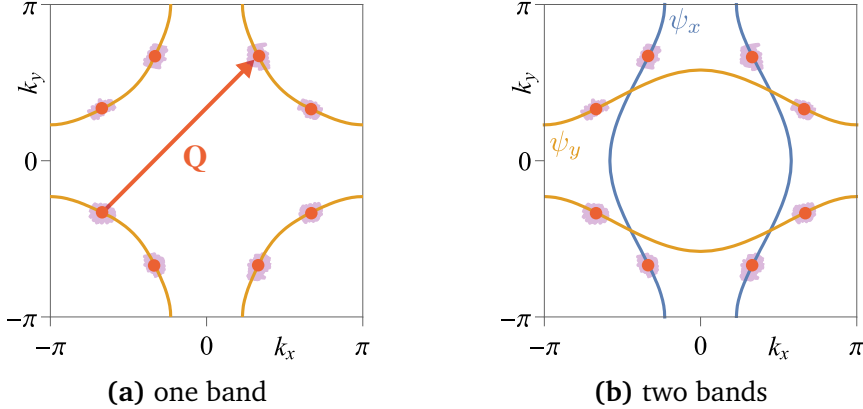


Figure 4.3: Non-interacting Fermi surfaces of (a) a one band model [one closed Fermi surface] and (b) a model with two separate fermion bands [vertical ψ_x and horizontal ψ_y Fermi surfaces]. In both cases the hot spots [orange dots linked by $\mathbf{Q} = (\pi, \pi)^T$] are in the same locations and the electronic dispersion in their vicinities is identical locally.

groups with \mathbf{Q} linking hot spots of one group with hot spots of the other group. By design of the new electronic bands only hot spots of one group are located on the horizontal Fermi surface and all hot spots of the other group are situated on the vertical Fermi surface. This separation is the new key property providing the freedom to write down an action with the desired \hat{T} -symmetry. Note that, by construction, both models are essentially identical locally around the hot spots and consequently the same low-energy theories applies close to the SDW QCP. The two-flavor model therefore provides an ideal environment to investigate the universal physics that emerges close to this QCP in sign-problem-free DQMC simulations.

Specifically, this lattice model is composed of two flavors of spin- $\frac{1}{2}$ fermions labeled ψ_x and ψ_y that are coupled to a real bosonic vector field $\vec{\varphi}$ representing the SDW order parameter. It is obtained from the general action (2.27) by distributing the coupling action S_{FB} over the two flavors. Explicitly, the action is $S = S_F + S_{FB} + S_B = \int_0^\beta d\tau (L_F + L_{FB} + L_B)$ with

$$L_F = \sum_{\substack{i,j,s \\ \alpha=x,y}} \psi_{\alpha is}^\dagger [(\partial_\tau - \mu) \delta_{ij} - t_{aij}] \psi_{\alpha js}, \quad (4.75a)$$

$$L_{FB} = \lambda \sum_{i,s,s'} e^{i\mathbf{Q} \cdot \mathbf{r}_i} [\vec{s} \cdot \vec{\varphi}_i]_{ss'} \psi_{xis}^\dagger \psi_{yis'} + \text{h.c.}, \quad (4.75b)$$

$$L_B = \frac{1}{2} \sum_i \frac{1}{c^2} \left(\frac{d\vec{\varphi}_i}{d\tau} \right)^2 + \frac{1}{2} \sum_{\langle i,j \rangle} (\vec{\varphi}_i - \vec{\varphi}_j)^2 + \sum_i \left[\frac{r}{2} \vec{\varphi}_i^2 + \frac{u}{4} (\vec{\varphi}_i^2)^2 \right]. \quad (4.75c)$$

This action is defined on a square lattice with sites labeled by i, j , where $\langle i, j \rangle$ are nearest neighbors. The two fermion flavors are indexed by $\alpha = x, y$, while $s, s' = \uparrow, \downarrow$ index the spin polarizations and $\vec{\sigma}$ are the Pauli matrices. As always imaginary time is denoted by τ and $\beta = 1/T$ is the inverse temperature. Generically, we impose periodic boundary conditions on the spatial lattice.

The Fermi surfaces shown in Fig. 4.3b are realized by setting “quasi one-dimensional” dispersions, where the ψ_x and ψ_y fermions have stronger dispersion in momentum direction k_x and k_y , respectively. They are implemented by setting different hopping amplitudes along the horizontal and vertical real space lattice directions. For the ψ_x fermions those are given by $t_{x,h} = 1$ and $t_{x,v} = 0.5$, respectively, and for the ψ_y fermions by $t_{y,h} = 0.5$ and $t_{y,v} = 1$. Translated to momentum space this gives $\epsilon_{\alpha k} = -2t_{\alpha,h} \cos k_x - 2t_{\alpha,v} \cos k_y - \mu$. Here the chemical potential is set to $\mu = -0.5$. In these units the Fermi energy, measured from the minimum of the lowest band to zero energy, is $E_F = 2.5$. The model is then fully C_4 -symmetric with a $\pi/2$ rotation mapping the ψ_x band to the ψ_y band and vice versa.

We use the parameter r to tune the system through its quantum critical point, while we will generally set the coefficient of quartic term, which effectively limits the strength of the SDW order parameter fluctuations, to $u = 1$. We will explore different values of the “Yukawa” coupling λ between fermions and order parameter field and of the bare bosonic velocity c .

4.3.1 Mean field

In Sec. 2.2.2 we have briefly discussed the mean-field solution of a single-band fermion model coupled to an SDW order parameter. We can subject the action (4.75) to an equivalent treatment. Assuming without loss of generality the mean-field expectation value of the order parameter to be aligned with the z -axis, $\langle \vec{\varphi}_q \rangle_{\text{MF}} = \varphi_0 \vec{e}_3$, the mean-field Hamiltonian is

$$\mathcal{H}_{\text{MF}} = \sum_{\mathbf{k}\alpha s} \epsilon_{\mathbf{k}\alpha} \psi_{\alpha\mathbf{k}s}^\dagger \psi_{\alpha\mathbf{k}s} + \lambda \varphi_0 \sum_{\mathbf{k}} \left[\psi_{x,\mathbf{k}+\mathbf{Q},\uparrow}^\dagger \psi_{y,\mathbf{k},\uparrow} - \psi_{x,\mathbf{k}+\mathbf{Q},\downarrow}^\dagger \psi_{y,\mathbf{k},\downarrow} + \text{h.c.} \right]. \quad (4.76)$$

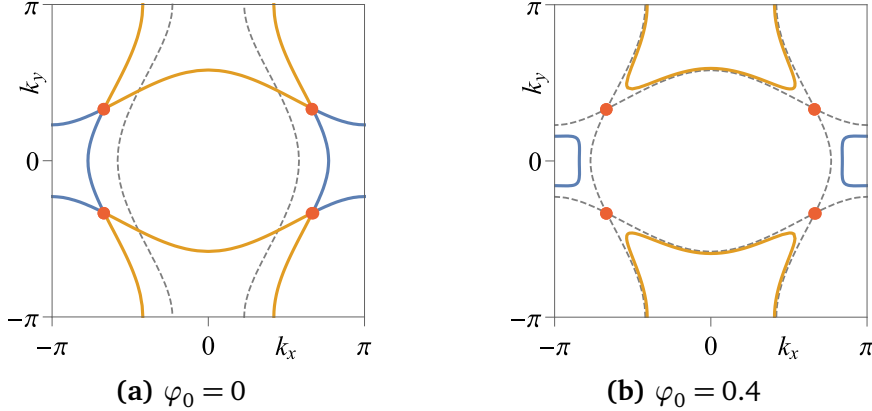


Figure 4.4: Mean-field Fermi surfaces for the dispersion $e_{k,\pm}$ of Eq. (4.78). (a) For the $\varphi_0 = 0$ case the non-interacting ψ_y Fermi surface of Fig. 4.3b is plotted with dashed lines. The hot spots (orange dots) are now at the intersections of the e_{\pm} Fermi surfaces. (b) Finite SDW order $\varphi_0 > 0$. The dashed lines repeat the $\varphi_0 = 0$ Fermi surfaces for reference.

In terms of the spinors $\Psi_k^\dagger = (\psi_{x,k+Q,\uparrow}^\dagger, \psi_{y,k,\downarrow}^\dagger, \psi_{x,k+Q,\downarrow}^\dagger, \psi_{y,k,\uparrow}^\dagger)$ we can write the Hamiltonian in the form $\mathcal{H}_{\text{MF}} = \sum'_k \Psi_k^\dagger h_k \Psi_k$ with the matrix

$$h_k = \begin{bmatrix} \varepsilon_{x,k+Q} & 0 & 0 & \lambda\varphi_0 \\ 0 & \varepsilon_{y,k} & -\lambda\varphi_0 & 0 \\ 0 & -\lambda\varphi_0 & \varepsilon_{x,k+Q} & 0 \\ \lambda\varphi_0 & 0 & 0 & \varepsilon_{y,k} \end{bmatrix}, \quad (4.77)$$

which has twofold degenerate eigenvalues

$$e_{k,\pm} = \frac{1}{2} \left[\varepsilon_{x,k+Q} + \varepsilon_{y,k} \pm \sqrt{(\varepsilon_{x,k+Q} - \varepsilon_{y,k})^2 + 4\lambda^2\varphi_0^2} \right]. \quad (4.78)$$

This hybridized dispersion gives rise to the Fermi surfaces shown in Fig. 4.4. Note that the non-interacting ψ_y band has effectively been shifted by the wavevector Q due to the presence of the coupling term in λ , such that in Fig. 4.4a the hot spots are now at the intersections of the e_{\pm} Fermi surfaces. In the presence of finite SDW order $\varphi_0 > 0$ these Fermi surfaces are reconstructed with gaps opening around the hot spots, see Fig. 4.4b. This is similar to the behavior of the mean-field solution of the single-band model in Fig. 2.4.

4.3.2 Single-fermion matrix structure and antiunitary symmetry

As detailed in Sec. 4.1 after discretizing imaginary time the partition function $\mathcal{Z} = \int D(\psi, \psi^\dagger, \vec{\varphi}) e^{-S}$ for model (4.75) takes the form

$$\mathcal{Z} = \int D\vec{\varphi} e^{-S_B} \text{Tr}_\psi \left[\prod_{\ell=m}^1 U_\ell \right] + O(\Delta\tau^2) \quad (4.79)$$

with operators

$$U_\ell = e^{-\frac{\Delta\tau}{2}\psi^\dagger K\psi} e^{-\Delta\tau\psi^\dagger V[\vec{\varphi}(\ell\Delta\tau)]\psi} e^{-\frac{\Delta\tau}{2}\psi^\dagger K\psi}. \quad (4.80)$$

Here ψ and ψ^\dagger are vectors of fermionic operators with the indexing taken in the following order, which turns out to be convenient for the formalism:

$$\psi^\dagger = (\psi_{a\sigma}^\dagger) = (\psi_{x1\uparrow}^\dagger, \dots, \psi_{xN_s\uparrow}^\dagger, \psi_{y1\downarrow}^\dagger, \dots, \psi_{yN_s\downarrow}^\dagger, \psi_{x1\downarrow}^\dagger, \dots, \psi_{xN_s\downarrow}^\dagger, \psi_{y1\uparrow}^\dagger, \dots, \psi_{yN_s\uparrow}^\dagger). \quad (4.81)$$

The matrix kernels K and $V_\ell \equiv V[\vec{\varphi}(\ell\Delta\tau)]$ are given by

$$K_{ij,aa',ss'} = \delta_{ss'} \delta_{aa'} (-t_{a,s,ij} - \mu \delta_{ij}), \quad (4.82a)$$

$$V_{\ell;ij,aa',ss'} = \lambda [\sigma_1]_{aa'} \delta_{ij} [\vec{s} \cdot \vec{\varphi}_i(\ell)]_{ss'}, \quad \sigma_1 = \begin{bmatrix} 0 & 1 \\ 1 & 0 \end{bmatrix}, \quad (4.82b)$$

where the Pauli matrix σ_1 acts on the flavor index and the Pauli matrices \vec{s} act on the spin index.

It is precisely the appearance of this σ_1 that allows us to define an antiunitary operator \hat{T} with the property $\hat{T}^2 = -\mathbb{1}$ which commutes with the action (4.75) guaranteeing the integrand in Eq. (4.79) to be positive definite by Theorem 4.1. Such an operator is given by

$$\hat{T} = -is_2 \sigma_3 C = \begin{bmatrix} 0 & -1 \\ 1 & 0 \end{bmatrix}_{(s)} \begin{bmatrix} 1 & 0 \\ 0 & -1 \end{bmatrix}_{(\alpha)} C \quad (4.83)$$

with $-is_2$ acting on the spin index, σ_3 acting on the flavor index, and C the complex conjugation. To check this symmetry it is helpful to assign numeric values to the indices: $\uparrow \hat{=} 1$, $\downarrow \hat{=} -1$, $x \hat{=} 1$, $y \hat{=} -1$. Then we find that $\psi^\dagger K \psi$ is invariant under

\hat{T} because we have

$$\hat{T} \sum_{\alpha,s} \psi_{\alpha,i,s}^\dagger \psi_{\alpha,j,s} \hat{T}^{-1} = \sum_{\alpha,s} (as)^2 \psi_{\alpha,i,-s}^\dagger \psi_{\alpha,j,-s} = \sum_{\alpha,s} \psi_{\alpha,i,s}^\dagger \psi_{\alpha,j,s}. \quad (4.84)$$

We also find that $\psi^\dagger V[\vec{\varphi}] \psi$ is invariant:

$$\begin{aligned} & \hat{T} \lambda \sum_i e^{i \mathbf{Qr}_i} \sum_{\substack{\alpha\alpha' \\ ss'}} [\sigma_1]_{\alpha\alpha'} [\vec{s} \cdot \vec{\varphi}_i]_{ss'} \psi_{\alpha,i,s}^\dagger \psi_{\alpha',i,s'} \hat{T}^{-1} \\ &= \lambda \sum_i e^{-i \mathbf{Qr}_i} \sum_{\substack{\alpha\alpha' \\ ss'}} [\sigma_1]_{\alpha\alpha'} [\vec{s} \cdot \vec{\varphi}_i]_{ss'}^* \alpha\alpha' ss' \psi_{\alpha,i,-s}^\dagger \psi_{\alpha',i,-s'} = \dots, \end{aligned} \quad (4.85)$$

where we calculate

- $[\sigma_1]_{\alpha\alpha'} \alpha\alpha' = \delta_{\alpha,-\alpha'} \alpha\alpha' = -\delta_{\alpha,\alpha'} = -[\sigma_1]_{\alpha\alpha'} ,$
- $[s_1]_{ss'}^* ss' = [s_1]_{ss'} ss' = -[s_1]_{ss'} ,$
- $[s_2]_{ss'}^* ss' = \delta_{s,-s} (-is)^* ss' = -\delta_{s,-s} (is) = [s_2]_{ss'} ss' ,$ and
- $[s_3]_{ss'}^* ss' = [s_3]_{ss'}^* ss' = \delta_{s,s'} sss' = [s_3]_{s,s'} ,$

and conclude

$$\begin{aligned} \dots &= \lambda \sum_i e^{+i \mathbf{Qr}_i} \sum_{\substack{\alpha\alpha' \\ ss'}} (-1) [\sigma_1]_{\alpha\alpha'} [-\varphi_i^1 s_1 + \varphi_i^2 s_2 + \varphi_i^3 s_3]_{s,s'} \psi_{\alpha,i,-s}^\dagger \psi_{\alpha',i,-s'} \\ &= \lambda \sum_i e^{i \mathbf{Qr}_i} \sum_{\substack{\alpha\alpha' \\ ss'}} (-1) [\sigma_1]_{\alpha\alpha'} [-\varphi_i^1 s_1 + \varphi_i^2 s_2 + \varphi_i^3 s_3]_{-s,-s'} \psi_{\alpha,i,s}^\dagger \psi_{\alpha',i,s'} \\ &= \lambda \sum_i e^{i \mathbf{Qr}_i} \sum_{\substack{\alpha\alpha' \\ ss'}} (-1) [\sigma_1]_{\alpha\alpha'} [-\varphi_i^1 s_1 - \varphi_i^2 s_2 - \varphi_i^3 s_3]_{s,s'} \psi_{\alpha,i,s}^\dagger \psi_{\alpha',i,s'} \\ &= \lambda \sum_i e^{i \mathbf{Qr}_i} \sum_{\substack{\alpha\alpha' \\ ss'}} [\sigma_1]_{\alpha\alpha'} [\vec{s} \cdot \vec{\varphi}_i]_{ss'} \psi_{\alpha,i,s}^\dagger \psi_{\alpha',i,s'}. \end{aligned} \quad (4.86)$$

4.3.3 Fermion determinant and $O(N)$ symmetric variations

Further following Sec. 4.1, we integrate out the fermions in Eq. (4.79) and obtain

$$\mathcal{Z} = \int D\vec{\varphi} e^{-S_B[\vec{\varphi}]} \det G_\varphi^{-1} + O(\Delta\tau^2) \quad (4.87)$$

with the equal-time Green's function, evaluated for a configuration $\vec{\varphi}$,

$$G_\varphi = \left[\mathbb{1} + \prod_{\ell=m}^1 B_\ell \right]^{-1}, \quad \text{where} \quad B_\ell = e^{-\frac{\Delta\tau}{2} K} e^{-\Delta\tau V[\vec{\varphi}(\ell\Delta\tau)]} e^{-\frac{\Delta\tau}{2} K}. \quad (4.88)$$

After partitioning the matrix exponential factors in B_ℓ into $N_s \times N_s$ -sized blocks, they read

$$e^{-\frac{\Delta\tau}{2} K} = \text{diag} \left[e^{-\frac{\Delta\tau}{2} K_x^\uparrow}, e^{-\frac{\Delta\tau}{2} K_y^\downarrow}, e^{-\frac{\Delta\tau}{2} K_x^\downarrow}, e^{-\frac{\Delta\tau}{2} K_y^\uparrow} \right], \quad (4.89a)$$

$$e^{-\Delta\tau V_\ell} = \begin{bmatrix} C & S & -X \\ S^* & C & X \\ X & C & S^* \\ -X & S & C \end{bmatrix}. \quad (4.89b)$$

For now we have $K_x^\uparrow \equiv K_x^\downarrow$ and $K_y^\uparrow \equiv K_y^\downarrow$, but in Chap. 5 we will appreciate some additional freedom in the definition of these matrices. The submatrices of $e^{-\Delta\tau V_\ell}$ are diagonal and have the following entries:

$$C_{ij} = \delta_{ij} \text{ch}(\Delta\tau\lambda|\vec{\varphi}_j(\ell)|), \quad (4.90a)$$

$$S_{ij} = \delta_{ij} [i\varphi_j^2(\ell) - \varphi_j^1(\ell)] \text{sh}(\Delta\tau\lambda|\vec{\varphi}_j(\ell)|)/|\vec{\varphi}_j(\ell)|, \quad (4.90b)$$

$$X_{ij} = \delta_{ij} \varphi_j^3(\ell) \text{sh}(\Delta\tau\lambda|\vec{\varphi}_j(\ell)|)/|\vec{\varphi}_j(\ell)|. \quad (4.90c)$$

Generically, the order parameter $\vec{\varphi}$ is of O(3) symmetry with three distinct vector components. It can, however, also be interesting to partially break its rotational symmetry.

In two spatial dimensions the Mermin-Wagner theorem [17] excludes the spontaneous breaking of continuous symmetries at finite temperature. Consequently, the O(3) model does not have an SDW ordered phase at $T > 0$. Only a crossover to an SDW ordered ground state can be tracked there. The reduced order parameter symmetry of an O(2) model, applicable for a physical system with *easy-plane magnetism*, is still continuous, but there a finite-temperature phase transition of Berezinskii-Kosterlitz-Thouless (BKT) character [137–139] is a possibility. The low-temperature phase in such a model is entirely critical, and while it cannot show true long-range order, its distinct correlations can be identified as quasi-long-range order. Finally, an O(1) model, corresponding to *easy-axis magnetism*, can have finite-temperature transitions belonging to the Ising universality class with a conventional long-range ordered SDW phase at low temperatures.

On a more technical level, lowering the rotational symmetry of $\vec{\varphi}$ introduces a new symmetry to the fermion action. To obtain an O(2) model we fix φ^3 to zero. This sets X in Eq. (4.89) to zero and we find

$$e^{-\Delta\tau V_\ell} = \begin{bmatrix} C & S \\ S^* & C \\ & C & S^* \\ & S & C \end{bmatrix} = \begin{bmatrix} \tilde{V}(\ell) & \\ & \tilde{V}(\ell)^* \end{bmatrix}, \quad (4.91)$$

where $\tilde{V}(\ell)$ is a complex $2N_s \times 2N_s$ matrix and consequently the Green's function is block diagonal. At this point we consider the matrix K to be real. If one sustains this or otherwise upholds the condition $K_\alpha^\uparrow = K_\alpha^{\downarrow,*}$,⁴ the Green's function decomposes into two blocks related by complex conjugation:

$$G_\varphi = \begin{bmatrix} \tilde{G}_\varphi & \\ & \tilde{G}_\varphi^* \end{bmatrix}. \quad (4.92)$$

Hence, we can write the partition function as

$$\mathcal{Z} = \int D\vec{\varphi} e^{-S_B[\vec{\varphi}]} \left| \det \tilde{G}_\varphi^{-1} \right|^2 + O(\Delta\tau^2). \quad (4.93)$$

Remarkably, the O(2) model can be seen to be sign-problem-free by determinant factorization without having to refer to Theorem 4.1. An important benefit of the decomposition (4.92) is that with \tilde{G}_φ all single-fermion matrices involved in the DQMC algorithm are of size $2N_s \times 2N_s$ instead of $4N_s \times 4N_s$ in the O(3) model. As we will see in Chap. 5, this reduces the computational cost of the most expensive operations by a factor of 8. Most results presented in this thesis have been obtained for the O(2) model.

We can implement an O(1) model by additionally fixing $\varphi^2 = 0$. Then the matrix in Eq. (4.91) is real and if K remains real, the Green's function matrix consists of two equal real blocks

$$G_\varphi = \begin{bmatrix} \tilde{G}_\varphi & \\ & \tilde{G}_\varphi \end{bmatrix}. \quad (4.94)$$

with the partition function as in Eq. (4.8). In simulations of such an O(1) model the numerical linear algebra can be entirely based on real numbers, which provides an

⁴Otherwise the antiunitary symmetry \hat{T} would be broken.

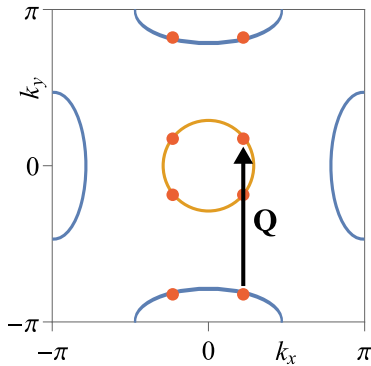


Figure 4.5: Fermi surface sketch fitting the pnictides. Hot spots on the central hole pocket (orange) are linked with hot spots on an electron pocket (blue) by the wavevector $\mathbf{Q} = (0, \pi)^T$.

additional speedup compared to the complex numbers otherwise necessary.

Interestingly, a model that is almost equivalent to the O(1) model, albeit with a simpler bosonic action that does not include dynamics or a quartic term and with a different form of the electronic dispersion, was already studied in 2003 by Assaad et. al [140].

4.3.4 Other types of Fermi surfaces

As we have seen at the beginning of this Section, the two-band model (4.75) is appropriate to understand the universal physics of a $\mathbf{Q} = (\pi, \pi)^T$ ordering SDW QCP on a single “large” Fermi surface, which is similar to the cuprates. The careful justification of moving to a two-band structure would not have been necessary in the case of other physically interesting systems such as the iron-based superconductors. Schematically, the Fermi surfaces of the pnictides have the structure shown in Fig. 4.5 [3, 141]. Models for these materials directly feature multiple orbitals. Already in the absence of SDW order there are electron and hole pockets. The QCP associated to stripe-like SDW order with a vertical ordering wavevector $\mathbf{Q} = (0, \pi)^T$, linking hot spots distributed over the separate bands, is described by the action (4.87) with appropriately set fermionic dispersion relations. It can be simulated in sign-problem-free DQMC simulations.

5 Numerical methodology

In this Chapter we discuss several important technical aspects of challenges faced in the implementation of DQMC simulations of the SDW model introduced in Sec. 4.3. We begin with the topic of numerical stabilization in Sec. 5.1, where a technique is introduced that is essential for obtaining correct results at all but the highest temperatures. Various Monte Carlo updating schemes are discussed in Sec. 5.2. These are important to correctly reach equilibrium and to collect as many statistically independent samples as possible in relatively short simulations. This is of particular significance in light of the high computational cost of the determinantal method. Notable areas where this cost can be lowered are pointed out in Sec. 5.3. In numerical simulations of itinerant electron systems finite-size effects can be very strong. Approaches to reduce their impact are the topic of Sec. 5.4. Finally, various aspects related to processing of data measured in DQMC simulations are given in Sec. 5.5.

5.1 Numerical stabilization

The central object of all DQMC simulations is the equal-time Green's function matrix at an imaginary-time slice $\tau = \ell \Delta\tau$ computed for a configuration of the bosonic field $\vec{\varphi}$

$$G_{\vec{\varphi}}(\tau = \ell \Delta\tau) = (\mathbb{1} + B_\ell B_{\ell-1} \cdots B_1 B_m B_{m-1} \cdots B_{\ell+1})^{-1}. \quad (5.1)$$

The determinant of its inverse gives the fermionic part of the statistical weight associated to the configuration $\vec{\varphi}$ and ratios of such determinants for different configurations provide transition probabilities for all Monte Carlo updates. Moreover, all fermionic observables are computed from $G_{\vec{\varphi}}$. Hence, in DQMC simulations it is essential to compute $G_{\vec{\varphi}}$ correctly. At low temperatures (large values $m = \beta/\Delta\tau$) the product of a long chain of matrices B_ℓ is formed and added to the identity matrix in Eq. (5.1). This must be done in a numerically controlled way to avoid that rounding errors, which are caused by the finite machine precision of floating point numbers, accumulate destructively such that after the matrix inversion all physical information would be lost. This is not a trivial feat since the matrix to be inverted is ill-conditioned.

To quantify this observation it is helpful to introduce the **condition number** $\kappa(A) = \|A\| \cdot \|A^{-1}\|$ for a matrix A , where $\|\cdot\|$ is a matrix norm. If we choose an

entrywise Euclidean norm, the condition number is given by $\kappa(A) = \sigma_{\max}(A)/\sigma_{\min}(A)$, the ratio of the maximal and minimal **singular values** of A [142, Sect. 2.6.2].¹ If A is ill-conditioned, $\kappa(A)$ is large, which signifies that the matrix is close to being singular (where $\kappa = \infty$). An order of magnitude estimate for $\kappa = 10^D$ is that after numerical inversion approximately D digits of floating point precision are lost [143, Chapt. 11]. To see how this can be problematic for the DQMC algorithm we can consider the fermionic matrix for a comparably mild problem: a non-interacting tight-binding model on a square lattice at zero chemical potential [82, Chapt. 7]. For $\mathcal{H} = \underline{c}^\dagger K \underline{c} = -t \sum_{\langle i,j \rangle} c_i^\dagger c_j$, the eigenvalues of K are $\varepsilon_{\mathbf{k}} = -2t(\cos k_x + \cos k_y)$, $-4t \leq \varepsilon_{\mathbf{k}} \leq 4t$, and the fermion matrix is just

$$G^{-1} = \mathbb{1} + e^{-\beta K}. \quad (5.2)$$

Since this matrix is positive definite, its singular values are equal to the eigenvalues and we find a condition number of $\kappa = e^{4\beta t}$. For a temperature of $T = 1/\beta = t/10$ we already have $\kappa \approx 10^{17}$ and the expected loss of precision after naive inversion just exceeds the accuracy of standard “double precision” floating point arithmetic. In this case T is small compared to electronic bandwidth of $8t$, highlighting that this is mainly an issue at low temperatures. This problem is amplified strongly when \mathcal{H} contains interaction terms that do not commute with the kinetic part and after Suzuki-Trotter decomposition we have to consider the chain of matrix products of Eq. (5.1). If too many ill-conditioned matrices are multiplied naively, a fatal loss of precision sets in already before the addition to $\mathbb{1}$ and the inversion.

The issue of ill-conditioned matrices is particularly relevant for simulations of fermionic systems. At low temperatures the Boltzmann distribution $e^{-\beta(\mathcal{H}-\mu N)}$ amplifies the weight of the lowest energy states far below the chemical potential μ . Due to the Pauli principle, however, these states cannot be occupied macroscopically. Rather, available states are filled up by single fermions up to the Fermi level. Hence, at low temperatures, important contributions to the dynamics only include comparatively high-energy states close to the Fermi energy, which are exponentially suppressed by their Boltzmann factors. If insufficient care is taken in the evaluation of Eq. (5.1), numerical scales corresponding to these low and high-energy states are mixed and, due to finite machine precision, information about high-energy states associated to small Boltzmann factors is lost. Effectively, this destroys the fermionic character of the system under study.

¹A matrix A can be factorized in a singular value decomposition $A = U\Sigma V$, where U and V are unitary matrices and Σ is a diagonal matrix with non-negative real entries. The entries σ_i of Σ are the singular values. Σ is unique under the convention that the σ_i are enumerated in descending order.

5.1.1 Matrix decomposition for the equal-time Green's function

An effective strategy to avoid these numerical stability problems is based on matrix decomposition techniques [87, 114, 144]. Perfect numerical stability cannot be achieved in finite-precision computations, but we can assure an operational stability allowing us to calculate matrix elements of the Green's function to a desired precision that is higher than the final statistical uncertainty of our Monte Carlo estimates.

We assume that we can evaluate the product of a number of $s < m$ matrices B_ℓ in a sufficiently stable manner. Practically, for an imaginary-time discretization $\Delta\tau = 0.1$, hopping constants $t \simeq 1$, and moderate coupling constants, a choice of $s = 10$ is viable. Having computed such a product, we can bring it into a suitably factorized form:

$$B_{(k+1)s} \cdots B_{ks+1} = UDV. \quad (5.3)$$

Here U and V are well-conditioned matrices of approximately unit scale and D is a diagonal matrix whose entries hold all numerical scales contained in the matrix $B_{(k+1)s} \cdots B_{ks+1}$. If U and V are unitary, for instance, their condition number is $\kappa(U) = \kappa(V) = 1$. The factorization allows to avoid the mixing of numerical scales of different magnitude in matrix products. We arrange matrix products in such a way that the different scales of D are never multiplied with each other. We do not need to exercise much care in multiplying the well-conditioned matrices U and V , since that will not lead to the loss of numerical precision.

Schematically the decomposition (5.3) has the following character:

$$UDV = \underbrace{\begin{bmatrix} x & x & x & x \\ x & x & x & x \\ x & x & x & x \\ x & x & x & x \end{bmatrix}}_{\text{unit scales}} \cdot \underbrace{\begin{bmatrix} X & & & \\ & X & & \\ & & X & \\ & & & x \end{bmatrix}}_{\text{diagonal}} \cdot \underbrace{\begin{bmatrix} x & x & x & x \\ x & x & x & x \\ x & x & x & x \\ x & x & x & x \end{bmatrix}}_{\text{unit scales}},$$

where the various sizes of the letter x represent different numerical scales. If we explicitly carried out the numeric multiplication of the right-hand side matrices, we would obtain a matrix of the form

$$U \cdot D \cdot V = \begin{bmatrix} X & X & X & X \\ X & X & X & X \\ X & X & X & X \\ X & X & X & X \end{bmatrix}$$

with the largest numerical scale dominating, while information at smaller scales is “washed out”. This is the situation to be avoided.

Notably, the decomposition (5.3) must itself be performed in a numerically stable way. The literature on numerical analysis holds a variety of appropriate decomposition techniques [145]. A good, stable choice is the singular value decomposition (SVD) as implemented in the Lapack routines xgesvd [146]. It has been used for all results presented in this thesis. With the SVD, U and V are unitary and D holds the singular values of the multiplied pack of matrices $B_{(k+1)s} \cdots B_{ks+1}$. Alternatively, one could base the procedure of factorization on the modified Gram-Schmidt method of orthogonalization, which may be faster at the cost of some numerical stability [82, Chapt. 7]. QR decompositions with column pivoting may also help improve performance at little cost of stability [147].

To compute the product of more than s matrices B_ℓ we start by forming groups of up to s matrices each and factorize the rightmost group into UDV . To successively obtain longer products in UDV decomposed form we proceed iteratively as explained in the following :

$$\underbrace{B_{(k+2)s} \cdots B_{(k+1)s+1}}_{\text{group } k+1} \cdot \underbrace{B_{(k+1)s} \cdots B_{ks+1}}_{\text{group } k \rightarrow \text{SVD}} = B_{(k+2)s} \cdots B_{(k+1)s+1} \cdot U_k D_k V_k = \dots \quad (5.4)$$

Now it is important to carry out the next matrix multiplications in the order indicated by the parentheses. We compute a partial product and factorize it into UDV form:

$$\dots = \underbrace{\left[(B_{(k+2)s} \cdots B_{(k+1)s+1} \cdot U_k) \cdot D_k \right]}_{\rightarrow \text{SVD}} \cdot V_k = U' D' V' \cdot V_k. \quad (5.5)$$

Here, multiplying the well-conditioned unit-scale matrix U_k from the right is not problematic. The following multiplication of D_k from the right does not mix any scales of D_k because each singular value in D_k rescale a separate column in the matrix to its left, schematically:

$$\begin{aligned} & (B_{(k+2)s} \cdots B_{(k+1)s+1} \cdot U_k) \cdot D_k \\ &= (B_{(k+2)s} \cdots B_{(k+1)s+1} \cdot U_k) \cdot \begin{bmatrix} \mathbf{X} & & & \\ & \mathbf{X} & & \\ & & \mathbf{X} & \\ & & & \mathbf{x} \end{bmatrix} = \begin{bmatrix} \mathbf{X} & \mathbf{X} & \mathbf{x} & \mathbf{x} \\ \mathbf{X} & \mathbf{X} & \mathbf{x} & \mathbf{x} \\ \mathbf{X} & \mathbf{X} & \mathbf{x} & \mathbf{x} \\ \mathbf{X} & \mathbf{X} & \mathbf{x} & \mathbf{x} \end{bmatrix}. \end{aligned}$$

In Eq. (5.5) it is important to first factorize this result before multiplying it with another matrix such that the different scales remain separated. We can now read off

the properly factorized form of the entire product in Eq. (5.4):

$$B_{(k+2)s} \cdots B_{(k+1)s+1} \cdot B_{(k+1)s} \cdots B_{ks+1} = U' D' V' \cdot V_k = U_{k+1,k} D_{k+1,k} V_{k+1,k}, \quad (5.6)$$

where we identify

$$U_{k+1,k} = U', \quad D_{k+1,k} = D', \quad \text{and} \quad V_{k+1,k} = V' V_k. \quad (5.7)$$

By repeating this procedure we can reliably compute product strings of matrices B_ℓ of arbitrary length.

Having obtained a stably factorized representation of the entire chain $B_m \dots B_1 = U_n D_n V_n$, we can calculate the equal-time Green's function $G_{\vec{\varphi}}(\tau = \beta = m\Delta\tau) \equiv G_m$ of Eq. (5.1) without requiring the numerical inversion of anything but a diagonal matrix:

$$\begin{aligned} G_m &= (\mathbb{1} + B_m \cdots B_1)^{-1} = (\mathbb{1} + U_n D_n V_n)^{-1} \\ &= \left(U_n \underbrace{[U_n^\dagger V_n^\dagger + D_n]}_{\rightarrow \text{SVD}} V_n \right)^{-1} = \left(U_n U_x D_x V_x V_n \right)^{-1} \\ &= (V_n^\dagger V_x^\dagger) D_x^{-1} (U_x^\dagger U_n^\dagger) = (V_x V_n)^\dagger D_x^{-1} (U_n U_x)^\dagger. \end{aligned} \quad (5.8)$$

In the second line we take the SVD of the sum of a matrix of unit scale and D_n , which does not mix the scales in D_n in a multiplicative way. In the third line we invert all factors individually, where we assume that the matrices U and V are unitary. The inversion of each scalar in D_x is safe over a very wide dynamic range and does not entail the loss of accuracy we would experience when inverting a non-diagonal matrix that holds the same scales. The smallest scales in G_m are lost in the final step in Eq. (5.8), but this is not of significance for the computation of matrix elements of the Green's function.

To obtain the equal-time Green's function $G_\ell = G_{\vec{\varphi}}(\ell\Delta\tau)$ at arbitrary imaginary-time slices $\ell < m$, we could repeat this procedure for differently ordered matrix sequences like $B_\ell B_{\ell-1} \cdots B_1 B_m B_{m-1} \cdots B_{\ell+1}$. This can become rather costly. It pays to store previously evaluated partial product chains in UDV factorized form to reduce the number of SVDs to be performed, which are the most expensive part of the algorithm. Additional memory requirements are less significant. To compute G_ℓ in this way we make use of two partial products in UDV form,

$$B_\ell \cdots B_1 = U_R D_R V_R \quad \text{and} \quad B_m \cdots B_{\ell+1} = U_L D_L V_L. \quad (5.9)$$

Then we find

$$\begin{aligned}
 G_\ell &= (\mathbb{1} + B_\ell \cdots B_1 B_m \cdots B_{\ell+1})^{-1} = (\mathbb{1} + U_R D_R V_R U_L D_L V_L)^{-1} \\
 &= \left(U_R \underbrace{[U_R^\dagger V_L^\dagger + D_R(V_R U_L) D_L]}_{\rightarrow \text{SVD}} V_L \right)^{-1} = (U_R U_x D_x V_x V_L)^{-1} \\
 &= (V_L^\dagger V_x^\dagger) D_x^{-1} (U_x^\dagger U_R^\dagger) = (V_x V_L)^\dagger D_x^{-1} (U_R U_x)^\dagger.
 \end{aligned} \tag{5.10}$$

In this computation it is important to hold the diagonal matrices D_R and D_L on the outer sides of the matrix product. Schematically the numerical scales in the term from which the SVD is computed are distributed like this:

$$\begin{aligned}
 &U_R^\dagger V_L^\dagger + D_R(V_R U_L) D_L \\
 &= \begin{bmatrix} x & x & x & x \\ x & x & x & x \\ x & x & x & x \\ x & x & x & x \end{bmatrix} + \begin{bmatrix} \mathbf{X} & & & \\ & \mathbf{X} & & \\ & & x & \\ & & & x \end{bmatrix} \cdot \begin{bmatrix} x & x & x & x \\ x & x & x & x \\ x & x & x & x \\ x & x & x & x \end{bmatrix} \cdot \begin{bmatrix} \mathbf{X} & & & \\ & \mathbf{X} & & \\ & & x & \\ & & & x \end{bmatrix} \\
 &= \begin{bmatrix} x & x & x & x \\ x & x & x & x \\ x & x & x & x \\ x & x & x & x \end{bmatrix} + \begin{bmatrix} \mathbf{XX} & \mathbf{XX} & \mathbf{X}_x & \mathbf{X}_x \\ \mathbf{XX} & \mathbf{XX} & \mathbf{X}_x & \mathbf{X}_x \\ x\mathbf{X} & x\mathbf{X} & xx & x_x \\ x\mathbf{X} & x\mathbf{X} & x_x & xx \end{bmatrix}.
 \end{aligned}$$

Evidently, some mixing of scales occurs, but the cut-off of the smallest scales occurs only at the final addition. Since this step is only performed a single time for each evaluation of G_ℓ , numerical rounding errors remain well controlled.

5.1.2 Efficient and stable DQMC sweep

In DQMC simulations changes to the bosonic field $\vec{\varphi}$ must be attempted continuously and, if they are accepted, the corresponding Green's function $G_{\vec{\varphi}}$ needs to be recomputed. The fundamental move is a local update, where changes to the field $\vec{\varphi}_i(\tau)$ are proposed at a single lattice site i in one imaginary-time slice τ . A sequence of such update attempts that encompasses the entire spacetime lattice is called a **sweep**. In Sec. 5.2 we will see that a local update at imaginary time τ can be implemented efficiently, provided the equal-time Green's function matrix $G_{\vec{\varphi}}(\tau)$ is available for the same τ . This Subsection details how such a sweep can be realized in an efficient and numerically stable way, essentially following the setup outlined by Assaad and Evertz [83].

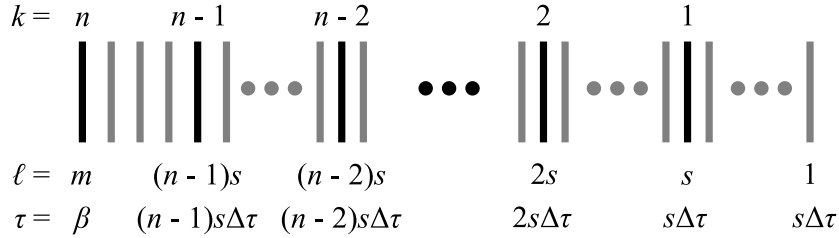


Figure 5.1: Imaginary-time intervals used in the sweep.

Knowing the Green's function G_ℓ at $\tau = \ell\Delta\tau$, we can compute it at the neighboring imaginary-time slices by “wrapping up”,

$$\begin{aligned} G_{\ell+1} &\equiv [\mathbb{1} + B_{\ell+1} \cdots B_1 B_m \cdots B_{\ell+2}]^{-1} \\ &= \left[B_{\ell+1} \left(\underbrace{B_{\ell+1}^{-1} B_{\ell+1}}_1 + B_\ell \cdots B_1 B_m \cdots B_{\ell+1} \right) B_{\ell+1}^{-1} \right]^{-1} \\ &= B_{\ell+1} \cdot G_\ell \cdot B_{\ell+1}^{-1}, \end{aligned} \quad (5.11)$$

or “wrapping down”,

$$\begin{aligned} G_{\ell-1} &\equiv [\mathbb{1} + B_{\ell-1} \cdots B_1 B_m \cdots B_\ell]^{-1} \\ &= \left[B_\ell^{-1} \left(\underbrace{B_\ell B_\ell^{-1}}_1 + B_\ell \cdots B_1 B_m \cdots B_{\ell+1} \right) B_\ell \right]^{-1} \\ &= B_\ell^{-1} \cdot G_\ell \cdot B_\ell. \end{aligned} \quad (5.12)$$

This is the fastest way to propagate the Green's function to a different imaginary time. If the checkerboard break up, that will be introduced in Sec. 5.3.1, is used, the B -matrices and their inverses are sparse and a wrapping step has a computational cost $O(N_s^2)$. However, as discussed at the beginning of this Section, the B -matrices are ill-conditioned and the wrapping procedure is numerically unstable. After moving s steps in imaginary time, where s is small enough such that a product of s matrices B_ℓ can be computed accurately without having to rely on factorization, the Green's function needs to be recomputed from scratch under application of the techniques of Sec. 5.1.1. This is more costly, since the SVDs and the products of dense matrices U and V are $O(N_s^3)$ operations.

We subdivide the inverse temperature $\beta = m \cdot \Delta\tau$ into n imaginary-time intervals of length $s \cdot \Delta\tau$ as illustrated in Fig. 5.1.² At those imaginary times labeled by

²If n is not a divisor of m , the last segment is shorter than s .

$k = 1, \dots, n$ in the figure a fresh Green's function is computed from scratch, while wrapping can be used at intermediate time slices.

To reduce the computational cost of computing the Green's function we maintain a storage of partial chains of B -matrices in UDV factorized form. After a Monte Carlo update that is local in imaginary time the B -matrices at other imaginary times remain valid for the new configuration $\vec{\varphi}$. Here we require some memory to store matrices labeled U_k , D_k , V_k for $0 \leq k \leq n$. We call the step of moving from a storage time slice k to $k+1$ or $k-1$, where the Green's function is to be recomputed, *advancing up* or *down*.

The precondition for **advancing up** from k to $k+1$ is that our UDV storage holds firstly $U_{k+1}D_{k+1}V_{k+1} = B_m \cdots B_{(k+1)s-1}$ and secondly $U_kD_kV_k = B_{ks} \cdots B_1$, where in both cases the B -matrices are currently valid. From the field $\vec{\varphi}$ at the intermediate time slices we compute the current $B_{(k+1)s} \cdots B_{ks+1}$. Multiplied to the left of $U_kD_kV_k$ via Eqs. (5.4)–(5.5), this yields $B_{(k+1)s} \cdots B_1$ in UDV form. Together with $U_{k+1}D_{k+1}V_{k+1}$ we compute the fresh Green's function at $\tau = (k+1)s\Delta\tau$ via Eq. (5.10). In the special case of advancing up to $\tau = \beta = m\Delta\tau$, $k+1 = n$, we apply Eq. (5.8) with the stable product of $U_kD_kV_k$ and $B_m \cdots B_{(n-1)s+1}$ computed from the current configuration of $\vec{\varphi}$, while we do not need $U_{k+1}D_{k+1}V_{k+1}$. At any k we put the SVD of $B_{(k+1)s} \cdots B_1$ into our storage as $U_{k+1}D_{k+1}V_{k+1}$ to prepare for the next advancing step.

The precondition for **advancing down** from k to $k-1$ is that our UDV storage contains firstly $U_kD_kV_k = B_m \cdots B_{ks+1}$ and secondly $U_{k-1}D_{k-1}V_{k-1} = B_{(k-1)s} \cdots B_1$. From the field $\vec{\varphi}$ at the intermediate time slices we compute the current $B_{ks} \cdots B_{(k-1)s+1}$ (or $B_m \cdots B_{(n-1)s+1}$). Multiplied to the right of $U_kD_kV_k$ via Eqs. (5.4)–(5.5), this yields $B_m \cdots B_{(k-1)s+1}$ in UDV form. Together with $U_{k-1}D_{k-1}V_{k-1}$ we compute the fresh Green's function at $\tau = (k-1)s\Delta\tau$ via Eq. (5.10). In the special case of advancing down to $\tau = 0$, which is equivalent to $\tau = \beta$, we apply Eq. (5.8) with the stable product of $U_kD_kV_k$ and $B_s \cdots B_1$ computed from the current configuration of $\vec{\varphi}$, while we do not need $U_{k-1}D_{k-1}V_{k-1}$. At any k we put the SVD of $B_m \cdots B_{(k-1)s+1}$ into our storage as $U_{k-1}D_{k-1}V_{k-1}$ to prepare for the next advancing step.

As explained above the advancing operations serve to refresh the Green's function to avoid over-accumulation of rounding errors from wrapping operations. In the following detailed prescription of the DQMC sweep we perform one extra step of wrapping before advancing. This signifies that there are two evaluations of the same Green's function matrix available. Here one should use the opportunity to check that the numerical difference between the version obtained by wrapping and the freshly computed one are sufficiently small. Otherwise the parameter s may need to be adjusted.

Initialization:

We start with some, e.g. random, initialization of the field configuration $\vec{\varphi}$. We compute $B_s \cdots B_1$ and store the SVD of the product in U_1, D_1, V_1 . Then we continue iteratively: Given the SVD of $B_{ks} \cdots B_1 = U_k D_k V_k$ we compute the SVD of $B_{(k+1)s} \cdots B_1$ and store the result in $U_{k+1}, D_{k+1}, V_{k+1}$ as detailed in Eqs. (5.4)–(5.5). After this initialization we have set up the *UDV* storage to contain

$$U_k D_k V_k = B_{ks} \cdots B_1, \quad \text{for } 1 \leq k \leq n. \quad (5.13)$$

We then compute the Green's function at $\tau = \beta$: $G_m = (\mathbb{1} + U_n D_n V_n)^{-1}$ using Eq. (5.8) and continue with the first sweep down.

Sweep down from $\tau = \beta$ to $\tau = \Delta\tau$ ($\ell = m$ to $\ell = 1$):

The precondition is to have computed the current Green's function at $\ell = m$ and that our storage contains $U_k D_k V_k = B_{ks} \cdots B_1$ for $1 \leq k \leq n$.

In the case that we incorporate a global update, see Sec. 5.2.2, we attempt it now.

Going from $\ell = m$ down to $\ell = (n-1) \cdot s$, for each $\tau = \ell \Delta\tau$ we attempt local updates at that time slice, update the Green's function G_ℓ accordingly and potentially take observable measurements, then wrap down using Eq. (5.12) to obtain $G_{\ell-1}$.

For the remaining time slices we go from $k = n-1$ down to $k = 1$. First we advance down from $k+1$ to k to fully refresh the Green's function at $\tau = ks\Delta\tau$. Then we go from $\ell = ks$ down to $\ell = (k-1)s$, where we propose changes of the field at $\tau = k\Delta\tau$, update the Green's function G_ℓ , potentially take measurements and wrap down to obtain $G_{\ell-1}$.

Finally, we refresh the Green's function at $\tau = 0$ by advancing it down from $k = 1$ to $k = 0$.

At this point we may do a replica exchange move, see Sec. 5.2.3.

In the course of this sweep down we have fully updated all auxiliary fields at all time slices $\beta \geq \tau \geq \Delta\tau$. Our *UDV* storage now contains

$$U_k D_k V_k = B_m \cdots B_{ks}, \quad \text{for } 0 \leq k \leq n. \quad (5.14)$$

We continue with a sweep up.

Sweep up from $\tau = \Delta\tau$ to $\tau = \beta$ ($\ell = 1$ to $\ell = m$):

The precondition is to have computed the current Green's function at $\ell = 0$ and that our storage contains $U_k D_k V_k = B_m \cdots B_{k_s}$ for $0 \leq k \leq n$.

We set the *UDV* storage for $k = 0$ to unity: $U_0 D_0 V_0 = \mathbb{1}$.

Then we go from $k = 0$ up to $k = n - 2$. For each k we go from $\ell = ks + 1$ up to $(k + 1)s$. We wrap up the Green's function at $\ell - 1$ to compute G_ℓ using Eq. (5.11), update the auxiliary fields and accordingly the Green's function at $\tau = \ell \Delta\tau$ and potentially take measurements. After s steps of wrapping up, we advance the Green's function up from k to $k + 1$ to refresh $G_{(k+1)s}$.

The highest time slices need to be handled separately to cover the possibility that s is not a divisor of m . Therefore we go from $\ell = (n - 1)s$ up to $\ell = m$: For each time slice we wrap up the Green's function from $\ell - 1$ to ℓ , where we update the auxiliary fields $\vec{\varphi}(\tau = \ell \Delta\tau)$ and accordingly the Green's function G_ℓ and potentially take measurements.

Finally, we refresh the Green's function at the highest time slice $\tau = \beta$ by advancing up from $n - 1$.

At this point we may do a replica exchange move, see Sec. 5.2.3.

In the course of this sweep up we have fully updated all auxiliary fields at all time slices $\Delta\tau \leq \tau \leq \beta$. Our *UDV* storage now contains

$$U_k D_k V_k = B_{k_s} \cdots B_1, \quad \text{for } 1 \leq k \leq n. \quad (5.15)$$

We continue with the next sweep down.

Thanks to the alternation of sweeps upwards and downwards in imaginary time we can optimally use the *UDV* storage to avoid unnecessary recalculations of factorized *B*-matrix product strings. The total computational effort of one DQMC sweep is of order $O(\beta N_s^3)$.

Note that, while the sweep in this Section has been described in terms of the full Green's function matrix $G_{\vec{\varphi}}$ and full-sized matrices B_ℓ , in the implementation of the O(1) and O(2) models introduced in Sec. 4.3.3, all these operations will be carried out on the reduced size Green's function $\tilde{G}_{\vec{\varphi}}$ and the corresponding matrices \tilde{B}_ℓ .

5.2 Monte Carlo updating schemes

In this Section we discuss the actual stochastic dynamics of the DQMC simulations. The basic mechanism is the Metropolis algorithm in the form given at the end of

Sec. 4.1.2. Most importantly, we use it for efficient local updates, as detailed below in Sec. 5.2.1, but also the global updates of Sec. 5.2.2, which are important for proper thermalization, are based on the Metropolis transition probability. Finally, the replica exchange mechanism introduced in Sec. 5.2.3 takes advantage of extending the standard grand-canonical ensemble. The dynamics in this extended ensemble is again controlled by the Metropolis algorithm. The careful combination of the various techniques described below is essential to ensure that the DQMC simulations properly converge and that statistical autocorrelation times are not too long, especially in the light of critical slowing down near a magnetic phase transition.

5.2.1 Local updates

The acceptance probability for an update of the bosonic field configuration $\vec{\varphi} \rightarrow \vec{\varphi}'$ is, see Eq. (4.20),

$$A(\vec{\varphi} \rightarrow \vec{\varphi}') = \min \left\{ 1, e^{-(S_B[\vec{\varphi}'] - S_B[\vec{\varphi}])} \det G_{\vec{\varphi}} / \det G'_{\vec{\varphi}} \right\}. \quad (5.16)$$

Here we consider a local update restricted to a lattice site i in a imaginary-time slice $\ell \Delta\tau$: $\vec{\varphi}_i(\ell) \rightarrow \vec{\varphi}'_i(\ell)$. The change of the bosonic action from Eq. (4.75) is given by

$$\begin{aligned} S_B[\vec{\varphi}'] - S_B[\vec{\varphi}] &= \frac{1}{c^2 \Delta\tau} \left[\{ \vec{\varphi}'_i(\ell)^2 - \vec{\varphi}_i(\ell)^2 \} - \{ \vec{\varphi}_i(\ell+1) + \vec{\varphi}_i(\ell-1) \} \{ \vec{\varphi}'_i(\ell) - \vec{\varphi}_i(\ell) \} \right] \\ &\quad + \frac{\Delta\tau}{2} \left[4 \{ \vec{\varphi}'_i(\ell)^2 - \vec{\varphi}_i(\ell)^2 \} - 2 \{ \vec{\varphi}'_i(\ell) - \vec{\varphi}_i(\ell) \} \cdot \sum_{j \text{ nn } i} \vec{\varphi}_j(\ell) \right] \\ &\quad + \Delta\tau \left[\frac{r}{2} \{ \vec{\varphi}'_i(\ell)^2 - \vec{\varphi}_i(\ell)^2 \} + \frac{u}{4} \{ \vec{\varphi}'_i(\ell)^4 - \vec{\varphi}_i(\ell)^4 \} \right], \end{aligned} \quad (5.17)$$

where the derivative in imaginary time has been explicitly discretized and the sum in the third line runs over the nearest neighbor sites j of i . To evaluate the determinant ratio in Eq. (5.16), from now denoted by R , we assume that we explicitly know the equal-time Green's function evaluated at the ℓ th time slice for the configuration $\vec{\varphi}$. Then we have

$$R \equiv \frac{\det G_{\vec{\varphi}}}{\det G'_{\vec{\varphi}}} \equiv \frac{\det G_\ell}{\det G'_\ell} = \frac{\det [\mathbb{1} + B'_\ell B_{\ell-1} \cdots B_1 B_m B_{m-1} \cdots B_{\ell+1}]}{\det [\mathbb{1} + B_\ell B_{\ell-1} \cdots B_1 B_m B_{m-1} \cdots B_{\ell+1}]} \quad (5.18)$$

$$= \det [(\mathbb{1} + B'_\ell B_{\ell-1} \cdots B_1 B_m \cdots B_{\ell+1}) \cdot G_\ell], \quad (5.19)$$

because all B -matrices apart from the one for the ℓ th time slice remain unchanged under the update. Since we have $G_\ell^{-1} - \mathbb{1} = B_\ell \cdots B_1 B_m \cdots B_{\ell+1}$, we can write

$$\begin{aligned} R &= \det[(\mathbb{1} + B'_\ell B_\ell^{-1}(G_\ell^{-1} - \mathbb{1})) \cdot G_\ell] \\ &= \det[G_\ell + B'_\ell B_\ell^{-1}(\mathbb{1} - G_\ell)] \\ &= \det[(B'_\ell B_\ell^{-1} - \mathbb{1})(\mathbb{1} - G_\ell) + \mathbb{1}] \\ &= \det[\mathbb{1} + \Delta(\mathbb{1} - G_\ell)] \end{aligned} \quad (5.20)$$

with the matrix $\Delta = B'_\ell B_\ell^{-1} - \mathbb{1}$ encoding the change of the Green's function. We can write it in the form

$$\begin{aligned} \Delta &= B'_\ell B_\ell^{-1} - \mathbb{1} = e^{-\Delta\tau K/2} e^{-\Delta\tau V'_\ell} e^{\Delta\tau V_\ell} e^{\Delta\tau K/2} - \mathbb{1} \\ &= e^{-\Delta\tau V'_\ell} e^{\Delta\tau V_\ell} - \mathbb{1} + O(\Delta\tau^2). \end{aligned} \quad (5.21)$$

Here it is legitimate to accept the error of $O(\Delta\tau^2)$, which is of the same order as the overall Suzuki-Trotter error. In the actual implementation of the DQMC simulation, where the checkerboard approximation of Sec. 5.3.1 is applied, this error vanishes in Eq. (5.21) because B -matrices of the effective form $B_\ell^{\text{eff}} = e^{-\Delta\tau V_\ell} \cdot e^{-\Delta\tau K_b/2} \cdot e^{-\Delta\tau K_a} \cdot e^{-\Delta\tau K_b/2}$ are used, where a and b are two different groups of lattice bonds, and the full form of G is only recovered before measuring observables.

If the proposed local change of $\vec{\varphi}$ is accepted in the simulation, the Green's function matrix needs to be updated accordingly. In analogy to Eq. (5.20) we can express the updated G'_ℓ in terms of the original G_ℓ and the matrix Δ :

$$\begin{aligned} G'_\ell &\equiv [\mathbb{1} + B'_\ell B_{\ell-1} \cdots B_1 B_m \cdots B_{\ell+1}]^{-1} \\ &= [\mathbb{1} + B'_\ell B_\ell^{-1}(G_\ell^{-1} - \mathbb{1})]^{-1} \\ &= [((B'_\ell B_\ell^{-1} - \mathbb{1})(\mathbb{1} - G_\ell) + \mathbb{1}) G_\ell^{-1}]^{-1} \\ &= G_\ell [\mathbb{1} + \Delta(\mathbb{1} - G_\ell)]^{-1}. \end{aligned} \quad (5.22)$$

Eqs. (5.20) and (5.22) are very convenient for numerical evaluation because the matrix $\mathbb{1} + \Delta(\mathbb{1} - G_\ell)$ has a very sparse structure.

For the O(3) SDW model $\Delta \equiv e^{-\Delta\tau V'_\ell} e^{\Delta\tau V_\ell} - \mathbb{1}$ is a $4N_s \times 4N_s$ matrix that has only a constant number of 16 non-zero entries, which correspond to the updated lattice site i . Letting Δ^i denote the 4×4 -matrix containing those elements, an explicit

formula for the entries of Δ is

$$\Delta_{r,s} = \sum_{k=0}^3 \sum_{l=0}^3 \Delta_{k,l}^i \delta_{r,kN+i} \delta_{s,lN+i}. \quad (5.23)$$

It is often convenient to write the relationships between matrices and submatrices in compact **slice notation**, where an index range $[a : b : c]$ stands for the indices $a, a+c, a+2c, \dots < b$. If a or b are left out, a is assumed to be the first possible index and b is assumed to be the maximal extend, respectively. If c is omitted the index step size is set to $c = 1$. In this notation we can write $\Delta^i = \Delta[i :: N_s, i :: N_s]$.

In the cases of the O(2) and O(1) models all equations in this Section are to be written in terms of $2N_s \times 2N_s$ matrices $\tilde{G}_\ell, \tilde{B}_\ell$, etc. Then $\tilde{\Delta} \equiv e^{-\Delta\tau\tilde{V}'_\ell} e^{\Delta\tau\tilde{V}_\ell} - \mathbb{1}$ has only 4 non-zero entries given by $\tilde{\Delta}_{r,s} = \sum_{k=0}^1 \sum_{l=0}^1 \tilde{\Delta}_{k,l}^i \delta_{r,kN+i} \delta_{s,lN+i}$ with a 2×2 matrix $\tilde{\Delta}^i$. Note that Eq. (5.16) reads $A(\vec{\varphi} \rightarrow \vec{\varphi}') = \min\{1, e^{-(S_B[\vec{\varphi}'] - S_B[\vec{\varphi}])} |\det \tilde{G}_{\vec{\varphi}} / \det \tilde{G}'_{\vec{\varphi}}|^2\}$ in this case, requiring the use of the squared modulus of R .

For all variations of the model the sparseness of Δ allows to compute the determinant ratio R and hence the Metropolis acceptance probability in constant time, independent of system size or inverse temperature. By the same virtue, the updated G'_ℓ can be computed in $O(N_s^2)$ operations. A naive code that does not take advantage of the structure of Δ would need $O(N_s^3)$ operations for these computations. Only by this realization the BSS algorithm became viable in the 1980s [8]. An entire sweep of local updates, where we go lexicographically over all $\beta/\Delta\tau$ imaginary-time slices and N_s sites, requires a computational effort of $O(\beta N_s^3)$. In the following two subsections we give detailed prescriptions how to compute R and how to update G_ℓ .

5.2.1.1 Computing the determinant ratio

To save some space this Subsection is written in terms of the O(2) model. The calculation can be transferred directly to the O(3) model.

To find an efficient way to compute $R = \det[\mathbb{1} + \tilde{\Delta}(\mathbb{1} - \tilde{G}_\ell)]$ it is helpful to visualize the structure of the matrix as in Fig. 5.2. A Laplace expansion of the determinant leads us to find

$$R = \det[\mathbb{1} + \tilde{\Delta}(\mathbb{1} - \tilde{G}_\ell)] = \det M, \quad (5.24)$$

where M is a 2×2 matrix, given in slice notation by

$$M = \mathbb{1}_2 + \Delta^i \cdot (\mathbb{1} - G_\ell)[i :: N_s, i :: N_s] = \mathbb{1}_2 + \Delta^i \cdot (\mathbb{1}_2 - G_\ell[i :: N_s, i :: N_s]). \quad (5.25)$$

$$\mathbb{1} + \Delta(\mathbb{1} - \tilde{G}_\ell) = \begin{bmatrix} 1 & & & & & & & & & & & \\ * & * & * & M_{00} & * & * & * & M_{01} & * & * & * & \leftarrow i \\ * & * & * & M_{10} & * & * & * & M_{11} & * & * & * & \leftarrow i + N_s \\ & & & & 1 & & & & & & & \\ & & & & & 1 & & & & & & \\ & & & & & & 1 & & & & & \\ & & & & & & & 1 & & & & \\ & & & & & & & & 1 & & & \\ & & & & & & & & & \ddots & & \\ & & & & & & & & & & 1 & \\ & & & & & & & & & & & 1 \end{bmatrix}$$

Figure 5.2: Structure of the matrix $\mathbb{1} + \Delta(\mathbb{1} - \tilde{G}_\ell)$. Here the asterisk $*$ stands for unspecified values that need not be zero.

The determinant of a 2×2 (or of a 4×4 matrix, in the O(3) case) can be computed in short constant time.

5.2.1.2 Updating the Green's function

A naive computation of the updated Green's function after an accepted local update via

$$G'_\ell = G_\ell [\mathbb{1} + \Delta(\mathbb{1} - G_\ell)]^{-1}, \quad (5.26)$$

or the corresponding equation for the O(1) and O(2) models, would require to invert a $nN_s \times nN_s$ matrix with $n = 4$ for O(3) or $n = 2$ for O(1) and O(2). However, because of the sparseness of Δ the matrix $\Delta(\mathbb{1} - G_\ell)$ only has a rank of n . By applying the Sherman-Morrison-Woodbury formula [142, Sect. 2.1.4], we can effectively replace the inversion by that of a small $n \times n$ matrix.

For two rectangular matrices U of size $N_s \times n$ and V of size $n \times N_s$ one form of the

Sherman-Morrison-Woodbury formula reads

$$[\mathbb{1}_{N_s} - U \cdot V]^{-1} = \mathbb{1}_{N_s} + U \cdot [\mathbb{1}_n - V \cdot U]^{-1} \cdot V. \quad (5.27)$$

For a direct proof of this identity we can multiply both sides by $(\mathbb{1}_{N_s} - U \cdot V)$ and perform a series of equivalence transformations:

$$\begin{aligned} \mathbb{1}_{N_s} &= \mathbb{1}_{N_s} - UV + U(\mathbb{1}_n - VU)^{-1}(V - VUV) \\ &= \mathbb{1}_{N_s} - UV + U(\mathbb{1}_n - VU)^{-1}(\mathbb{1}_n - VU)V \\ &= \mathbb{1}_{N_s} - UV + UV \\ &= \mathbb{1}_{N_s}. \end{aligned} \quad (5.28)$$

We rewrite Eq. (5.26) in an appropriate form:

$$\mathbb{1} + \Delta(\mathbb{1} - G_\ell) = \mathbb{1} - U \cdot V \quad (5.29)$$

where U and V are rectangular matrices whose entries are given by

$$U_{r,s} \equiv U[r,s] = \sum_{k=0}^3 \Delta^i[k,s] \delta_{r,i+kN}, \quad (5.30a)$$

$$V_{r,s} \equiv V[r,s] = \sum_{k=0}^3 (G_\ell - \mathbb{1})[r,k] \delta_{s,i+kN}. \quad (5.30b)$$

In slice notation we have

$$U[i :: N, :] = \Delta^i, \quad (5.31a)$$

where the remaining elements of U are zero, and

$$V = (G_\ell - \mathbb{1})[i :: N, :]. \quad (5.31b)$$

U is the matrix built from the non-empty columns of Δ , while V is the matrix built from all the rows of $(G_\ell - \mathbb{1})$ that enter the matrix product in Eq. (5.29). We can now apply Eq. (5.27) to Eq. (5.26):

$$\begin{aligned} G'_\ell &= G_\ell [\mathbb{1} + \Delta(\mathbb{1} - G_\ell)]^{-1} \\ &= G_\ell + (G_\ell U) ([\mathbb{1}_n - VU]^{-1} V) \end{aligned}$$

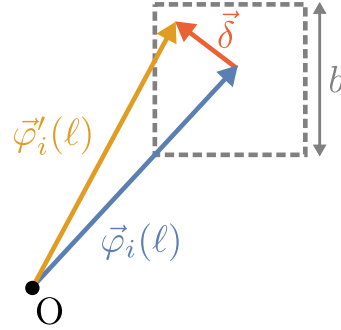


Figure 5.3: Visualization of a local update $\vec{\varphi}_i(\ell) \rightarrow \vec{\varphi}'_i(\ell) = \vec{\varphi}_i(\ell) + \vec{\delta}$. The displacement $\vec{\delta}$ has been chosen from a box of size b .

$$\begin{aligned}
 &= G_\ell + (G_\ell[:, i :: N_s] \cdot \Delta^i) \cdot \left(\underbrace{[\mathbb{1}_n - G_\ell[i :: N_s, i :: N_s] \cdot \Delta^i + \Delta^i]^{-1}}_{M^{-1} \text{ with } M \text{ generalized from Eq. (5.25)}} \cdot V \right) \\
 &= G_\ell + (G_\ell[:, i :: N_s] \cdot \Delta^i) \cdot (M^{-1} \cdot V).
 \end{aligned} \tag{5.32}$$

The matrix products should be carried out in the order indicated by the parentheses. Then only a total of $O(N_s^2)$ operations is needed. The computing time needed to invert the $n \times n$ matrix M does not scale with the system size.

5.2.1.3 Form of the proposed local updates

We have discussed at length how to decide whether a local update should be *accepted* according to the Metropolis criterion and how to consequently update the Green's function. It remains to decide on the *proposal* probability $g(\vec{\varphi} \rightarrow \vec{\varphi}')$, which enters the transition probability $W(\vec{\varphi} \rightarrow \vec{\varphi}') = g(\vec{\varphi} \rightarrow \vec{\varphi}')A(\vec{\varphi} \rightarrow \vec{\varphi}')$ together with the acceptance probability. In order not to break detailed balance, a symmetric form $g(\vec{\varphi} \rightarrow \vec{\varphi}') = g(\vec{\varphi}' \rightarrow \vec{\varphi})$ should be chosen. A simple, correct and effective update is to choose a random displacement $\vec{\delta}$ and to add that to $\vec{\varphi}_i(\ell)$ to form the proposed $\vec{\varphi}'_i(\ell)$. We pick the tip of the vector $\vec{\delta}$ uniformly distributed from a box of side length b around its origin, as visualized for an example in Fig. 5.3. For an $O(N)$ model the formal proposal probability is

$$g(\vec{\varphi}_i(\ell) \rightarrow \vec{\varphi}_i(\ell) + \vec{\delta}) = \begin{cases} \frac{1}{b^N}, & -\frac{b}{2} \leq \delta^n \leq \frac{b}{2} \quad \text{for all } n = 1, \dots, N, \\ 0, & \text{else.} \end{cases} \tag{5.33}$$

An important feature of this update is that the length of $\vec{\varphi}_i(\ell)$ is *not* conserved.

The parameter b can be adjusted to tune the effective acceptance ratio in a

simulation. Generally we aim for a target acceptance ratio of 0.5. If the acceptance ratio is much higher, the displacements $\vec{\delta}$ are very small, leading to little change in the $\vec{\varphi}_i(\ell)$. Conversely, if its much smaller, $\vec{\varphi}_i(\ell)$ does not change in most Monte Carlo steps, again leading to little effective change. In both cases statistical autocorrelation times are longer than at 0.5 acceptance.

While b must be kept constant during the simulation, because otherwise detailed balance would be broken, we are free to modify its value at the beginning of an initial thermalization phase before measurements are taken. The following procedure leads to quick convergence sufficiently close to the target acceptance ratio: We start with a default box size, say $b = 1$. During the first half of thermalization we measure the effective acceptance ratio over periods of 100 time-slice-local sweeps. After each such period we check if less than 50% of the local updates have been accepted. In that case we shrink the box size, $b \rightarrow 0.95b$. If more than 50% have been accepted, we grow the box size, $b \rightarrow 1.05b$. During the second half of thermalization and during the main measurement phase we keep b fixed to its final value.

5.2.2 Global updates

A simulation that makes use of nothing else than the local updates of the previous Subsection suffers from overlong times necessary to equilibrate the system. This can be explained in part because the field $\vec{\varphi}$ is not normalized and changes localized to separate lattice sites cannot easily lead to an overall rescaling.

A simple and effective global “shift” move consists in adding the same random displacement $\vec{\delta}$ to $\vec{\varphi}$ at all sites in all imaginary-time slices: $\vec{\varphi}_i(\ell) \rightarrow \vec{\varphi}'_i(\ell) = \vec{\varphi}_i(\ell) + \vec{\delta}$ for all i and all ℓ . The displacement $\vec{\delta}$ is chosen in the same way as for the local updates of the previous Subsection. This move necessitates a full recomputation of the equal-time Green’s function by Eq. (5.8), which entails rebuilding the entire *UDV* storage. Consequently, the global move is rather expensive with $O(\beta N_s^3)$ needed operations. In combination with the replica exchange mechanism of Sec. 5.2.3 we have found it sufficient to do one global update every 10 DQMC sweeps. Note that this global move is not ergodic on its own and can only be used in combination with local updates.

The Metropolis acceptance probability is given by Eq. (5.16). While the change of the bosonic action can be computed directly, some care is necessary to evaluate the ratio of Green’s function determinants correctly. Since we have $G_{\vec{\varphi}}$ and $G'_{\vec{\varphi}}$ available in *UDV*-decomposed form, we can express the determinant, up to a phase factor, as

the product of the singular values of the Green's function matrix:

$$\begin{aligned} |\det G_{\vec{\varphi}}| &= |[\det(\mathbb{1} + B_m \cdots B_1)]^{-1}| = |[\det UDV]^{-1}| \\ &= |\det D^{-1}| = \prod_{\nu} (\sigma_{(\nu)})^{-1}, \end{aligned} \quad (5.34)$$

where the unitarity of U and V and the positivity of the singular values $\sigma_{(\nu)}$, that form the diagonal matrix D , have been used. For our sign-problem-free model we have $|\det G_{\vec{\varphi}}| = \det G_{\vec{\varphi}}$ and we can directly use the singular-value product in place of the determinant. Hence, the determinant ratio is

$$R = \frac{\det G_{\vec{\varphi}}}{\det G'_{\vec{\varphi}}} = \prod_{\nu} \frac{\sigma'_{(\nu)}}{\sigma_{(\nu)}}. \quad (5.35)$$

Since the singular values before and after the global move are ordered by magnitude, arranging the factors like this in the product reduces the mixing of numerical scales. However, directly computing R in this way still turns out to be unstable from the mixing of large and small numbers exceeding the limits of floating point precision. Therefore, the ratio should be evaluated logarithmically, which reduces the numerical dynamic range:

$$R = \exp \sum_{\nu} [\ln \sigma'_{(\nu)} - \ln \sigma_{(\nu)}]. \quad (5.36)$$

For the O(2) symmetric model we need to compute $|\tilde{R}|^2$ with $\tilde{R} = \det \tilde{G}'_{\vec{\varphi}} / \det \tilde{G}_{\vec{\varphi}}$ to evaluate the transition probability, such that it is also sufficient to compute absolute values of the determinants via the singular values.

In O(N) symmetric classical spin models the problem of critical slowing down is solved by Wolff's single cluster algorithm [148]. We cannot use it directly for our model with coupling to the fermions, since the linear algebra required during the construction of a cluster of $\vec{\varphi}_i(\ell)$ would be very expensive. However, we can consider a variation, where we ignore the fermionic part of the action while we construct and flip a cluster, and after recomputing the Green's function decide whether we accept or reject this new configuration with probability $\min \{1, \det G_{\vec{\varphi}} / \det G'_{\vec{\varphi}}\}$. This update is not ergodic on its own because it does not vary the lengths of the $\vec{\varphi}_i(\ell)$ and must be used in combination with local updates. Finally, despite its conceptual allure we have not measured any performance improvements from this variation of the single cluster update over the global shift update used on its own. The replica exchange mechanism that is introduced in the next Subsection is more useful.

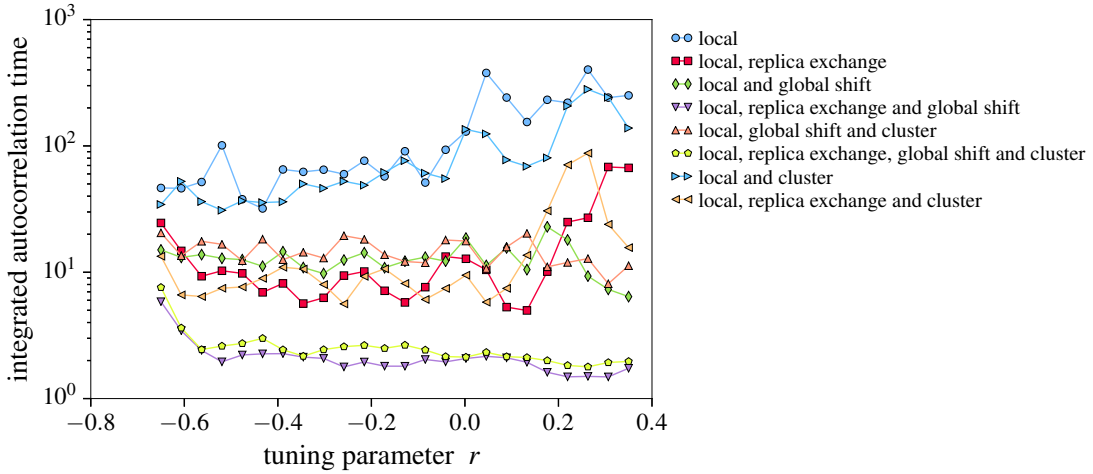


Figure 5.4: Comparison of different combinations of Monte Carlo update algorithms in simulations of the O(2) SDW model with $\lambda = c = 1$ at $L = 8$ and $\beta = 1/T = 8$. Shown is the integrated autocorrelation time τ_{int} of the finite-system magnetization $m_\varphi = \frac{\Delta\tau}{\beta N_s} \langle |\sum_{i,\ell} \vec{\varphi}_i(\ell)| \rangle$ in units of Monte Carlo sweeps on a logarithmic scale. The system undergoes a phase transition at $r \approx 0.2$. If activated, global updates were attempted every 5 sweeps and replica exchanges were proposed every 10 sweeps in these simulations. The same linearly spaced distribution of tuning parameter values r was used in all simulations.

A quantitative example for the performance of different combinations of Monte Carlo update algorithms is given in Fig. 5.4, where short autocorrelation times correspond to low statistical errors in the estimates of observables. Here it is evident that activating either the global shift update or the replica exchange mechanism (introduced in the next Subsection) provides an improvement of roughly an order of magnitude compared to purely local updates. When both these moves are used in combination, almost an extra order of magnitude is gained. This stands in stark contrast to the single-cluster update, which does not give any clear improvement in combination with any of the other update mechanisms.

To see how essential the global shift update is for proper thermalization of the system in the vicinity of a phase transition it is instructive to look at the results obtained in comparatively long simulations (520 000 sweeps) for a small system. By studying the complete time series obtained in these simulations, we can set different effective lengths of the thermalization period by discarding certain amounts of initial samples. In order not to skew the results we then always consider an equal number of 50 000 Monte Carlo sweeps over which observable averages are taken for measurements. Defining $\bar{\varphi} = \frac{\Delta\tau}{\beta N_s} |\sum_{i,\ell} \vec{\varphi}_i(\ell)|$ we examine two quantities, the finite-system magnetization $m_{\bar{\varphi}} = \langle \bar{\varphi} \rangle$ and a measure for its fluctuations $\tilde{\chi}_\varphi =$

$\beta N_s [\langle \bar{\varphi}^2 \rangle - \langle \bar{\varphi} \rangle^2]$. At the phase transition, $m_{\bar{\varphi}}$ is expected to drop by a finite amount, while $\tilde{\chi}_{\varphi}$ shows a peak. In simulations with activated replica exchange, but *without* global updates, the apparent location of this phase transition shifts tremendously with the allowed time for thermalization, see Fig. 5.5. Clearly it takes very long to reach thermal equilibrium. Results obtained *with* additionally activated global shift updates show a diametrically opposed behavior in Fig. 5.6a: There is virtually no difference for the various periods of thermalization, which all agree with the situation in Fig. 5.5 for the longest thermalization phase of 470 000 sweeps. Without replica exchange, but with activated global updates the situation is similar to Fig. 5.6a, but with larger error bars (not shown). To further anticipate the benefits of the replica exchange mechanism see Fig. 5.6b where only local updates have been used without replica exchange or global updates and the system never reaches equilibrium.

5.2.3 Replica exchange

The idea of parallel tempering or replica exchange schemes [149, 150] is one realization of an *extended ensemble* [151], here composed of multiple canonical or grand-canonical ensembles with some control parameter taking on different values.³ In a Monte Carlo simulation one then considers K different *replicas* of the system for different values of this control parameter, each being represented by a separate system configuration. The control parameter is then treated as a dynamical variable by allowing exchanges of the configurations between replicas of different parameter values (or equivalently swapping control parameter settings between the replicas without moving configurations). In this way shorter autocorrelation times in some regions of this parameter space can be utilized to accelerate the simulation in other regions. Replica exchange especially helps in situations with free-energy landscapes with high barriers between multiple local or global minima. The replica exchange mechanism aids in escaping local minima that do not correspond to typical physical equilibrium configurations, thus accelerating thermalization. In other situations such as in the vicinity of continuous phase transitions, where conventional Monte Carlo dynamics are affected by critical slowing down, replica exchange can provide sizable speed-ups. Fig. 5.7a illustrates the random walk of various replicas in the extended ensemble of a replica exchange simulation. In Fig. 5.7b improved thermalization in our SDW model is demonstrated for an activated replica exchange mechanism.

Traditionally, in classical parallel tempering Monte Carlo simulations one usually varies the temperature to benefit from quick decorrelation at higher temperatures.

³A thorough discussion of various approaches to parallel tempering is given for instance in the author's diploma thesis [152].

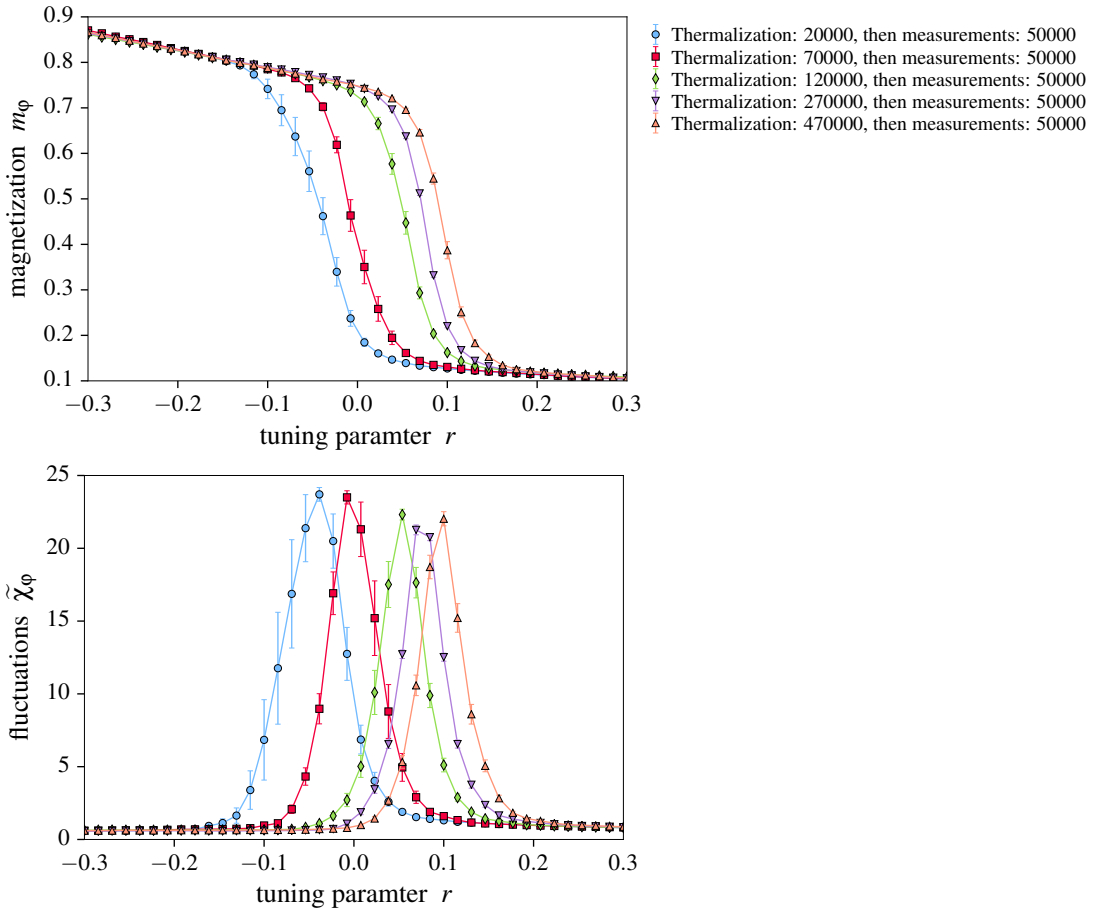


Figure 5.5: Simulation results obtained with activated replica exchange, but *without* global updates, of the O(2) model with $\lambda = c = 1$ for $L = 4$ and $\beta = 1/T = 16$. Colors and symbols correspond to different periods of thermalization.

For the DQMC simulations of the SDW model this is not the most convenient choice. If the discretization $\Delta\tau$ is kept constant, different temperatures correspond to different numbers of imaginary time slices m and it is not clear how an exchange of system configurations between neighboring replicas could be set up. While one could keep m constant and vary $\Delta\tau$, this would lead to slight changes in physical properties compared to measurements taken in regular simulations. Also this would mean that the computational effort for the high-temperature simulations becomes as large as that at low temperatures, which may not outbalance the gain in statistical efficiency from parallel tempering.

A more appropriate choice is to take the parameter r in the bosonic part of the

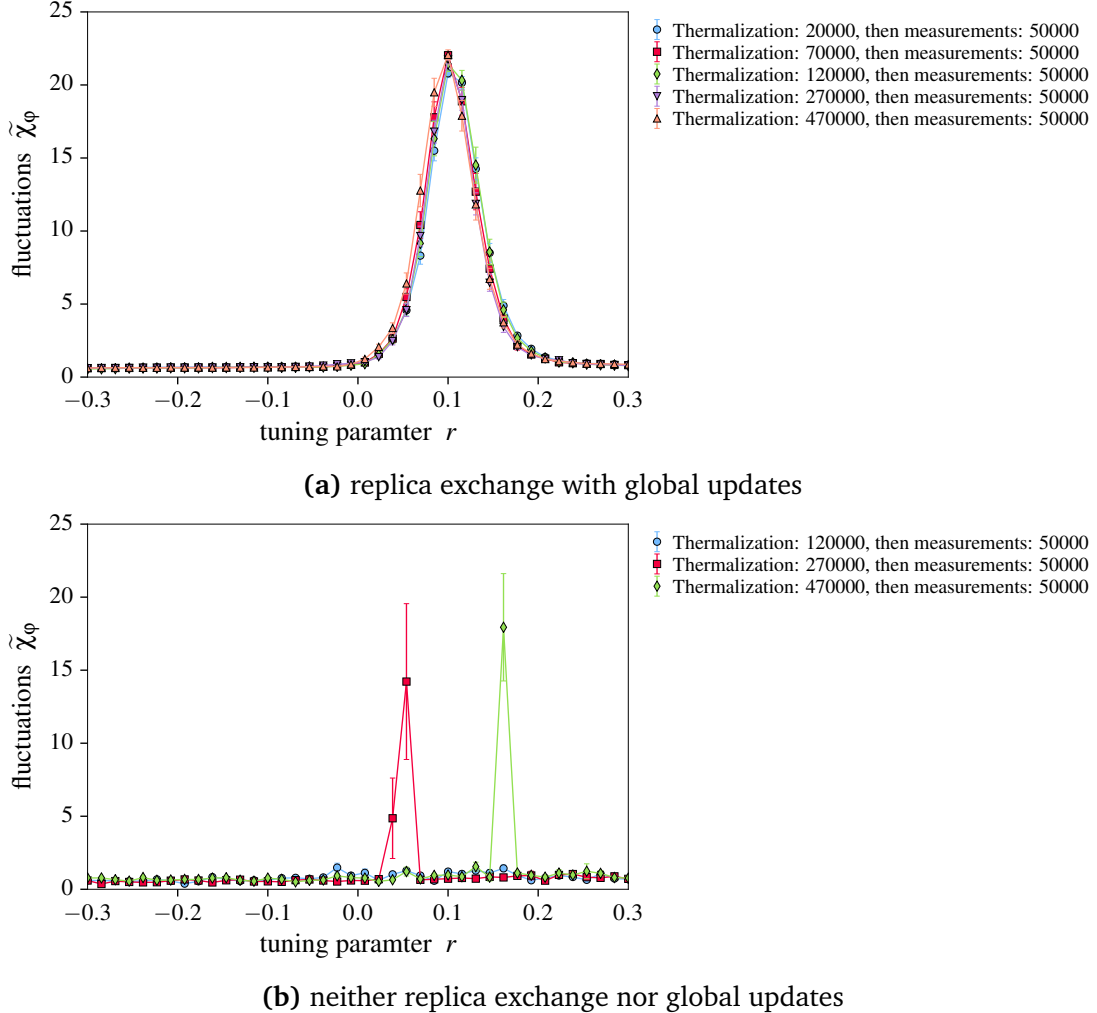


Figure 5.6: Results from simulations equal to those shown in Fig. 5.5, but (a) with local and global updates, combined with replica exchange, and (b) only local updates.

action (4.75), which tunes across the quantum critical point, as a dynamic variable. As we will see in the following, since the fermionic parts of the action do not explicitly depend on this value, in this special situation we can avoid re-evaluating Green's function determinants when we decide on replica exchanges.

With the parameter r taking on different values $r_1 < r_2 < \dots < r_K$ the partition function of the extended ensemble is given by a product $Z_{\text{ext}} = \prod_{\kappa=1}^K Z(r_\kappa)$ of

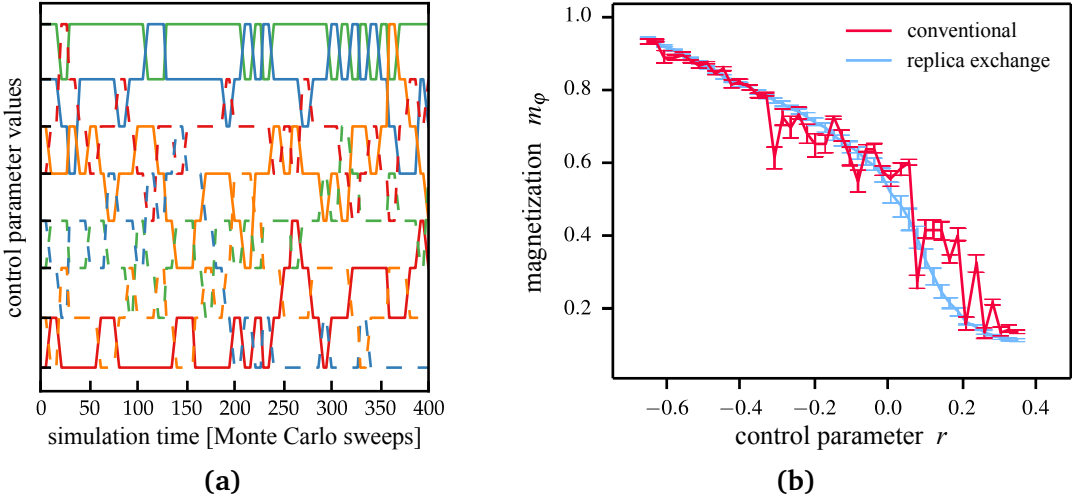


Figure 5.7: (a) Visualization of replica trajectories (differentiated by colors and dashes) in control parameter space over the course of a short simulation (adapted from Ref. [152]). (b) Example data for the finite-system magnetization $m_\varphi = \frac{\Delta\tau}{\beta N_s} \langle |\sum_{i,\ell} \vec{\varphi}_i(\ell)| \rangle$ obtained in short DQMC simulation runs of the O(2) SDW model with $\lambda = c = 1$ on an 8×8 square lattice at temperature $T = 1/16$, comparing results obtained with conventional updates to those obtained with activated replica exchange, which greatly eases equilibration around the phase transition.

grand-canonical partition functions $\mathcal{Z}(r_\kappa)$. Here we have

$$\mathcal{Z}_{\text{ext}} = \int D(\vec{\varphi}^{(1)}, \dots, \vec{\varphi}^{(K)}) \prod_{\kappa=1}^K e^{-S_B[\vec{\varphi}^{(\kappa)}, r_\kappa]} \det G_{\vec{\varphi}^{(\kappa)}}^{-1}, \quad (5.37)$$

where the fermionic equal-time Green's function depends on the replica index κ only via the bosonic field configuration $\vec{\varphi}^{(\kappa)}$, while the value of r_κ only enters S_B . The equilibrium probability of an extended configuration $\{\vec{\varphi}^{(\kappa)}\}$ for a set of parameters $\{r_\kappa\}$ is given by

$$P(\{\vec{\varphi}^{(\kappa)}\}, \{r_\kappa\}) = \prod_{\kappa=1}^K P_{\text{eq}}(\vec{\varphi}^{(\kappa)}, r_\kappa) \quad (5.38)$$

with

$$P_{\text{eq}}(\vec{\varphi}^{(\kappa)}, r_\kappa) = e^{-S_B[\vec{\varphi}^{(\kappa)}, r_\kappa]} \det G_{\vec{\varphi}^{(\kappa)}}^{-1} / \mathcal{Z}(r_\kappa). \quad (5.39)$$

To supplement the single-replica local and global Monte Carlo updates, that are still carried out as in regular grand-canonical simulations, we construct an additional

Monte Carlo move between replicas to achieve a random walk in the extended ensemble. In such an update we propose the exchange of configurations $\{\vec{\varphi}\}$ and $\{\vec{\varphi}'\}$ between the κ -th and η -th replicas. To ensure detailed balance we require

$$\begin{aligned} P(\dots, \vec{\varphi}, r_\kappa, \dots, \vec{\varphi}', r_\eta, \dots) W(\vec{\varphi}, r_\kappa | \vec{\varphi}', r_\eta) \\ = P(\dots, \vec{\varphi}', r_\kappa, \dots, \vec{\varphi}, r_\eta, \dots) W(\vec{\varphi}', r_\kappa | \vec{\varphi}, r_\eta), \end{aligned} \quad (5.40)$$

where W is the transition probability for a replica configuration exchange. The ratio of these transition probabilities is hence given by

$$\frac{W(\vec{\varphi}, r_\kappa | \vec{\varphi}', r_\eta)}{W(\vec{\varphi}', r_\kappa | \vec{\varphi}, r_\eta)} = \frac{e^{-S_B[\vec{\varphi}', r_\kappa] - S_B[\vec{\varphi}, r_\eta]} \det G_{\vec{\varphi}'}^{-1} \det G_{\vec{\varphi}}^{-1}}{e^{-S_B[\vec{\varphi}, r_\kappa] - S_B[\vec{\varphi}', r_\eta]} \det G_{\vec{\varphi}}^{-1} \det G_{\vec{\varphi}'}^{-1}} = e^{-\Delta}, \quad (5.41)$$

where the determinants cancel and $\Delta = (r_\kappa - r_\eta) \cdot \frac{1}{2} \sum_{\ell,i} [\vec{\varphi}'_i(\ell)^2 - \vec{\varphi}_i(\ell)^2]$. To fulfill the relation (5.40) we choose the exchange probabilities according to the Metropolis criterion

$$W(\vec{\varphi}, r_\kappa | \vec{\varphi}', r_\eta) = \min \{1, e^{-\Delta}\}. \quad (5.42)$$

A similar replica exchange mechanism could also be set up for any other parameter of the action. Note that if it is a parameter appearing in the fermionic part, the change of the Green's function determinants would have to be calculated explicitly.

Since in our case the exchange algorithm does not require the recomputation of Green's functions or the evaluation of their determinants, it poses very little overhead in computation or communication between parallel processes. This allows us to perform a replica-exchange sweep after every single sweep of regular updates, which has been very beneficial for obtaining sufficient statistics at low temperatures.

5.2.3.1 Selection of tuning parameter values

A highly nontrivial question is how to best choose the distribution of the tuning parameter values r_κ for a replica exchange simulation. In the simulation we propose exchanges between replicas with neighboring values of r_κ . First of all, these need to be selected sufficiently close to each other with overlapping distributions of $\vec{\varphi}^2$ such that Δ is not prohibitively small. A traditionally followed strategy was to optimize this distribution for constant overlap of the action in neighboring replicas or (approximately equivalently) constant exchange acceptance ratio [153]. This approach, however, is of limited utility in complex free-energy landscapes or in the vicinity of phase transitions. There, simulation dynamics are so slow that replicas

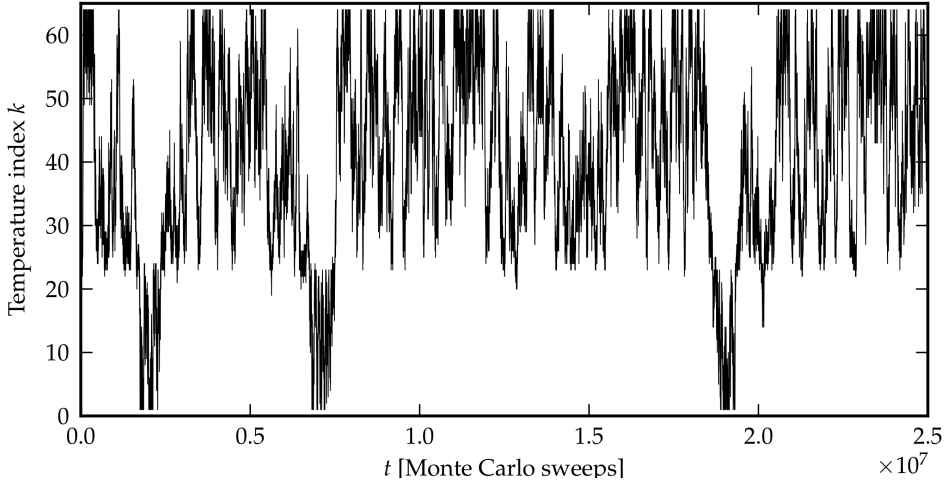


Figure 5.8: Trajectory of a single replica in a long Monte Carlo simulation of a classical spin model, where the temperatures are distributed such that exchange acceptance probabilities are approximately constant for replicas at neighboring temperatures. Diffusion through the temperature location of a phase transition (at $k \approx 20$) is rare. Figure reproduced from Ref. [152].

have little chance to tunnel through a barrier before they move back in the opposite direction. Such a “bottleneck” is visualized in Fig. 5.8. This greatly impedes the effectiveness of the replica exchange mechanism: Decorrelation across a phase transition requires input from the disordered phase. A more successful approach takes into account the dynamics of the replica exchange process, minimizing average *round trip times* between the lowest and highest control parameter values [154–156]. To do so we track the movement of replicas up and down in control parameter space and form the fraction

$$f_{\text{up}}(r_\kappa) = \frac{n_{\text{up}}(r_\kappa)}{n_{\text{up}}(r_\kappa) + n_{\text{down}}(r_\kappa)}, \quad (5.43)$$

where $n_{\text{up}}(r_\kappa)$ counts the number of times a replica has visited r_κ in the course of a simulation after having last visited r_1 and not r_K , and $n_{\text{down}}(r_\kappa)$ is the analogue for the opposite direction. Interpreting r as a continuous variable, this fraction can be related to the steady-state current of replicas moving up, which to first order in the derivative reads

$$j_{\text{up}} = D(r)\eta(r)\frac{df_{\text{up}}}{dr}, \quad (5.44)$$

and is constant in r , since this current is proportional to the rate of replica round trips. Here, $D(r)$ is a local diffusivity and $\eta(r)$ is the probability density for a replica to be at r_κ . For a discrete distribution $\{r_\kappa\}$ it is approximated by $\eta(r) = C/\Delta r$ for $r \in [r_\kappa, r_{\kappa+1}]$, where $\Delta r = r_{\kappa+1} - r_\kappa$. C is a constant ensuring $\int dr \eta(r) = 1$. Note that at any given time there is exactly one replica at each r_κ . From Eq. (5.44) there is a simple measure of the local diffusivity at r

$$D(r) \propto \frac{\Delta r}{df_{\text{up}}/dr}. \quad (5.45)$$

Our aim is to maximize the current j_{up} by finding the optimal probability distribution $\eta^{\text{opt}}(r)$, corresponding to an optimal selection of control parameter values $\{r_\kappa^{\text{opt}}\}$. Following Ref. [154], this is realized by a distribution related to the diffusivity like

$$\eta^{\text{opt}}(r) \propto 1/\sqrt{D(r)}, \quad (5.46)$$

which puts more replicas into regions with low diffusivity. Inserting this into Eq. (5.44), we find

$$\eta^{\text{opt}}(r) \propto \frac{df_{\text{up}}^{\text{opt}}}{dr} \propto \frac{1}{\Delta r^{\text{opt}}}, \quad (5.47)$$

where $\Delta r^{\text{opt}} = r_{\kappa+1}^{\text{opt}} - r_\kappa^{\text{opt}}$ is the optimal spacing of control parameter points for the interval enclosing r . The optimal spacing implies a constant decay of the fraction, measured in control parameter indices:

$$\Delta f^{\text{opt}} = f_{\text{up}}^{\text{opt}}(r_{\kappa+1}^{\text{opt}}) - f_{\text{up}}^{\text{opt}}(r_\kappa^{\text{opt}}) = \frac{1}{K-1}. \quad (5.48)$$

In the **feedback optimized** replica exchange algorithm [155, 156] we iteratively optimize the distribution $\eta(r)$ to approach $\eta^{\text{opt}}(r)$. In an initial simulation with arbitrarily distributed r_κ we measure $f_{\text{up}}(r_\kappa)$ and compute the derivative df_{up}/dr by linear regression. Then we obtain an improved distribution

$$\eta'(r) = \frac{C'}{\Delta r'} = C' \sqrt{\frac{1}{\Delta r} \frac{df_{\text{up}}}{dr}}, \quad (5.49)$$

where C' is a normalization constant. $\eta'(r)$ is still a step function defined for the original control parameter points. The new points are found by successively solving

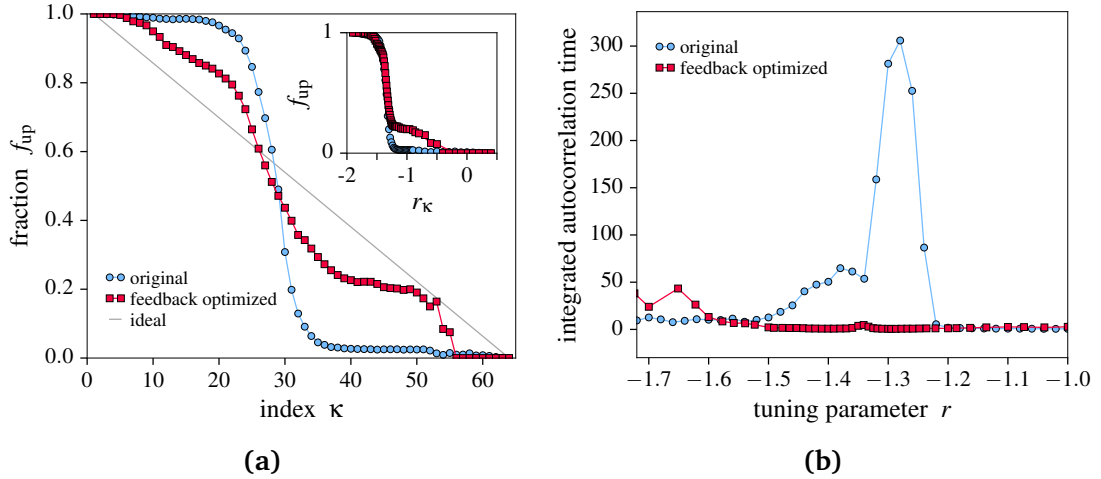


Figure 5.9: Data from replica exchange simulations of the O(2) SDW model with $\lambda = 1$, $c = 3$ for $L = 12$ and $\beta = 1/T = 15$. The original values of the tuning parameter r are chosen ad hoc with dense linear spacing at low r , including the region of the phase transition, and with a coarser equal-spaced grid at high r . The feedback-optimized distribution is obtained in one iterative step. (a) Replica movement fraction f_{up} as a function of the tuning parameter index κ (main panel) and as a function of the tuning parameter value r_κ (inset). (b) Integrated autocorrelation time τ_{int} around the phase transition at $r \approx -1.3$.

the integral equation

$$\int_{r'_1}^{r'_K} dr \eta(r) = \frac{\kappa}{K} \quad (5.50)$$

for the upper bound r'_κ for $1 < \kappa < K$ with $r_1 = r'_1$ and $r_K = r'_K$ kept fixed. These steps can be repeated multiple times with further simulations yielding progressively improved distributions $\eta(r)$, which converge towards $\eta^{\text{opt}}(r)$.

5.2.3.2 Feedback optimization for the metallic SDW model

In our DQMC simulations of the metallic SDW model at high temperatures we achieve good diffusion already with a simple linear spacing of the values of r . At lower temperatures, however, the magnetic phase transition constitutes a more significant barrier to the random walk in r -space. Here a feedback-optimized distribution, which effectively clusters the r_κ close to the spin-density-wave phase transition at $r_{\text{SDW}}(T)$, has been very useful.⁴ Already a single step of the iteration delivers

⁴For the optimization we have used a code by S. Trebst, which implements the steps outlined above.

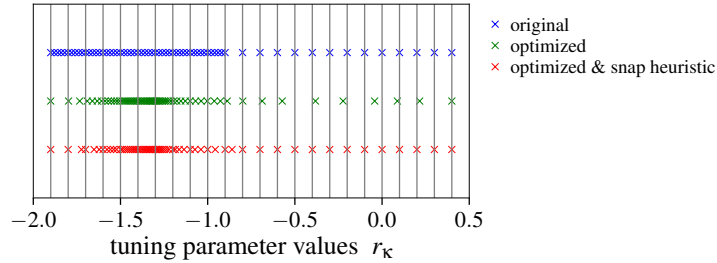


Figure 5.10: Tuning parameter values r_κ for the $O(2)$ model with $\lambda = c = 1$, here for $L = 10$, $\beta = 15$: Original distribution, feedback-optimized distribution, and feedback-optimized distribution with an additional heuristic to force values at integer multiples of 0.1. The number of replicas $K = 64$ is kept constant for all three distributions.

sizable improvements of diffusion. A distribution generated in this way is useful also at lower temperatures provided that the transition point does not move too far with temperature. An example for the result of the feedback optimization is given in Fig. 5.9. The simulation that makes use of the optimized distribution shows a fraction $f_{\text{up}}(\kappa)$ that is close to the ideal diagonal line and, most importantly, significantly reduced autocorrelation times in the region of the phase transition, where the algorithm has clustered the tuning parameter points. Since we use the same number of replicas K in both simulations, there is a small trade-off: The spacing of r_κ is actually larger far from the phase transition, which can lead to a slight enhancement of autocorrelation times there. Additional iterations of the optimization procedure on the new simulation data are expected to mitigate this adverse impact, but generally this does not present a major problem. Firstly, we are less interested in accurate data far away from the quantum critical point. Secondly, critical slowing down will greatly exacerbate the problem of long autocorrelation times for larger systems and lower temperatures close to the phase transition, while there will be much less of an aggravation far in the ordered and disordered phases.

In many cases it is useful to obtain data at precisely the same values of r for different system sizes and temperatures. With feedback optimization leading to different distributions this condition is not always satisfied. Often we have therefore used a heuristic variation of the optimization algorithm which slightly moves the generated tuning parameter points to force some of them to reside on a desired grid, see Fig. 5.10 for an example. An alternative would be to use the reweighting procedure introduced in Sec. 5.5.1, which can, however, be quite elaborate for fully frequency and momentum resolved observables.

5.3 Efficient linear algebra

In the previous Section we have seen how to improve the statistical efficiency of DQMC simulations of the SDW model to reduce the number of Monte Carlo sweeps necessary to reach equilibrium and to compute observable estimates with small statistical error. In this Section we discuss two aspects helping to improve numerical efficiency, i.e. the computational effort necessary to perform a single Monte Carlo sweep. The checkerboard approximation of Sec. 5.3.1 is used to replace many dense matrix products in the formulation of the DQMC algorithm by sparse products, thereby improving the cost of many operations to $O(\beta N_s^2)$ from the overall $O(\beta N_s^3)$ scaling of computing time. The delayed update procedure of Sec. 5.3.2 is an implementation of the fundamental local updates (discussed in Sec. 5.2.1) that is favorably adapted to the cache architecture of modern CPUs.

5.3.1 Checkerboard break up

When propagating between imaginary-time slices in the DQMC algorithm, we frequently need to compute product chains of B -matrices or their inverses, such as, for $\ell_1 \Delta\tau = \tau_1 > \tau_2 = \ell_2 \Delta\tau$,

$$B(\tau_1, \tau_2) = B_{\ell_1} B_{\ell_1-1} \cdots B_{\ell_2+2} B_{\ell_2+1} \quad \text{and} \quad (5.51a)$$

$$B(\tau_1, \tau_2)^{-1} = B_{\ell_2+1}^{-1} B_{\ell_2+2}^{-1} \cdots B_{\ell_1-1}^{-1} B_{\ell_1}^{-1} \quad \text{with} \quad (5.51b)$$

$$B_\ell = e^{-\Delta\tau K/2} e^{-\Delta\tau V[\vec{\varphi}_\ell]} e^{-\Delta\tau K/2} \quad \text{and} \quad (5.51c)$$

$$B_\ell^{-1} = e^{\Delta\tau K/2} e^{\Delta\tau V[\vec{\varphi}_\ell]} e^{\Delta\tau K/2}. \quad (5.51d)$$

While K and V are usually sparse matrices, their matrix exponentials can be dense. In the case of the SDW model, where we only have on-site interactions, $e^{V[\vec{\varphi}_\ell]}$ is a matrix composed of several diagonal blocks that can be multiplied quickly in $O(N_s^2)$ operations to any matrix. However, K contains hopping terms between all nearest-neighbor pairs of sites. While these only lead to only $O(N_s)$ non-zero entries in K , in this case the matrix exponential of K is a dense matrix. Multiplying it to another matrix is more expensive with $O(N_s^3)$ operations needed.

The checkerboard break-up, whose name is historical, is a way to transfer the sparseness of K to $e^{\pm\Delta\tau K/2}$. This entails an approximation with a controlled systematic error, which can be kept on the same order as the overall Suzuki-Trotter error of the fundamental DQMC setup. If T is one of the blocks K_α^s of K , its structure for

nearest-neighbor hopping is

$$T = \sum_{\langle i,j \rangle} T_{ij}, \quad T_{ij} = \begin{bmatrix} & i & & j \\ & \downarrow & & \downarrow \\ 0 & \dots & 0 & \dots & 0 & \dots & 0 \\ \vdots & & \vdots & & \vdots & & \vdots \\ 0 & \dots & 0 & \dots & t_{ij} & \dots & 0 \\ \vdots & & \vdots & & \vdots & & \vdots \\ 0 & \dots & t_{ij} & \dots & 0 & \dots & 0 \\ \vdots & & \vdots & & \vdots & & \vdots \\ 0 & \dots & 0 & \dots & 0 & \dots & 0 \end{bmatrix} \begin{array}{l} \leftarrow i \\ \leftarrow j \end{array}. \quad (5.52)$$

Since there are only two non-zero elements in each T_{ij} , it can be exponentiated easily, yielding a sparse matrix $e^{\pm \Delta \tau T_{ij}/2}$, which can be multiplied to an $N_s \times N_s$ matrix A in only $O(N_s)$ operations. The multiplication $Ae^{\pm \Delta \tau T_{ij}/2}$ only changes columns i and j of A , while $e^{\pm \Delta \tau T_{ij}/2}A$ only affects rows i and j of A . Explicitly, the exponential is given by:

$$e^{\pm \Delta \tau T_{ij}/2} = \begin{bmatrix} & i & & j \\ & \downarrow & & \downarrow \\ 1 & & & & & & & \\ & \ddots & & & & & & \\ & & 1 & & & & & \\ & & & \text{ch}(\Delta \tau t_{ij}/2) & & & \pm \text{sh}(\Delta \tau t_{ij}/2) & \\ & & & & 1 & & & \\ & & & & & \ddots & & \\ & & & & & & 1 & \\ & & & & & & & \pm \text{sh}(\Delta \tau t_{ij}/2) \\ & & & & & & & & \text{ch}(\Delta \tau t_{ij}/2) \\ & & & & & & & & 1 \\ & & & & & & & & & \ddots \\ & & & & & & & & & & 1 \end{bmatrix} \begin{array}{l} \leftarrow i \\ \leftarrow j \end{array}. \quad (5.53)$$

The checkerboard break-up is an additional Suzuki-Trotter-like decomposition. Loh and Gubernatis [87] suggest to approximate

$$e^{\pm \Delta \tau T/2} = e^{\pm \Delta \tau \sum_{\langle i,j \rangle} T_{ij}/2} \approx \prod_{\langle i,j \rangle} e^{\pm \Delta \tau T_{ij}/2}, \quad (5.54)$$

which when multiplied to an $N_s \times N_s$ -matrix as a series of sparse products will cost $O(N_b N_s)$ operations, where N_b is the number of hopping bonds, which gives $O(N_s^2)$ for nearest neighbor hopping, where $N_b = 2N_s$ for a square lattice. The magnitude of the systematic error caused by this approximation is determined by the order of the individual exponential factors in this product. A prescription to minimize this error is to form groups of the hopping matrices T_{ij} such that within a group all matrices commute. Then breaking the exponentials only introduces errors when factors of different groups are multiplied. As a simple example we can consider the case of a periodic one-dimensional chain with nearest-neighbor hopping. Its kinetic matrix can be written as

$$T = T_a + T_b, \quad T_a = \sum_i T_{2i, 2i+1} \equiv \sum_{\langle i, j \rangle^a} T_{ij}, \quad T_b = \sum_i T_{2i+1, 2i+2} \equiv \sum_{\langle i, j \rangle^b} T_{ij}, \quad (5.55)$$

where T_a contains hoppings on pairs of sites $(0, 1), (2, 3), (4, 5), \dots, (N_s - 1, N_s)$ and T_b on pairs of sites $(1, 2), (3, 4), (5, 6), \dots, (N_s, 0)$. For some matrix A we have

$$\begin{aligned} Ae^{\pm \Delta\tau T/2} &= Ae^{\pm \Delta\tau T_a/2} e^{\pm \Delta\tau T_b/2} + O(\Delta\tau^2) \\ &= A \prod_{\langle i, j \rangle^a} e^{\pm \Delta\tau T_{ij}/2} \prod_{\langle i, j \rangle^b} e^{\pm \Delta\tau T_{ij}/2} + O(\Delta\tau^2), \end{aligned} \quad (5.56)$$

where the Suzuki-Trotter error is introduced only a single time. The order of the factors within the two products is irrelevant. For a model defined on the two-dimensional square lattice with nearest neighbor hopping an equivalent separation can be performed for each Cartesian axis [86]. Here we have

$$\begin{aligned} T &= T_a^x + T_a^y + T_b^x + T_b^y \\ Ae^{\pm \Delta\tau T/2} &= Ae^{\pm \Delta\tau T_a^x/2} e^{\pm \Delta\tau T_a^y/2} e^{\pm \Delta\tau T_b^x/2} e^{\pm \Delta\tau T_b^y/2} + O(\Delta\tau^2). \end{aligned} \quad (5.57)$$

5.3.1.1 Optimized form for the square lattice

For our square lattice we follow Assaad [85], who proposes a break-up with only two groups of commuting matrices $T = T_A + T_B$ as shown in Fig. 5.11, where the individual matrices now describe hopping between *four* sites. If $-t_1$ is the hopping constant for horizontal movement and $-t_2$ the constant for vertical movement, one

such matrix is given by

$$T_{A,ijkl} = \begin{bmatrix} i & j & k & l \\ \downarrow & \downarrow & \downarrow & \downarrow \\ \ddots & & & \\ & t_1 & \dots & t_2 \\ t_1 & & & t_2 \\ \vdots & & & \vdots \\ & t_2 & \dots & t_1 \\ t_2 & t_2 & \dots & t_1 \\ & & & \ddots \end{bmatrix} . \quad (5.58)$$

Its exponential reads explicitly (omitting factors $\Delta\tau/2$)

$$e^{\pm T_{A,ijkl}} = \begin{bmatrix} i & j & k & l \\ \downarrow & \downarrow & \downarrow & \downarrow \\ 1 & \ddots & 1 & \ddots \\ & & \begin{matrix} \text{ch}(t_1)\text{ch}(t_2) & \pm \text{ch}(t_2)\text{sh}(t_1) \\ \pm \text{ch}(t_2)\text{sh}(t_1) & \text{ch}(t_1)\text{ch}(t_2) \end{matrix} & \begin{matrix} \pm \text{ch}(t_1)\text{sh}(t_2) & \text{sh}(t_1)\text{sh}(t_2) \\ \text{sh}(t_1)\text{sh}(t_2) & \pm \text{ch}(t_1)\text{sh}(t_2) \end{matrix} \\ & & 1 & \ddots \\ & & \ddots & \begin{matrix} \pm \text{ch}(t_1)\text{sh}(t_2) & \text{sh}(t_1)\text{sh}(t_2) \\ \text{sh}(t_1)\text{sh}(t_2) & \pm \text{ch}(t_1)\text{sh}(t_2) \end{matrix} & \begin{matrix} \text{ch}(t_1)\text{ch}(t_2) & \pm \text{ch}(t_2)\text{sh}(t_1) \\ \pm \text{ch}(t_2)\text{sh}(t_1) & \text{ch}(t_1)\text{ch}(t_2) \end{matrix} \\ & & & 1 & \ddots \\ & & & & 1 \end{bmatrix} . \quad (5.59)$$

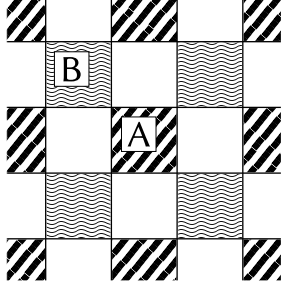


Figure 5.11: Nearest neighbor square lattice checkerboard decomposition following Assaad [85]. T_A contains hopping along the boundaries of the stripy squares; T_B contains hoppings along the boundaries of the wavy squares.

The multiplication with $e^{\pm\Delta\tau T/2}$ is now represented by two groups of $N_s/4$ plaquette factors each:

$$A \cdot e^{\pm\Delta\tau T/2} = A \cdot \prod_{[ijkl]_A}^{N/4} e^{\pm\Delta\tau T_{A,ijkl}/2} \cdot \prod_{[ijkl]_B}^{N/4} e^{\pm\Delta\tau T_{B,ijkl}/2} + O(\Delta\tau^2), \quad (5.60)$$

which has a combined computational cost of $O(N_s^2)$. Each four-plaquette factor will change four rows or columns when multiplied to the left or right of a matrix. Only a single checkerboard break-up contributes to the error of $O(\Delta\tau^2)$, which is of the same order as the overall Suzuki-Trotter error of the DQMC formalism. If we had chosen a “random” order of single-bond matrices in Eq. (5.54), this error would grow macroscopically $O(N_s\Delta\tau^2)$.

5.3.1.2 Factor grouping with the symmetric Suzuki-Trotter decomposition

Since we use a *symmetric* Suzuki-Trotter decomposition in the formulation of the DQMC algorithm

$$e^{-\Delta\tau \sum_\ell [K+V[\vec{\varphi}_\ell]]} = \prod_\ell e^{-\Delta\tau K/2} e^{-\Delta\tau V[\vec{\varphi}_\ell]} e^{-\Delta\tau K/2} + O(\Delta\tau^2), \quad (5.61)$$

we also apply the checkerboard break-up symmetrically:

$$\begin{aligned} B_\ell &= e^{-\Delta\tau K/2} e^{-\Delta\tau V[\vec{\varphi}_\ell]} e^{-\Delta\tau K/2} \\ &= e^{-\Delta\tau K_a/2} e^{-\Delta\tau K_b/2} e^{-\Delta\tau V[\vec{\varphi}_\ell]} e^{-\Delta\tau K_b/2} e^{-\Delta\tau K_a/2} + O(\Delta\tau^2). \end{aligned} \quad (5.62)$$

We group the factors that form the entire product in the following way:

$$e^{-\Delta\tau \sum_\ell [K + V[\vec{\varphi}_\ell]]} = e^{-\Delta\tau K_a/2} e^{-\Delta\tau K_b/2} \\ \times \left(\prod_\ell \underbrace{e^{-\Delta\tau V[\vec{\varphi}_\ell]} e^{-\Delta\tau K_b/2} e^{-\Delta\tau K_a} e^{-\Delta\tau K_b/2}}_{B_\ell^{\text{eff}}} \right) e^{\Delta\tau K_b/2} e^{\Delta\tau K_a/2} + O(\Delta\tau^2). \quad (5.63)$$

Here the brace marks the effective B -matrix factors for the implementation of the simulation. Compared to the form in Eq. (5.62), using these these effective factors saves one sparse matrix multiplication of a hopping group exponential per application of each factor B_ℓ . The outer factors $e^{-\Delta\tau K_a/2} e^{-\Delta\tau K_b/2}$ and $e^{\Delta\tau K_a/2} e^{\Delta\tau K_b/2}$ are not important for the statistical weight during the Monte Carlo sampling because they cancel under the determinant: $\det[\mathbb{1} + A^{-1}BA] = \det[\mathbb{1} + BAA^{-1}] = \det[\mathbb{1} + B]$ for square matrices A and B . But they need to be considered when measuring fermionic observables. We obtain the correct equal-time Green's function from the one constructed from the B_ℓ^{eff} by applying the missing factors to the left and right:

$$G_\ell = [\mathbb{1} + B_\ell \cdots B_1 B_m \cdots B_{\ell+1}]^{-1} \\ = e^{-\Delta\tau K_a/2} e^{-\Delta\tau K_b/2} [\mathbb{1} + B_\ell^{\text{eff}} \cdots B_1^{\text{eff}} B_m^{\text{eff}} \cdots B_{\ell+1}^{\text{eff}}]^{-1} e^{\Delta\tau K_a/2} e^{\Delta\tau K_b/2} \\ = e^{-\Delta\tau K_a/2} e^{-\Delta\tau K_b/2} G_\ell^{\text{eff}} e^{\Delta\tau K_a/2} e^{\Delta\tau K_b/2}. \quad (5.64)$$

5.3.2 Delayed updates

Delayed updating is a technique by the means of which the update of the equal-time Green's function matrix after an accepted local Monte Carlo move is sped up. To put the Green's function into a valid state $G_\ell \rightarrow G'_\ell$ after a local change of the bosonic field $\vec{\varphi}_i(\ell) \rightarrow \vec{\varphi}'_i(\ell)$ the standard procedure is, see Eq. (4.7),

$$G'_\ell = G_\ell + (G_\ell[:, i :: N_s] \cdot \Delta^i) \cdot (M^{-1} \cdot V), \quad (5.65)$$

where $V = (G_\ell - \mathbb{1})[i :: N_s, :]$, $\Delta^i = (e^{-\Delta\tau V'_\ell} e^{\Delta\tau V_\ell} - \mathbb{1})[i :: N_s, i :: N_s]$, and $M = \mathbb{1}_4 - G_\ell[i :: N_s, i :: N_s] \cdot \Delta^i + \Delta^i$ in the slice notation of p. 75.⁵ During a sweep of local updates this step has to be done after each accepted local change of the field $\vec{\varphi}$.

The idea of delayed updates [157] is to instead perform one combined update of the Green's function after a series of k accepted local moves. To determine

⁵For compactness this Section is written in terms of updating the full $4N_s \times 4N_s$ Green's function matrix G_ℓ . The transfer to the $2N_s \times 2N_s$ matrix \tilde{G}_ℓ used for the implementation of the O(1) and O(2) models is straightforward.

acceptance probabilities while the update is still delayed, only the change of some rows and columns of G_ℓ needs to be computed. Maintaining this leads to additional calculations of $O(jN_s)$ in the j th step ($j \leq k$), while the update of G_ℓ after k steps will have a cost of $O(kN_s^2)$ operations, which is of the same order as a series of k updates according to Eq. (5.65). Nevertheless, delayed updates are expected to be more efficient on modern computers due to their better memory locality which benefits more from caching [158]. Submatrix updates [159] are a variation of the delayed updates that promises to reduce the additional computational effort from $O(jN)$ to $O(j^2)$, which, however, is the least worrisome part. In the following we show how regular delayed updates can be implemented for the SDW model.

We first rewrite Eq. (5.65) for the updated Green's function after an accepted local move at site i_0 as an addition and a $(4N_s \times 4) \cdot (4 \times 4N_s)$ matrix product:

$$G_{\ell,1} = G_{\ell,0} + X_0 Y_0 \quad (5.66)$$

with $X_0 := G_{\ell,0} U_0$ and $Y_0 := (\mathbb{I}_4 - V_0 U_0)^{-1} V_0$. Here we write $V_0 = R_0^{i_0} - \mathbb{I}^{i_0}$, where $R_0^{i_0} \equiv G_{\ell,0}[i_0 :: N_s, :]$ are the 4 rows of $G_{\ell,0}$ belonging to site i_0 and $\mathbb{I}^{i_0} \equiv [\underline{e}_{i_0}, \underline{e}_{i_0+N_s}, \underline{e}_{i_0+2N_s}, \underline{e}_{i_0+3N_s}]^\top$ are the corresponding rows of the identity matrix, while the non-zero entries of U_0 are given by those of the matrix Δ^{i_0} (corresponding to Δ^i below Eq. (5.65)). Explicitly, the entries of X_0 read

$$\begin{aligned} X_0[r,s] &= (G_{\ell,0} U_0)[r,s] = \sum_t^{4N_s} G_{\ell,0}[r,t] U_0[t,s] \\ &= \sum_k^4 G_{\ell,0}[r, i_0 + kN_s] \Delta^{i_0}[k,s], \end{aligned} \quad (5.67)$$

such that we have $X_0 = C_0^{i_0} \Delta^{i_0}$, where $C^{i_0} := G_{\ell,0}[:, i_0 :: N_s]$ are the columns of $G_{\ell,0}$ corresponding to site i_0 . For the product $V_0 U_0$ we find

$$\begin{aligned} (V_0 U_0)[r,s] &= \sum_t^{4N_s} (R_0^{i_0} - \mathbb{I}^{i_0})[r,t] \sum_k^4 \Delta^{i_0}[k,s] \delta_{t,i_0+kN_s} \\ &= \sum_k^4 (R_0^{i_0}[r, i_0 + kN_s] - \delta_{rk}) \Delta^{i_0}[k,s] \end{aligned} \quad (5.68)$$

or $V_0 U_0 = S_0^{i_0} \Delta^{i_0} - \Delta^{i_0}$ with $S_0^{i_0} := R_0^{i_0}[:, i_0 :: N_s] \equiv G_{\ell,0}^{i_0}[i_0 :: N_s, i_0 :: N_s]$ as the 4×4

submatrix of $G_{\ell,0}$ with entries corresponding to i_0 . In total we have

$$X_0 = C_0^{i_0} \Delta^{i_0}, \quad [4N_s \times 4] \quad (5.69)$$

$$Y_0 = (\underbrace{\mathbb{1}_4 - S_0^{i_0} \Delta^{i_0} + \Delta^{i_0}}_{M_0})^{-1} (R_0^{i_0} - \mathbb{1}^{i_0}), \quad [4 \times 4N_s] \quad (5.70)$$

and we need 4 columns and 4 rows of $G_{\ell,0}$ to compute $G_{\ell,1}$.

After a second spin-flip at site i_1 we have

$$G_{\ell,2} = G_{\ell,0} + X_0 Y_0 + X_1 Y_1 \quad (5.71)$$

with $X_1 = C_1^{i_1} \Delta^{i_1}$ and $Y_1 = (\mathbb{1}_4 - S_1^{i_1} \Delta^{i_1} + \Delta^{i_1})^{-1} (R_1^{i_1} - \mathbb{1}^{i_1}) = M_1^{-1} (R_1^{i_1} - \mathbb{1}^{i_1})$. Here we only have to compute

$$\begin{aligned} R_1^{i_1} &\equiv G_{\ell,1}[i_1 :: N_s, :] = (G_{\ell,0} + X_0 \cdot Y_0)[i_1 :: N_s, :] \\ &= G_{\ell,0}[i_1 :: N_s, :] + (X_0[i_1 :: N_s, :]) \cdot Y_0 \end{aligned} \quad (5.72)$$

and

$$\begin{aligned} C_1^{i_1} &\equiv G_{\ell,1}[:, i_1 :: N_s] = (G_{\ell,0} + X_0 \cdot Y_0)[:, i_1 :: N_s] \\ &= G_{\ell,0}[:, i_1 :: N_s] + X_0 \cdot (Y_0[:, i_1 :: N_s]), \end{aligned} \quad (5.73)$$

which is of order $O(N_s)$.

Iterating this procedure, we arrive at the following equation to update G_0 after k accepted spin-flips:

$$G_{\ell,k} = G_{\ell,0} + \sum_{j=0}^{k-1} X_j \cdot Y_j \quad \text{with} \quad (5.74)$$

$$X_j = C_j^{i_j} \Delta^{i_j} \quad \text{and} \quad (5.75)$$

$$Y_j = (\underbrace{\mathbb{1}_4 - S_j^{i_j} \Delta^{i_j} + \Delta^{i_j}}_{M_j})^{-1} (R_j^{i_j} - \mathbb{1}^{i_j}), \quad (5.76)$$

where we have to recompute at each step j the relevant rows and columns of $G_{\ell,j-1}$:

$$R_j^{i_j} = G_{\ell,0}[i_j :: N_s, :] + \sum_{l=0}^{j-1} (X_l[i_j :: N_s, :]) \cdot Y_l, \quad (5.77)$$

$$S_j^{i_j} = R_j^{i_j}[:, i_j :: N_s], \quad (5.78)$$

$$G_j^{i_j} = G_{\ell,0}[:, i_j :: N_s] + \sum_{l=0}^{j-1} X_l \cdot (Y_l[:, i_j :: N_s]). \quad (5.79)$$

The matrix products here are $(4N_s \times 4) \cdot (4 \times 4)$, hence the additional computations at step j amount to $O(jN_s)$. There are additional storage requirements for the matrices X_j and Y_j . We can decide whether to accept the spin-flip at site i_j by computing a 4×4 determinant

$$\begin{aligned} r_j &= \det(\mathbb{1}_4 - \Delta^{i_j} \cdot V_j[:, i_j :: N_s]) = \det(\mathbb{1}_4 - V_j[:, i_j :: N_s] \cdot \Delta^{i_j}) \\ &= \det(\mathbb{1}_4 - S_j^{i_j} \cdot \Delta^{i_j} + \Delta^{i_j}) = \det M_j. \end{aligned} \quad (5.80)$$

The advantage of the delayed update scheme is that $B_\varphi(\ell) = e^{-\Delta\tau V(\varphi_\ell)} e^{-\Delta\tau K}$ the sum in Eq. (5.74) can be understood as a $(4N_s \times 4k) \cdot (4k \times 4N_s)$ matrix product:

$$G_{\ell,k} = G_{\ell,0} + \hat{X} \cdot \hat{Y} \quad (5.81)$$

with $\hat{X} = [X_0, X_1, \dots, X_{k-1}]$ and $\hat{Y} = [Y_0, Y_1, \dots, Y_{k-1}]^\top$. Evaluating Eq. (5.81) is of order $O(kN_s^2)$, but numerically computing this single matrix-matrix product is expected to be more efficient than applying Eq. (5.65) k times, each time involving $(4N_s \times 4) \cdot (4 \times 4N_s)$ matrix products. It is important to stress that delayed updates do not influence numerical stability or introduce any additional errors. Within floating point precision results are fully equivalent to those obtained with regular updates.

In our simulations of the metallic SDW model we find that delayed updates do speed up the linear algebra for local updates, see Fig. 5.12. But the advantage is lost if the Green's function update is delayed by too many steps when the computational overhead of the delayed updates becomes significant. Here the optimum number of delayed steps is roughly 6 or 8. The improvements are rather modest in comparison to what has been achieved with the Hubbard model. This may be due to the more intricate structure of the interaction matrix in the SDW model or due to the computer architecture (Intel Xeon X5650). Possibly submatrix updates [159] could provide performance gains with higher numbers of delayed steps. However, these improvements are outbalanced by the time needed for numerical stabilization by matrix decomposition in actual simulations, see Fig. 5.13a in comparison to Fig. 5.13b.

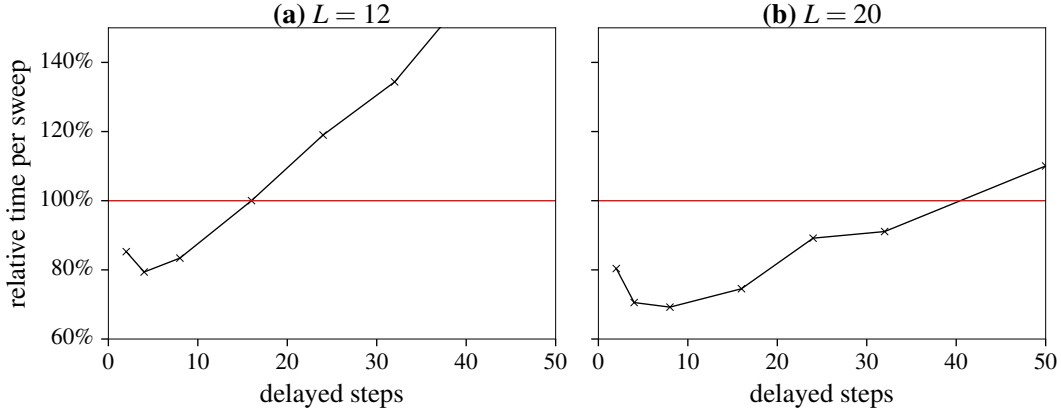


Figure 5.12: Wall clock time per Monte Carlo sweep for delayed updates in comparison to regular updates (at 100%) with different numbers of delayed steps in short (100 sweeps) simulations of the O(3) SDW model at $\beta = 2$ and $r = 1.5$ for (a) $L = 12$ and (b) $L = 20$. Only the time needed for operations local to the imaginary-time slice was measured.

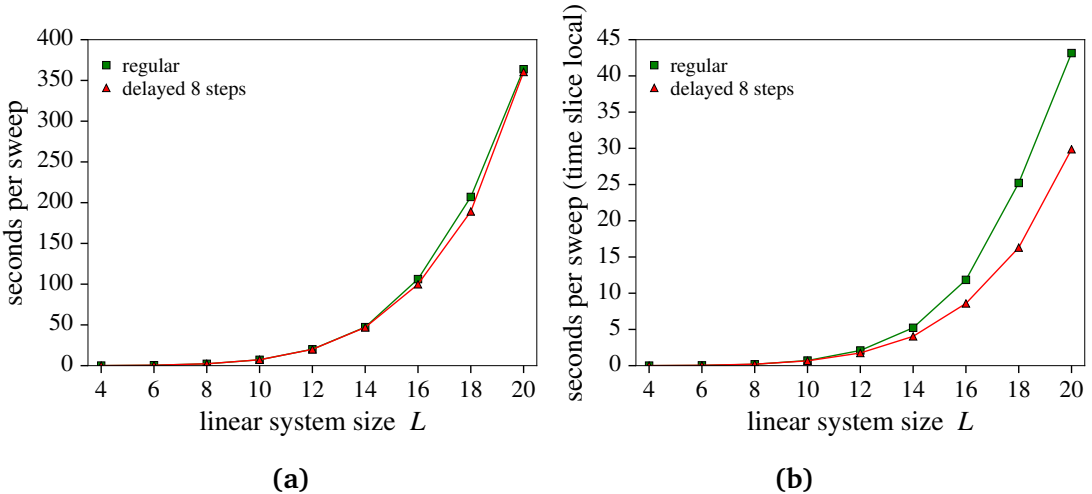


Figure 5.13: Wall clock time per Monte Carlo sweep in short (100 sweeps) simulations of the O(3) SDW model at $\beta = 2$ and $r = 1.5$, comparing regular and delayed local updates (delayed by 8 steps). The time needed for setup, measurements and file system operation has been excluded in both plots. Panel (b) only shows the time needed for updates that are local in imaginary time, i.e. the timings do not include the numerically stabilized propagation of the Green's function. All data are consistent with an L^6 power law.

5.4 Finite-size effects

Metallic systems such as the SDW model are particularly susceptible to strong finite-size effects at low temperatures. Conversely, insulators, which are characterized by the localization of their wave function, are much less sensitive to the presence of boundaries in finite systems. Since the computational cost of the DQMC method limits us to study rather small systems, reducing the severity of such finite-size effects is very important.

5.4.1 Perpendicular magnetic field

Interestingly, finite-size effects can be remarkably reduced in the presence of a magnetic field acting on the electron orbits, imposed perpendicular to the system [85, 160]. Possibly, this may be attributed to the breaking of lattice translational invariance, which may lower the influence of the system boundary.

A prototypical example for the worst case of finite-size effects in a metal is a non-interacting spinless tight-binding model. Here we follow Refs. [85, 160]. On a periodic square lattice its bare form without external fields is defined by the nearest-neighbor hopping Hamiltonian

$$\mathcal{H} = -t \sum_{\langle i,j \rangle} c_i^\dagger c_j + \text{h.c.} \quad (5.82)$$

A magnetic field $\mathbf{B}(\mathbf{r}) = \nabla \times \mathbf{A}(\mathbf{r})$ can be introduced by incorporating Peirls phase factors [23, Sec. 12.1]:

$$\mathcal{H}[\mathbf{A}] = -t \sum_{\langle i,j \rangle} e^{iA_{ij}} c_i^\dagger c_j + \text{h.c.} \quad (5.83)$$

with phases $A_{ij} = \frac{2\pi}{\Phi_0} \int_{\mathbf{r}_i}^{\mathbf{r}_j} \mathbf{A} \cdot d\ell$ and the magnetic flux quantum Φ_0 . To realize a constant magnetic field orthogonal to the lattice plane, $\mathbf{B} = B\mathbf{e}_3$, we choose the Landau gauge $\mathbf{A}(\mathbf{r}_i) = -Bi_2\mathbf{e}_1$, where $\mathbf{r}_i = (i_1, i_2)^\top$. We find

$$A_{ij} = \begin{cases} -\frac{2\pi}{\Phi_0} Bi_2, & \text{for } \mathbf{r}_i = \mathbf{r}_j + \mathbf{e}_1, \\ \frac{2\pi}{\Phi_0} Bi_2, & \text{for } \mathbf{r}_i = \mathbf{r}_j - \mathbf{e}_1, \\ 0, & \text{for } \mathbf{r}_i = \mathbf{r}_j \pm \mathbf{e}_2 \text{ or non-neighboring sites.} \end{cases} \quad (5.84)$$

The periodic $L \times L$ lattice has the topology of a torus. Our boundary conditions for the fermionic operators c_i^\dagger, c_i must be chosen to be compatible with this topology

also in presence of the magnetic field. Therefore we require

$$\exp(iA_{i+L\mathbf{e}_1,j+L\mathbf{e}_1})c_{i+L\mathbf{e}_1}^\dagger c_{j+L\mathbf{e}_1} \stackrel{!}{=} \exp(iA_{ij})c_i^\dagger c_j \quad \text{and} \quad (5.85a)$$

$$\exp(iA_{i+L\mathbf{e}_2,j+L\mathbf{e}_2})c_{i+L\mathbf{e}_2}^\dagger c_{j+L\mathbf{e}_2} \stackrel{!}{=} \exp(iA_{ij})c_i^\dagger c_j \quad (5.85b)$$

for all lattice sites i and j . This condition can be fulfilled by imposing special boundary conditions in \mathbf{e}_2 direction,

$$c_{i+L\mathbf{e}_2}^\dagger = c_i^\dagger e^{-\frac{2\pi i}{\Phi_0} BLi_1} \quad \text{and} \quad c_{i+L\mathbf{e}_2} = c_i e^{\frac{2\pi i}{\Phi_0} BLi_1} \quad (5.86)$$

with the phase depending explicitly on i_1 , while regular periodic boundary conditions are upheld in \mathbf{e}_1 direction. Incorporating these boundary conditions, the explicit Peirls phases in Eq. (5.83) read

$$A_{ij} = \begin{cases} -\frac{2\pi}{\Phi_0} Bi_2 & \text{if } i_1 = 0, \dots, L-2 \text{ and } j_1 = i_1 + 1 \\ & \text{or } i_1 = L-1 \text{ and } j_1 = 0, \\ +\frac{2\pi}{\Phi_0} Bi_2 & \text{if } i_1 = 1, \dots, L-1 \text{ and } j_1 = i_1 - 1 \\ & \text{or } i_1 = 0 \text{ and } j_1 = L-1, \\ +\frac{2\pi}{\Phi_0} BLi_1 & \text{if } i_2 = L-1 \text{ and } j_2 = 0, \\ -\frac{2\pi}{\Phi_0} BLi_1 & \text{if } i_2 = 0 \text{ and } j_2 = L-1, \\ 0 & \text{otherwise,} \end{cases} \quad (5.87)$$

where the lattice sites vectors are indexed from 0 to $L-1$ in each direction.

Under these boundary conditions the Hamiltonian commutes with translations by the linear lattice size,

$$[\mathcal{H}[\mathbf{A}], T_{L\mathbf{e}_1}] = [\mathcal{H}[\mathbf{A}], T_{L\mathbf{e}_2}] = 0, \quad (5.88)$$

where the magnetic translation operators $T_{L\mathbf{e}_1}$, $T_{L\mathbf{e}_2}$ form a magnetic algebra [23, Sec. 12.1]. This imposes an additional restriction for the magnetic field. For the torus topology we have

$$T_{L\mathbf{e}_1} T_{L\mathbf{e}_2} = e^{-i2\pi \frac{(L\mathbf{e}_1 \times L\mathbf{e}_2) \cdot \mathbf{B}}{\Phi_0}} T_{L\mathbf{e}_2} T_{L\mathbf{e}_1} \quad (5.89)$$

and the wave function cannot be single valued unless the right-hand side prefactor is 1. Therefore the flux must be quantized: $\frac{(L\mathbf{e}_1 \times L\mathbf{e}_2) \cdot \mathbf{B}}{\Phi_0} = n \in \mathbb{Z}$. Hence, the smallest

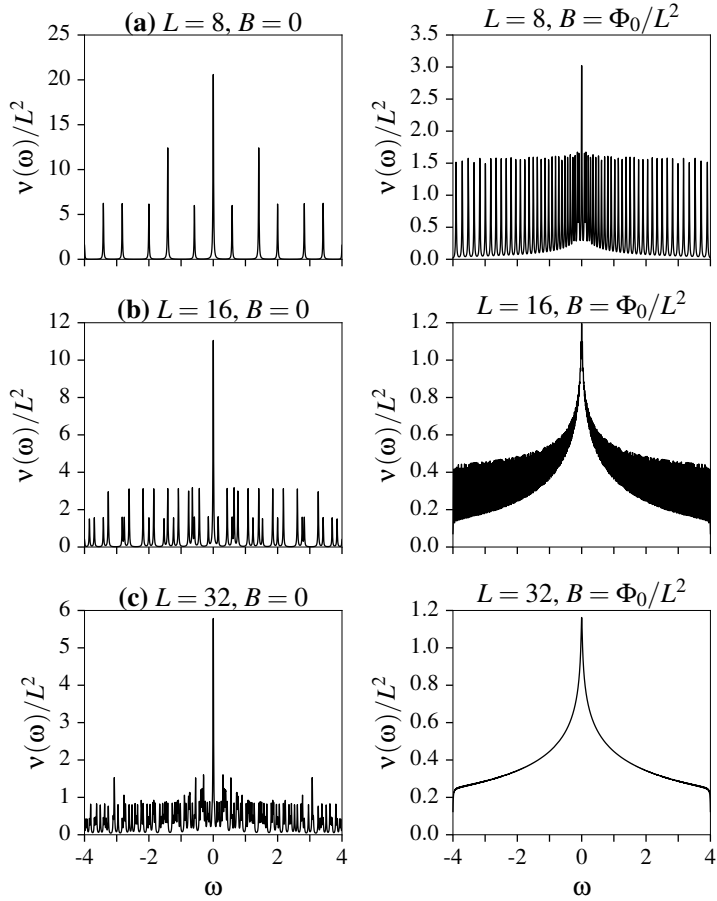


Figure 5.14: Single-particle energy density of states $\nu(\omega)$, approximated with $\delta = 0.01$, for a tight-binding model on (a) $L = 8$, (b) $L = 16$, and (c) $L = 32$ square lattices. Left-hand column: no magnetic field, right-hand column: a single magnetic flux is threaded through the system. In these units $t = 1$.

possible finite field, perpendicular to the lattice plane, has a magnitude of

$$B = \frac{\Phi_0}{L^2}. \quad (5.90)$$

With this choice of B , all values of A_{ij} in Eq. (5.87) tend to 0 in the thermodynamic limit $L \rightarrow \infty$ such that, in this limit, the Hamiltonians (5.82) and (5.83) are equivalent. However, we see in the following that the finite-size Hamiltonian (5.83) with the weak magnetic field (5.90) approaches this limit *faster*.

A striking illustration of this can be found in the single-particle energy density of

states

$$v(\omega) = \sum_n \delta(\omega - \varepsilon_n) = \frac{-1}{\pi} \text{Im} \sum_n \frac{1}{\omega - \varepsilon_n + i\delta} \quad (5.91)$$

with $\delta \rightarrow 0^+$ and where ε_n are the single-particle eigenvalues of \mathcal{H} [25, Sec. 3.3]. For a non-interacting model the values of ε_n are readily obtained by diagonalizing the matrix kernel of \mathcal{H} . The result is plotted in Fig. 5.14 with and without magnetic field. Finite-size effects dominate for all lattices if no magnetic field is active, whereas the Van Hove singularity is well reproduced already for $L \geq 16$ with a magnetic flux. Here it is apparent how the degenerate states of the $B = 0$ case are distributed smoothly over the energy range for $B > 0$, as they would in the exact $L \rightarrow \infty$ limit. Landau levels have a degeneracy of $L^2 B / \Phi_0 = 1$ for the minimal value of B chosen here. Without breaking symmetries on finite lattices the original degeneracy could not be removed. This reduction of finite-size effects carries over to thermodynamic observables.

5.4.2 Fictitious “magnetic” field for the SDW model

For the metallic SDW model we cannot introduce a magnetic field without breaking the generalized time-reversal symmetry that ensures the absence of the fermion sign problem in DQMC simulations, which has been discussed in detail in Sec. 4.3.2. However, we are free to incorporate a fictitious generalized field with an appropriate dependence on flavor and spin indices $\alpha = x, y$ and $s = \uparrow, \downarrow$ that makes sure the symmetry under $\hat{T} = -is_2\sigma_3C$ is not broken. Generalizing the discussion of the previous Subsection, we add Peirls phase factors $e^{iA_{ij}^{\alpha s}}$ to the kinetic part of the action and require

$$\hat{T} \sum_{\alpha, s} e^{iA_{ij}^{\alpha s}} \psi_{\alpha, i, s}^\dagger \psi_{\alpha, j, s} \hat{T}^{-1} = \sum_{\alpha, s} e^{-iA_{ij}^{\alpha s}} \psi_{\alpha, i, -s}^\dagger \psi_{\alpha, j, -s} \stackrel{!}{=} \sum_{\alpha, s} e^{iA_{ij}^{\alpha s}} \psi_{\alpha, i, s}^\dagger \psi_{\alpha, j, s}. \quad (5.92)$$

This is fulfilled for $A_{ij}^{\alpha\uparrow} = -A_{ij}^{\alpha\downarrow}$. We let the sign of the perpendicular “magnetic” field depend on flavor and spin as in

$$B^{x\uparrow} = B^{y\downarrow} = -B^{x\downarrow} = -B^{y\uparrow} = \frac{\Phi_0}{L^2} \quad (5.93)$$

and otherwise set everything as discussed above for the tight-binding model. In Eq. (5.93) there is an extra sign change between the two fermionic bands, which is not required for the absence of the sign problem, but convenient for the implementation.

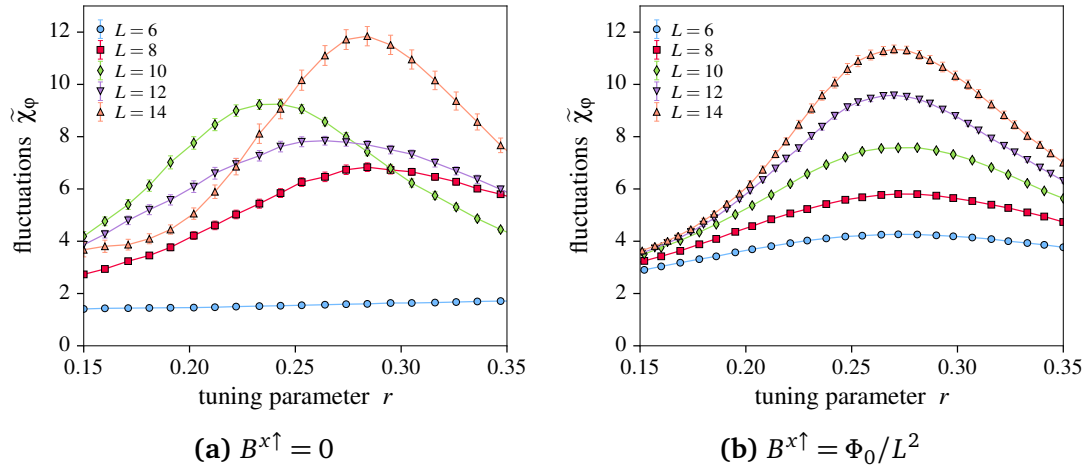


Figure 5.15: DQMC data for the O(2) SDW model with $\lambda = 1 = c$ at $\beta = 1/T = 10$ (a) without and (b) with a perpendicular flux. The plotted quantity $\tilde{\chi}_\varphi = \beta N_s [\langle \varphi^2 \rangle - \langle \bar{\varphi} \rangle^2]$ with $\bar{\varphi} = \frac{\Delta\tau}{\beta N_s} \left| \sum_{i,\ell} \varphi_i(\ell) \right|$ is an estimate for SDW fluctuations. The location of its peak is related to that of the phase transition and the peak height should scale with the system size L .

As in the case of the non-modified model, the O(2) and O(1) variations of the model with fictitious field can be implemented in terms of half sized single-fermion matrices, see Sec. 4.3.3.

In the implementation, the checkerboard approximation of Sec. 5.3.1 requires some attention. Two-site hopping matrices

$$T = \begin{bmatrix} 0 & e^{iA_{ij}} t_{ij} \\ e^{-iA_{ij}} t_{ij} & 0 \end{bmatrix} \quad (5.94)$$

can easily be exponentiated:

$$e^{\alpha T} = \begin{bmatrix} \operatorname{ch}(\alpha t_{ij}) & e^{iA_{ij}} \operatorname{sh}(\alpha t_{ij}) \\ e^{-iA_{ij}} \operatorname{sh}(\alpha t_{ij}) & \operatorname{ch}(\alpha t_{ij}) \end{bmatrix}, \quad (5.95)$$

but the exponentials of four-site (plaquette) hopping matrices, which lead to a smaller systematic error (see Sec. 5.3.1.1), cannot easily be brought into a simple analytic form. Here it is necessary to compute the matrix exponentials numerically. Since they can be precomputed once at the start of the simulation, this does not introduce any significant computational cost.

The artificial flux is very effective in controlling finite-size effects that set in already at moderately low temperatures. See Fig. 5.15 for an example for the drastic improvements realized with the fictitious field. The location of the peak in Fig. 5.15a

does not only move strongly between different system sizes, but the peak value is also very erratic: The maximum of $\tilde{\chi}_\varphi$ is smaller for $L = 12$ than for $L = 10$. In contrast, the behavior in Fig. 5.15b is much more systematic with a smooth development starting at the smallest lattice size shown.

5.4.3 Twisted boundary conditions

The artificial orthogonal pseudo-magnetic field works very well to lower unsystematic finite-size effects. Unfortunately it cannot be applied in all situations. Since it breaks lattice translational invariance, we cannot analyze non-local fermionic correlation functions such as the momentum-resolved Green's function from data obtained in simulations with the field.

One major source of finite-size effects in these quantities is the discretized momentum resolution for small systems. The first Brillouin zone for a $L \times L$ system only has L distinct momentum values per direction. To enhance this resolution we have run additional simulations without the perpendicular flux, but instead with *in-plane* vector potentials

$$\mathbf{A}^{\alpha s} = \pm(n_1, n_2, 0)^\top \frac{\Phi_0}{4L} \quad (5.96)$$

with $n_i = 0, 1, 2, 3$, the positive sign for $\alpha s \in \{x\uparrow, y\downarrow\}$, and the negative sign for $\alpha s \in \{x\downarrow, y\uparrow\}$. Note that here $\mathbf{B}^{\alpha s} = \nabla \times \mathbf{A}^{\alpha s} = \mathbf{0}$. Upon introduction of this vector potential the hopping terms of the fermionic action transform like

$$\psi_{ais}^\dagger \psi_{ajs} \rightarrow \psi_{ais}^\dagger \psi_{ajs} e^{\pm i \frac{2\pi}{4L} [n_1(j_1 - i_1) + n_2(j_2 - i_2)]} = \tilde{\psi}_{ais}^\dagger \tilde{\psi}_{ajs}, \quad (5.97)$$

where we have introduced basis transformed fermionic operators

$$\tilde{\psi}_{ajs}^\dagger = e^{\pm i \frac{2\pi}{4L} [n_1 j_1 + n_2 j_2]}, \quad (5.98a)$$

$$\tilde{\psi}_{ajs} = e^{\mp i \frac{2\pi}{4L} [n_1 j_1 + n_2 j_2]}. \quad (5.98b)$$

In terms of these operators we have **twisted boundary conditions** instead of explicit Peirls phases:

$$\tilde{\psi}_{\alpha,j+L\mathbf{e}_1,s}^\dagger = e^{\pm i \frac{2\pi}{4L} [n_1(j_1 + L) + n_2 j_2]} \tilde{\psi}_{\alpha,j+L\mathbf{e}_1,s}^\dagger = e^{\pm i \frac{2\pi}{4L} n_1} \tilde{\psi}_{\alpha j s}^\dagger \quad (5.99)$$

and equivalently for the \mathbf{e}_2 direction. Twisted boundary conditions affect momentum

space:

$$\begin{aligned}\tilde{\psi}_{aks}^\dagger &\equiv \frac{1}{\sqrt{N_s}} \sum_j e^{i\mathbf{k}\cdot\mathbf{r}_j} \tilde{\psi}_{ajs}^\dagger \stackrel{!}{=} \frac{1}{\sqrt{N_s}} \sum_j e^{i\mathbf{k}\cdot(\mathbf{r}_j + L\mathbf{e}_1 + L\mathbf{e}_2)} \tilde{\psi}_{a,j+L\mathbf{e}_1+L\mathbf{e}_2,s}^\dagger \\ &= \frac{1}{\sqrt{N_s}} \sum_j e^{i\mathbf{k}\cdot\mathbf{r}_j} \underbrace{e^{ik_1 L \pm i \frac{2\pi}{4L} n_1} e^{ik_2 L \pm i \frac{2\pi}{4L} n_2}}_{\stackrel{!}{=} 1} \tilde{\psi}_{ajs}^\dagger,\end{aligned}\quad (5.100)$$

such that the allowed momenta are

$$\mathbf{k} = \frac{2\pi}{4L}(4n_{k1} \mp n_1, 4n_{k2} \mp n_2)^\top \quad (5.101)$$

for integer n_{k1}, n_{k2} . This signifies of course that in a single simulation we obtain data at different \mathbf{k} values for the $x\uparrow, y\downarrow$ fermions than for the $x\downarrow, y\uparrow$ fermions. But since we run separate simulations for all combinations of $n_i = 0, 1, 2$, and 3, in combination we have data for all spin and flavor indices at these momenta. Effectively we achieve a fourfold enhancement of momentum space resolution in each lattice direction for fermionic observables. Note that for the O(2) and O(1) models the blocks of the Green's function corresponding to cross terms for mixed \mathbf{k} values are zero.

Averaging over multiple such twisted boundary conditions has been suggested as an effective means to reduce finite-size effects [161–163]. This would be an alternative to the orthogonal pseudo-magnetic field for local fermionic observables, which, however, entails a higher computational cost due to the necessity of running multiple simulations.

5.5 Aspects of data analysis

In the previous sections of this Chapter we have discussed various technical aspects related to the generation of time series of observable measurements in DQMC simulations. Here we direct our attention to the evaluation of these data.

One advantage of the Monte Carlo method is that it is “embarrassingly parallel”. We can easily run independent simulations for multiple random seeds in parallel and average over the combined data, once they all have reached equilibrium. This simple method of parallelization is applied on top of the parallelized replica exchange mechanism and helps to reduce the “wall clock time” needed to obtain data of a desired statistical quality. We simply concatenate the equilibrium time series obtained in such independent simulations. Typically we combine between 2 and 5 equivalent simulations.

Statistical errors are estimated by the jackknife method or, when sufficient, by simple blocking [164].

Since there is a great variety of fermionic and bosonic correlation functions that can be of physical interest, it has turned out to be useful to save entire spacetime configurations of the bosonic field $\vec{\varphi}$ at roughly every 10th measurement sweep. In this way various fermionic observables can be implemented and evaluated after having run the simulations. While this requires to recompute the Green's function for each sample, that is much faster than rerunning the simulations. This has also eased collaboration, allowing to use Y. Schattner's code for the evaluation of imaginary-time displaced fermionic correlation functions on data obtained in replica exchange DQMC simulations. While this procedure entails high storage requirements, they are manageable (~ 20 TB from those simulations that were run for the data presented in this thesis).

We discuss two aspects related to data analysis in more detail: The multiple histogram reweighting method to combine data obtained at different values of the tuning parameter r in an statistically optimized way in Sec. 5.5.1 and how to efficiently evaluate momentum and frequency resolved correlation functions in Sec. 5.5.2.

5.5.1 Multiple histogram reweighting

The structure of the action (4.75) of the SDW model introduced in Sec. 4.3, where the dependence on the tuning parameter r is fully contained in the bosonic part S_φ , allows to easily relate the grand canonical probability distribution of a configuration $\vec{\varphi}$ at a value r , $p_r[\vec{\varphi}]$, to the distribution at another value r' : $p_{r'}[\vec{\varphi}] \propto e^{-(r'-r)E(\vec{\varphi})} p_r(\vec{\varphi})$, where $E(\vec{\varphi}) = \frac{\Delta\tau}{2} \sum_{\ell,i} \vec{\varphi}_i(\ell)^2$. From this relation one finds an expression for the expectation value of an observable \mathcal{O} at r' in terms of expectation values at r , which in turn can be estimated by time series averages from a Monte Carlo simulation carried out at r :

$$\langle \mathcal{O} \rangle_{r'} = \frac{\langle \mathcal{O} e^{-(r'-r)E} \rangle_r}{\langle e^{-(r'-r)E} \rangle_r} \approx \frac{\sum_n \mathcal{O}_n e^{-(r'-r)E_n}}{\sum_n e^{-(r'-r)E_n}}, \quad (5.102)$$

where n goes over the series of measured samples and \mathcal{O}_n and E_n are computed from the same system configuration. This **reweighting** procedure [165] is effective over quite a wide range around r , see Fig. 5.16a.

In our replica exchange simulations we obtain Monte Carlo data for multiple close values of r . Building on the observation (5.102), we can use the combined information from these time series for r_κ , $\kappa = 1, \dots, K$, to obtain improved observable

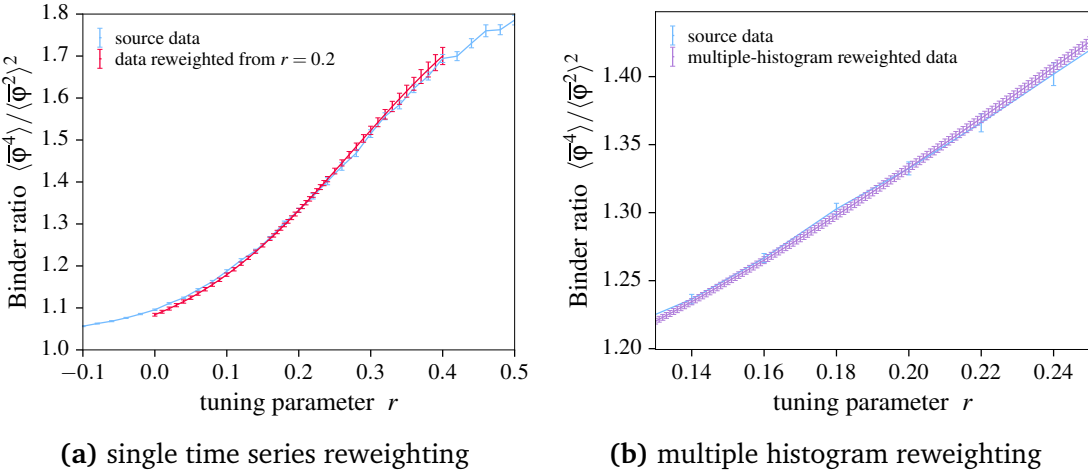


Figure 5.16: DQMC data for the ratio $\langle \bar{\varphi}^4 \rangle / \langle \bar{\varphi}^2 \rangle^2$ related to the Binder parameter of $\bar{\varphi} = \frac{\Delta\tau}{\beta N_\kappa} \left| \sum_{i,\ell} \vec{\varphi}_i(\ell) \right|$ for the O(2) model at $L = 6 = \beta$. (a) Comparison to data reweighted from a single time series at $r = 0.2$, (b) comparison to multiple-histogram reweighted data, incorporating all time series [zoomed in]. In each case error bars have been estimated by performing the entire analysis on jackknife blocked time series.

estimates at $r_1 \leq r \leq r_K$ using the technique of **multiple histogram reweighting** [166, 167].⁶ To do so we write the expectation value as

$$\begin{aligned} \langle \mathcal{O} \rangle_r &= \frac{\int dE \Omega(E) e^{-rE} \mathcal{O}(E)}{\int dE \Omega(E) e^{-rE}} \quad \text{with} \\ \mathcal{O}(E) &= \frac{\int D\vec{\varphi} \delta(E[\vec{\varphi}] - E) \mathcal{O}[\vec{\varphi}]}{\int D\vec{\varphi} \delta(E[\vec{\varphi}] - E)}, \end{aligned} \quad (5.103)$$

where all non- r -dependent parts of the action are contained in the density of states $\Omega(E)$. We discretize E into levels E_a spaced ΔE apart and search the optimal estimator for $\Omega(E_a)$, which reads

$$\hat{\Omega}_a = \frac{\sum_\kappa H_{a\kappa} [g_{a\kappa} (1 - \Delta E \hat{\Omega}_a e^{-r_\kappa E_a + f_\kappa})]^{-1}}{\sum_\kappa M_\kappa \Delta E e^{-r_\kappa E_a + f_\kappa} [g_{a\kappa} (1 - \Delta E \hat{\Omega}_a e^{-r_\kappa E_a + f_\kappa})]^{-1}}. \quad (5.104)$$

Here $H_{a\kappa}$ is the count of samples with $E \in [E_a, E_a + \Delta E]$ in the time series with $r = r_\kappa$, $g_{a\kappa}$ is a statistical inefficiency factor related to the integrated autocorrelation

⁶A detailed discussion of the multiple histogram reweighting method is also given in the author's diploma thesis [152].

time of the indicator function for this count, M_κ is the total number of samples for r_κ , and $f_\kappa = -\ln Z(r_\kappa)$ is given by

$$f_\kappa = -\ln \sum_a \hat{\Omega}_a \Delta E e^{-r_\kappa E_a}. \quad (5.105)$$

Empirically, we find it adequate to set $g_{ak} \equiv 1$. Iteration of Eqs. (5.104) and (5.105) yields a converged estimate of $\hat{\Omega}_a$ and following Eq. (5.103) we compute the estimate of $\langle O \rangle_r$ as a weighted average of the time series of O for the different r_κ :

$$\hat{O}(r) = \frac{\sum_{\kappa=1}^K \sum_{n=1}^{M_\kappa} O_{\kappa n} w_{\kappa n}(r)}{\sum_{\kappa=1}^K \sum_{n=1}^{M_\kappa} w_{\kappa n}(r)} \quad (5.106)$$

with weights

$$w_{\kappa n}(r) = \sum_a \frac{\chi_{a\kappa n} \hat{\Omega}_a e^{-r E_a}}{\sum_\kappa H_{a\kappa}}, \quad (5.107)$$

where $\chi_{a\kappa n}$ is the indicator function for $E \in [E_a, E_a + \Delta E]$ evaluated at the n -th sample of the time series for r_κ .

The multiple histogram reweighting method allows us to finely interpolate between the original values r_κ of our simulations. In addition it provides a reduction of statistical error bars in the reweighted estimates compared to averages from single time series, see Fig. 5.16b. In this work we have used the method for bosonic observables related to the magnetic transition, although it can be extended directly to all fermionic observables.

5.5.2 Correlation functions via fast Fourier transform (FFT)

Momentum and Matsubara frequency resolved correlation functions can be computed efficiently from real space and imaginary time data, when a routine for fast Fourier transform (FFT, implemented for instance in FFTW [168]) is applied [90, Sec. 3.6]. From a bosonic configuration $\vec{\varphi}_i(\tau)$ we can compute the frequency and momentum

resolved SDW susceptibility as follows:

$$\begin{aligned}
 \chi(\mathbf{q}, i\omega_n) &= \frac{1}{N_s \beta} \sum_{i,j} \int \int_0^\beta d\tau_1 d\tau_2 e^{i\omega_n(\tau_1 - \tau_2) - i\mathbf{q} \cdot (\mathbf{r}_i - \mathbf{r}_j)} \langle \vec{\varphi}_i(\tau_1) \vec{\varphi}_j(\tau_2) \rangle \\
 &= N_s \beta \left\langle \frac{\Delta\tau}{N_s \beta} \sum_{i,\ell_1} e^{i\omega_n \ell_1 \Delta\tau - i\mathbf{q} \cdot \mathbf{r}_i} \vec{\varphi}_i(\ell_1 \Delta\tau) \cdot \frac{\Delta\tau}{N_s \beta} \sum_{j,\ell_2} e^{-i\omega_n \ell_2 \Delta\tau + i\mathbf{q} \cdot \mathbf{r}_j} \vec{\varphi}_j(\ell_2 \Delta\tau) \right\rangle \\
 &= N_s \beta \left\langle \sum_{n=1}^N |\tilde{\varphi}^n(\mathbf{k}, \omega_n)|^2 \right\rangle.
 \end{aligned} \tag{5.108}$$

Here $\tilde{\varphi}^n(\mathbf{k}, \omega_n)$ is the Fourier transform in imaginary time and space of the n th components of the bosonic configuration $\vec{\varphi}_i(\tau)$, which can be computed quickly by FFT.

Part III

Numerical results

6 Phase diagrams and competing orders

Having presented the numerical methods applied for the DQMC simulations of this thesis, we now turn to discussing the physical results obtained in this way. Here we focus on the O(2) variation of the metallic spin-density wave (SDW) model introduced in Sec. 4.3. For convenience we repeat the definition of its action (4.75)

$$S = S_F + S_{FB} + S_B = \int_0^\beta d\tau (L_F + L_{FB} + L_B) \text{ with}$$

$$\begin{aligned} L_F &= \sum_{\substack{i,j,s \\ \alpha=x,y}} \psi_{\alpha is}^\dagger [(\partial_\tau - \mu)\delta_{ij} - t_{aij}] \psi_{\alpha js}, \\ L_{FB} &= \lambda \sum_{i,s,s'} e^{i\mathbf{Q}\cdot\mathbf{r}_i} [\vec{s} \cdot \vec{\varphi}_i]_{ss'} \psi_{xis}^\dagger \psi_{yis'} + \text{h.c.}, \\ L_B &= \frac{1}{2} \sum_i \frac{1}{c^2} \left(\frac{d\vec{\varphi}_i}{d\tau} \right)^2 + \frac{1}{2} \sum_{\langle i,j \rangle} (\vec{\varphi}_i - \vec{\varphi}_j)^2 + \sum_i \left[\frac{r}{2} \vec{\varphi}_i^2 + \frac{u}{4} (\vec{\varphi}_i^2)^2 \right]. \end{aligned}$$

Here the fermions are coupled to a real bosonic vector field $\vec{\varphi}$ representing fluctuations of a commensurate SDW order parameter at wavevector $\mathbf{Q} = (\pi, \pi)^\top$. At zero temperature the parameter r tunes through a quantum phase transition (QPT) at $r = r_c$ with antiferromagnetic electronic order for $r < r_c$ and paramagnetism for $r > r_c$. We expect this transition to be continuous such that r_c marks the location of a quantum critical point (QCP).

Despite the low spatial dimension $d = 2$ the O(2) symmetry of $\vec{\varphi}$ allows a quasi-long-range ordered SDW phase to occur also at finite temperatures. Since the tendency towards this order is explicitly put into the model, we can generally expect to find such a phase at low values of r and low temperatures T . Apart from this phase, instabilities towards other types of electronic order can realize additional phases as *emergent* phenomena from the coupling to the SDW order parameter. The most prominent among these is an unconventional d -wave superconducting (SC) phase, which has long been anticipated to be formed by SDW fluctuations in the vicinity of a QCP, see Sec. 2.2.3.

In this Chapter we discuss the finite-temperature phase diagrams of the O(2) SDW model obtained in unbiased numerically exact DQMC simulations for various values of the Yukawa coupling λ and the bare bosonic velocity c . These are mainly characterized by the competition of SDW and SC quasi-long-range order, but we

also examine tendencies towards additional types of order. These data have been obtained in a collaborative effort: Y. Schattner has evaluated all fermionic observables analyzed in the following, in part from the same replica exchange simulations used to compute the bosonic SDW correlation functions and in part from additional grand canonical DQMC simulations.

This Chapter contains the following sections: In Sec. 6.1 we describe how a finite-temperature SDW transition is identified in the O(2) model. Sec. 6.2 describes the phase diagram for the $\lambda = 1, c = 1$ model obtained in this way. In Sec. 6.3 we focus on the identification of the transition into a superconducting phase. The rich phase diagram of the $\lambda = 3, c = 2$ model is then discussed in Sec. 6.4. In Sec. 6.5 we focus on the phase diagrams for additional parameter sets: $\lambda = 1, 1.5, 2$ with $c = 3$, and we show a general trend for the dependence of the maximum superconducting T_c . The results of this Chapter are discussed in Sec. 6.6.

6.1 Analysis of the spin-density wave (SDW) transition

As stated by the Mermin-Wagner theorem [17] the metallic O(2) SDW model on a two-dimensional lattice cannot show magnetic long-range order at any $T > 0$. Nevertheless, a finite-temperature phase transition of the Berezinskii-Kosterlitz-Thouless (BKT) type [137–139] is not precluded in this O(2)-symmetric model.

From the SDW order parameter $\vec{\varphi}$ we define a local magnetization density $\vec{m}_i = \frac{1}{\beta} \int_0^\beta d\tau \vec{\varphi}_i(\tau)$ and the total magnetization density $\vec{m} = \frac{1}{L^2} \sum_i \vec{m}_i$. In the thermodynamic limit of our model, $N_s \rightarrow \infty$, the expectation value $\langle |\vec{m}| \rangle$ vanishes at any $T > 0$. Below a transition temperature T_{SDW} there is quasi-long-range order with $\langle |\vec{m}| \rangle(L) \neq 0$ only for finite systems.

When approaching the BKT temperature T_{SDW} from above, the magnetic correlation length ξ diverges exponentially

$$\xi \sim \exp(b(T - T_{\text{SDW}})^{-\nu}), \quad T \rightarrow T_{\text{SDW}}^+, \quad (6.1)$$

with an exponent $\nu = 1/2$ and ξ stays infinite for all $T \leq T_{\text{SDW}}$. Hence, the entire low-temperature BKT phase is critical. Spatial correlation functions of local magnetization fluctuations decay exponentially above T_{SDW} and with a power law below T_{SDW} :

$$\langle \vec{m}_i \cdot \vec{m}_{i+\mathbf{x}} \rangle \sim \begin{cases} e^{-|\mathbf{x}|/\xi}, & T > T_{\text{SDW}}, \\ |\mathbf{x}|^{-\eta(T)}, & T \leq T_{\text{SDW}}. \end{cases} \quad (6.2)$$

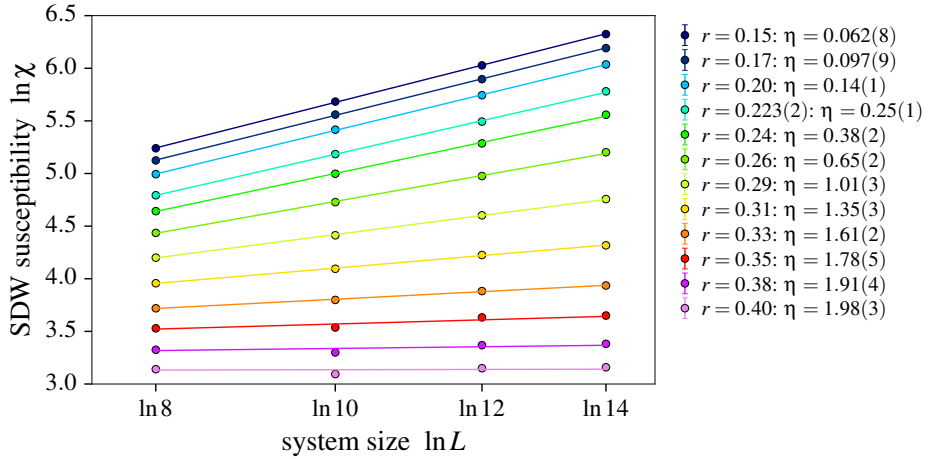


Figure 6.1: System size dependence of the SDW susceptibility χ in the $O(2)$ model with $\lambda = 1 = c$ at $\beta = 1/T = 14$ for various values of the tuning parameter r . Lines show best fits of $\chi \sim L^{2-\eta}$ with $\eta < 1/4$ inside the SDW phase and $\eta = 1/4$ identifying the BKT transition.

Here the critical exponent η depends on temperature and takes on a *universal* value of $\eta(T_{\text{SDW}}) = \eta_c \equiv 1/4$ at the BKT transition.

To identify T_{SDW} from our numerical data we follow the procedure suggested in Refs. [169, 170]. We study the finite-size scaling of the spin-density wave susceptibility for order at wavevector \mathbf{Q} , which is given by

$$\chi = \beta \sum_i \langle \vec{m}_i \cdot \vec{m}_0 \rangle = \int_0^\beta d\tau \sum_i \langle \vec{\varphi}_i(\tau) \vec{\varphi}_0(0) \rangle = \beta L^2 \langle \vec{m}^2 \rangle. \quad (6.3)$$

From Eq. (6.2) we expect a finite-size scaling behavior like

$$\begin{aligned} \chi &= \beta \sum_i \langle \vec{m}_i \cdot \vec{m}_0 \rangle \sim \beta \sum_i |\mathbf{r}_i|^{-\eta(T)} \sim \beta \int_{L^2} d^2r |\mathbf{r}|^{-\eta(T)} \\ &= \beta \int_0^{2\pi} d\theta \int_0^L dr r^{1-\eta(T)} \sim \beta L^{2-\eta(T)} \end{aligned} \quad (6.4)$$

for $T \leq T_{\text{SDW}}$ and for slightly higher temperatures, where ξ still exceeds L . While this scaling law can only be expected to hold perfectly for large system sizes, we find the numerical data on the limited range of L available to us to be mostly well consistent with this power law, see Fig. 6.1 for an illustration.

The multiple-histogram reweighting method provides data to us with very high

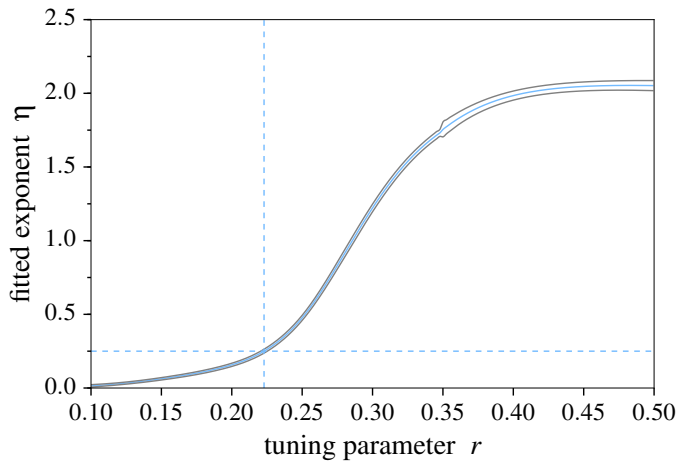


Figure 6.2: Fitted exponent η as a function of the tuning parameter r for the scaling law of the SDW susceptibility $\chi \sim L^{2-\eta}$, here shown for $\lambda = 1 = c$ at $\beta = 1/T = 14$. From this data $r_{\text{SDW}} = 0.223(2)$ is identified by the universal value $\eta_c = 0.25$ (dashed lines). The statistical error of η is larger for $r \gtrsim 0.35$ than at lower values because data sets from two separate replica exchange simulations have been combined in this figure.

resolution in the tuning parameter r . We scan over r for a constant temperature T and fit the relation $\ln \chi = \alpha + (2 - \eta(r)) \ln L$ at each point to determine $\eta(r)$. Here we identify points (r, T) in the phase diagram where this fit to our data is successful with $\eta \leq 1/4$ as belonging to the quasi-long-range ordered SDW phase. We search for $\eta(r_{\text{SDW}}) = 1/4$ to pinpoint the location of the BKT transition at this temperature $T = T_{\text{SDW}}$ as visualized in Fig. 6.2. This estimate for r_{SDW} coincides approximately with the intersection point of the scaled SDW susceptibility $\chi/L^{2-\eta_c}$ for different L . This is shown in Fig. 6.3 for the data set of Sec. 6.4.

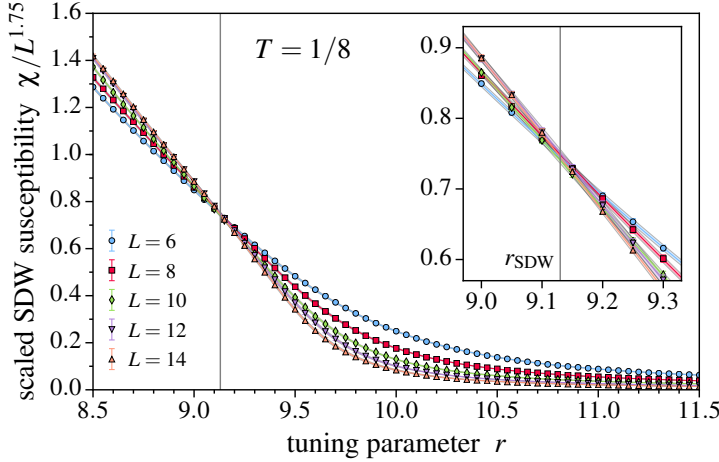


Figure 6.3: Scaled SDW susceptibility $\chi/L^{2-\eta_c}$ with $\eta_c = 1/4$ for $T = 1/8$ and various system sizes, here shown for $\lambda = 3$, $c = 2$. The vertical line marks r_{SDW} as estimated from fitting $\chi \sim L^{2-\eta}$ with $\eta = \eta_c$. Symbols with error bars are estimates from single- r data. Continuous lines with surrounding error regions are results of the multiple-histogram reweighting analysis. The inset shows an enlarged view of the region around the intersection.

6.2 Phase diagram for $\lambda = 1 = c$

By performing the η -fit procedure for a range of temperatures $1/30 \leq T \leq 2$ we have obtained the $\lambda = 1$, $c = 1$ phase diagram displayed in Fig. 6.4. Here we show the BKT transition temperature T_{SDW} in dependence of the tuning parameter r . The transition line separates a quasi-long-range ordered SDW phase at low T and low r from the paramagnetic phase. Interestingly, this line is essentially straight at high temperatures, but at $T \approx 1/8$ we observe a deviation with $T_{\text{SDW}}(r)$ bending down from the extrapolated straight line. A quantum phase transition can be anticipated to lie in the range $0.2 < r_c < 0.3$, while a continuation of the linear behavior at high temperatures would yield $\tilde{r}_c \approx 0.4$.

At this low value of the Yukawa coupling λ the influence of the SDW order parameter on the fermions is rather weak. The temperatures accessed by us apparently are not low enough to tune sufficiently close to the anticipated QCP to observe strong features. For instance no signs of superconductivity can be seen. Since the computational cost of going to lower temperatures is high, we focus on other parameter regimes in the following. Firstly, we enhance the Yukawa coupling λ . Secondly, we also adjust the bare bosonic velocity c to larger values. This tunes the model further away from the purely bosonic φ^4 quantum field theory (decoupled from the fermions, $c = \infty$ would correspond to a classical model). By taking into account

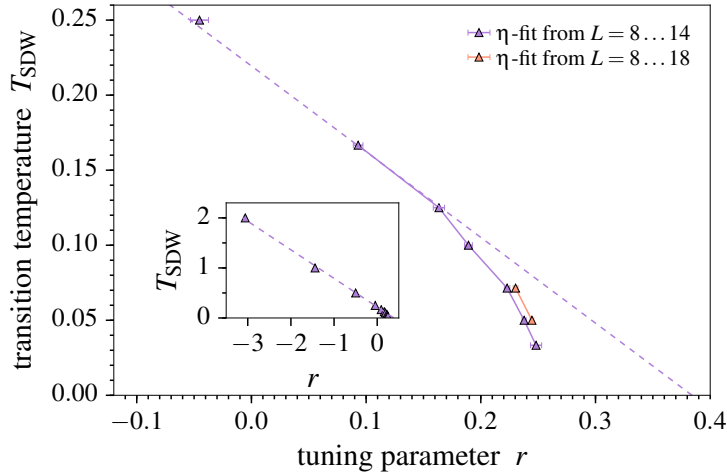


Figure 6.4: Phase diagram for $\lambda = 1 = c$. Shown is the BKT transition temperature T_{SDW} , estimated by a fit of $\chi \sim L^{2-\eta}$, as a function of the tuning parameter r . Fits generally considered a range of system sizes $L = 8, \dots, 14$, with a complementary wider range $L = 8, \dots, 18$ used for two data points. The inset shows data on a large temperature scale. The dashed line is a linear fit to $T_{\text{SDW}}(r)$ at high T . Continuous lines are guides to the eye.

multiple parameter sets we also avoid accidentally focusing on a single special point, while we seek to understand *universal* phenomena.

6.3 Identification of the superconducting transition

In this Section, before discussing in detail the rich phase diagram of the $\lambda = 3$, $c = 2$ SDW model in Sec. 6.4, we outline how to identify the transition into a superconducting phase from numerical data.

Our starting point is that a superconducting state can be characterized by the current response to a vector potential \mathbf{A} . Here we follow Scalapino et al. [171, 172]. The kinetic part of the action in absence of \mathbf{A} reads

$$\underline{\psi}^\dagger K \underline{\psi} = - \sum_{\substack{\alpha, s, \\ \langle i, j \rangle}} t_{ij}^{\alpha s} (\psi_{ias}^\dagger \psi_{jas} + \psi_{jas}^\dagger \psi_{ias}). \quad (6.5)$$

A vector field $\mathbf{A}(\mathbf{r}_l, t) = (A_1(\mathbf{r}_l, t), 0, 0)^\top$ is implemented via Peirls phase factors

$$\psi_{\alpha, l+\mathbf{e}_1, s}^\dagger \psi_{\alpha, l, s} \rightarrow e^{ieA_1(\mathbf{r}_l)} \psi_{\alpha, l+\mathbf{e}_1, s}^\dagger \psi_{\alpha, l, s} \quad (6.6)$$

with the electronic charge e . Inserting these into Eq. (6.5) and expanding to order A^2 yields

$$\underline{\psi}^\dagger K_A \underline{\psi} = \underline{\psi}^\dagger K \underline{\psi} - \sum_l \left[eA_1(\mathbf{r}_l) i \underbrace{\sum_{\alpha,s} t_l^{\alpha s} (\psi_{\alpha,l+\mathbf{e}_1,s}^\dagger \psi_{\alpha,l,s} - \psi_{\alpha,l,s}^\dagger \psi_{\alpha,l+\mathbf{e}_1,s})}_{j_1^P(\mathbf{r}_l)} + \frac{1}{2} e^2 A_1^2(\mathbf{r}_l) \underbrace{\sum_{\alpha,s} (-t_l^{\alpha s}) (\psi_{\alpha,l+\mathbf{e}_1,s}^\dagger \psi_{\alpha,l,s} + \psi_{\alpha,l,s}^\dagger \psi_{\alpha,l+\mathbf{e}_1,s})}_{k_1(\mathbf{r}_l)} \right] \quad (6.7)$$

with the first component of the paramagnetic current density $e j_1^P(\mathbf{r}_l)$ and the kinetic energy density $k_1(\mathbf{r}_l)$ associated to \mathbf{e}_1 -oriented bonds. The total current density is obtained from

$$j_1(\mathbf{r}_l) = -\frac{\delta K}{\delta A_1(\mathbf{r}_l)} = e j_1^P(\mathbf{r}_l) + e^2 k_1(\mathbf{r}_l) A_1(\mathbf{r}_l). \quad (6.8)$$

For a plane wave vector potential $A_1(\mathbf{r}_l, t) = \text{Re}[A_1(\mathbf{q}, \omega)e^{i\mathbf{q}\cdot\mathbf{r}_l-i\omega t}]$ the linear current response $\langle j_1(\mathbf{r}_l, t) \rangle = \text{Re}[\langle j_1(\mathbf{q}, \omega) \rangle e^{i\mathbf{q}\cdot\mathbf{r}_l-i\omega t}]$ is given by the Kubo formula

$$\langle j_1(\mathbf{q}, \omega) \rangle = -[e^2 (\langle -k_1 \rangle - \Lambda_{11}(\mathbf{q}, \omega)) A_1(\mathbf{q}, \omega)]. \quad (6.9)$$

Here the real-frequency current-current correlator $\Lambda_{11}(\mathbf{q}, \omega)$ can be retrieved by analytic continuation, $i\omega_n \rightarrow \omega + i0^+$, from the Matsubara-frequency resolved correlator

$$\Lambda_{11}(\mathbf{q}, i\omega_n) = \frac{1}{N_s} \int_0^\beta d\tau e^{i\omega_n \tau} \langle j_1^P(\mathbf{q}, \tau) j_1^P(-\mathbf{q}, 0) \rangle, \quad (6.10)$$

which can be directly accessed in DQMC simulations. For our applications the static $\omega = 0$ correlator is sufficient at this point.

The Meissner effect in a superconductor follows from London's equations, i.e. when the current-density response in a transverse ($\mathbf{q} \cdot \mathbf{A} = 0$), static and long-wavelength ($q_2 \rightarrow 0$) vector potential [173] is given by

$$j_1(q_2) = \frac{1}{4\pi} \frac{1}{\lambda^2} A_1(q_2), \quad (6.11)$$

which causes the magnetic field to be expelled exponentially with a penetration

depth $\lambda = \sqrt{\frac{m}{4\pi\rho_s e^2}}$ with the **superfluid density** ρ_s and the electron mass m . For a general static long-wavelength vector potential \mathbf{A} we have

$$\langle j_1(\mathbf{q}) \rangle = f(\mathbf{q}) \left[\delta_{ij} - \frac{q_i q_j}{\mathbf{q}^2} \right] A_j(\mathbf{q}) \quad (6.12)$$

and in a superconductor we find

$$\frac{-f(\mathbf{q} \rightarrow 0)}{e^2} = \frac{\rho_s}{m} \equiv \frac{D_s}{4\pi e^2}, \quad (6.13)$$

where we have introduced the **superfluid weight** D_s . Combining Eqs. (6.9), (6.12), and (6.13) we have

$$\frac{D_s}{4\pi e^2} = \frac{1}{4} [\langle -k_1 \rangle - \Lambda^T], \quad (6.14a)$$

$$0 = \frac{1}{4} [\langle -k_1 \rangle - \Lambda^L] \quad (6.14b)$$

with the limiting longitudinal and transverse responses

$$\Lambda^L = \Lambda_{11}(q_1 \rightarrow 0, q_2 = 0, i\omega_m = 0), \quad (6.15a)$$

$$\Lambda^T = \Lambda_{11}(q_1 = 0, q_2 \rightarrow 0, i\omega_m = 0). \quad (6.15b)$$

Setting $m = 1$, we obtain a combined expression for the superfluid density

$$\rho_s = \frac{1}{4} [\Lambda^L - \Lambda^T], \quad (6.16)$$

which is non-zero if $\Lambda_{11}(\mathbf{q}, i\omega_m = 0)$ has different limits depending on the order of q_1 and q_2 approaching zero. That is the case for long-range paramagnetic current-current correlations in a superconductor. Note that in principle similar relations can be derived to access the Drude weight and compute conductivity and resistivity, which, however, may require an explicit analytic continuation [171, 172].

The finite-temperature transition into the superconducting phase is expected to be of BKT character. At a BKT transition a universal relation involving a jump of the superfluid density holds [174]. In the thermodynamic limit, ρ_s is zero right above the critical temperature T_c and just below T_c it takes on a value $\Delta\rho_s$ related to T_c by the universal relation

$$T_c = \frac{\pi}{2} \Delta\rho_s. \quad (6.17)$$

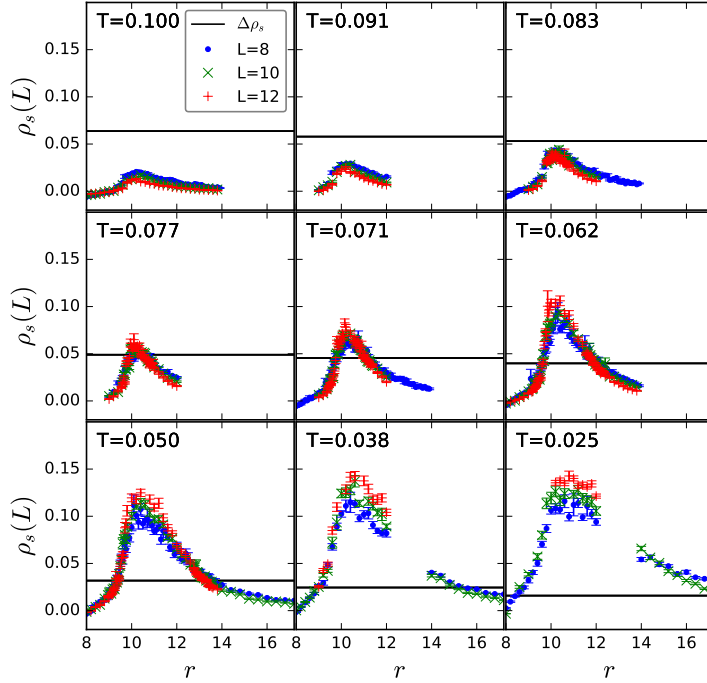


Figure 6.5: Finite-size superfluid density $\rho_s(L)$ for $L = 8, 10, 12$ at various temperatures T across the phase diagram of the $\lambda = 3, c = 2$ model. The universal value $\Delta\rho = 2T/\pi$ at the BKT transition is indicated by a horizontal solid line in each panel. In the three top row panels the system is never superconducting.

We follow Paiva et al. [175] to estimate T_c from our DQMC data making use of this universal jump. On finite systems we cannot directly take the momentum limits in Eq. (6.15a). Instead we define

$$\Lambda^L(L) = \Lambda_{11}(q_1 = 2\pi/L, q_2 = 0, i\omega_m = 0), \quad (6.18a)$$

$$\Lambda^T(L) = \Lambda_{11}(q_1 = 0, q_2 = 2\pi/L, i\omega_m = 0), \quad (6.18b)$$

where the limits for q_1 and q_2 are replaced by the smallest finite momenta for that system size. In the limit $L \rightarrow \infty$ we retain $\Lambda^L(L) \rightarrow \Lambda^L$ and $\Lambda^T(L) \rightarrow \Lambda^T$. A **finite-size superfluid density** can then be defined by

$$\rho_s(L) = \frac{1}{4} [\Lambda^L(L) - \Lambda^T(L)] \quad (6.19)$$

and $\rho_s(L) \rightarrow \rho_s$ for $L \rightarrow \infty$. Our strategy to find the boundaries of a superconducting phase is to scan over all values of the tuning parameter r at constant temperature

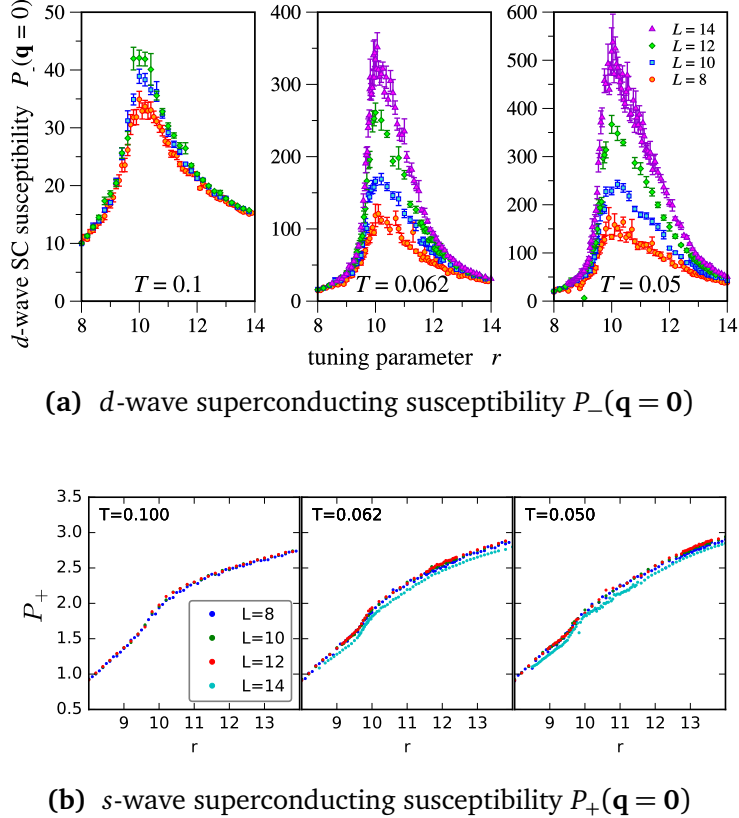


Figure 6.6: Superconducting susceptibility for order parameters of (a) d -wave symmetry, $P_-(\mathbf{q} = \mathbf{0})$, and (b) s -wave symmetry, $P_+(\mathbf{q} = \mathbf{0})$, across the phase diagram of the $\lambda = 3$, $c = 2$ SDW model.

and to identify those points where $\rho_s(L) > \Delta\rho_s$ as part of the superconducting phase. There is a slight size dependence, which constitutes the major source of error in determining the superconducting T_c . The behavior of $\rho_s(L)$ is shown for the $\lambda = 3$, $c = 2$ model in Fig. 6.5. This method of finding T_c has the advantage of not relying on a particular symmetry of the superconducting order parameter.

In a complementary approach we study the uniform **pairing susceptibilities**

$$P_\zeta(\mathbf{q} = \mathbf{0}) = \int_0^\beta d\tau \sum_i \langle \Delta_\zeta^\dagger(\mathbf{r}_i, \tau) \Delta_\zeta(\mathbf{0}, \tau) \rangle \quad \text{with} \quad (6.20a)$$

$$\Delta_\zeta = 2 \left(\psi_{xi\uparrow}^\dagger \psi_{xi\downarrow}^\dagger + \zeta \psi_{yi\uparrow}^\dagger \psi_{yi\downarrow}^\dagger \right) \quad (6.20b)$$

for the two signs $\zeta = \pm$. The positive sign corresponds to s -wave symmetry with Δ_+ not changing sign under a $\pi/2$ lattice rotation, which transforms between the x

and y fermion bands. Under the same rotation Δ_- changes sign, corresponding to d -wave symmetry. Similarly to the SDW transition discussed in Sec. 6.1, close to the superconducting BKT transition the appropriate pairing susceptibility scales as $L^{2-\eta}$ with continuously varying η , which takes on a value of $\eta = 0.25$ at T_c . Without performing a detailed analysis, it is evident from the data shown in Fig. 6.6 that the superconducting phase of the SDW model has d -wave symmetry, rather than s -wave symmetry. Inside the superconducting phase $P_-(\mathbf{q} = \mathbf{0})$ increases rapidly with system size, while $P_+(\mathbf{q} = \mathbf{0})$ is of much smaller magnitude and virtually independent of system size.

6.4 Phase diagram for $\lambda = 3, c = 2$

Using the techniques of Secs. 6.1 and 6.3 we have computed the finite-temperature phase diagram of the $\lambda = 3, c = 2$, O(2) SDW model displayed in Fig. 6.7. There is a quasi-long-range ordered SDW phase with a transition temperature T_{SDW} that decreases with increasing r . A magnetic quantum phase transition can be anticipated where T_{SDW} approaches zero. In the vicinity of this point we find a dome-shaped phase with quasi-long-range d -wave superconducting order. The superconducting T_c reaches a maximum of $T_c^{\max} \approx 0.08$ at $r_{\text{opt}} \approx 10.2$. In these units the Fermi energy is $E_F = 2.5 \approx 30T_c^{\max}$. Both quasi-long-range ordered phases coexist in an intermediate region. We focus on this region, where BKT scaling may no longer hold for the SDW transition, in Subsec. 6.4.1 below.

A prominent feature of the phase diagram is how the SDW phase boundary line $T_{\text{SDW}}(r)$ bends downwards. We have already seen before in the $\lambda = 1, c = 1$ phase diagram that this transition line departs from a straight line at a low temperature $T \approx 0.12$, but in the $\lambda = 3, c = 2$ case this deviation starts at a lower temperature $T \approx 0.08$, which approximately matches T_c^{\max} of the superconducting transition, and T_{SDW} as a function of r is almost vertical from a point slightly above the crossing of the superconducting dome. This bending is also shadowed in the SDW susceptibility χ over a wide range of the tuning parameter r on the magnetically disordered side of the phase diagram, see Fig. 6.8a. For fixed r the susceptibility χ is non-monotonic in temperature with a maximum close to T_c , see Fig. 6.8b.

The non-interacting ($\lambda = 0$) variation of our two-band fermion model has a orbital magnetic susceptibility, that is paramagnetic in sign. Likewise, the high-temperature magnetic response of the interacting $\lambda = 3, c = 2$ model is paramagnetic. However, in a temperature regime starting already above T_c we find the orbital magnetic susceptibility to be diamagnetic. The temperature T_{dia} where the orbital susceptibility changes sign is approximately proportional to the superconducting

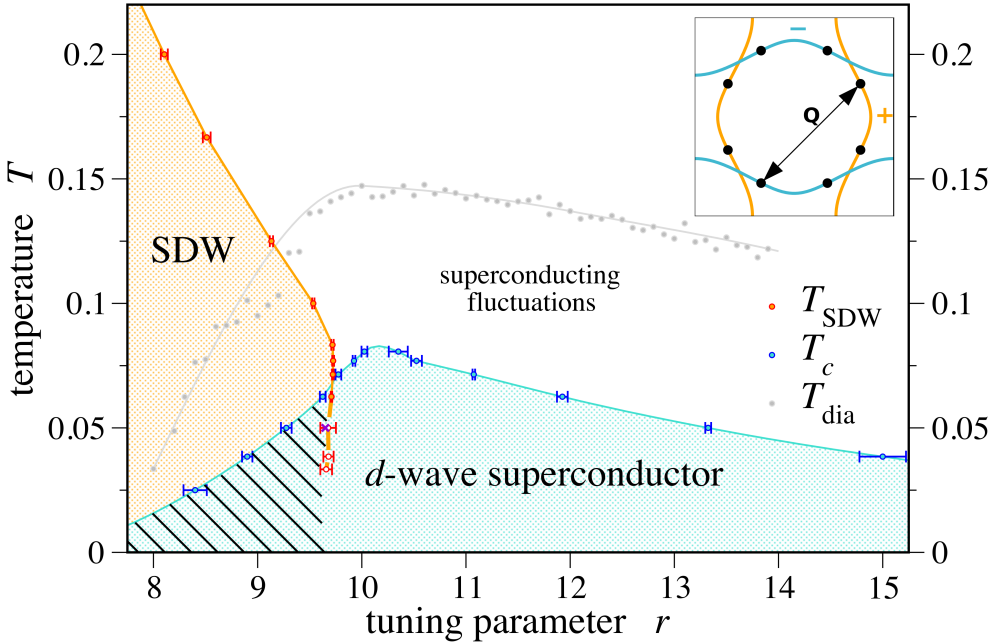


Figure 6.7: Finite-temperature phase diagram for $\lambda = 3$, $c = 2$ showing the transition temperature T_{SDW} to magnetic spin-density wave (SDW) quasi-long-range order, the superconducting (SC) T_c , and the onset of diamagnetism at T_{dia} . Lines are guides to the eye. Where they are solid, the transition is of the Berezinskii-Kosterlitz-Thouless type. Inside the SC dome the SDW transition is possibly weakly first order, indicated by a dashed line. The diagonally hatched region features coexistence between SDW and SC quasi-long-range orders. In the inset we show the non-interacting Fermi surfaces with the colors indicating the sign of the SC order parameter.

transition temperature, $T_{\text{dia}} \propto T_c$, in a wide region of the phase diagram in Fig. 6.7. Its maximum is $T_{\text{dia}}^{\max} \approx 0.15 \approx 2T_c^{\max}$.

It would be very interesting to evaluate the single-particle density of states $N(\omega, T)$, but this would require an analytic continuation from our DQMC data at imaginary times. However, we can use the relation [176]

$$\tilde{N}(T) = \frac{1}{\pi L^2 T} \text{Tr } G_\varphi(\tau = \beta/2, 0) = \int_{-\infty}^{\infty} \frac{d\omega}{2\pi T \text{ch}(\beta\omega/2)} N(\omega, T) \quad (6.21)$$

to extract information about the low-energy density of states from the imaginary-time displaced single-particle Green's function G_φ . Since $\tilde{N}(T \rightarrow 0) = N(\omega = 0, T = 0)$, this **integrated density of states** is closely related to the ground state density of states at low temperatures. $\tilde{N}(T)$ is shown in Fig. 6.9. It displays a reduction slightly above the magnetic transition temperature T_{SDW} (see panels (a) and (b) in Fig. 6.9),

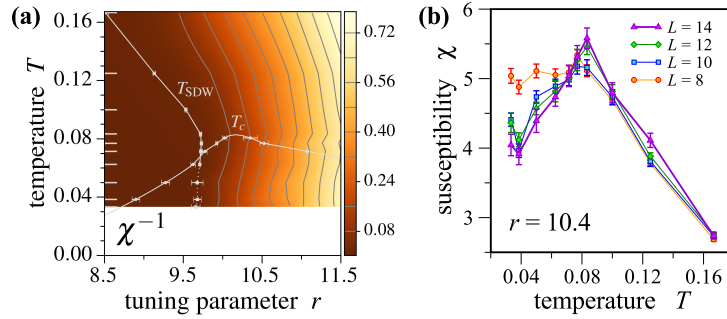


Figure 6.8: (a) Inverse SDW susceptibility χ^{-1} across the $\lambda = 3, c = 2$ phase diagram. Contour lines of χ^{-1} are indicated gray. Here we show data obtained at $L = 14$ at those temperatures indicated by ticks on the left hand inside of the panel. In between those temperatures the data is interpolated linearly. The resolution in the tuning parameter is very high thanks to multiple-histogram reweighting. (b) SDW susceptibility χ as a function of temperature near the maximum of the superconducting dome for various system sizes L .

which is consistent with a partial gapping of the Fermi surface triggered by the onset of SDW fluctuations. Similarly, a second decrease of $\tilde{N}(T)$ sets in already above the superconducting T_c (see panels (b), (c), and (d) in Fig. 6.9). A low-temperature extrapolation of $\tilde{N}(T)$ suggests to reach zero already at finite temperature, see for instance Fig. 6.9c. This indicates that the superconducting state is fully gapped. Hence the superconducting order parameter is nodeless despite its d -wave symmetry. This is allowed by the two-band structure of the SDW model, see the inset of Fig. 6.7.

We interpret the onset of diamagnetism and the gapping of the Fermi surface above T_c as signatures of a regime of substantial finite-range superconducting fluctuations as labeled in the phase diagram of Fig. 6.7.

In Fig. 6.10 we show the finite-size superfluid density $\rho_s(L)$ at a low temperature across the superconducting dome. Notably, it depends only weakly on the tuning parameter r and no minimum is apparent inside the superconducting phase.

In addition to the quantities discussed so far we have evaluated charge-density wave (CDW), pair-density wave (PDW), and bond-density wave (BDW) susceptibilities to investigate whether there are further competing orders in this phase diagram. The results are presented in Subsec. 6.4.2 below.

6.4.1 Competition and coexistence of magnetic and superconducting order

We have already discussed two effects of the competition between SDW and superconducting orders in the $\lambda = 3, c = 2$ phase diagram: First, the phase boundaries

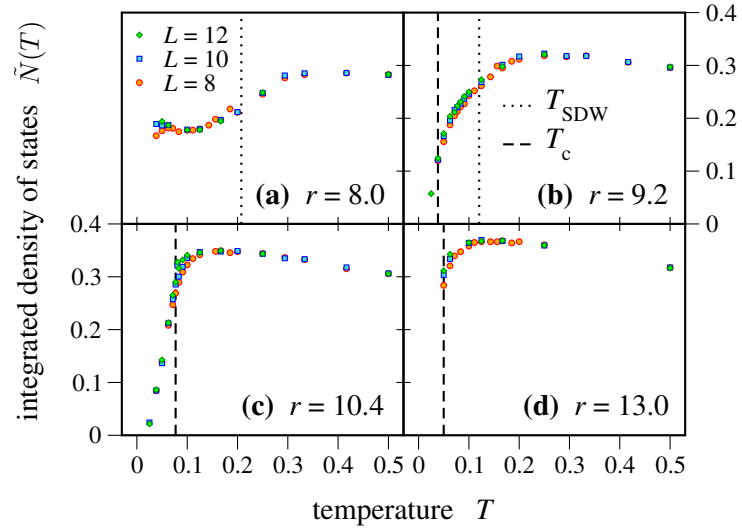


Figure 6.9: Integrated density of states $\tilde{N}(T)$ as a function of temperature for multiple values of r in the $\lambda = 3$, $c = 2$ model. The dotted lines mark the SDW transition temperature and the dashed lines mark the SC transition temperature for each panel.

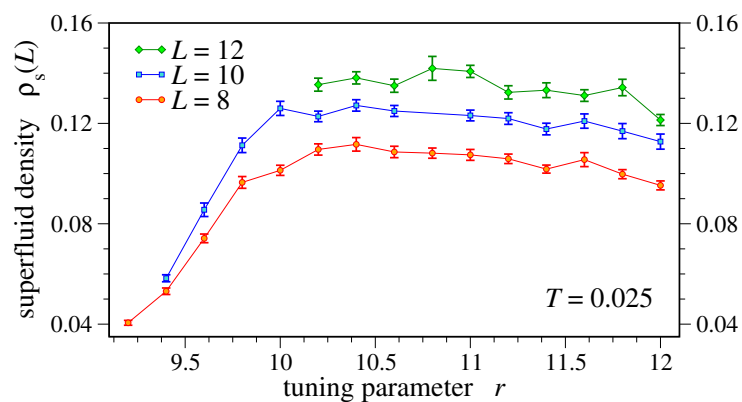


Figure 6.10: Finite-size superfluid density $\rho_s(L)$ within the superconducting phase of the $\lambda = 3$, $c = 2$ phase diagram at $T = 1/40$.

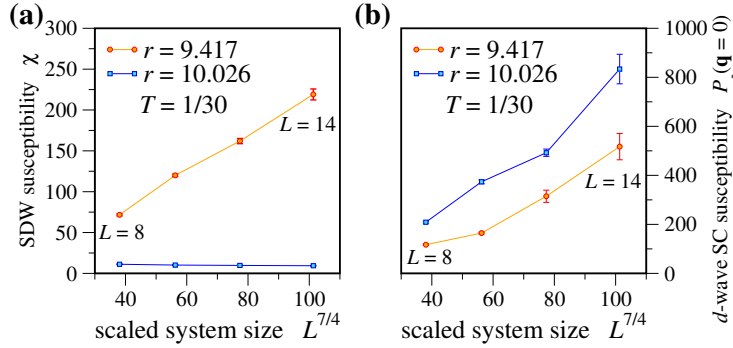


Figure 6.11: Finite-size scaling of (a) the SDW susceptibility χ and (b) the d -wave superconducting susceptibility $P_{\perp}(\mathbf{q} = \mathbf{0})$ at $T = 1/30$ in the region of phase coexistence at $r = 9.417$ and in the non-magnetic superconducting phase at $r = 10.026$ of the $\lambda = 3, c = 2$ phase diagram.

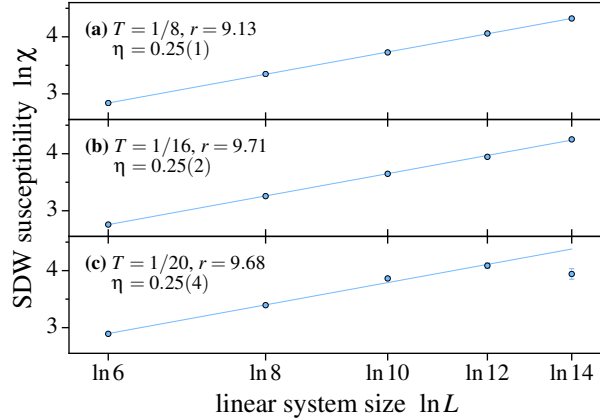


Figure 6.12: Best fits of $\ln \chi = \alpha + (2 - \eta) \ln L$ yielding $\eta = 1/4$ for the $\lambda = 3, c = 2$ model at (a) $T = 1/8$, (b) $T = 1/16$, and (c) $T = 1/20$.

apparently avoid each other by a kink-like deflection. Second, the SDW susceptibility is non-monotonic in temperature when it enters the superconducting dome.

We will now focus on the region where both quasi-long-range ordered phases overlap in Fig. 6.7. Here both the SDW and the superconducting susceptibilities grow faster than $\sim L^{7/4}$ with the system size, see Fig. 6.11. This signifies that here both types of quasi-long-range order indeed coexist since we are below the respective BKT transition temperatures, where the susceptibilities scale proportionally to $L^{7/4}$.

However, we have some reservations concerning the character of the SDW transition inside this coexistence region. As demonstrated in Fig. 6.12, at sufficiently high temperatures $T \gtrsim 0.06$ the SDW susceptibility χ is consistent with BKT theory and nicely follows the expected scaling behavior $\chi \propto L^{2-\eta}$ with a continuously varying

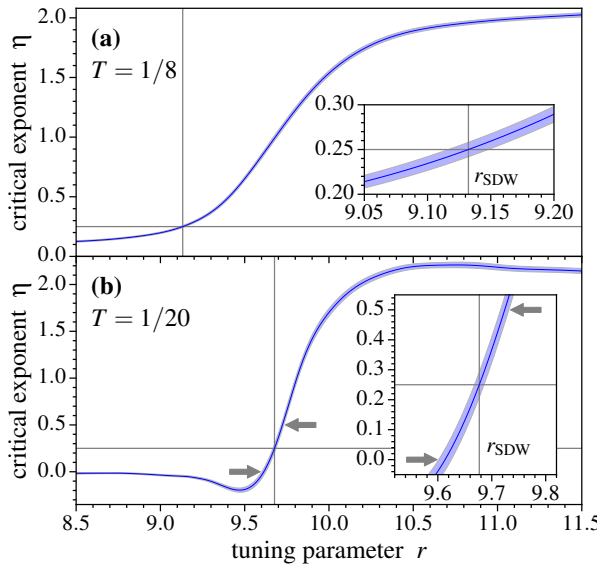


Figure 6.13: Critical exponent $\eta(r)$ estimated for the $\lambda = 3, c = 2$ model at (a) $T = 1/8$ and (b) $T = 1/20$. In each panel the continuous line shows the result of fitting $\ln \chi = \alpha + (2 - \eta) \ln L$ to the DQMC data interpolated by reweighting with a shaded surrounding region giving a statistical error estimate. The cross marks the estimate for r_{SDW} where $\eta = 1/4$. The fits that went into panel (b) are of lower quality. Here the gray arrows indicate a more conservative estimate of the error on r_{SDW} , namely that η takes on any value from $[0, 0.5]$ for r in the error interval around r_{SDW} .

exponent η allowing to identify the phase transition by the universal value $\eta_c = 0.25$. But at lower temperatures $T \lesssim 0.05$, which lie within the superconducting phase, we observe systematic deviations from this scaling behavior on the range of lattice sizes we have accessed. To account for a systematic error at these low temperatures we give a wider estimate of the error on r_{SDW} , allowing for values of $\eta \in [0, 0.5]$ (see Fig. 6.13b), while at higher temperatures we provide purely statistical error estimates computed from the variance-covariance matrix of the linear fit. A precise quantification of the systematic error in this finite-size scaling analysis would require system sizes L that are larger by orders of magnitude and hence out of computational reach. In Table 6.1 we summarize our results for $r_{SDW}(T)$ as determined from fits over five values $L = 6, \dots, 14$, which are used to plot the SDW phase boundary in Fig. 6.7, and show in comparison results for a reduced range $L = 8, \dots, 14$. In Fig. 6.7 the data points where we were not able to obtain a good fit ($T_{SDW} \leq 1/20$), are connected by bold dashed lines.

While we cannot exclude that these deviations are caused by finite-size effects, we have some indications that the magnetic transition turns weakly first-order inside the superconducting region, instead of being of BKT type. We have carried out

Table 6.1: Location of the SDW transition point r_{SDW} in the $\lambda = 3, c = 2$ phase diagram for different temperatures T as estimated by fitting the ansatz $\ln \chi_0 = \alpha + (2 - \eta) \ln L$ to the data $\ln \chi$ and searching for $\eta = 1/4$ for two ranges of system sizes $L = 6, \dots, 14$ ($n = 5$ data points) and $L = 8, \dots, 14$ ($n = 4$). $\chi^2_{\text{dof}} = \frac{1}{n-2} \sum \left[\frac{\ln \chi^{-1} - \ln \chi}{\varepsilon/\chi} \right]^2$ is a measure to help with estimating the validity of the fit, where ε is the statistical error of χ . For $T \leq 1/20$ the ansatz does not fit the data well.

1/T	$L = 6, \dots, 14$		$L = 8, \dots, 14$	
	r_{SDW}	χ^2_{dof}	r_{SDW}	χ^2_{dof}
4	7.54(3)	0.6	7.6(1)	0.3
5	8.10(3)	1.4	8.07(5)	1.6
6	8.51(4)	1.3	8.499(2)	1.1
8	9.13(2)	0.9	9.12(3)	1.4
10	9.53(1)	0.4	9.52(3)	0.5
12	9.72(1)	1.8	9.73(3)	2.5
13	9.73(1)	0.1	9.73(1)	0.1
14	9.72(1)	4.0	9.76(1)	0.3
16	9.71(1)	0.5	9.71(1)	0.6
20	9.68(8)	10.2	9.7(1)	13.6
26	9.68(5)	11.0	9.66(7)	7.8
30	9.66(6)	4.4	9.62(9)	3.7

extensive additional simulations at $T = 0.05$ for $L = 14$ for values of r in the vicinity of the magnetic phase transition. These have allowed to resolve histograms of the finite-system magnetization density $|\vec{m}|$ to sufficiently high precision to make out a shallow double-peak structure when r is tuned to an intermediate value between the magnetically quasi-long-range ordered and disordered phases, see Fig. 6.14. The location of this point is marked by a small cross in the phase diagram of Fig. 6.7. If this dip grows deeper for larger systems, this bimodal distribution can be understood as a sign of phase coexistence at a first-order transition [177]. In our DQMC simulations close to the approximate transition point we also observe noticeably longer statistical autocorrelation times at $T \leq 1/20$ than at slightly higher temperatures, which may be explained by a first-order nature of this transition.

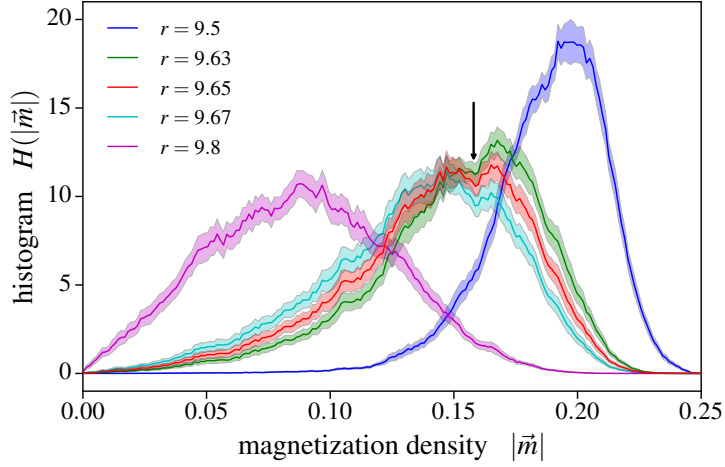


Figure 6.14: Histograms of the finite-system magnetization density $|\vec{m}|$ with statistical error bands for the $\lambda = 3, c = 2$ model at $T = 1/30$ and $L = 14$, resolved for various values of the tuning parameter r . The histograms show a small suppression (indicated by an arrow) between two peaks at $r \approx 9.65$ close to the estimated location of the SDW phase transition. The location of this point is marked with a small x in the phase diagram of Fig. 6.7.

6.4.2 Charge-density wave (CDW) and pair-density wave (PDW) susceptibilities

To explore possible additional instabilities competing with superconductivity, we turn to examine the susceptibilities of various density-wave orders near the magnetic quantum phase transition (QPT). We begin by defining zero-frequency charge-density wave (CDW) and pair-density wave (PDW) susceptibilities

$$C_\zeta(\mathbf{q}) = \sum_i \int_0^\beta d\tau e^{-\mathbf{q} \cdot \mathbf{r}_i} \langle \tilde{\Delta}_\zeta^\dagger(\mathbf{r}_i, \tau) \tilde{\Delta}_\zeta(\mathbf{r}_0, 0) \rangle, \quad (6.22a)$$

$$P_\zeta(\mathbf{q}) = \sum_i \int_0^\beta d\tau e^{-\mathbf{q} \cdot \mathbf{r}_i} \langle \Delta_\zeta^\dagger(\mathbf{r}_i, \tau) \Delta_\zeta(\mathbf{r}_0, 0) \rangle, \quad (6.22b)$$

where $\tilde{\Delta}_\zeta(\mathbf{r}_i) = \sum_{s=\uparrow,\downarrow} (\psi_{xis}^\dagger \psi_{xis} + \zeta \psi_{yis}^\dagger \psi_{yis})$, $\Delta_\zeta(\mathbf{r}_i) = 2(\psi_{xi\uparrow}^\dagger \psi_{xi\downarrow}^\dagger + \zeta \psi_{yi\uparrow}^\dagger \psi_{yi\downarrow}^\dagger)$ with two possible signs $\zeta = \pm$. For both order parameters the positive sign corresponds to d -wave symmetry and the negative sign to s -wave symmetry.

In Fig. 6.15 we show the momentum dependence of the d -wave susceptibilities $C_-(\mathbf{q})$ and $P_-(\mathbf{q})$ close to the magnetic QPT. C_- shows the most interesting structure with a peak slightly off $\mathbf{q} = (\pi, \pi)^T$. In contrast P_- is strongly peaked at $\mathbf{q} = \mathbf{0}$

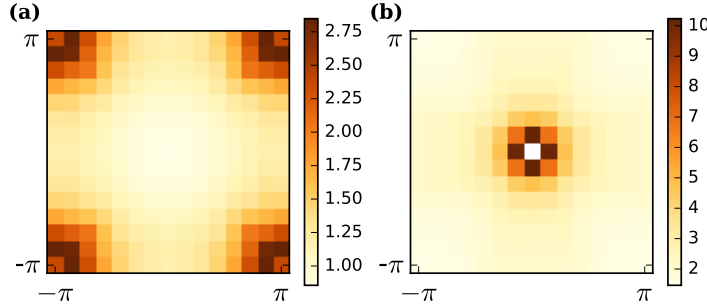


Figure 6.15: (a) d -wave CDW susceptibility $C_-(\mathbf{q})$ and (b) d -wave PDW susceptibility $P_-(\mathbf{q})$ as a function of momentum, shown here for $\lambda = 3, c = 2, L = 14, T = 1/12$, and $r = 10.4$. The data point $P_-(\mathbf{q} = 0)$, corresponding to the uniform superconducting susceptibility, has been excluded from the data.

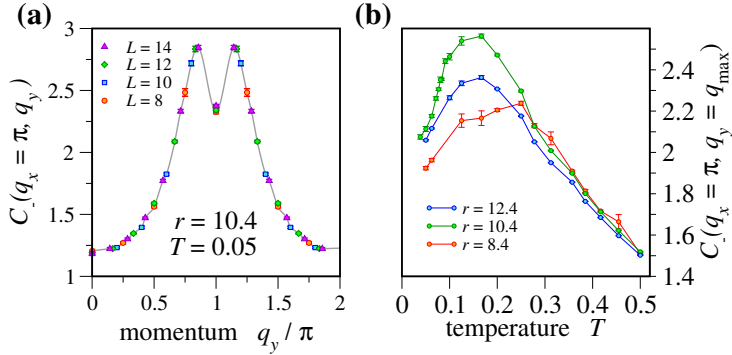


Figure 6.16: (a) d -wave CDW susceptibility $C_-(\mathbf{q})$ along a cut $\mathbf{q} = (\pi, q_y)^T$ of the Brillouin zone for different system sizes in the $\lambda = 3, c = 2$ model. (b) Temperature dependence of $C_-(\mathbf{q} = (\pi, q_{\max})^T)$ for various values of r at the momentum where it is maximal, here for $L = 12$.

and does not show distinct structure at finite momenta, indicating that there is no noticeable tendency towards PDW order.

The momentum dependence of C_- is shown along a high-symmetry cut $\mathbf{q} = (\pi, q_y)^T$ through the Brillouin zone in Fig. 6.16a. Here there is little dependence on the system size with the data for different L almost collapsing on the same curve. This suggests that the correlation length for CDW correlations is short compared to these lattice sizes and that the results are already equivalent to the thermodynamic limit. There does not appear to be any long-range or quasi-long-range CDW order in the d -wave channel. In Fig. 6.16b we show the temperature dependence of $C_-(\mathbf{q} = (\pi, q_{\max})^T)$ for three values of r across the phase diagram. The CDW wavevector $\mathbf{q}_{\max} = (\pi, q_{\max} \approx 0.83)^T$ corresponds to the maximum of $C_-(\mathbf{q})$. Apparently $C_-(\mathbf{q}_{\max})$

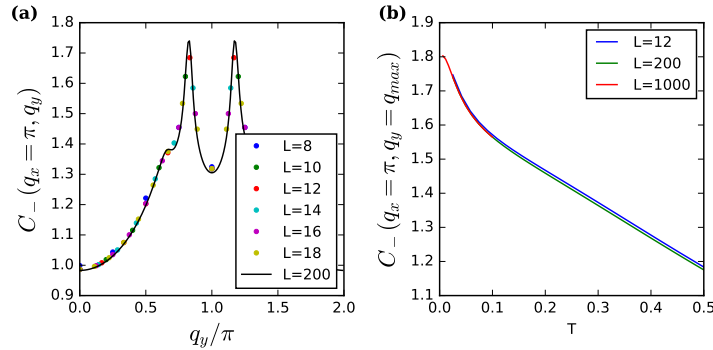


Figure 6.17: (a) CDW susceptibility in the non-interacting model along a cut $\mathbf{q} = (\pi, q_y)^T$ of the Brillouin zone for different system sizes, shown here for $T = 1/40$. (b) Temperature dependence at its maximizing momentum.

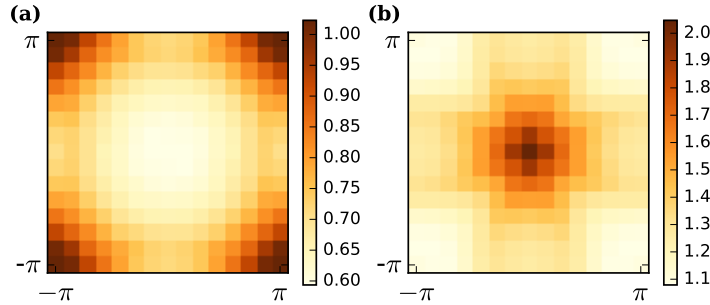


Figure 6.18: (a) s -wave CDW susceptibility $C_+(\mathbf{q})$ and (b) s -wave PDW susceptibility $P_+(\mathbf{q})$ as a function of momentum, shown here for $\lambda = 3$, $c = 2$, $L = 14$, $T = 1/12$, and $r = 10.4$.

is maximal at a temperature close to $\max\{T_c, T_{\text{SDW}}\}$, potentially as a consequence to a reduced density of states below that temperature where superconducting or SDW order sets in. As a function of the tuning parameter r the susceptibility C_- is maximized close to the location of T_c^{\max} , i.e. in the vicinity of the SDW quantum phase transition. Nevertheless, the PDW susceptibility P_- remains larger by an order of magnitude there.

The enhancement of C_- at \mathbf{q}_{\max} may be understood already from the non-interacting $\lambda = 0$ model. In that case the CDW susceptibility is peaked at the same wavevector $\mathbf{q}_{\max} \approx (\pi, 0.83)^T$, see Fig. 6.17a. Note that \mathbf{q}_{\max} is distinct from the wavevector $\mathbf{Q} = (\pi, \pi)^T$ linking two hot spots. As the temperature is lowered $C_-(\mathbf{q}_{\max})$ increases and finally saturates, see Fig. 6.17b. At the maximum, the numerical value of the non-interacting CDW susceptibility is about 40% lower than C_- for the $\lambda = 3$, $c = 2$ model.

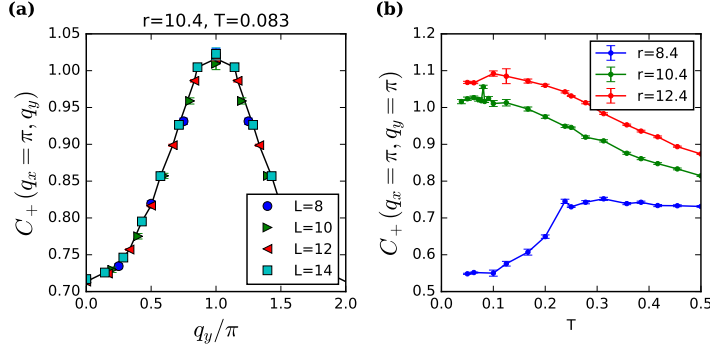


Figure 6.19: (a) s -wave CDW susceptibility $C_+(\mathbf{q})$ along a cut $\mathbf{q} = (\pi, q_y)^\top$ of the Brillouin zone for different system sizes in the $\lambda = 3, c = 2$ model. (b) Temperature dependence of $C_-(\mathbf{q} = (\pi, \pi)^\top)$ for various values of r , here for $L = 12$.

We continue with the s -wave susceptibilities C_+ and P_+ . Their momentum dependence close to the magnetic QPT is shown in Fig. 6.18. $C_+(\mathbf{q})$ is peaked at $(\pi, \pi)^\top$ or very close to that wavevector. Its maximal value is approximately three times lower than that of C_- . Similarly to P_- , P_+ does not show features at finite momenta. At the same time its amplitude is much smaller than that of P_+ . Much like C_- the s -wave CDW susceptibility does not show any strong size dependence as shown in Fig. 6.19a. It only depends moderately on temperature, see Fig. 6.19b.

In addition to the CDW susceptibilities C_\pm we have also examined the bond-density wave (BDW) susceptibilities

$$B_{\zeta, \eta}(\mathbf{q}) = \int_0^\beta d\tau \langle b_{\zeta, \eta}^\dagger(\mathbf{q}, \tau) b_{\zeta, \eta}(\mathbf{q}, 0) \rangle \quad \text{with} \quad (6.23a)$$

$$b_{\zeta, \eta}(\mathbf{q}) = \frac{1}{4} \sum_{s, \mathbf{k}} \left[\psi_{x, \mathbf{k}, s}^\dagger \psi_{x, \mathbf{k} + \mathbf{q}, s} + \eta \psi_{y, \mathbf{k}, s}^\dagger \psi_{y, \mathbf{k} + \mathbf{q}, s} \right] \\ \times \left[\cos(k_x) + \cos(k_x + q_x) + \zeta \cos(k_y) + \zeta \cos(k_y + q_y) \right] \quad (6.23b)$$

for $\zeta, \eta = \pm$, shown in Fig. 6.20. There are peaks at momenta far from $(\pi, \pi)^\top$, but the dependence on system size and temperature is weak. These data for alternative form factors support the finding that there is no long-range CDW order in the SDW model.

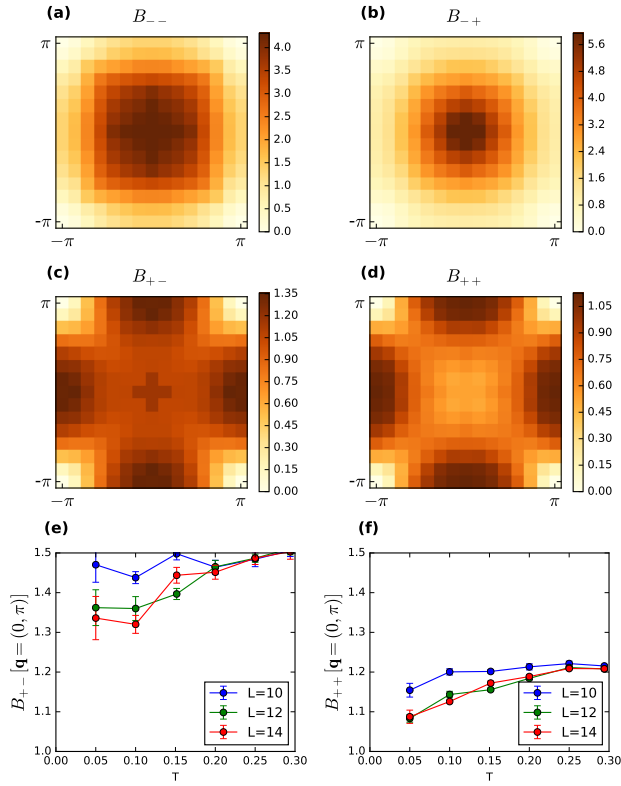


Figure 6.20: (a-d) Bond-density wave susceptibilities across the Brillouin zone for the $\lambda = 3$, $c = 2$ model at $T = 0.1$, $L = 14$, and $r = 10.4$. Here the $\mathbf{q} = \mathbf{0}$ value is interpolated from the four neighboring momenta. (e-f) Temperature and system size dependence of $B_{+,η}$ at $\mathbf{q} = (0, \pi)^T$, where it is maximal.

6.5 Phase diagrams for several values of λ and $c = 3$

To complement the detailed discussion of the $\lambda = 3$, $c = 2$ phase diagram of the previous Section and to provide a wider perspective, we have run additional replica-exchange simulations with the bare bosonic velocity $c = 3$ at three smaller value of the Yukawa coupling $\lambda = 1, 1.5, 2$. Carrying out the same type of analysis as before, we have evaluated the phase diagrams shown in Fig. 6.21.

As in the other phase diagrams presented above, we find a quasi-long-range ordered SDW phase with a transition temperature T_{SDW} that decreases with increasing values of the tuning parameter r . An extrapolation of these phase boundaries has provided an estimate for the location of the magnetic quantum phase transition at $r = r_c$ for each value of λ . While the finite-temperature SDW transition may become weakly first-order at low temperatures, for the temperature range considered here

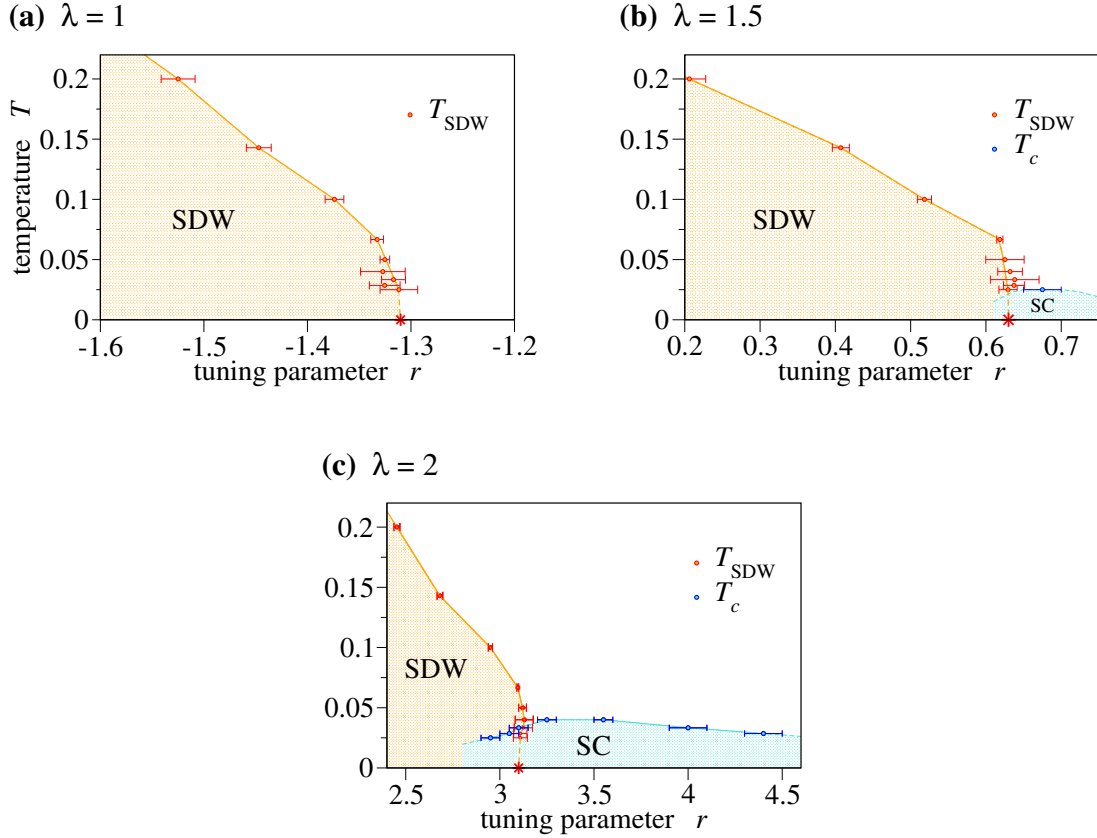


Figure 6.21: Finite-temperature phase diagram for $\lambda = 1, 1.5$, and 2 at $c = 3$. Shown are the transition temperature into SDW quasi-long-range order T_{SDW} and the estimated location r_c of the magnetic quantum phase transition at $T = 0$ (marked by a star). Where applicable the superconducting (SC) transition temperature T_c is also shown. Lines are guides to the eye.

the transition remains mostly continuous. For $\lambda = 1$ the SDW phase remains the only ordered phase down to the lowest temperature $T = 1/40$ we have accessed in this study. For the higher values of the Yukawa coupling λ an additional superconducting phase emerges close to the quantum phase transition. At $\lambda = 1.5$ the tip of a d -wave superconducting phase can just be resolved with $T_c^{\max} \approx 1/40$, while we can clearly map out a d -wave superconducting dome with $T_c^{\max} \approx 1/20$ for $\lambda = 2$.

All three phase diagrams in Fig. 6.21 feature a change of slope of the T_{SDW} boundary at a low temperature $T \approx 0.07$. We observe this bending already at a slightly higher temperature $T \approx 0.12$ in the $\lambda = 1 = c$ phase diagram of Fig. 6.4. In these cases this change of curvature does not seem to be directly related to a superconducting phase. On the other hand in the $\lambda = 3, c = 2$ phase diagram of Fig. 6.7, where T_c^{\max} is higher, a similar bending tracks the superconducting T_c and also sets in at a

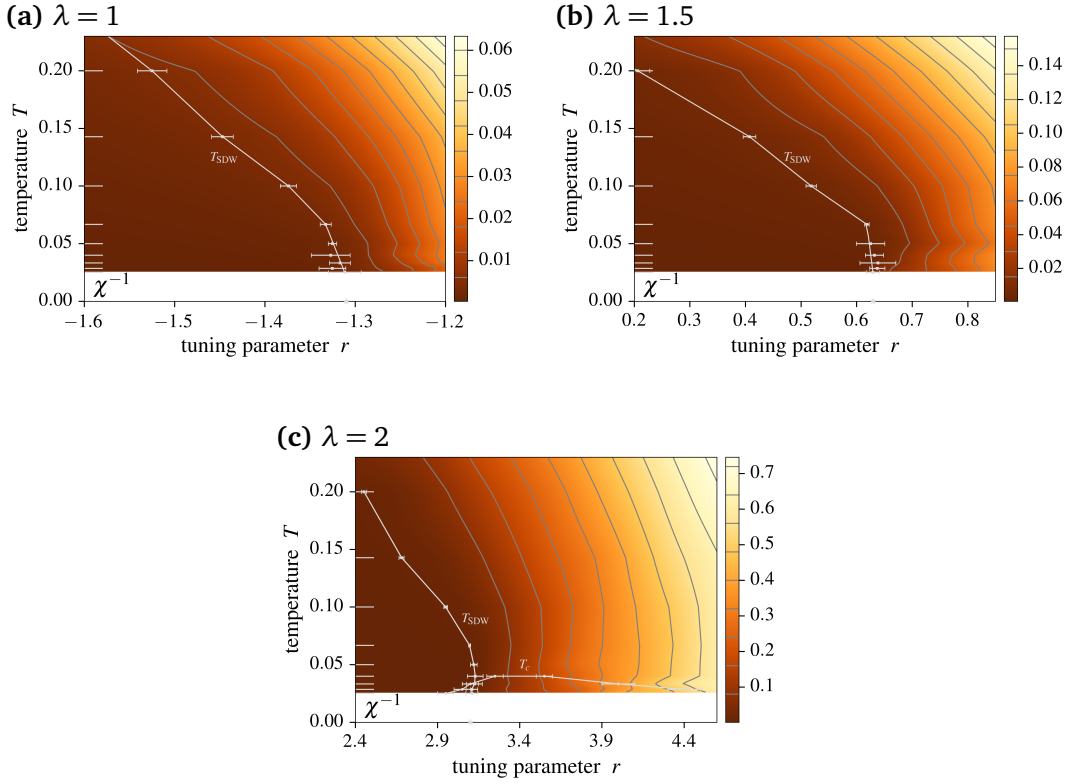


Figure 6.22: Inverse SDW susceptibility χ^{-1} across the phase diagrams for three values of λ and $c = 3$. Contour lines of χ^{-1} are indicated gray. Here we show data obtained at $L = 14$ at those temperatures indicated by ticks on the left hand inside of the panel. In between those temperatures the data is interpolated linearly. The resolution in the tuning parameter is very high thanks to multiple-histogram reweighting. Compare to Fig. 6.8b for $\lambda = 3, c = 2$.

temperature $T \approx 0.07$. The curvature of the T_{SDW} line for $\lambda = 1, 1.5, 2$ and $c = 3$ is also reflected in the contour lines of the SDW susceptibility χ in the paramagnetic phase, see Fig. 6.22.

Comparing the phase diagrams of Fig. 6.21 with the $\lambda = 3, c = 2$ phase diagram of Fig. 6.7, we find that T_c^{\max} grows with the Yukawa coupling λ . This is an example for the more general trend demonstrated by Fig. 6.23 where we display the dependence of T_c^{\max} , some times only roughly estimated, on λ and the bare bosonic velocity c . Up to an intermediate value $\lambda \approx 3$, T_c^{\max} rapidly grows as $T_c^{\max} \sim \lambda^2$. At higher coupling strength it saturates eventually. Note that the physical interpretation of the parameter λ is not totally straight forward: To a certain degree a change of its value can be balanced by rescaling the bosonic field $\vec{\varphi}$, mere variables of integration in the partition function. It is best to compare T_c^{\max} with all other parameters fixed.

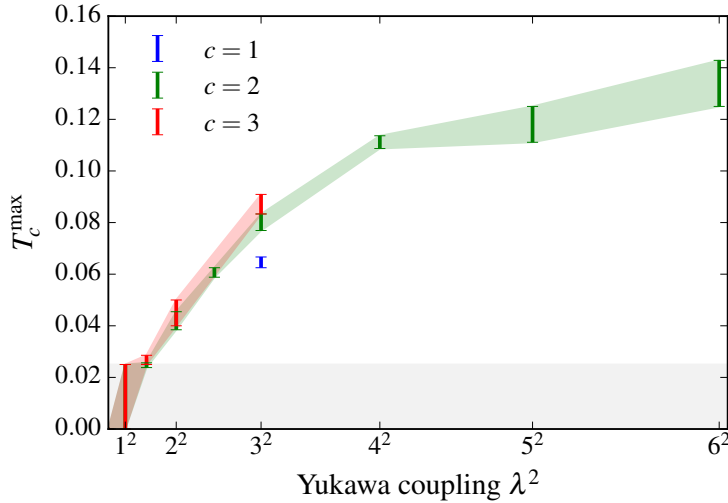


Figure 6.23: Dependence of the maximal superconducting transition temperature T_c^{\max} on the Yukawa coupling λ for three values of the bare bosonic velocity c . Temperatures $T < 0.025$ have not been accessed in this study (gray region).

6.6 Discussion

With the results shown in this Chapter we have, to our knowledge, for the first time obtained the full finite-temperature phase diagram of a metal coupled to an SDW order parameter in a controlled, unbiased way. Our data provides the numerically exact solution of a model featuring an SDW quantum phase transition. Without any approximation beyond the finite sizes of the lattices we have studied and the discretization of imaginary time our results prove that a quasi-long-range ordered d -wave superconducting phase emerges in the vicinity of such a quantum critical point. This has been expected for long time, but has not been shown explicitly without uncontrolled approximations before. Our results are expected to hold *universally* for an O(2) SDW quantum critical point in a metal on a square lattice as long as the important physics are driven by the hot spots on the Fermi surface.

The d -wave superconducting phase of the $\lambda = 3$, $c = 2$ model has a highest transition temperature of the order $T_c^{\max} \approx E_F/30$, where E_F is the Fermi energy. Hence, a system described by this model can truly be characterized as a high-temperature superconductor. Above T_c we find a regime of strong superconducting fluctuations where the orbital magnetic response is diamagnetic and we observe a reduction in the single-particle density of states. Inside the superconducting phase our results indicate a region of coexistence with SDW order. It has been pointed out before that itinerant SDW order can coexist with an unconventional

superconducting state for a system where that would not be possible for conventional, non-sign changing s -wave pairing [178].

The numerically obtained phase diagram in Fig. 6.7 is strikingly similar to the experimental phase diagrams of many unconventional superconductors like the electron-doped cuprates, iron-based superconductors, or organic superconductors, see Chap. 3. This suggests that physics in these materials may essentially be driven by the same universal mechanism captured by our itinerant SDW model.

To describe the phenomenology of the most widely studied class of high- T_c superconductors, the hole-doped cuprates, frequently models are employed that are very similar to the one studied by us. Therefore it is interesting to compare our results to the experimental findings. At first sight, our phase diagram with a d -wave superconducting dome in proximity to a Néel ordered SDW phase is similar to those of the hole-doped cuprates. However, in those phase diagrams no region of coexistence between the two types of orders is observed. Rather both transition temperature lines collapse to zero before they meet, cf. Fig. 3.2 on p. 26. The normal state at temperatures above the SDW phase, this intermediate region, and the underdoped side of the superconducting dome has received much attention because it features the puzzling pseudogap phase. As predicted for a similar spin-fermion model [179], our model exhibits a gap in the single-particle energy spectrum at temperatures above the ordered phases. However, this gap sets in at a temperature roughly proportional to the superconducting T_c and never larger than approximately $2T_c$. Thus it should be discerned from the pseudogap phenomenon of the cuprates, which extends over a far larger region of the phase diagram. The diamagnetic fluctuations seen above T_c in our model, however, are similar to observations in the hole-doped cuprates [180, 181].

In all our numerical phase diagrams we find a characteristic downward bending of the magnetic phase transition line T_{SDW} as the quantum phase transition is approached (see Fig. 6.4 for $\lambda = c = 1$, Fig. 6.7 for $\lambda = 3, c = 2$, and Fig. 6.21 for $\lambda = 1, 1.5, 2, c = 3$), which is reflected in the contour lines of the SDW susceptibility χ (see Fig. 6.8a for $\lambda = 3, c = 2$ and Fig. 6.22 for $\lambda = 1, 1.5, 2, c = 3$). For $\lambda = 3, c = 2$ and possibly $\lambda = 1, c = 3$, where T_c^{\max} is high, this phenomenon could be associated to the competition between the SDW and superconducting order parameters. A related shift of the quantum critical point has been predicted to arise from the competition between the two order parameters [182, 183] and a comparable behavior has been observed in unconventional superconductors such as $\text{Ba}_{1-x}\text{Co}_x\text{Fe}_2\text{As}_2$ [184]. Moreover, the kink-like change of slope of the two phase boundaries in the r - T plane upon meeting each other corresponds to the behavior expected in Landau theory for two order parameters coupled through a repulsive quartic term [185, Sec. 4.6]. However, in the cases of $\lambda = 1$ and $\lambda = 1.5$, where T_c

is lower, the SDW transition line appears to bend downwards without the influence of the superconducting phase, which suggests that this may be caused by a different mechanism. In the $\lambda = 2$, $c = 3$ phase diagram of Fig. 6.21c, which exhibits an intermediate T_c^{\max} , the curvature of T_{SDW} possibly changes two distinct times, once at $T \approx 0.07$ and another time at a lower temperature shortly before entering the superconducting phase, but error bars on the available data do not allow to say with certainty. In Hertz-Millis theory a linear dependence $T_{\text{SDW}}(r)$ would be predicted, but the case of spatial dimension $d = 2$ and dynamical critical exponent $z = 2$ is marginal [30] and, more fundamentally, the Hertz-Millis approach lacks formal justification in $d = 2$ [20, 34].

To probe our model for emergent orders in addition to superconductivity we have examined charge-density wave (CDW), pair-density wave (PDW), and bond-density wave (BDW) susceptibilities in the vicinity of the magnetic quantum phase transition. Compared with the non-interacting model, we have found a moderate enhancement of CDW fluctuations with d -wave form factor. However, these are not long ranged and certainly there is no indication of a near-degeneracy between superconducting and CDW order parameters close to the quantum phase transition. This suggests that spin fluctuations do not provide an interaction that leads to strong CDW fluctuations on their own and that additional, non-magnetic interactions would be necessary to stabilize a CDW phase. This conclusion is consistent with Refs. [186–189] and indicates that a linearization of the Fermi surface close to the hot spots, mentioned in Sec. 2.2.3, may be too strong an approximation.

We have also studied the superfluid density across the phase diagram of the $\lambda = 3$, $c = 2$ model. It has been proposed that a sharp minimum of the low-temperature superfluid density could be used generically to locate a magnetic quantum critical point inside a superconducting phase [3, 190] after it had been observed in the iron-based superconductor $\text{BaFe}_2(\text{As}_{1-x}\text{P}_x)_2$ [191]. The data from our DQMC simulations do not show such a minimum anywhere inside the superconducting phase. This is consistent with field theoretical analysis [192] and measurements of a different iron-based superconductor $\text{Ba}_{1-x}\text{Co}_x\text{Fe}_2\text{As}_2$ [184], suggesting that quantum criticality does not drive such a mechanism [193].

The results presented in this Chapter do not directly address questions on metallic SDW quantum criticality. Since in our model the magnetic quantum phase transition always lies inside the superconducting phase, we cannot directly study the pure quantum critical point. This is further complicated by the possibly first-order nature of the SDW transition at low temperatures. Nevertheless, in the following Chapter we will see that we can access a crossover regime above the superconducting T_c where the physics is dominated by the quantum critical phase underlying the superconducting dome.

7 Manifestations of quantum critical behavior

In this Chapter we analyze critical correlations caused by the magnetic quantum critical point (QCP) of the metallic O(2) SDW model. Due to the instability towards d -wave superconductivity we expect the QCP to be always shadowed by a superconducting phase at sufficiently low temperature. Since physics are fundamentally altered inside this gapped phase, the best way to study the properties of the *underlying* QCP from Monte Carlo data is not by zero temperature simulations¹, but by studying the model at intermediate temperatures *above* the superconducting T_c , with the parameters tuned such that we can still access the quantum critical regime associated to the QCP. To this end we have mainly studied the model at the Yukawa coupling $\lambda = 1.5$ with bare bosonic velocity $c = 3$, corresponding to one of the phase diagrams of Sec. 6.5. At this coupling strength T_c , is just barely reached in our DQMC simulations.

This Chapter is structured as follows: In Sec. 7.1 we give a detailed analysis of the SDW susceptibility across the phase diagrams, not only with Yukawa coupling $\lambda = 1.5$, but also with $\lambda = 1$ and $\lambda = 2$. In Sec. 7.2 we study the single-fermion properties of the $\lambda = 1.5$ model, indicating a breakdown of Fermi liquid theory. Sec. 7.3 provides a complementary investigation of the gap structure in the superconducting phase for $\lambda = 3$, $c = 2$. Finally the results are discussed in Sec. 7.4.

Like the results of the previous Chapter, the data presented here has been obtained in a collaborative effort. As such a code developed by Y. Schattner has been used to compute fermionic imaginary-time displaced observables for the analysis in Sec. 7.1 and he has evaluated the data shown in Secs. 7.2 and 7.3.

7.1 Magnetic correlations

In this Section we present a thorough examination of SDW fluctuations across the entire finite-temperature phase diagrams for values of the Yukawa coupling $\lambda = 1, 1.5, 2$ and bare bosonic velocity $c = 3$. To investigate magnetic fluctuations we analyze two susceptibilities evaluated independently from the same DQMC simulations: The susceptibility of the bosonic order parameter $\vec{\varphi}$ and a fermionic

¹Zero temperature simulations could be carried out in the framework of projector quantum Monte Carlo (PQMC), a method closely related to the finite-temperature DQMC method we employ.

bilinear of the same symmetry. As we will see in the following, the behavior of both susceptibilities is in good agreement, supporting the robustness of our conclusions.

7.1.1 Bosonic SDW susceptibility

We consider the following, momentum and Matsubara frequency resolved susceptibility computed from the bosonic SDW order parameter $\vec{\varphi}$:

$$\chi(\mathbf{q}, i\omega_n, r, T) = \sum_i \int_0^\beta d\tau e^{i\omega_n\tau - i(\mathbf{q}-\mathbf{Q})\cdot\mathbf{r}_i} \langle \vec{\varphi}_i(\tau) \cdot \vec{\varphi}_0(0) \rangle. \quad (7.1)$$

Here $\omega_n = 2\pi n T$ and we measure momenta \mathbf{q} relative to the magnetic ordering wavevector $\mathbf{Q} = (\pi, \pi)^T$. Previously we considered the static SDW susceptibility for order at \mathbf{Q} , $\chi(r, T) = \sum_i \int_0^\beta d\tau \langle \vec{\varphi}_i(\tau) \cdot \vec{\varphi}_0(0) \rangle$. It is related to the more general definition (7.1) by $\chi(r, T) = \chi(\mathbf{Q}, 0, r, T)$. We give the temperature T and tuning parameter r , at which the DQMC simulations are run to estimate the expectation values, as explicit parameters.

At low temperature we find that we can very well fit the form

$$\chi_0^{-1}(\mathbf{q}, i\omega_n, r, T \rightarrow 0) = a_q(\mathbf{q} - \mathbf{Q})^2 + a_\omega |\omega_n| + a_r(r - r_{c0}), \quad (7.2)$$

which is consistent with Hertz theory [29], to our data. Here a_q , a_ω and a_r are non-universal fitting parameters that describe the momentum dependence, Landau damping, and the dependence on the tuning parameter r , respectively. χ_0 diverges when r is tuned to the fitting parameter r_{c0} . In presence of the superconducting phase at low temperatures r_{c0} may differ from the actual location of the SDW quantum phase transition at r_c . Nevertheless we find $r_{c0} \approx r_c$ when we estimate r_c by extrapolating the finite-temperature SDW phase boundary to $T = 0$, cf. the phase diagrams in Fig. 6.21 of Sec. 6.5. The high consistency of the measured susceptibility $\chi(\mathbf{q}, i\omega_n, r, T)$ with the functional form χ_0 is illustrated in Fig. 7.1 (p. 146). There we show collapses of the data obtained on the magnetically disordered side of the phase diagram for each coupling at temperature scales above the superconducting phase. We restrict the included data to a small range of momenta $\mathbf{q} - \mathbf{Q}$, small Matsubara frequencies ω_n , low temperatures $T \leq 0.1$, and tuning parameter values $r > r_{c0}$. Finite-size effects are rather small. We find that the fit is slightly worse for stronger coupling λ and consequently the spread of the data points in Fig. 7.1 is larger. The decreased fit quality may follow from the smaller temperature window available above the superconducting T_c and the associated regime of superconducting fluctuations at $T \gtrsim T_c$ discussed in Sec. 6.4 for $\lambda = 3$, $c = 2$. This regime extends to

higher temperatures with increased Yukawa coupling $\lambda \sim \sqrt{T_c^{\max}}$, cf. Fig. 6.23 in Sec. 6.5.

To further support the general validity of the functional form χ_0 in Eq. (7.2) we turn to a detailed analysis of the individual dependence of χ_0 on the tuning parameter r , frequency ω_n , and momentum $\mathbf{q} - \mathbf{Q}$. First, the dependence on the tuning parameter r is illustrated for the inverse susceptibility $\chi^{-1}(\mathbf{q} = \mathbf{Q}, i\omega_n = 0)$ in Fig. 7.2 (p. 147) at $T = 0.1$ and the three values of the Yukawa coupling λ . For tuning parameters $r \gtrsim r_{c0}$ we find that the data for different system sizes follows a linear dependence. The moderate deviation from a perfect kink-like behavior at r_{c0} is likely a combination of finite-size and finite-temperature effects, which are somewhat enhanced at the larger values of λ . Finite-size trends are shown in the insets of the three panels in Fig. 7.2.

Second, we find that for a range of values $r \geq r_{c0}$ the frequency dependence of $\chi^{-1}(\mathbf{q}, i\omega_n)$ is linear for small Matsubara frequencies ω_n with an apparent cusp at $\omega_n = 0$, signaling overdamped dynamics of the order parameter field $\vec{\varphi}$. This holds both for $\mathbf{q} = \mathbf{Q}$ and for small finite momentum differences $\mathbf{q} - \mathbf{Q}$. See Fig. 7.3 (p. 148) for an illustration. At finite Matsubara frequencies ω_n , finite-size effects are negligibly small, as evident in the data collapse of χ^{-1} for different system sizes in the left hand panels of Fig. 7.3. The cusp at $\omega_n = 0$ can clearly be seen at all three values of the Yukawa coupling λ . For $\lambda = 2$ we show data at a higher temperature $T = 1/20$, rather than $T = 1/40$, which is above T_c . To establish the presence of a $|\omega_n|$ term in χ^{-1} , we fit it at low frequencies to the form $b_0 + b_1|\omega_n| + b_2\omega_n^2$, with the fits also shown in Fig. 7.3, where the $|\omega_n|$ contribution is evidently dominant in this frequency range. Inside the superconducting phase the frequency dependence is significantly altered. There the term in $|\omega_n|$ is suppressed, presumably because the fermions are gapped out. We illustrate this with data from deep within the superconducting phase in Fig. 7.4 (p. 149), where we have chosen a data set with different values of the Yukawa coupling $\lambda = 3$ and bosonic velocity $c = 2$, corresponding to the phase diagram of Sec. 6.4 with $T_c^{\max} \approx 0.08$ reaching about twice the value for $\lambda = 2$, $c = 3$.

Finally, for the same range of r the momentum dependence of $\chi^{-1}(\mathbf{q}, i\omega_n)$ is consistent with a quadratic form in $\mathbf{q} - \mathbf{Q}$, which holds both for $\omega_n = 0$ and small finite frequencies ω_n , see Fig. 7.5 (p. 150). Note that due to the discretization of the Brillouin zone finite-size effects are more pronounced here than for the frequency dependence.

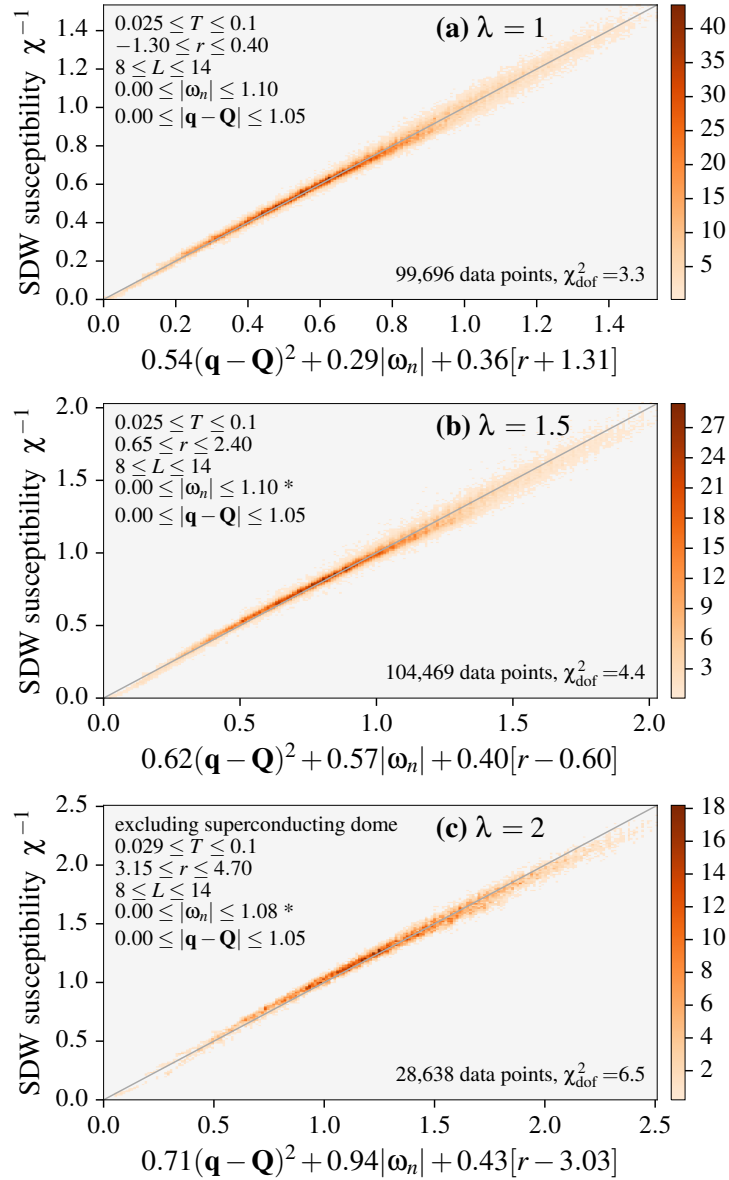


Figure 7.1: Comparison between the inverse SDW susceptibility χ^{-1} and the functional form $\chi_0^{-1} = a_q(\mathbf{q} - \mathbf{Q})^2 + a_\omega|\omega_n| + a_r(r - r_{c0})$, which has been fitted for small frequencies ω_n and momenta $\mathbf{q} - \mathbf{Q}$ at low temperatures T and tuning parameters $r > r_{c0}$ in the magnetically disordered phase, for (a) $\lambda = 1$, (b) $\lambda = 1.5$, and (c) $\lambda = 2$. Data inside the superconducting phase has been excluded from the fit. For temperatures $T \leq 2T_c^{\max}$ we restrict the fit to finite frequencies $|\omega_n| > 0$, indicated by the asterisk *. The correspondence of χ^{-1} with the fitted form is shown in the form of 2D histograms over all data points, which are normalized over the total area. In each fit we have minimized $\chi^2_{\text{dof}} = \frac{1}{N_{\text{dof}}} \sum \left[\frac{\chi^{-1} - \chi_0^{-1}}{\varepsilon} \right]^2$, where N_{dof} is the number of degrees of freedom of the fit and ε is the statistical error of the data.

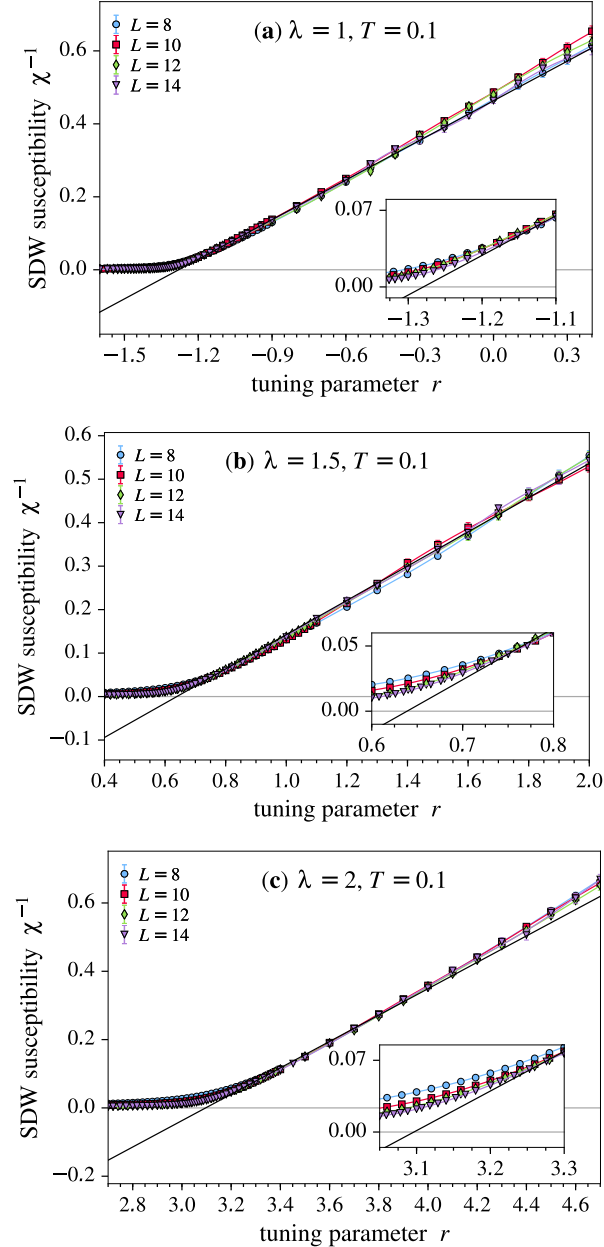


Figure 7.2: Bosonic SDW susceptibility $\chi^{-1}(\mathbf{q} = \mathbf{Q}, i\omega_n = 0)$ as a function of the tuning parameter r for (a) $\lambda = 1$, (b) $\lambda = 1.5$, and (c) $\lambda = 2$ at $T = 0.1$. The black line is a linear fit to the data for $L = 14$ and (a) $r > -1.2$, (b) $r > 0.7$, (c) $r > 3.2$. Continuous colored lines through data points have been obtained by a reweighting analysis.

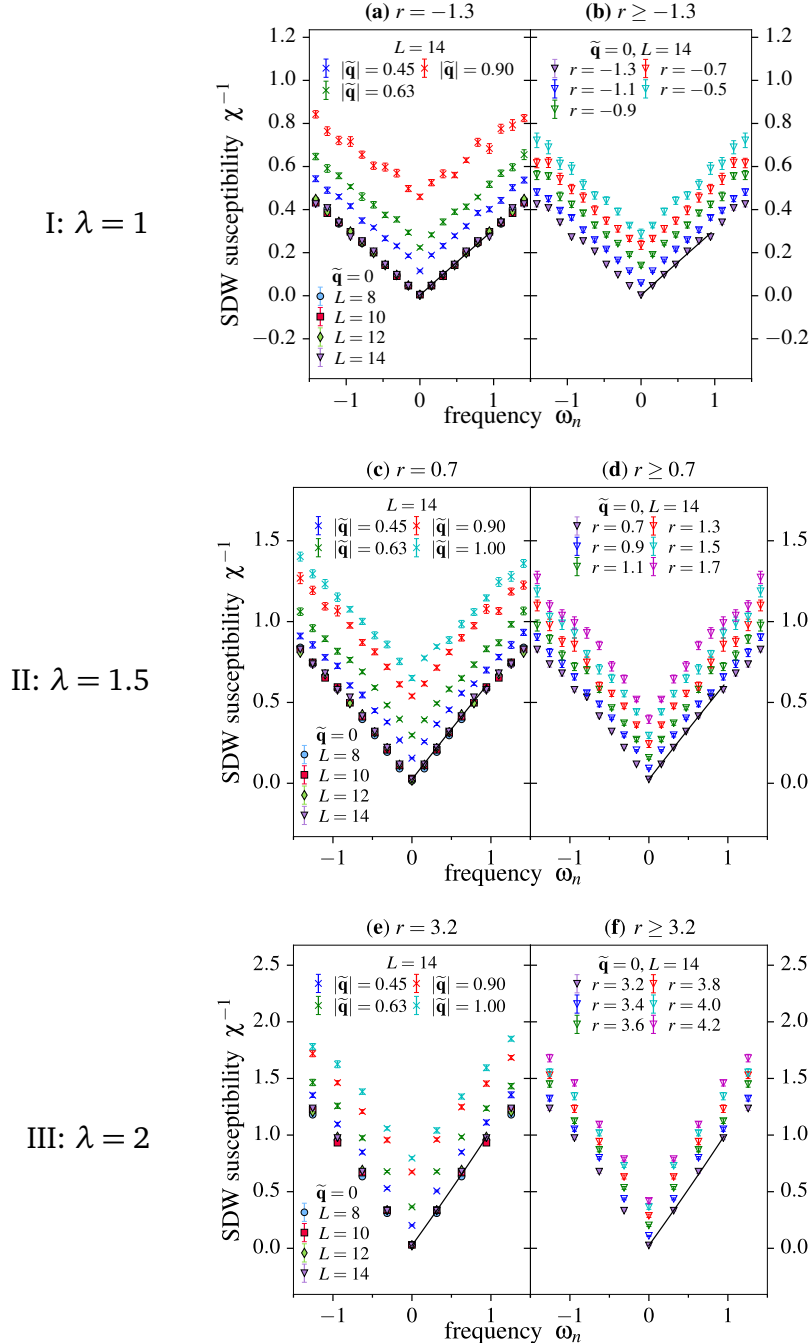


Figure 7.3: Frequency dependence of the inverse bosonic SDW susceptibility χ^{-1} for I: $\lambda = 1.5$ and II: $\lambda = 1.5$ at $T = 1/40$, and for III: $\lambda = 2$ at $T = 1/20$ (a), (c), (e) shown at $r \approx r_{c0}$ for various momenta $\mathbf{q} = \mathbf{Q} + \tilde{\mathbf{q}}$ and (b), (d), (f) shown at various values $r > r_{c0}$ for $\mathbf{q} = \mathbf{Q}$. The black line is the best fit of a second degree polynomial $b_0 + b_1|\omega_n| + b_2\omega_n^2$ to the $\mathbf{q} = \mathbf{Q}$, $L = 14$ low-frequency data.

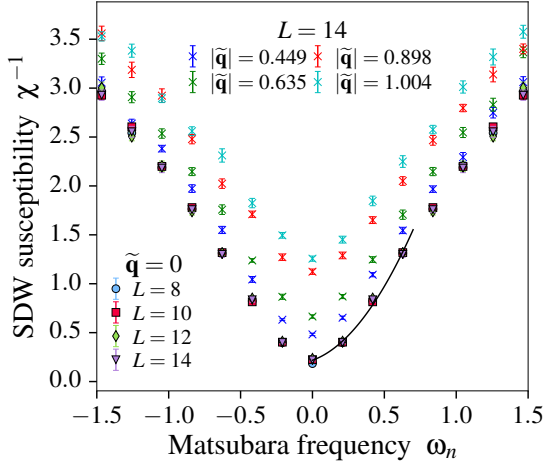


Figure 7.4: Frequency dependence of the SDW susceptibility χ^{-1} for $\lambda = 3$, $c = 2$ at $T = 1/30 < T_c$ and $r = 10.37 \approx r_{\text{opt}}$, close to where T_c is highest for this set of parameters, shown for various momenta $\mathbf{q} = \mathbf{Q} + \tilde{\mathbf{q}}$. The black line is the best fit of a second degree polynomial $b_0 + b_1|\omega_n| + b_2\omega_n^2$ to the $\mathbf{q} = \mathbf{Q}$, $L = 14$ low-frequency data.

7.1.2 Fermion bilinear SDW susceptibility

To confirm that the form χ_0 in Eq. (7.2) captures the universal physics in the quantum critical regime it is useful to affirm its validity for other SDW order parameters of the same symmetry. To this end we have examined the correlations of a *fermion* bilinear order parameter:

$$\begin{aligned} S_{xx}(\mathbf{q}, i\omega_n, r, T) &= \sum_i \int_0^\beta d\tau e^{i\omega_n\tau - i\mathbf{q}\cdot\mathbf{r}_i} \langle S_i^x(\tau)S_0^x(0) \rangle \\ &\equiv \sum_i \int_0^\beta d\tau e^{i\omega_n\tau - i\mathbf{q}\cdot\mathbf{r}_i} \frac{1}{2} [\langle S_i^x(\tau)S_0^x(0) \rangle + \langle S_i^y(\tau)S_0^y(0) \rangle], \end{aligned} \quad (7.3)$$

where we make use of spin rotational symmetry around the z axis, which improves the statistical quality of our Monte Carlo estimates. S_i^x and S_i^y in Eq. (7.3) are inter-flavor fermion spin operators, which are given by

$$\vec{S}_i = (S_i^x, S_i^y, S_i^z) = \sum_{s,s'} \vec{s}_{ss'} \psi_{xis'}^\dagger \psi_{yis'} + \text{h.c.} \quad (7.4)$$

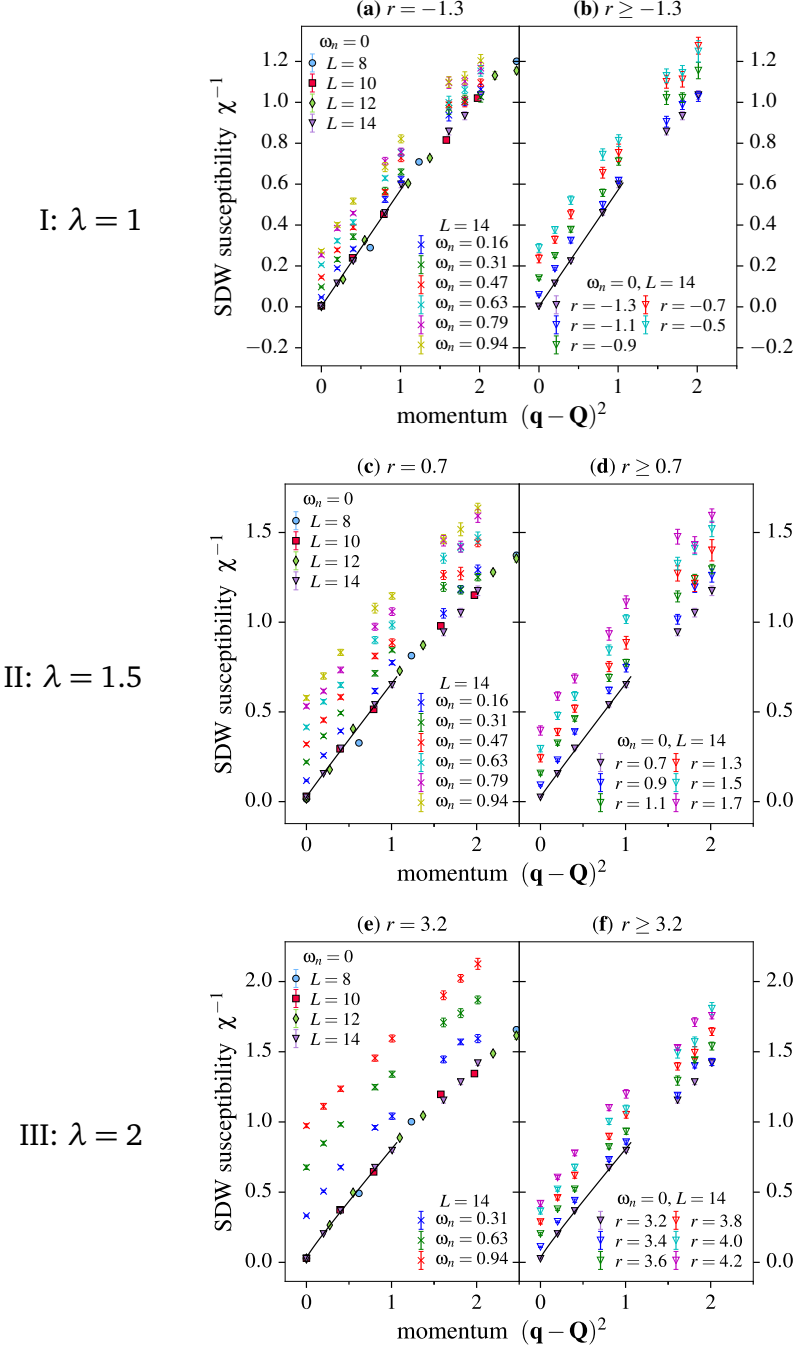


Figure 7.5: Inverse bosonic SDW susceptibility χ^{-1} as a function of momentum $\mathbf{q} = \mathbf{Q} + \tilde{\mathbf{q}}$ for I: $\lambda = 1$ and II: $\lambda = 1.5$ at $T = 1/40$, and III: $\lambda = 2$ at $T = 1/20$ (a), (c), (e) shown at $r \approx r_{c0}$ for various frequencies ω_n and (b), (d), (f) shown at various values $r \gtrsim r_{c0}$ for $\omega_n = 0$. The black line is the best fit of $a_0 + a_2 \tilde{\mathbf{q}}^2$ to the $\omega_n = 0, L = 14$ small-momentum data.

Indeed, we find that at small frequencies and momenta, the fermion bilinear SDW susceptibility S_{xx} follows the same functional form (7.2) as the bosonic SDW susceptibility χ discussed above, establishing the consistency of our analysis. The dependence on momentum and frequency of the fermionic bilinear susceptibility is shown in Fig. 7.6 (p. 152), to be compared with the respective dependence of the bosonic susceptibility appearing in Figs. 7.3 and 7.5.

7.1.3 Temperature dependence

To conclude this Section we turn to discuss the temperature dependence of the numerically computed bosonic and fermionic inverse SDW susceptibilities χ^{-1} and S_{xx}^{-1} , shown in Fig. 7.7 (p. 154) for two values of the tuning parameter r at each value of the Yukawa coupling $\lambda = 1, 1.5, 2$, one value close to the estimated location of the quantum phase transition $r \gtrsim r_{c0}$ and one value further on the paramagnetic side $r > r_{c0}$.

At all settings for the Yukawa coupling λ there are evidently multiple scaling regimes with increasing temperature. Focusing first on the intermediate value $\lambda = 1.5$, at sufficiently high temperatures, $T \gtrsim 0.35$, the susceptibilities $\chi^{-1}(\mathbf{q} = \mathbf{Q}, i\omega_n = 0)$ and $S_{xx}^{-1}(\mathbf{q} = \mathbf{Q}, i\omega_n = 0)$ are approximately linearly dependent on temperature, as shown in the insets of Fig. 7.7c and e. In an intermediate temperature regime, however, we observe a crossover to a different functional temperature dependence as shown in the main panels of Fig. 7.7c and e. In this intermediate temperature window, $0.05 \lesssim T \lesssim 0.35$, our numerical data is found to reasonably fit functions of a power-law form $a_0 + a_2 T^\alpha$ with $\alpha \simeq 2 \pm 0.3$, i.e. it is consistent with a *quadratic* law. Unlike the leading dependence on the tuning parameter, frequency or momentum discussed in the previous section, this power-law dependence is not as robust. Note that the crossover temperature between the high- T linear and intermediate- T quadratic behaviors does not depend strongly on the tuning parameter r . Notably, even for $r \approx r_{c0}$ this intermediate regime does not disappear.

At still lower temperatures $T \lesssim 0.05$ our data might indicate a second crossover to yet different behavior. With the tuning parameter r tuned close to its critical value r_{c0} both χ and S_{xx} are found to be non-monotonic for the smallest temperatures and largest system sizes accessed in this study. The apparent upturn, whose precise location is hard to determine due to finite-size effects (which are strongest for $r \approx r_{c0}$) and the enhanced statistical uncertainty at low temperatures, is most likely a precursor effect of superconductivity, which for $\lambda = 1.5$ sets in just at the lowest temperature we have accessed in this work, $T_c \approx 1/40$.

For the lower value of the Yukawa coupling $\lambda = 1$, where T_c is reduced, the temperature range well described by a quadratic law extends down to a lower

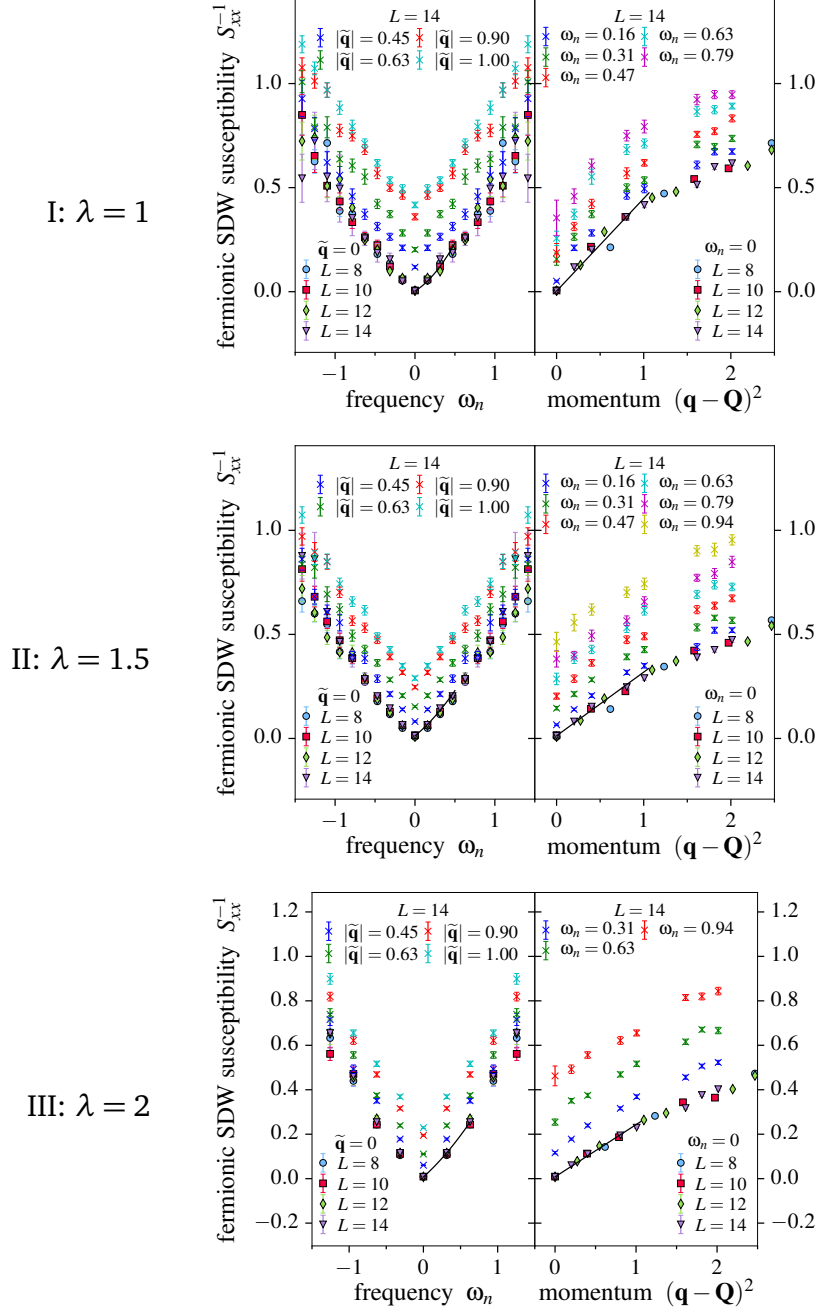


Figure 7.6: Inverse fermionic SDW susceptibility S_{xx}^{-1} at $r = 0.7 \approx r_{c0}$ for I: $\lambda = 1$ and II: $\lambda = 1.5$ at $T = 1/40$, and III: $\lambda = 2$ at $T = 1/20$. (Left hand side) Frequency dependence for various momenta $\mathbf{q} = \mathbf{Q} + \tilde{\mathbf{q}}$. The black line is a fit of the second degree polynomial $b_0 + b_1|\omega_n| + b_2\omega_n^2$ to the $\mathbf{q} = \mathbf{Q}$, $L = 14$ low-frequency data. (Right hand side) Momentum dependence for various frequencies ω_n . The black line is a fit of $a_0 + a_2\tilde{\mathbf{q}}^2$ to the $\omega_n = 0$, $L = 14$ small-momentum data.

temperature for $r \approx r_{c0}$, see Fig. 7.7a. However, finite-size effects appear to be stronger than at $\lambda = 1.5$. Conversely, at the higher value $\lambda = 2$ the temperature range consistent with a quadratic law is smaller. On the other hand the high-temperature linear regime is apparently more robust and continues down to slightly lower temperatures. For $\lambda = 2$ all data shown in Fig. 7.7e and f is taken in the superconducting phase for temperatures $T \leq 0.05$. As expected with the higher T_c , the non-monotonic behavior is indeed found to be more pronounced than for $\lambda = 1.5$. Moreover, for $\lambda = 2$ at $r = 3.1 \approx r_{c0}$ the system is partially inside the quasi-long-range ordered magnetic phase, cf. the phase diagram in Fig. 6.21.

Note that over the range of temperatures displayed in the contour plot of the inverse $\lambda = 1$ SDW susceptibility χ^{-1} in Fig. 6.22a of Sec. 6.5 the leading temperature dependence of χ^{-1} is quadratic. This is reflected in the contour lines of χ^{-1} in the $r - T$ plane, which have a form $T \sim \sqrt{\chi^{-1} - a_r(r - r_{c0})}$, approaching infinite slope at low temperatures.

Since the data does not allow us to identify a simple functional form for the temperature dependence of χ^{-1} , we have opted against taking into account any temperature dependence in the fits for the data collapses shown in Fig. 7.1. Instead we have constrained the included data to $T < 0.1$ where the overall temperature dependence is rather weak.

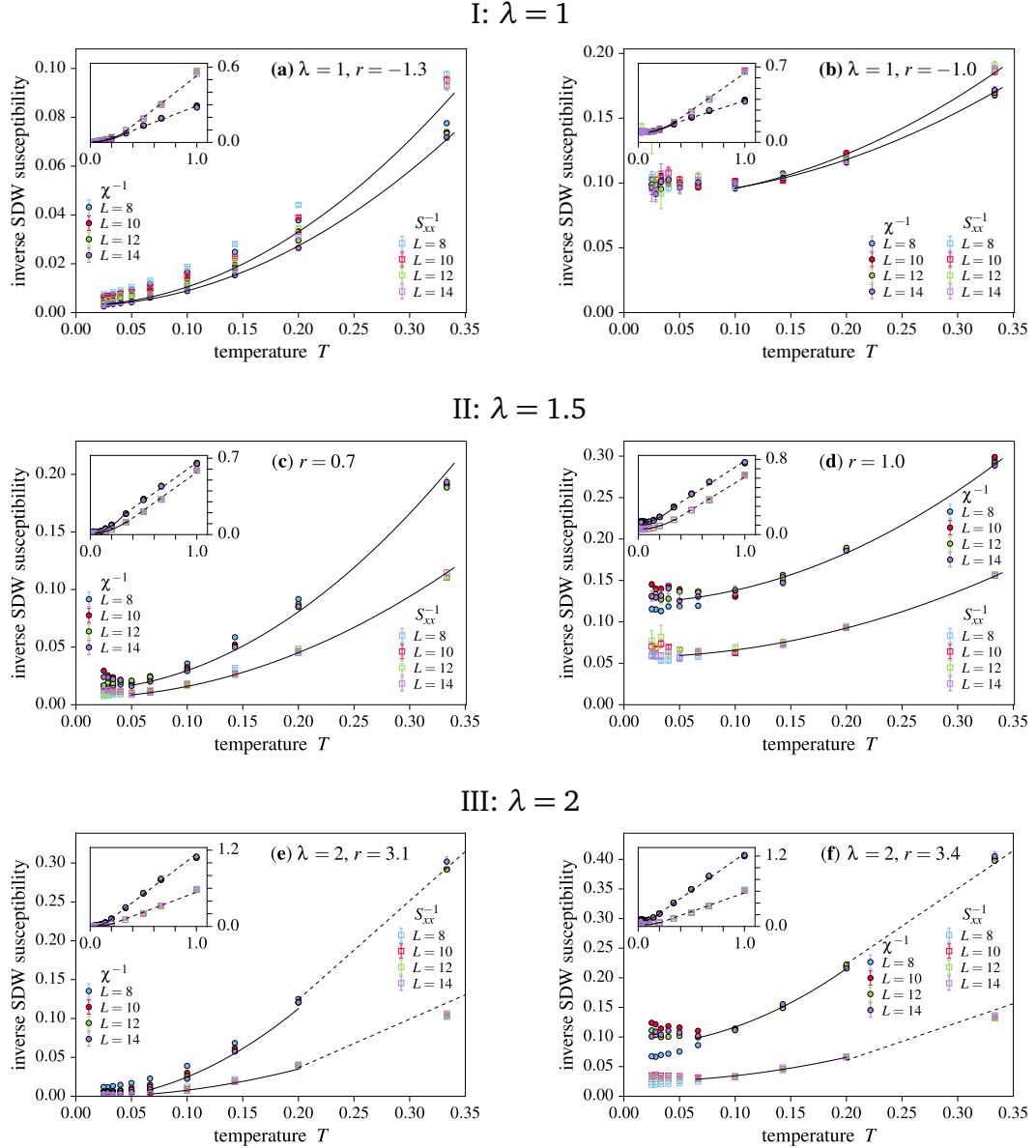


Figure 7.7: Inverse bosonic SDW susceptibility $\chi^{-1}(\mathbf{q} = \mathbf{Q}, i\omega_n = 0)$ and inverse fermionic SDW susceptibility $S_{xx}^{-1}(\mathbf{q} = \mathbf{Q}, i\omega_n = 0)$ as a function of temperature for I: $\lambda = 1$ at (a) $r = -1.3 \approx r_{c0}$ and at (b) $r = -1.0 > r_{c0}$, II: $\lambda = 1.5$ at (c) $r = 0.7 \approx r_{c0}$ and at (d) $r = 1.0 > r_{c0}$, as well as III: $\lambda = 2$ at (e) $r = 3.1 \approx r_{c0}$ and at (f) $r = 3.4 > r_{c0}$. Solid lines indicate fits of $a_0 + a_2 T^2$ to the $L = 14$ data at intermediate temperatures. Dashed lines are linear fits to the high-temperature data. In each figure the inset shows the same data as the main plot over a more extended temperature range.

7.2 Single-fermion correlations

In this Section we examine fermionic spectral properties in the metallic state for temperatures above the superconducting phase. We focus on the Yukawa coupling set to $\lambda = 1.5$ with bare bosonic velocity $c = 3$. Accessing real-time dynamics from data obtained in DQMC simulations is inherently difficult since we can only directly measure correlations in imaginary time. Without performing a full analytic continuation we can still extract information about the momentum resolved spectral function $A_{\mathbf{k}}(\omega)$ by using the relation [176]

$$G_{\mathbf{k}}(\tau, 0) = \int_{-\infty}^{\infty} d\omega \frac{e^{-\omega(\tau-\beta/2)}}{2 \operatorname{ch} \beta \omega / 2} A_{\mathbf{k}}(\omega) \quad (7.5)$$

with the imaginary-time ordered Green's function $G_{\mathbf{k}}(\tau, 0) = \langle \psi_{\mathbf{k}}(\tau) \psi_{\mathbf{k}}^\dagger(0) \rangle$ for momentum \mathbf{k} , where $0 \leq \tau \leq \beta$. Here and in the remainder of this Section we focus on a single band-spin sector $y \downarrow$ of the Green's function, suppressing indices α, s of the fermions ψ . According to Eq. (7.5) the behavior of $G_{\mathbf{k}}(\tau, 0)$ at long imaginary times $\tau \approx \beta/2$ provides information about the spectral function $A_{\mathbf{k}}(\omega)$ integrated over a real frequency window of width T around 0.

In order to be able to evaluate momentum resolved single-fermion observables we could not use data obtained in presence of the orthogonal fictitious pseudo-magnetic field we usually employ to reduce finite-size effects. Instead we have carried out additional DQMC simulations with different sets of twisted boundary conditions, in combination providing a four-fold enhancement of momentum resolution, as described in Sec. 5.4.3.

Evaluated at a sufficiently low temperature $T = 0.05 \approx 2T_c^{\max}$, the maxima of $G_{\mathbf{k}}(\tau = \beta/2, 0)$ can serve to study the Fermi surfaces of the interacting model. We show the non-interacting Fermi surfaces in Fig. 7.8a to provide a reference. In Fig. 7.8b-d we show $G_{\mathbf{k}}(\tau, 0)$ across a quarter section of the Brillouin zone at three different values of the tuning parameter r to gauge the evolution of the Fermi surface across the phase diagram. Compared to the magnetically disordered phase (panel d), near the magnetic quantum critical point (panel c) there is a substantial loss of spectral weight in the immediate vicinity of the hot spots. Tuning r below r_c , we see that a gap opens around the hot spots upon entering the magnetic phase (panel b).

Usually one characterizes a Fermi liquid by the quasiparticle weight $Z_{\mathbf{k}_F}$ and the Fermi velocity $\mathbf{v}_{\mathbf{k}_F}$, quantities that are only strictly defined at zero temperature. We expect that the metallic SDW model is always superconducting at $T = 0$, which prevents direct access to $Z_{\mathbf{k}_F}$ and $\mathbf{v}_{\mathbf{k}_F}$. Instead we consider two different types of proxies for these quantities at finite temperature and study their behavior over an

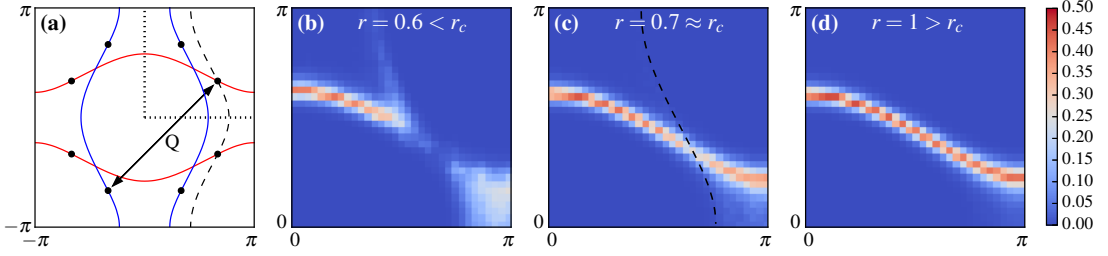


Figure 7.8: (a) Non-interacting Fermi surfaces. A pair of hot spots is connected by the magnetic ordering wavevector \mathbf{Q} . The dashed curve corresponds to the Fermi surface of the ψ_x band, shifted by \mathbf{Q} , with a hot spot now at the intersection with the ψ_y band. (b-d) Imaginary-time displayed Green's function $G_{\mathbf{k}}(\tau = \beta/2, 0)$ evaluated for the ψ_y fermions on a quadrant of the Brillouin zone, dotted in (a), for three values of the tuning parameter r in the $\lambda = 1.5$, $c = 3$ model at $L = 16$, $T = 0.05$. The dashed curve in panel (c) corresponds to the shifted non-interacting ψ_x Fermi surface.

intermediate temperature range $E_F > T > T_c$. The first type of proxy, $Z_{\mathbf{k}_F}^{\tau}(T)$ and $\mathbf{v}_{\mathbf{k}_F}^{\tau}(T)$, can be extracted by considering the imaginary-time dependence of $G_{\mathbf{k}}(\tau, 0)$ near $\tau = \beta/2$ and fitting it to the Fermi liquid form [194]

$$G_{\mathbf{k}}(\tau \sim \beta/2, 0) = Z_{\mathbf{k}}^{\tau}(T) \frac{e^{-\epsilon_{\mathbf{k}}(\tau - \beta/2)}}{2 \operatorname{ch}(\beta \epsilon_{\mathbf{k}}/2)} \quad (7.6)$$

with $\epsilon_{\mathbf{k}} = \mathbf{v}_{\mathbf{k}_F}^{\tau}(T) \cdot (\mathbf{k} - \mathbf{k}_F)$. A complementary second type of proxy, $Z_{\mathbf{k}_F}^{\omega}$ and $\mathbf{v}_{\mathbf{k}_F}^{\omega}(T)$, can be evaluated by considering the Matsubara frequency dependence of the Green's function $G_{\mathbf{k}}(\omega_n) = \int_0^{\beta} d\tau e^{i\omega_n \tau} G_{\mathbf{k}}(\tau, 0)$ with fermionic Matsubara frequencies $\omega_n = (2n - 1)\pi T$. In a Fermi liquid at low temperatures we have, to leading order in temperature, Matsubara frequency, and momentum distance to the Fermi surface [23, Sect. 2.5]

$$G_{\mathbf{k}}(\omega_n) \approx Z_{\mathbf{k}} \left[i\omega_n - \mathbf{v}_{\mathbf{k}_F} \cdot (\mathbf{k} - \mathbf{k}_F) \right]^{-1}. \quad (7.7)$$

This relation motivates the definition of the finite-temperature quantities

$$Z_{\mathbf{k}_F}^{\omega}(T) = \frac{\omega_1}{\operatorname{Im} G_{\mathbf{k}_F}^{-1}(\omega_1)}, \quad (7.8a)$$

$$\mathbf{v}_{\mathbf{k}_F}^{\omega}(T) = \omega_1 \left. \frac{\partial \operatorname{Re} G_{\mathbf{k}}(\omega_1)}{\partial \mathbf{k}} \right|_{\mathbf{k}=\mathbf{k}_F} \quad (7.8b)$$

in terms of the first Matsubara frequency $\omega_1 = \pi T$ at temperature T .

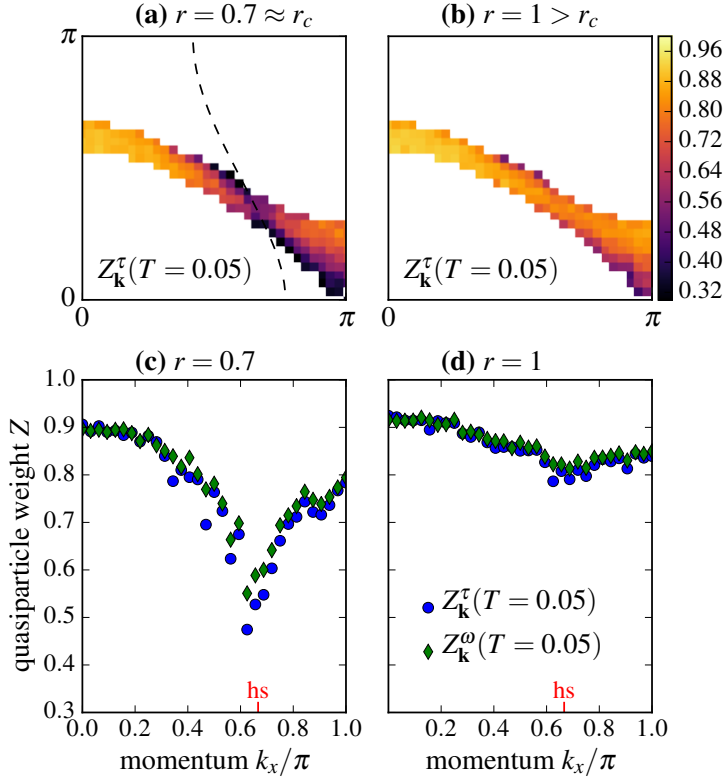


Figure 7.9: (a-b) Proxy for the quasiparticle weight $Z_{\mathbf{k}}^{\tau}(T = 0.05)$ in a quadrant of the Brillouin zone. The dashed line in panel (a) corresponds to the noninteracting Fermi surface of the ψ_x fermions, shifted by \mathbf{Q} . (c-d) Proxies for the quasiparticle weight $Z_{\mathbf{k}}^{\tau}(T = 0.05)$ and $Z_{\mathbf{k}}^{\omega}(T = 0.05)$ along the Fermi surface. The location of the hot spot (hs) is indicated by a red marker. Here we show data obtained for the $\lambda = 1.5$, $c = 3$ model with $L = 16$.

Both types of proxies are appropriately defined at low temperatures, since $Z_{\mathbf{k}_F}^{\omega}(T \rightarrow 0) = Z_{\mathbf{k}_F}^{\tau}(T \rightarrow 0) = Z_{\mathbf{k}_F}$ and $v_{\mathbf{k}_F}^{\omega}(T \rightarrow 0) = v_{\mathbf{k}_F}^{\tau}(T \rightarrow 0) = v_{\mathbf{k}_F}$.

The momentum dependence of $Z_{\mathbf{k}}^{\tau}(T = 0.05)$ is visualized in Fig. 7.10. In panels (a) and (c) the system is tuned close to the quantum critical point, $r \approx r_c$, while panels (b) and (d) correspond to the magnetically disordered phase. $Z_{\mathbf{k}}^{\tau}$ is strongly suppressed in the vicinity of the hot spots with the system close to the quantum critical point, while it is mostly featureless away from it. The alternative proxy to the quasiparticle weight $Z_{\mathbf{k}}^{\omega}$ agrees qualitatively with $Z_{\mathbf{k}}^{\tau}$ as shown in panels (c) and (d), where we scan along the Fermi surface by identifying the maximum of $G_{\mathbf{k}}(\tau = \beta/2, 0)$ for each fixed value of the momentum component k_x .

In Fig. 7.10 we show the temperature dependence of $Z_{\mathbf{k}}^{\tau}(T)$ for several momenta on the Fermi surface. Away from the hot spots ($k_x = 0$ and $k_y = \pi$), $Z_{\mathbf{k}}^{\tau}(T)$ is

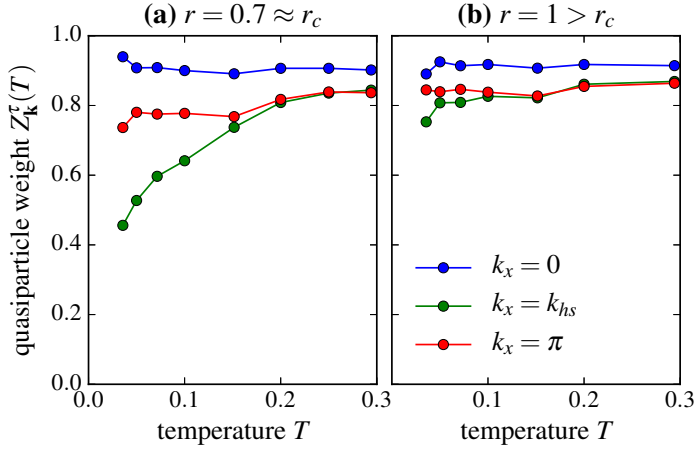


Figure 7.10: Temperature dependence of the proxy for the quasiparticle weight $Z_k^\tau(T)$ for different momenta k_x along the Fermi surface (a) in the vicinity of the QCP at r_c and (b) on the disordered side, $r > r_c$. Here we show data obtained for the $\lambda = 1.5$, $c = 3$ model with $L = 16$.

mostly flat in temperature both for $r \approx r_c$ and for $r > r_c$. However, at the hot spots, with $k_x = k_{hs}$, $Z_{k=k_{hs}}^\tau(T)$ only remains flat in temperature far in the magnetically disordered phase. Conversely, with r tuned close to the quantum critical point r_c the proxy to the quasiparticle weight $Z_{k=k_{hs}}^\tau(T)$ decreases substantially as the temperature is lowered. While we cannot extrapolate this data cleanly to $T = 0$, it is consistent with a vanishing of the hot spot quasiparticle weight $Z_{k=k_{hs}}$ at the quantum critical point. This would indicate a breakdown of Fermi-liquid behavior for momenta close to the hot spots.

The momentum dependence of the two proxies to the Fermi velocity, $v_{k_F}^\omega$ and $v_{k_F}^\tau$, is shown for momenta along the Fermi surface at temperature $T = 0.05$ in Fig. 7.11. In its behavior we do not see a substantial qualitative difference between $r \approx r_c$ close to the quantum critical point and $r > r_c$ in the magnetically disordered phase. In the lower panels of Fig. 7.11 we show the ratio $v_k^\omega(T = 0.05)/v_k^{\text{nonint}}$ with the Fermi velocity v_k^{nonint} of the non-interacting system. Even if a small feature close to the hot spot for $r \approx r_c$ may be visible, it does not provide evidence for a substantial suppression of the Fermi velocity.

Finally, we examine the Matsubara frequency dependence of the self energy Σ_k , defined via $G_k(\omega_n) = (i\omega_n - \varepsilon_k - \Sigma_k(\omega_n))^{-1}$. We show its imaginary in Fig. 7.12. Close to the quantum critical point, $r \approx r_c$, for momenta close to the hot spots the imaginary part of the self energy appears to be nearly independent of frequency. This is consistent with a *constant* scattering rate $\gamma = -\text{Im } \Sigma_{k_{hs}}(\omega_n \rightarrow 0^+) \approx 0.13$, which depends only weakly on temperature. Away from the hot spot and still close

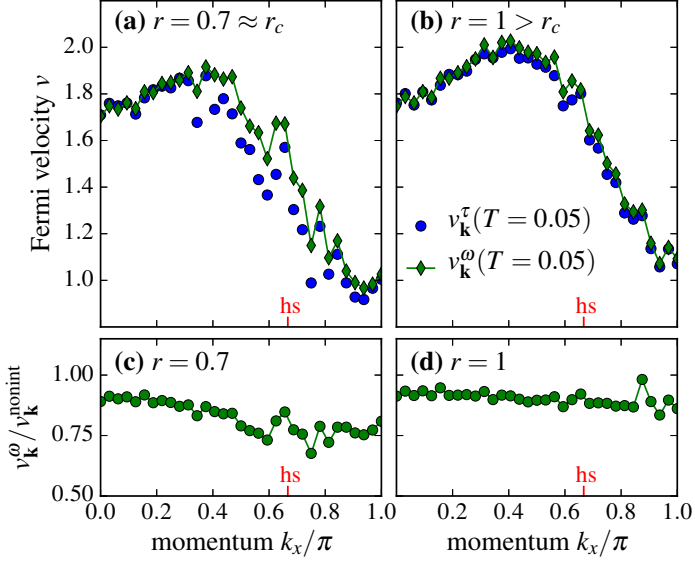


Figure 7.11: (a)-(b) Finite-temperature proxies $v_k^\tau(T)$ and $v_k^\omega(T)$ to the velocity v_k along the Fermi surface. (c)-(d) Velocity renormalization $v_k^\omega(T = 0.05)/v_k^{\text{nonint}}$. The location of the hot spot (hs) is indicated by a red marker. Here we show data obtained for the $\lambda = 1.5$, $c = 3$ model with $L = 16$ at $T = 0.05$.

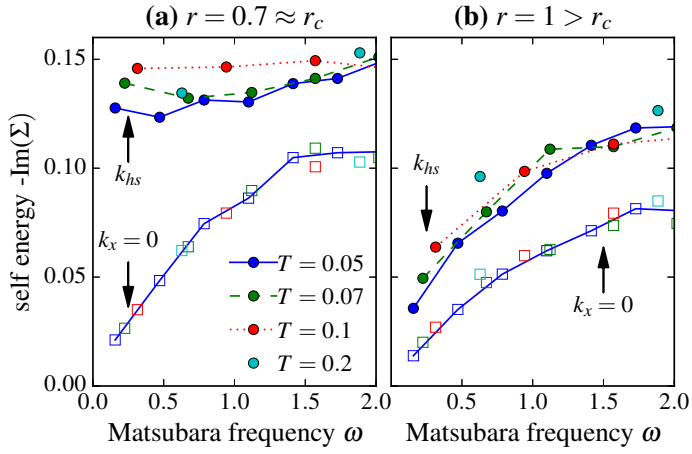


Figure 7.12: Imaginary part of the Matsubara self energy $\text{Im } \Sigma$ for different temperatures and two momenta along the Fermi surface, (a) in the vicinity of the quantum critical point at r_c and (b) on the magnetically disordered side of the phase diagram. Here we show data obtained for $L = 14$. The data for $\mathbf{k} = \mathbf{k}_{hs}$ is indicated by full circles, the momentum away from the hotspot is indicated by empty squares.

to the quantum critical point as well as for any momentum at $r > r_c$ the self energy decreases rapidly as the frequency is lowered to zero.

7.3 Superconducting state

In the previous two sections we have focused on manifestations of quantum critical behavior in the normal state, i.e. at temperatures above the superconducting phase. In this Section we consider the influence of the quantum critical point on the superconducting state that emerges in its vicinity. Here we choose parameters $\lambda = 3$ and $c = 2$, corresponding to the phase diagram of Sec. 6.4, such that T_c^{\max} is sufficiently high to explore properties far below T_c .

For temperatures $T \ll T_c$ we can extract the single-particle excitation energy E_k from the single-particle Green's function $G_k(\tau, 0)$ as explained in the following. We find $G_k(\tau, 0)$ to evolve in imaginary time as shown in the characteristic examples of Fig. 7.13. For intermediate imaginary times $\tau_0 < \tau < \beta/2$ above a microscopic scale $\tau_0 \sim 1$ the single-particle Green's function decays exponentially,

$$G_k(\tau, 0) \propto e^{-E_k^p \tau}, \quad (7.9)$$

and similarly for imaginary times $\beta/2 < \tau < \beta - \tau_0$,

$$G_k(\tau, 0) \propto e^{-E_k^h (\beta - \tau)}. \quad (7.10)$$

At long imaginary times $\tau \approx \beta/2$ statistical errors dominate the signal. The decay constants E_k^p and E_k^h can be extracted by appropriate exponential fits and we define the single-particle excitation energy as their minimum $E_k = \min\{E_k^p, E_k^h\}$.

We can understand the behavior of $G_k(\tau, 0)$ qualitatively. Its exponential decay can be seen to arise from a peak of the spectral function density $A_k(\omega)$ at $\omega \neq 0$, cf. Eq. (7.5). In a Fermi liquid there is a single, sharp peak in the spectral function for some momentum at the corresponding quasiparticle energy. In such a case $G_k(\tau, 0)$ has the form of a monotonic single exponential and is discontinuous, in concordance with the antiperiodic boundary condition in imaginary time. It follows either Eq. (7.9) for particle-like quasiparticles or Eq. (7.10) for hole-like quasiparticles. The behavior is different in a Bardeen-Cooper-Schrieffer (BCS) superconductor, where hole-like and particle-like excitations are allowed in superposition and the spectral function has two δ -peaks at $\omega = \pm E_k$. Then the Green's function takes the form

$$G_k(\tau, 0) = \frac{1}{1 + e^{-\beta E_k}} (a_k^2 e^{-E_k \tau} + b_k^2 e^{-E_k (\beta - \tau)}). \quad (7.11)$$

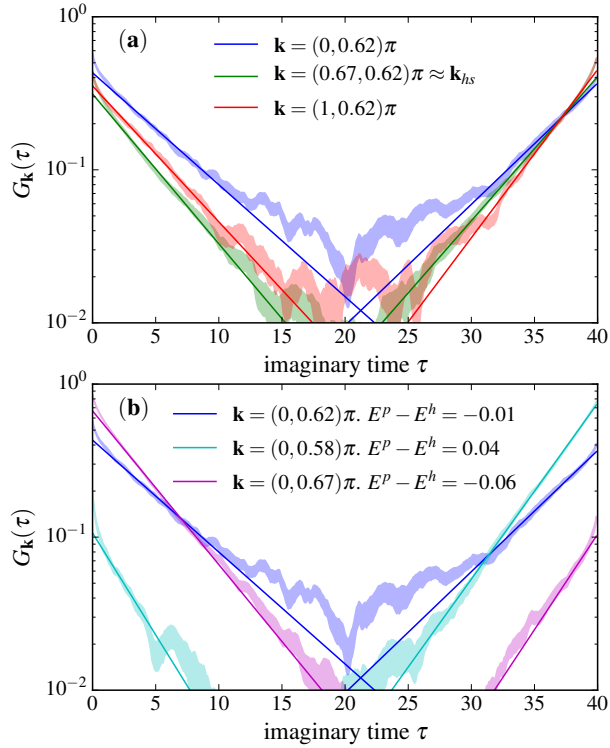


Figure 7.13: Imaginary time evolution of the single-particle Green's function $G_{\mathbf{k}}(\tau) \equiv G_{\mathbf{k}}(\tau, 0)$ for (a) several momenta along the noninteracting Fermi surface and (b) several momenta along a cut perpendicular to the Fermi surface. Here, $L = 12$, $T = 1/40$, $\lambda = 3$, and $c = 2$. Shaded regions indicate the statistical uncertainty. The solid lines are exponential fits.

Here $E_{\mathbf{k}} = \sqrt{\Delta_{\mathbf{k}}^2 + \epsilon_{\mathbf{k}}^2}$ with the quasiparticle dispersion $\epsilon_{\mathbf{k}}$ and the gap $\Delta_{\mathbf{k}}$, and $a_{\mathbf{k}}$, $b_{\mathbf{k}}$ are particle and hole amplitudes, respectively. $G_{\mathbf{k}}(\tau, 0)$ is non-monotonic with a minimum at some $\tau > 0$.

Our numerical data at $T < T_c$ is very similar to the BCS form (7.11) with two reservations. First, the clear exponential behavior is not seen at the shortest imaginary times $\tau < \tau_0$. Second, particle and hole excitation energies differ, $E_{\mathbf{k}}^p \neq E_{\mathbf{k}}^h$, and their difference is larger further away from the Fermi surface, see Fig. 7.13b.

By extracting $E_{\mathbf{k}} = \min \{E_{\mathbf{k}}^p, E_{\mathbf{k}}^h\}$ from our numerical data obtained from simulations at a low temperature $T = 0.025 \approx 0.3T_c$ with r tuned close to the quantum phase transition (such that T_c is close to maximal), we have obtained the momentum resolved plot in Fig. 7.14a for the ψ_y fermions. Across the Brillouin zone $E_{\mathbf{k}}$ has a broad minimum close to the non-interacting Fermi surface. We take the superconducting gap Δ_{k_x} to be the minimum of $E_{\mathbf{k}}$ with respect to k_y and show the extracted Δ_{k_x} in Fig. 7.14b. It varies smoothly as a function of momentum, with no

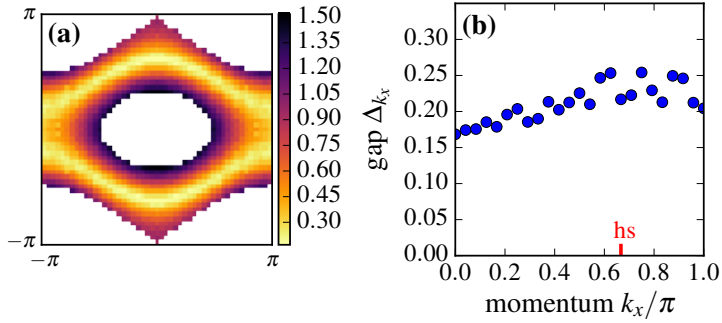


Figure 7.14: (a) Single-particle excitation energy $E_{\mathbf{k}}$ of the ψ_y fermions, as extracted from the imaginary-time evolution of the Green's function $G_{\mathbf{k}}(\tau)$ across the Brillouin zone, cf. Fig. 7.13. (b) Single-particle gap Δ_{k_x} . For both panels data is for parameters $\lambda = 3$, $c = 2$, $r = 10.2$ and $T = 0.025 \approx 0.3 T_c$ and a system size of $L = 12$.

apparent feature at the hot spots. For the data shown in Fig. 7.14 we have combined several DQMC simulations with different twisted boundary conditions to enhance the momentum resolution.

7.4 Discussion

In this Chapter we have focused on the quantum critical regime in the vicinity of the SDW quantum phase transition, yet at temperatures above the superconducting phase. This region of the phase diagram is characterized by the rapid growth of SDW correlations, which we find to be well described by the form

$$\chi_0(\mathbf{q}, \omega_n, r, T) = \frac{1}{a_q(\mathbf{q} - \mathbf{Q})^2 + a_\omega |\omega_n| + a_r(r - r_{c0}) + f(r, T)}. \quad (7.12)$$

over a broad range of parameters. Here the function $f(r, T)$ tends to zero for $T \rightarrow 0$. Remarkably, $\chi_0(\mathbf{q}, \omega_n, r, T \rightarrow 0)$ has the precise form predicted by Hertz and Millis [29, 30]. Accordingly, the critical dynamics of the SDW order parameter are described by a dynamical critical exponent $z = 2$ and strong Landau damping. On the other hand, the function $f(r, T)$ does not show the behavior anticipated by Millis. Close to the estimated location of the quantum critical point in a window of temperatures above T_c we find it to be consistent with a power-law $f(r \approx r_{c0}, T) \sim T^\alpha$ with $\alpha \simeq 2$, while a linear dependence is predicted by Millis theory [30] as stated explicitly in Sachdev's textbook [4, Sec. 18.4]. These findings hold consistently well for correlations of the bosonic SDW order parameter field and for those of a

fermionic bilinear SDW order parameter of the same symmetry.

That Hertz-Millis theory agrees with our data to a large extend is a non-trivial observation. After all in two spatial dimensions it lacks formal justification, even in the large- N limit [20, 34]. Hertz-Millis theory is least successful in describing our data at finite temperature, where the predicted temperature dependence $\chi(T) \sim 1/T$ at criticality conflicts with our findings. Possibly, effects beyond the one-fermion-loop approximation of Hertz-Millis theory become most important at finite temperature. Alternatively, this could well be due to the limited temperature window accessible to us above the superconducting T_c , while fully Hertz-Millis-like behavior might be opaquely hidden under the superconducting dome.

In the same quantum critical regime our analysis of the fermionic Green's function has provided evidence for strong quasiparticle scattering near the hot spots on the Fermi surfaces, where the quasiparticle weight is substantially reduced. This leads to a breakdown of Fermi liquid theory localized to these points of the Brillouin zone. At the hot spots the fermion self energy is only weakly dependent on frequency and the quasiparticle scattering rate extracted there depends only slightly on temperature, down to $T \approx 2T_c$. At that temperature we assume superconducting fluctuations to become important in the metallic state. At lower temperatures the superconducting phase emerges from this state of preformed pairs.

We have also studied the structure of the superconducting gap close to the SDW quantum phase transition. In contrast to the sharp features at the hot spots seen in the analysis of the normal-state single-fermion correlations, we find the gap function to vary smoothly across the Fermi surface. Our model therefore does not reproduce the experimentally found broad maximum near the hot spots in the electron doped cuprate $\text{Pr}_{0.89}\text{LaCe}_{0.11}\text{CuO}_4$ [195].

In our studies we have always found the SDW quantum critical point to be hidden below a superconducting phase, where the Fermi surface is gapped. Consequently, with our model it may never be possible to access a quantum critical regime in the metallic phase that extends over a sufficiently broad range of parameter values to clearly extract scaling exponents. If we could associate the Hertz-Millis form (7.12) with critical exponents, we would obtain a mean-field exponent $\nu = 1/2$ for the correlation length $\xi \sim |r - r_{c0}|^{-\nu}$ and a dynamical critical exponent $z = 2$, $|\mathbf{k}|^z \sim \omega_n$. Then we would expect a scaling law $\text{Im } \Sigma(\omega_n) \sim \sqrt{\omega_n}$ for the fermion self-energy at the hot spots (see e.g. [4, Sec. 18.3.4]). However, the scaling behavior for the fermionic quasi-particles we see in our data disagrees with these expectations, rendering this picture too simple.

8 Concluding remarks and outlook

As stressed before, the numerical phase diagram of our two-band metallic SDW model, discussed in Chap. 6, bears close resemblance to those obtained experimentally for many unconventional superconductors, such as the iron-based superconductors or the electron-doped cuprates. Subsequent work [196] has shown in the mean time by considering a very similar model under variation of the angle between the Fermi velocities in DQMC simulations and in an Eliashberg approximation that it is indeed the hot spots that govern the superconducting transition temperature and the temperature dependence of the superconducting phase. This affirms the assessment that we have captured a universal mechanism in our model that would transfer also to more realistic band structures, which may be inaccessible in sign-problem-free simulations, but share the same hot spot structure. Since the essential physics of many high-temperature superconductors is apparently realized in our model, there are several auspicious future paths of research. With applications in mind, the most interesting questions may concern a better understanding of how the maximum critical temperature depends on the various parameters of the model. As it stands the model is quite basic. It will be very interesting to consider extensions that include more realistic features specific to certain materials. These could include a multi-component SDW order parameter as fitting for the iron pnictides, multiple electronic bands, or additional competing order parameters. Initial studies that explore this direction have appeared in the literature [197, 198].

One such interaction could serve to enhance the weak tendency towards charge-density wave order in our model. We have identified a candidate term that could be added to the action without reintroducing a sign problem. The technical details concerning its implementation are collected in Appendix B. It would be interesting to see in a future investigation if and under which conditions this interaction can promote charge order close to SDW quantum criticality.

Despite its similarities to many materials, our model does not reproduce all properties of the most intensively studied class of high-temperature superconductors, the hole-doped cuprates. It remains to be seen whether models that show a spin-density wave transition like the model studied in this thesis, but with a phase diagram extended into an orthogonal direction, e.g. showing a topologically ordered phase [199], capture their physics, including the pseudogap phase, more closely.

By all appearances in our model the SDW quantum phase transition always occurs inside the superconducting phase. Hence, close to the transition point, the Fermi surface is gapped and in our O(2) model we expect criticality of the $d = 2 + 1$

XY universality class. At temperatures above the superconducting T_c we observe a different functional form of the order parameter susceptibility with prominent similarities to Hertz-Millis theory that we associate to the quantum critical regime of a bare metallic SDW quantum critical point. Here we may actually observe a crossover regime where for instance the single-particle Green's function may not yet exhibit its asymptotic behavior.

In experiments, frequently strong magnetic fields are passed through samples to suppress superconductivity. We presume that a similar effect could be achieved in our model by incorporating a term that explicitly breaks time reversal and inversion symmetries to lift the degeneracy between fermions of opposite momenta, which would remove the Cooper instability. However, with the present DQMC approach such a term would introduce a sign problem, which makes it very hard or impossible to lower temperatures far enough to sufficiently approach a then exposed pure quantum critical point. As of now no alternative formulation of our model is in sight that would not pick up a sign problem when time reversal is broken.

Recently a non-perturbative controlled analytic calculation of the low-energy theory of an O(3) symmetric SDW quantum critical point has appeared [37], where the hot spot structure is equal to the one of our model. The authors find a functional form for the SDW order parameter susceptibility $\chi^{-1}(\mathbf{q}, i\omega_n, \mathbf{r} \rightarrow \mathbf{r}_c, T \rightarrow 0) \sim |\omega_n| + |\mathbf{q}|$, i.e. the dynamical critical exponent is $z = 1$. This result is not in agreement with our numerical data for the O(2) model, which is consistent with a functional form quadratic in momentum. It would be very interesting to see if a similar calculation to Ref. [37] could be carried out for an O(2) symmetric order parameter to be able to compare more directly with our data. O(3) variations of our models have been studied previously in DQMC [11, 200], but not as comprehensively as we have investigated the O(2) model. While the computational cost is significantly higher in the O(3) case, simulations remain feasible and it should be possible to numerically clarify the nature of the SDW correlations with moderate effort, now that the methodology has been developed to the state presented in this thesis. This would clarify if there really is such a striking mismatch for different order parameter dimensions. Of course it could also be the case that we still have not pushed T_c low enough to enter the true quantum critical regime. It could also turn out to be useful to consider a variation of our model with an O(1) Ising-like symmetry, where the superconducting T_c will presumably be reduced due to overall lower energy scales. The superconducting instability was not taken into account in Ref. [37].

Generally, it would be desirable to compare our results to calculations made for the same model with other methods, e.g. in a functional renormalization group (FRG) scheme [45]. It would be interesting to see if an RG flow leads to a strange metal fixed point and if superconductivity comes along with that.

To make closer contact to experimental studies, where transport measurements yielding for instance a T -linear resistivity are the hallmark of strange metal behavior associated to quantum criticality, it would be a worthwhile prospect to evaluate similar quantities from our data. Ideally, this would entail the computation of dynamic quantities, which would make it necessary to perform an analytic continuation.

To obtain the results presented in this thesis we have invested quite a lot of computing time and stretched the DQMC method close to its limits. Finite-size effects have always been a major concern. While we could avoid the worst impact of our limited lattice sizes by imposing an artificial pseudo-magnetic flux, our results close to criticality would benefit from scaling over a wider range of system sizes. Apart from quantum Monte Carlo there is no other well performing numerically exact method available to study fermionic systems on two-dimensional lattices. However, it could turn out to be worthwhile to test alternative flavors of quantum Monte Carlo on the SDW model. The most promising direction for such an endeavor might be the hybrid Monte Carlo method. In Appendix C we show how the formalism can be applied to our model.

Appendix A

Identities for fermionic many-particle states

In this Appendix we review several formal properties of fermionic many-particle states that are essential for the DQMC algorithm. We follow Refs. [83, 87].

Our starting point is a single-particle Hamiltonian, that is bilinear in fermionic creation and annihilation operators:

$$\mathcal{H}_0 = \sum_{a,b} c_a^\dagger [H_0]_{a,b} c_b, \quad (\text{A.1})$$

where the matrix H_0 is Hermitian and $a, b = 1, \dots, N_s$ index the single-particle states. H_0 can always be diagonalized via a unitary matrix U such that $U^\dagger H_0 U = \Lambda$ and Λ is a diagonal matrix. Then we have

$$\mathcal{H}_0 = \sum_a \Lambda_a d_a^\dagger d_a, \quad d_a = \sum_b U_{a,b}^\dagger c_b, \quad d_a^\dagger = \sum_b c_b^\dagger U_{b,a}. \quad (\text{A.2})$$

Under the unitary transformation U the anticommutation relations are preserved for the operators d, d^\dagger : $\{d_a, d_b\} = 0$ and $\{d_a^\dagger, d_b\} = \delta_{a,b}$. Now we are prepared to construct a many-particle eigenstate of \mathcal{H}_0 . A state of N_p particles is characterized by the occupation of N_p different single-particle energy levels $\alpha_1, \dots, \alpha_{N_p}$:

$$d_{\alpha_1}^\dagger d_{\alpha_2}^\dagger \cdots d_{\alpha_{N_p}}^\dagger |0\rangle = \prod_{n=1}^{N_p} \left(\sum_a c_a^\dagger U_{a,\alpha_n} \right) |0\rangle = \prod_{n=1}^{N_p} (c^\dagger P)_n |0\rangle, \quad (\text{A.3})$$

where $|0\rangle$ is the Fock vacuum state, $c^\dagger = (c_1^\dagger, \dots, c_{N_s}^\dagger)$ is a vector of length N_s , and P is the $N_s \times N_p$ matrix that characterizes this many-particle state.

The first property we need shows that the propagation of an N_p -particle state with a single-particle propagator will again produce an N_p -particle state:

Property A.1. For a Hermitian or anti-Hermitian matrix T we have

$$e^{\underline{c}^\dagger T \underline{c}} \prod_{n=1}^{N_p} (\underline{c}^\dagger P)_n |0\rangle = \prod_{n=1}^{N_p} (\underline{c}^\dagger e^T P)_n |0\rangle. \quad (\text{A.4})$$

Proof. First we transform T to a basis where it is diagonal. We find a unitary matrix U with $U^\dagger TU = \Lambda$, where the diagonal matrix Λ is real for Hermitian T and imaginary for anti-Hermitian T . We define new fermionic operators $\underline{d}^\dagger = \underline{c}^\dagger U$ and have:

$$\begin{aligned} e^{\underline{c}^\dagger T \underline{c}} \prod_{n=1}^{N_p} (\underline{c}^\dagger P)_n |0\rangle &= \exp(\underline{d}^\dagger \Lambda \underline{d}) \prod_{n=1}^{N_p} (\underline{d}^\dagger U^\dagger P)_n |0\rangle \\ &= \sum_{\alpha_1, \dots, \alpha_{N_p}} \exp\left(\sum_a \Lambda_a d_a^\dagger d_a\right) d_{\alpha_1}^\dagger d_{\alpha_2}^\dagger \cdots d_{\alpha_{N_p}}^\dagger |0\rangle (U^\dagger P)_{\alpha_1, 1} \cdots (U^\dagger P)_{\alpha_{N_p}, N_p} = \dots \end{aligned}$$

Here we have written out the matrix-vector products that include $\underline{d}^{(\dagger)}$. Since we have $[d_a^\dagger d_a, d_b^\dagger d_b] = 0$, $e^{\lambda d_a^\dagger d_a} d_a^\dagger = e^\lambda d_a^\dagger$, $e^{\lambda d_a^\dagger d_a} d_b^\dagger = d_b^\dagger e^{\lambda d_a^\dagger d_a}$ for $a \neq b$, and $e^{\lambda d_a^\dagger d_a} |0\rangle = |0\rangle$, we can distribute the terms from the exponential as follows:

$$\begin{aligned} \dots &= \sum_{\alpha_1, \dots, \alpha_{N_p}} e^{\Lambda_{\alpha_1}} d_{\alpha_1}^\dagger \cdots e^{\Lambda_{\alpha_{N_p}}} d_{\alpha_{N_p}}^\dagger |0\rangle (U^\dagger P)_{\alpha_1, 1} \cdots (U^\dagger P)_{\alpha_{N_p}, N_p} \\ &= \prod_{n=1}^{N_p} (\underline{d}^\dagger e^\Lambda U^\dagger P)_n |0\rangle = \prod_{n=1}^{N_p} (\underline{c}^\dagger U e^\Lambda U^\dagger P)_n |0\rangle = \prod_{n=1}^{N_p} (\underline{c}^\dagger e^T P)_n |0\rangle. \end{aligned}$$

□

The second property allows us to compute the overlap of two N_p -particle states as a determinant:

Property A.2. The overlap of the states

$$|\Psi\rangle = \prod_{n=1}^{N_p} (\underline{c}^\dagger P)_n |0\rangle, \quad |\Phi\rangle = \prod_{n=1}^{N_p} (\underline{c}^\dagger Q)_n |0\rangle \quad (\text{A.5})$$

is

$$\langle \Psi | \Phi \rangle = \det[P^\dagger Q]. \quad (\text{A.6})$$

Proof.

$$\begin{aligned}\langle \Psi | \Phi \rangle &= \langle 0 | \prod_{n=N_p}^1 (P^\dagger \underline{c})_n \prod_{m=1}^{N_p} (\underline{c}^\dagger Q)_m | 0 \rangle \\ &= \sum_{\substack{\alpha_1, \dots, \alpha_{N_p} \\ \beta_1, \dots, \beta_{N_p}}} P_{N_p, \alpha_{N_p}}^\dagger \cdots P_{1, \alpha_1}^\dagger Q_{\beta_1, 1} \cdots Q_{\beta_{N_p}, N_p} \langle 0 | c_{\alpha_{N_p}} \cdots c_{\alpha_1} c_{\beta_1}^\dagger \cdots c_{\beta_{N_p}}^\dagger | 0 \rangle\end{aligned}$$

The matrix element has non-zero value only if none of the creation or annihilation operators appear more than once and if there is a matching creator for each annihilator:

$$\langle 0 | c_{\alpha_{N_p}} \cdots c_{\alpha_1} c_{\beta_1}^\dagger \cdots c_{\beta_{N_p}}^\dagger | 0 \rangle = \begin{cases} (-1)^\pi, & \begin{array}{l} \bullet \text{ all } \alpha_i \text{ are distinct for } i = 1, \dots, N_p \text{ and} \\ \bullet \text{ a permutation } \pi \in S_{N_p} \text{ exists such that} \\ \quad \beta_i = \alpha_{\pi(i)} \text{ for all } i, \end{array} \\ 0, & \text{else.} \end{cases}$$

$(-1)^\pi$ is the sign of the permutation. We obtain:

$$\langle \Psi | \Phi \rangle = \sum_{\alpha_1, \dots, \alpha_{N_p}} \sum_{\pi \in S_{N_p}} (-1)^\pi P_{N_p, \alpha_{N_p}}^\dagger \cdots P_{1, \alpha_1}^\dagger Q_{\alpha_{\pi(1)}, 1} \cdots Q_{\alpha_{\pi(N_p)}, N_p}.$$

Here the condition that all $\alpha_1, \dots, \alpha_{N_p}$ need to be distinct is implicitly satisfied. All terms where some α_i are equal appear twice under the sum over all permutations, but with different signs, and therefore cancel. Reordering some terms we find

$$\begin{aligned}\langle \Psi | \Phi \rangle &= \sum_{\alpha_1, \dots, \alpha_{N_p}} \sum_{\pi \in S_{N_p}} (-1)^\pi P_{N_p, \alpha_{N_p}}^\dagger \cdots P_{1, \alpha_1}^\dagger Q_{\alpha_1, \pi(1)} \cdots Q_{\alpha_{N_p}, \pi(N_p)} \\ &= \sum_{\pi \in S_{N_p}} (-1)^\pi (P^\dagger Q)_{1, \pi(1)} \cdots (P^\dagger Q)_{N_p, \pi(N_p)} \\ &= \det[P^\dagger Q]\end{aligned}$$

via the Leibniz formula. □

Finally we show the relation that allows us to evaluate traces in fermionic Fock space as matrix determinants in the DQMC algorithm:

Property A.3. For Hermitian $N_s \times N_s$ matrices T_1, \dots, T_n we have

$$\text{Tr} \left[e^{\underline{c}^\dagger T_1 \underline{c}} e^{\underline{c}^\dagger T_2 \underline{c}} \cdots e^{\underline{c}^\dagger T_n \underline{c}} \right] = \det [\mathbb{1} + e^{T_1} e^{T_2} \cdots e^{T_n}]. \quad (\text{A.7})$$

Proof. We set two shorthands $B = e^{T_1} e^{T_2} \cdots e^{T_n}$ and $U = e^{\underline{c}^\dagger T_1 \underline{c}} e^{\underline{c}^\dagger T_2 \underline{c}} \cdots e^{\underline{c}^\dagger T_n \underline{c}}$ and evaluate the determinant

$$\begin{aligned} \det(\mathbb{1} + B) &= \sum_{\pi \in S_{N_s}} (-1)^\pi (\delta_{\pi(1),1} + B_{\pi(1),1}) \cdots (\delta_{\pi(N_s),N_s} + B_{\pi(N_s),N_s}) \\ &= \sum_{\pi \in S_{N_s}} (-1)^\pi \delta_{\pi(1),1} \delta_{\pi(2),2} \cdots \delta_{\pi(N_s),N_s} \\ &\quad + \sum_a \sum_{\pi \in S_{N_s}} (-1)^\pi B_{\pi(a),a} \delta_{\pi(1),1} \cdots \widehat{\delta_{\pi(a),a}} \cdots \delta_{\pi(N_s),N_s} \\ &\quad + \sum_{a,b} \sum_{\substack{\pi \in S_{N_s} \\ b > a}} (-1)^\pi B_{\pi(a),a} B_{\pi(b),b} \delta_{\pi(1),1} \cdots \widehat{\delta_{\pi(a),a}} \cdots \widehat{\delta_{\pi(b),b}} \cdots \delta_{\pi(N_s),N_s} \\ &\quad + \sum_{a,b,c} \sum_{\substack{\pi \in S_{N_s} \\ c > b > a}} (-1)^\pi B_{\pi(a),a} B_{\pi(b),b} B_{\pi(c),c} \cdot \\ &\quad \quad \cdot \delta_{\pi(1),1} \cdots \widehat{\delta_{\pi(a),a}} \cdots \widehat{\delta_{\pi(b),b}} \cdots \widehat{\delta_{\pi(c),c}} \cdots \delta_{\pi(N_s),N_s} \\ &\quad + \cdots . \end{aligned}$$

Factors like $\widehat{\delta_{\pi(a),a}}$ are those omitted from the product. In the first and second sum above only the unit permutation $\pi = \mathbb{1}$ survives the summation over the Kronecker deltas. The third sum is reduced to two terms, one with the unit permutation and one with the exchange $\pi(a) = b$, $\pi(b) = a$. Each following sum runs over permutations of increasingly larger sets:

$$\begin{aligned} \det(\mathbb{1} + B) &= 1 + \sum_a B_{a,a} + \sum_{a,b} \sum_{\substack{\pi \in S(\{a,b\}) \\ b > a}} (-1)^\pi B_{\pi(a),a} B_{\pi(b),b} + \\ &\quad + \sum_{a,b,c} \sum_{\substack{\pi \in S(\{a,b,c\}) \\ c > b > a}} (-1)^\pi B_{\pi(a),a} B_{\pi(b),b} B_{\pi(c),c} + \cdots . \end{aligned}$$

The addends are the determinants of all submatrices (including the non-contiguous

ones) of B that include parts of its diagonal, ordered by particle number:

$$\det(\mathbb{1} + B) = 1 + \sum_a \det(B_{a,a}) + \sum_{\substack{a,b \\ b>a}} \det \begin{pmatrix} B_{a,a} & B_{a,b} \\ B_{b,a} & B_{b,b} \end{pmatrix} + \sum_{\substack{a,b,c \\ c>b>a}} \det \begin{pmatrix} B_{a,a} & B_{a,b} & B_{a,c} \\ B_{b,a} & B_{b,b} & B_{b,c} \\ B_{c,a} & B_{c,b} & B_{c,c} \end{pmatrix} + \dots .$$

To aid with the formalism we introduce a set of sparse rectangular matrices with the purpose of selecting appropriate rows and columns of B . For the two particle case we choose a $N_s \times 2$ matrix $P^{(a,b)}$ with two entries set to 1 and all others to 0 and its transpose $P^{(a,b),\dagger}$:

$$P^{(a,b)} = \begin{pmatrix} 0 & 0 \\ \vdots & \vdots \\ 1 & 0 \\ \vdots & \vdots \\ 0 & 1 \\ \vdots & \vdots \\ 0 & 0 \end{pmatrix} \xleftarrow{a} \quad , \quad P^{(a,b),\dagger} = \begin{pmatrix} a & b \\ \downarrow & \downarrow \\ 0 & \cdots & 1 & \cdots & 0 & \cdots & 0 \\ 0 & \cdots & 0 & \cdots & 1 & \cdots & 0 \end{pmatrix}.$$

Generalizing this for all particle numbers N_p we can write

$$\begin{aligned} \det(\mathbb{1} + B) = 1 + \sum_a \det(P^{(a),\dagger} B P^{(a)}) + \sum_{\substack{a,b \\ b>a}} \det(P^{(a,b),\dagger} B P^{(a,b)}) + \\ + \sum_{\substack{a,b,c \\ c>b>a}} \det(P^{(a,b,c),\dagger} B P^{(a,b,c)}) + \dots . \end{aligned}$$

Making use of property A.2 we identify each determinant as the overlap of two many-particle states, e.g. for $N_p = 2$:

$$\det(P^{(a,b),\dagger} B P^{(a,b)}) = \langle 0 | \prod_{n=2}^1 (P^{(a,b),\dagger} \underline{c})_n \prod_{m=1}^2 (\underline{c}^\dagger B P^{(a,b)})_m | 0 \rangle .$$

By the means of property A.1 we successively convert each factor e^{T_i} in B into the corresponding factor $e^{\underline{c}^\dagger T_i \underline{c}}$ from U :

$$\begin{aligned}\det(P^{(a,b),\dagger} B P^{(a,b)}) &= \langle 0 | \prod_{n=2}^1 (P^{(a,b),\dagger} \underline{c})_n U \prod_{m=1}^2 (\underline{c}^\dagger P^{(a,b)})_m | 0 \rangle \\ &= \langle 0 | c_a c_b U c_b^\dagger c_a^\dagger | 0 \rangle.\end{aligned}$$

In total we obtain

$$\begin{aligned}\det(\mathbb{1} + B) &= \langle 0 | 0 \rangle + \sum_a \langle 0 | c_a U c_a^\dagger | 0 \rangle + \sum_{\substack{a,b \\ b>a}} \langle 0 | c_a c_b U c_b^\dagger c_a^\dagger | 0 \rangle + \\ &\quad + \sum_{\substack{a,b,c \\ c>b>a}} \langle 0 | c_a c_b c_c U c_c^\dagger c_b^\dagger c_a^\dagger | 0 \rangle + \dots \\ &= \text{Tr } U,\end{aligned}$$

which is precisely the trace of U in Fock space. \square

Appendix B

Promoting charge-density wave order

In Chap. 6 we did not find any indication for a strong tendency towards charge-density wave (CDW) order in the SDW model. It would be interesting to see whether an additional interaction could be added to the action that encourages such order in the vicinity of the quantum critical point, in competition with superconductivity. In order not to re-introduce a sign problem we are of course limited in the choice of such interactions that must be compatible with the symmetry of Sec. 4.3.2. A permitted choice is the term

$$\hat{V}_U = -U^2 \sum_i (n_{x,i} - n_{y,i})^2, \quad (\text{B.1})$$

where $n_{\alpha,i} = \psi_{\alpha,i\uparrow}^\dagger \psi_{\alpha,i\uparrow} + \psi_{\alpha,i\downarrow}^\dagger \psi_{\alpha,i\downarrow}$ are local charge operators for flavors $\alpha = x, y$.

This operator has the convenient form of a perfect square, which allows it to be implemented with a discrete variation of the Hubbard-Stratonovich transformation that basically amounts to the expansion of an \exp [201, 202]. To implement this additional interaction we replace terms $\exp(-\Delta\tau \underline{\psi}^\dagger V[\vec{\varphi}(\Delta\tau)] \underline{\psi}) \equiv e^{-\Delta\tau \hat{V}_\varphi}$ by

$$\begin{aligned} e^{-\frac{1}{2}\Delta\tau \hat{V}_\varphi} e^{-\Delta\tau \hat{V}_U} e^{-\frac{1}{2}\Delta\tau \hat{V}_\varphi} &= \sum_{\{l_i=\pm 1, \pm 2\}} \left[\prod_{i=1}^N \frac{\gamma_{l_i}}{4} \right] e^{-\frac{1}{2}\Delta\tau \hat{V}_\varphi} e^{\hat{D}[\{\eta_i\}]} e^{-\frac{1}{2}\Delta\tau \hat{V}_\varphi} + O(\Delta\tau^4) \\ &\propto \sum_{\{l_i=\pm 1, \pm 2\}} \left[\prod_{i=1}^N \gamma_{l_i} \right] e^{-\frac{1}{2}\Delta\tau \hat{V}_\varphi} e^{\hat{D}[\{\eta_i\}]} e^{-\frac{1}{2}\Delta\tau \hat{V}_\varphi} + O(\Delta\tau^4) \\ &= \sum_{\{l_i=\pm 1, \pm 2\}} \left[\prod_{i=1}^N \gamma_{l_i} \right] \underline{\psi}^\dagger e^{-\frac{1}{2}\Delta\tau V_\varphi} e^{D[\{\eta_i\}]} e^{-\frac{1}{2}\Delta\tau V_\varphi} \underline{\psi} + O(\Delta\tau^4) \end{aligned} \quad (\text{B.2})$$

with

$$\begin{aligned}
 \gamma_{\pm 1} &= 1 + \frac{\sqrt{6}}{3}, & \gamma_{\pm 2} &= 1 - \frac{\sqrt{6}}{3}, \\
 \eta_{\pm 1} &= \pm \sqrt{2(3 - \sqrt{6})}, & \eta_{\pm 2} &= \pm \sqrt{2(3 + \sqrt{6})}, \\
 D &= \begin{pmatrix} \underline{d} & \underline{d} & -\underline{d} & -\underline{d} \end{pmatrix}, & d_i &= \sqrt{\Delta\tau} \cdot U \cdot \eta_i \\
 V_\varphi &= \lambda \begin{pmatrix} \underline{a} & \underline{b}^* & \underline{b} & -\underline{a} \\ \underline{a} & \underline{b} & -\underline{a} & -\underline{b}^* \end{pmatrix}, & a_i &= \varphi_i^3, \quad b_i = \varphi_i^1 - i\varphi_i^2 \quad (\text{B.3})
 \end{aligned}$$

such that

$$\begin{aligned}
 e^{-\frac{1}{2}\Delta\tau V_\varphi} e^{D[\{\eta_i\}]} e^{-\frac{1}{2}\Delta\tau V_\varphi} \\
 = \begin{pmatrix} \underline{\text{ch}}^\varphi \circ \underline{\text{ch}}^D + \underline{\text{sh}}^D & \underline{\text{ch}}^\varphi \circ \underline{\text{ch}}^D + \underline{\text{sh}}^D & -\underline{a} \circ \underline{\text{sh}}^\varphi \circ \underline{\text{ch}}^D & -\underline{b} \circ \underline{\text{sh}}^\varphi \circ \underline{\text{ch}}^D \\ -\underline{a} \circ \underline{\text{sh}}^\varphi \circ \underline{\text{ch}}^D & -\underline{b} \circ \underline{\text{sh}}^\varphi \circ \underline{\text{ch}}^D & \underline{\text{ch}}^\varphi \circ \underline{\text{ch}}^D - \underline{\text{sh}}^D & \underline{a} \circ \underline{\text{sh}}^\varphi \circ \underline{\text{ch}}^D \\ -\underline{b}^* \circ \underline{\text{sh}}^\varphi \circ \underline{\text{ch}}^D & \underline{a} \circ \underline{\text{sh}}^\varphi \circ \underline{\text{ch}}^D & \underline{\text{ch}}^\varphi \circ \underline{\text{ch}}^D - \underline{\text{sh}}^D & \underline{\text{ch}}^\varphi \circ \underline{\text{ch}}^D - \underline{\text{sh}}^D \end{pmatrix} \quad (\text{B.4})
 \end{aligned}$$

with

$$\begin{aligned}
 \text{ch}_i^\varphi &= \cosh(\lambda\Delta\tau|\vec{\varphi}_i|) & \text{sh}_i^\varphi &= \frac{\sinh(\lambda\Delta\tau|\vec{\varphi}_i|)}{|\vec{\varphi}_i|} \\
 \text{ch}_i^D &= \cosh(\sqrt{\Delta\tau}U\eta_{l_i}) & \text{sh}_i^D &= \sinh(\sqrt{\Delta\tau}U\eta_{l_i}) \quad (\text{B.5})
 \end{aligned}$$

and

$$\prod_{i=1}^N \gamma_{l_i} = \left(1 + \frac{1}{3}\sqrt{6}\right)^{\#\{l_i=\pm 1\}} \left(1 - \frac{1}{3}\sqrt{6}\right)^{\#\{l_i=\pm 2\}}. \quad (\text{B.6})$$

The inverse of Eq. (B.4) is given by

$$e^{\frac{1}{2}\Delta\tau V_\varphi} e^{-D[\{n_i\}]} e^{\frac{1}{2}\Delta\tau V_\varphi}$$

$$= \begin{pmatrix} \underline{\text{ch}}^\varphi \circ \underline{\text{ch}}^D - \underline{\text{sh}}^D & \underline{\text{ch}}^\varphi \circ \underline{\text{ch}}^D - \underline{\text{sh}}^D & \underline{a} \circ \underline{\text{sh}}^\varphi \circ \underline{\text{ch}}^D & \underline{b} \circ \underline{\text{sh}}^\varphi \circ \underline{\text{ch}}^D \\ \underline{a} \circ \underline{\text{sh}}^\varphi \circ \underline{\text{ch}}^D & \underline{b} \circ \underline{\text{sh}}^\varphi \circ \underline{\text{ch}}^D & \underline{b}^* \circ \underline{\text{sh}}^\varphi \circ \underline{\text{ch}}^D & -\underline{a} \circ \underline{\text{sh}}^\varphi \circ \underline{\text{ch}}^D \\ \underline{b}^* \circ \underline{\text{sh}}^\varphi \circ \underline{\text{ch}}^D & -\underline{a} \circ \underline{\text{sh}}^\varphi \circ \underline{\text{ch}}^D & \underline{\text{ch}}^\varphi \circ \underline{\text{ch}}^D + \underline{\text{sh}}^D & \underline{\text{ch}}^\varphi \circ \underline{\text{ch}}^D + \underline{\text{sh}}^D \end{pmatrix} \quad (\text{B.7})$$

It should be noted that these formulas are valid for all the $O(N)$ variations of the SDW model with $N = 1, 2, 3$, but should be implemented on reduced size matrices for the $O(1)$ and $O(2)$ models. Underlined quantities are vectors of N_s entries or the corresponding diagonal $N_s \times N_s$ matrices. The symbol \circ denotes element-wise multiplication. Moreover, here we use a different order of the components of the fermion spinors ψ^\dagger than in the presentation of the formalism in Part II. We further remark that recombining the exponents into a single exponential in place of the matrix structure (B.4) would introduce a worse Suzuki-Trotter error of $O(\Delta\tau^2)$ per imaginary-time slice instead of $O(\Delta\tau^3)$.

We do not include the factors γ_{l_i} in the definition of the B -matrices, from which the Green's function is computed, as that would quickly blow up the numerical scales. Instead we count them as a separate contribution to the weight of a configuration. The partition function then reads:

$$\mathcal{Z} = \int D\vec{\varphi} Dl e^{-S_\varphi} \cdot \left[\prod_{i=1}^N \prod_{k=1}^m \gamma_{l_i(k)} \right] \cdot \det G_\varphi^{-1} \quad (\text{B.8})$$

The $\gamma_{l_i(\tau)}$ only need to be accounted for during the (local) updates of the $l_i(\tau)$ field. Generally, for a local update at site i in time-slice τ we need to evaluate the determinant of the following 4×4 -matrix, whose structure has not changed

significantly by the inclusion of the new discrete field terms,

$$\Delta^i = \begin{pmatrix} \text{ch}_i^\varphi' \text{ch}_i^D' + \text{sh}_i^D' & & -a'_i \text{sh}_i^\varphi' \text{ch}_i^D' & -b'_i \text{sh}_i^\varphi' \text{ch}_i^D' \\ & \text{ch}_i^\varphi' \text{ch}_i^D' + \text{sh}_i^D' & -b_i'^* \text{sh}_i^\varphi' \text{ch}_i^D' & a'_i \text{sh}_i^\varphi' \text{ch}_i^D' \\ -a'_i \text{sh}_i^\varphi' \text{ch}_i^D' & -b'_i \text{sh}_i^\varphi' \text{ch}_i^D' & \text{ch}_i^\varphi' \text{ch}_i^D' - \text{sh}_i^D' & \\ -b_i'^* \text{sh}_i^\varphi' \text{ch}_i^D' & a'_i \text{sh}_i^\varphi' \text{ch}_i^D' & & \text{ch}_i^\varphi' \text{ch}_i^D' - \text{sh}_i^D' \end{pmatrix} \\ \cdot \begin{pmatrix} \text{ch}_i^\varphi \text{ch}_i^D + \text{sh}_i^D & & -a_i \text{sh}_i^\varphi \text{ch}_i^D & -b_i \text{sh}_i^\varphi \text{ch}_i^D \\ & \text{ch}_i^\varphi \text{ch}_i^D + \text{sh}_i^D & -b_i'^* \text{sh}_i^\varphi \text{ch}_i^D & a_i \text{sh}_i^\varphi \text{ch}_i^D \\ -a_i \text{sh}_i^\varphi \text{ch}_i^D & -b_i \text{sh}_i^\varphi \text{ch}_i^D & \text{ch}_i^\varphi \text{ch}_i^D - \text{sh}_i^D & \\ -b_i'^* \text{sh}_i^\varphi \text{ch}_i^D & a_i \text{sh}_i^\varphi \text{ch}_i^D & & \text{ch}_i^\varphi \text{ch}_i^D - \text{sh}_i^D \end{pmatrix} - \mathbb{1}_4, \quad (\text{B.9})$$

and there is an additional contributing factor to the transition probability: $\gamma'_{l_i(\tau)} / \gamma_{l_i(\tau)}$.

While we have implemented the additional interaction of this Appendix and have checked that with $U = 0$ results are equivalent to those obtained with the regular code, we have not yet thoroughly investigated its effect. Setting $U > 0$ seems to favor a checkerboard distribution of charges seen in the equal-time equal-flavor charge structure factor, which one would already expect naively from the interaction \hat{V}_U . We did not see any interesting structure at a different momentum. However, it may well be that we have not probed the model sufficiently close to the quantum phase transition. It would also be interesting to study the CDW and BDW susceptibilities of Sec. 6.4.2, which include time-displaced information, in presence of this interaction.

Appendix C

Hybrid Monte Carlo

On a regular basis in high energy physics lattice gauge theories are simulated on significantly larger spacetime lattices than typically achieved in condensed matter physics with fermionic quantum Monte Carlo methods. The reason for this high performance lies in the application of *hybrid* Monte Carlo (HMC) methods that incorporate a molecular dynamics process to stochastically evaluate the fermion determinant [203]. Theoretically the computational effort of HMC scales only slightly worse than linearly with the inverse temperature and system size $\beta \cdot N_s$, although the ill condition of fermion matrices at low temperatures slows down the convergence of the conjugate gradient method used to solve a sparse matrix-vector equation, that is central to the algorithm, such that worse scaling is achieved in reality. Nevertheless, it would be worthwhile to check if improvements over the $O(\beta N_s^3)$ scaling of DQMC can be achieved for the SDW model.

Scalettar et al. have described an HMC algorithm for the simulation of many-electron systems and described an implementation for the Hubbard model [204]. In the following we see that the formalism can be readily applied for the O(2) SDW model.

Our starting point is the partition function with the fermions integrated out already:

$$\mathcal{Z} = \int D\vec{\varphi} e^{-S_B} \det \left[\mathbb{1} + \prod_{\ell=m}^1 B_\ell \right]. \quad (\text{C.1})$$

In DQMC we evaluate this determinant directly, which contains a product chain of $m \equiv \beta/\Delta\tau$ matrices of size $4N_s \times 4N_s$, which for the O(2) model can be reduced to $2N_s \times 2N_s$. But equivalently the same determinant can also be computed from a single, larger matrix of size $(4mN_s) \times (4mN_s)$:

$$\mathcal{Z} = \int D\vec{\varphi} e^{-S_B} \det M \quad (\text{C.2})$$

with

$$M = \begin{bmatrix} \mathbb{1} & 0 & 0 & \dots & 0 & B_m \\ -B_1 & \mathbb{1} & 0 & \dots & 0 & 0 \\ 0 & -B_2 & \mathbb{1} & 0 & \dots & 0 \\ 0 & 0 & \ddots & \ddots & & \vdots \\ \vdots & & \ddots & -B_{m-2} & \mathbb{1} & 0 \\ 0 & \dots & & 0 & -B_{m-1} & \mathbb{1} \end{bmatrix}. \quad (\text{C.3})$$

Evaluating this matrix directly would be much more expensive at low temperatures with $O([\beta N_s]^3)$ operations, but that is to be avoided in HMC. For the O(2) SDW model we know that the determinant factorizes as

$$\det M = \det M_1 \det M_2 = |\det M_1|^2 = \det(M_1^\dagger M_1) \quad (\text{C.4})$$

since $M_1 = M_2^*$. This can be seen easily by thinking in the representation (C.1) of the determinant. M_1 is the equivalent of M , but restricted to the $x\uparrow, y\downarrow$ sector of fermion indices, a $(2mN_s) \times (2mN_s)$ matrix. It is useful to set $O = M_1^\dagger M_1$ since that is a Hermitian positive-definite matrix. This allows us to use a Gaussian integral identity for vectors of complex variables

$$\int d\underline{\chi}^* d\underline{\chi} e^{-\underline{\chi}^\dagger O^{-1} \underline{\chi}} = \det O. \quad (\text{C.5})$$

We obtain for the partition function

$$\mathcal{Z} = \int D\vec{\varphi} e^{-S_B} \det O = \int D\vec{\varphi} D\chi^* D\chi e^{-S_{\text{eff}}} \quad (\text{C.6})$$

with the effective action $S_{\text{eff}} = S_B + \underline{\chi}^\dagger O^{-1} \underline{\chi}$. The new complex field χ is also called a “pseudo fermion” field. From this starting point the HMC sampling algorithm can be implemented as detailed in Ref. [204].

The HMC method has not found wide use for models of strongly correlated many-electron systems. One reason for this is that it has not been found to be stable in its early applications to the Hubbard model. However, these problems were most likely really issues of lacking *ergodicity* [205]. While $\det O$ is always positive by construction, $\det M_1$ can also be negative. If it is negative, there will also be field configurations for which it is zero. In such a case the effective action diverges, $S_{\text{eff}} \rightarrow \infty$, which can pose an insurmountable barrier to the HMC algorithm if a

Hubbard-Stratonovich transformation is used that leads to strictly real determinants $\det M_1$ as it is commonly done for the Hubbard model. In the O(2) SDW model these determinants are complex by construction and consequently the topology of the complex plane allows for some freedom to avoid the zero. It is therefore plausible that a well performing and ergodic HMC algorithm can be set up for the O(2) SDW model. Initial results for the repulsive Hubbard model with a specially adapted Hubbard-Stratonovich transformation that avoids this issue show some potential [205].

Bibliography

- [1] P. Gegenwart, Q. Si, and F. Steglich, Quantum criticality in heavy-fermion metals, *Nat. Phys.* **4**, 186 (2008).
- [2] S. Sachdev, Quantum criticality and the phase diagram of the cuprates, *Phys. C Supercond.* **470**, S4 (2010).
- [3] T. Shibauchi, A. Carrington, and Y. Matsuda, A Quantum Critical Point Lying Beneath the Superconducting Dome in Iron Pnictides, *Annu. Rev. Condens. Matter Phys.* **5**, 113 (2014).
- [4] S. Sachdev, *Quantum Phase Transitions*, 2nd ed. (Cambridge University Press, Cambridge, UK, 2011).
- [5] H. v. Löhneysen, A. Rosch, M. Vojta, and P. Wölfle, Fermi-liquid instabilities at magnetic quantum phase transitions, *Rev. Mod. Phys.* **79**, 1015 (2007).
- [6] A. Abanov, A. V. Chubukov, and J. Schmalian, Quantum-critical theory of the spin-fermion model and its application to cuprates: Normal state analysis, *Adv. Phys.* **52**, 119 (2003).
- [7] D. J. Scalapino, A common thread: The pairing interaction for unconventional superconductors, *Rev. Mod. Phys.* **84**, 1383 (2012).
- [8] R. Blankenbecler, D. J. Scalapino, and R. L. Sugar, Monte Carlo calculations of coupled boson-fermion systems. I, *Phys. Rev. D* **24**, 2278 (1981).
- [9] E. Y. Loh, J. E. Gubernatis, R. T. Scalettar, S. R. White, D. J. Scalapino, and R. L. Sugar, Sign problem in the numerical simulation of many-electron systems, *Phys. Rev. B* **41**, 9301 (1990).
- [10] C. Wu and S.-C. Zhang, Sufficient condition for absence of the sign problem in the fermionic quantum Monte Carlo algorithm, *Phys. Rev. B* **71**, 155115 (2005).
- [11] E. Berg, M. A. Metlitski, and S. Sachdev, Sign-Problem-Free Quantum Monte Carlo of the Onset of Antiferromagnetism in Metals, *Science* **338**, 1606 (2012).
- [12] M. Vojta, Quantum phase transitions, *Rep. Prog. Phys.* **66**, 2069 (2003).
- [13] S. L. Sondhi, S. M. Girvin, J. P. Carini, and D. Shahar, Continuous quantum phase transitions, *Rev. Mod. Phys.* **69**, 315 (1997).
- [14] B. Widom, Surface tension and molecular correlations near the critical point, *J. Chem. Phys.* **43**, 3892 (1965).
- [15] K. G. Wilson, Renormalization Group and Critical Phenomena. I. Renormalization Group and the Kadanoff Scaling Picture, *Phys. Rev. B* **4**, 3174 (1971).
- [16] K. G. Wilson, Renormalization Group and Critical Phenomena. II. Phase-Space Cell Analysis of Critical Behavior, *Phys. Rev. B* **4**, 3184 (1971).

Bibliography

- [17] N. D. Mermin and H. Wagner, Absence of ferromagnetism or antiferromagnetism in one- or two-dimensional isotropic Heisenberg models, *Phys. Rev. Lett.* **17**, 1133 (1966).
- [18] M. Imada, A. Fujimori, and Y. Tokura, Metal-insulator transitions, *Rev. Mod. Phys.* **70**, 1039 (1998).
- [19] C. Castellani, C. Di Castro, and M. Grilli, The charge-density-wave quantum-critical-point scenario, *Phys. C Supercond.* **282-287**, 260 (1997).
- [20] M. A. Metlitski and S. Sachdev, Quantum phase transitions of metals in two spatial dimensions. I. Ising-nematic order, *Phys. Rev. B* **82**, 075127 (2010).
- [21] S. Lederer, Y. Schattner, E. Berg, and S. A. Kivelson, Enhancement of Superconductivity near a Nematic Quantum Critical Point, *Phys. Rev. Lett.* **114**, 097001 (2015).
- [22] J. Hubbard, Electron Correlations in Narrow Energy Bands, *Proc. R. Soc. London A Math. Phys. Eng. Sci.* **276**, 238 (1963).
- [23] E. Fradkin, *Field Theories of Condensed Matter Physics*, 2nd ed. (Cambridge University Press, Cambridge, UK, 2013).
- [24] S. Sachdev, A. V. Chubukov, and A. Sokol, Crossover and scaling in a nearly antiferromagnetic Fermi liquid in two dimensions, *Phys. Rev. B* **51**, 14874 (1995).
- [25] A. Altland and B. Simons, *Condensed Matter Field Theory*, 2nd ed. (Cambridge University Press, Cambridge, UK, 2010).
- [26] P. Kopietz, *Bosonization of Interacting Fermions in Arbitrary Dimensions*, Lecture Notes in Physics Monographs, Vol. 48 (Springer, Berlin, 1997).
- [27] A. Abanov and A. Chubukov, Spin-Fermion Model near the Quantum Critical Point: One-Loop Renormalization Group Results, *Phys. Rev. Lett.* **84**, 5608 (2000).
- [28] A. V. Chubukov, D. Pines, and J. Schmalian, A Spin Fluctuation Model for d-Wave Superconductivity, in *Superconductivity: Conventional and Unconventional Superconductors*, edited by K. H. Bennemann and J. B. Ketterson (Springer, Berlin, 2008) pp. 1349–1413.
- [29] J. A. Hertz, Quantum critical phenomena, *Phys. Rev. B* **14**, 1165 (1976).
- [30] A. J. Millis, Effect of a nonzero temperature on quantum critical points in itinerant fermion systems, *Phys. Rev. B* **48**, 7183 (1993).
- [31] A. Abanov and A. Chubukov, Anomalous Scaling at the Quantum Critical Point in Itinerant Antiferromagnets, *Phys. Rev. Lett.* **93**, 255702 (2004).
- [32] M. A. Metlitski and S. Sachdev, Quantum phase transitions of metals in two spatial dimensions. II. Spin density wave order, *Phys. Rev. B* **82**, 075128 (2010).
- [33] S. A. Hartnoll, D. M. Hofman, M. A. Metlitski, and S. Sachdev, Quantum critical response at the onset of spin-density-wave order in two-dimensional metals, *Phys. Rev. B* **84**, 125115 (2011).

- [34] S.-S. Lee, Low-energy effective theory of Fermi surface coupled with U(1) gauge field in 2+1 dimensions, Phys. Rev. B **80**, 165102 (2009).
- [35] D. F Mross, J. McGreevy, H. Liu, and T. Senthil, Controlled expansion for certain non-Fermi-liquid metals, Phys. Rev. B **82**, 045121 (2010).
- [36] D. Dalidovich and S.-S. Lee, Perturbative non-Fermi liquids from dimensional regularization, Phys. Rev. B **88**, 245106 (2013).
- [37] A. Schlief, P Lunts, and S.-S. Lee, Exact critical exponents for the antiferromagnetic quantum critical metal in two dimensions, eprint (2016), arXiv:1608.06927 [cond-mat.str-el].
- [38] J. Rech, C. Pépin, and A. V. Chubukov, Quantum critical behavior in itinerant electron systems: Eliashberg theory and instability of a ferromagnetic quantum critical point, Phys. Rev. B **74**, 195126 (2006).
- [39] K. B. Efetov, H. Meier, and C. Pépin, Pseudogap state near a quantum critical point, Nat. Phys. **9**, 442 (2013).
- [40] J. Lee, P Strack, and S. Sachdev, Quantum criticality of reconstructing Fermi surfaces in antiferromagnetic metals, Phys. Rev. B **87**, 045104 (2013).
- [41] A. L. Fitzpatrick, S. Kachru, J. Kaplan, and S. Raghu, Non-Fermi-liquid behavior of large- N_B quantum critical metals, Phys. Rev. B **89**, 165114 (2014).
- [42] T. Holder and W. Metzner, Anomalous dynamical scaling from nematic and U(1) gauge field fluctuations in two-dimensional metals, Phys. Rev. B **92**, 041112 (2015).
- [43] C. M. Varma, Quantum Criticality in Quasi-Two-Dimensional Itinerant Antiferromagnets, Phys. Rev. Lett. **115**, 186405 (2015).
- [44] C. M. Varma, L. Zhu, and A. Schröder, Quantum critical response function in quasi-two-dimensional itinerant antiferromagnets, Phys. Rev. B **92**, 155150 (2015).
- [45] S. A. Maier and P. Strack, Universality in antiferromagnetic strange metals, Phys. Rev. B **93**, 165114 (2016).
- [46] D. Scalapino, E. Loh, and J. Hirsch, d -wave pairing near a spin-density-wave instability, Phys. Rev. B **34**, 8190 (1986).
- [47] A. Abanov, A. V. Chubukov, and A. M. Finkel'stein, Coherent vs. incoherent pairing in 2D systems near magnetic instability, EPL (Europhys. Lett.) **54**, 488 (2001).
- [48] A. Abanov, A. V. Chubukov, and M. R. Norman, Gap anisotropy and universal pairing scale in a spin-fluctuation model of cuprate superconductors, Phys. Rev. B **78**, 220507 (2008).
- [49] M. A. Metlitski and S. Sachdev, Instabilities near the onset of spin density wave order in metals, New J. Phys. **12**, 105007 (2010).

- [50] Y. Wang and A. Chubukov, Superconductivity at the Onset of Spin-Density-Wave Order in a Metal, *Phys. Rev. Lett.* **110**, 127001 (2013).
- [51] L. E. Hayward, D. G. Hawthorn, R. G. Melko, and S. Sachdev, Angular Fluctuations of a Multicomponent Order Describe the Pseudogap of $\text{YBa}_2\text{Cu}_3\text{O}_{6+x}$, *Science* **343**, 1336 (2014).
- [52] H. Meier, C. Pépin, M. Einenkel, and K. B. Efetov, Cascade of phase transitions in the vicinity of a quantum critical point, *Phys. Rev. B* **89**, 195115 (2014).
- [53] C. Pépin, V. S. de Carvalho, T. Kloss, and X. Montiel, Pseudogap, charge order, and pairing density wave at the hot spots in cuprate superconductors, *Phys. Rev. B* **90**, 195207 (2014).
- [54] Y. Wang and A. Chubukov, Charge-density-wave order with momentum $(2Q, 0)$ and $(0, 2Q)$ within the spin-fermion model: Continuous and discrete symmetry breaking, preemptive composite order, and relation to pseudogap in hole-doped cuprates, *Phys. Rev. B* **90**, 035149 (2014).
- [55] Y. Wang, D. F. Agterberg, and A. Chubukov, Interplay between pair-and charge-density-wave orders in underdoped cuprates, *Phys. Rev. B* **91**, 115103 (2015).
- [56] Y. Wang, D. F. Agterberg, and A. Chubukov, Coexistence of charge-density-wave and pair-density-wave orders in underdoped cuprates, *Phys. Rev. Lett.* **114**, 197001 (2015).
- [57] J. G. Bednorz and K. A. Müller, Possible high- T_c superconductivity in the Ba-La-Cu-O system, *Z. Phys. B* **64**, 189 (1986).
- [58] A. J. Leggett, What DO we know about high T_c ? *Nat. Phys.* **2**, 134 (2006).
- [59] J. Bardeen, L. N. Cooper, and J. R. Schrieffer, Theory of Superconductivity, *Phys. Rev.* **108**, 1175 (1957).
- [60] F. Steglich, J. Aarts, C. D. Bredl, W. Lieke, D. Meschede, W. Franz, and H. Schäfer, Superconductivity in the Presence of Strong Pauli Paramagnetism: CeCu_2Si_2 , *Phys. Rev. Lett.* **43**, 1892 (1979).
- [61] D. Jérôme, A. Mazaud, M. Ribault, and K. Bechgaard, Superconductivity in a synthetic organic conductor $(\text{TMTSF})_2\text{PF}_6$, *J. Physique Lett.* **41**, 95 (1980).
- [62] Y. Kamihara, H. Hiramatsu, M. Hirano, R. Kawamura, H. Yanagi, T. Kamiya, and H. Hosono, Iron-Based Layered Superconductor: LaOFeP , *J. Am. Chem. Soc.* **128**, 10012 (2006).
- [63] M. Nicklas, O. Stockert, T. Park, K. Habicht, K. Kiefer, L. D. Pham, J. D. Thompson, Z. Fisk, and F. Steglich, Magnetic structure of Cd-doped CeCoIn_5 , *Phys. Rev. B* **76**, 052401 (2007).
- [64] L. D. Pham, T. Park, S. Maquilon, J. D. Thompson, and Z. Fisk, Reversible Tuning of the Heavy-Fermion Ground State in CeCoIn_5 , *Phys. Rev. Lett.* **97**, 056404 (2006).

- [65] N. P. Armitage, P. Fournier, and R. L. Greene, Progress and perspectives on electron-doped cuprates, *Rev. Mod. Phys.* **82**, 2421 (2010).
- [66] R. M. Fernandes, D. K. Pratt, W. Tian, J. Zarestky, A. Kreyssig, S. Nandi, M. G. Kim, A. Thaler, N. Ni, P. C. Canfield, R. J. McQueeney, J. Schmalian, and A. I. Goldman, Unconventional pairing in the iron arsenide superconductors, *Phys. Rev. B* **81**, 140501 (2010).
- [67] S. Sachdev and B. Keimer, Quantum criticality, *Physics Today* **64**, 29 (2011).
- [68] N. Doiron-Leyraud, P. Auban-Senzier, S. René de Cotret, C. Bourbonnais, D. Jérôme, K. Bechgaard, and L. Taillefer, Correlation between linear resistivity and T_c in the Bechgaard salts and the pnictide superconductor $\text{Ba}(\text{Fe}_{1-x}\text{Co}_x)_2\text{As}_2$, *Phys. Rev. B* **80**, 214531 (2009).
- [69] B. Keimer, S. A. Kivelson, M. R. Norman, S. Uchida, and J. Zaanen, From quantum matter to high-temperature superconductivity in copper oxides, *Nature* **518**, 179 (2015).
- [70] E. Fradkin, S. A. Kivelson, and J. M. Tranquada, Colloquium: Theory of intertwined orders in high temperature superconductors, *Rev. Mod. Phys.* **87**, 457 (2015).
- [71] H. Fehske, R. Schneider, and A. Weiße, eds., *Computational Many-Particle Physics*, Lecture Notes in Physics, Vol. 739 (Springer, Berlin, 2008).
- [72] A. Avella and F. Mancini, eds., *Strongly Correlated Systems Numerical Methods*, Springer Series in Solid-State Sciences, Vol. 176 (Springer, Berlin, 2013).
- [73] C. Lanczos, An iteration method for the solution of the eigenvalue problem of linear differential and integral operators, *J. Res. Natl. Bur. Stand.* **45**, 255 (1950).
- [74] A. M. Läuchli, Numerical Simulations of Frustrated Systems, in *Introduction to Frustrated Magnetism: Materials, Experiments, Theory*, edited by C. Lacroix, P. Mendels, and F. Mila (Springer, Berlin, 2011) pp. 481–511.
- [75] S. R. White, Density matrix formulation for quantum renormalization groups, *Phys. Rev. Lett.* **69**, 2863 (1992).
- [76] U. Schollwöck, The density-matrix renormalization group, *Rev. Mod. Phys.* **77**, 259 (2005).
- [77] U. Schollwöck, The density-matrix renormalization group in the age of matrix product states, *Ann. Phys. (N. Y.)* **326**, 96 (2011).
- [78] E. Stoudenmire and S. R. White, Studying Two-Dimensional Systems with the Density Matrix Renormalization Group, *Annu. Rev. Condens. Matter Phys.* **3**, 111 (2012).
- [79] J. Eisert, M. Cramer, and M. B. Plenio, Colloquium: Area laws for the entanglement entropy, *Rev. Mod. Phys.* **82**, 277 (2010).
- [80] S. Yan, D. A. Huse, and S. R. White, Spin-Liquid Ground State of the $S = 1/2$ Kagome Heisenberg Antiferromagnet, *Science* **332**, 1173 (2011).

- [81] G. Ehlers, J. Sólyom, Ö. Legeza, and R. M. Noack, Entanglement structure of the Hubbard model in momentum space, *Phys. Rev. B* **92**, 235116 (2015).
- [82] J. Gubernatis, N. Kawashima, and P. Werner, *Quantum Monte Carlo methods: Algorithms for lattice models* (Cambridge University Press, Cambridge, UK, 2016).
- [83] F. Assaad and H. Evertz, World-line and determinantal quantum Monte Carlo methods for spins, phonons and electrons, in *Computational Many-Particle Physics*, edited by H. Fehske, R. Schneider, and A. Weiße (Springer, Berlin, 2008) pp. 277–356.
- [84] R. G. Melko, Stochastic series expansion quantum Monte Carlo, in *Strongly Correlated Systems: Numerical Methods*, edited by A. Avella and F. Mancini (Springer, Berlin, 2013) pp. 185–206.
- [85] F. F. Assaad, Quantum Monte Carlo methods on lattices: The determinantal approach, in *Quantum Simulations of Complex Many-Body Systems: From Theory to Algorithms*, NIC Series, Vol. 10, edited by J. Grotendorst, D. Marx, and A. Muramatsu (John von Neumann Institute for Computing, Jülich, 2002) pp. 99–156.
- [86] R. R. dos Santos, Introduction to quantum Monte Carlo simulations for fermionic systems, *Braz. J. Phys.* **33**, 36 (2003).
- [87] E. Loh Jr. and J. E. Gubernatis, Stable numerical simulations of models of interacting electrons in condensed-matter physics, in *Electronic Phase Transitions, Modern Problems in Condensed Matter Sciences*, Vol. 32, edited by W. Hanke and Y. Kopaev (North-Holland, Amsterdam, 1992) Chap. 4, pp. 177–235.
- [88] M. Suzuki, General Review of Quantum Statistical Monte Carlo Methods, in *Quantum Monte Carlo Methods in Equilibrium and Nonequilibrium Systems*, Springer Series in Solid-State Sciences, Vol. 74, edited by M. Suzuki (Springer, Berlin, 1987) pp. 2–22.
- [89] R. M. Fye, New results on Trotter-like approximations, *Phys. Rev. B* **33**, 6271 (1986).
- [90] M. E. J. Newman and G. T. Barkema, *Monte Carlo Methods In Statistical Physics* (Oxford University Press, Oxford, 1999).
- [91] B. A. Berg, *Markov chain Monte Carlo simulations and their statistical analysis* (World Scientific, Singapore, 2004).
- [92] D. P. Landau and K. Binder, *A Guide to Monte Carlo Simulations in Statistical Physics*, 3rd ed. (Cambridge University Press, Cambridge, UK, 2009).
- [93] W. Krauth, *Statistical Mechanics: Algorithms And Computations* (Oxford University Press, Oxford, 2006).
- [94] K. Binder and D. Heermann, *Monte Carlo Simulation in Statistical Physics: An Introduction*, 5th ed. (Springer, Heidelberg, 2010).

- [95] W. Janke, Monte Carlo Methods in Classical Statistical Physics, in *Computational Many-Particle Physics*, Lecture Notes in Physics, Vol. 739, edited by H. Fehske, R. Schneider, and A. Weiße (Springer, Berlin, 2008) pp. 79–140.
- [96] H. G. Katzgraber, Introduction to Monte Carlo Methods, eprint (2000), arXiv:0905.1629 [cond-mat.stat-mech].
- [97] K. Rummukainen, Simulation methods in physics, (2003; accessed September 9, 2016), <http://www.helsinki.fi/~rummukai/simu/>.
- [98] S. Weinzierl, Introduction to Monte Carlo methods, eprint (2000), arXiv:hep-ph/0006269 .
- [99] N. Metropolis, A. W. Rosenbluth, M. N. Rosenbluth, A. H. Teller, and E. Teller, Equation of State Calculations by Fast Computing Machines, *J. Chem. Phys.* **21**, 1087 (1953).
- [100] A. Sokal, Monte Carlo Methods in Statistical Mechanics: Foundations and New Algorithms, in *Functional Integration: Basics and Applications*, NATO ASI Series B: Physics, Vol. 361, edited by C. DeWitt-Morette, P. Cartier, and A. Folacci (Springer, New York, 1997) pp. 131–192.
- [101] W. Janke, Statistical Analysis of Simulations: Data Correlations and Error Estimation, in *Quantum Simulations of Complex Many-Body Systems: From Theory to Algorithms*, NIC Series, Vol. 10, edited by J. Grotendorst, D. Marx, and A. Muramatsu (John von Neumann Institute for Computing, Jülich, 2002) pp. 423–445.
- [102] K. B. Petersen and M. S. Pedersen, *The Matrix Cookbook* (Technical University of Denmark, Lyngby, 2012) version November 15, 2012, <http://www2.imm.dtu.dk/pubdb/p.php?3274>.
- [103] R. Žitko, SNEG – Mathematica package for symbolic calculations with second-quantization-operator expressions, *Comput. Phys. Commun.* **182**, 2259 (2011).
- [104] J. E. Hirsch, D. J. Scalapino, R. L. Sugar, and R. Blankenbecler, Efficient Monte Carlo Procedure for Systems with Fermions, *Phys. Rev. Lett.* **47**, 1628 (1981).
- [105] J. E. Hirsch, R. L. Sugar, D. J. Scalapino, and R. Blankenbecler, Monte Carlo simulations of one-dimensional fermion systems, *Phys. Rev. B* **26**, 5033 (1982).
- [106] T. Nakamura, Vanishing of the negative-sign problem of quantum Monte Carlo simulations in one-dimensional frustrated spin systems, *Phys. Rev. B* **57**, R3197 (1998).
- [107] M. Troyer and U.-J. Wiese, Computational Complexity and Fundamental Limitations to Fermionic Quantum Monte Carlo Simulations, *Phys. Rev. Lett.* **94**, 170201 (2005).
- [108] S. Mertens, Computational Complexity for Physicists, *Comput. Sci. Eng.* **4**, 31 (2002).

Bibliography

- [109] R. K. Kaul, R. G. Melko, and A. W. Sandvik, Bridging Lattice-Scale Physics and Continuum Field Theory with Quantum Monte Carlo Simulations, *Annu. Rev. Condens. Matter Phys.* **4**, 179 (2013).
- [110] F. Barahona, On the computational complexity of Ising spin glass models, *J. Phys. A. Math. Gen.* **15**, 3241 (1982).
- [111] F. Gebhard, *The Mott Metal-Insulator Transition*, Springer Tracts in Modern Physics, Vol. 137 (Springer, Berlin, 1997).
- [112] J. E. Hirsch, Monte Carlo Study of the Two-Dimensional Hubbard Model, *Phys. Rev. Lett.* **51**, 1900 (1983).
- [113] J. E. Hirsch, Two-dimensional Hubbard model: Numerical simulation study, *Phys. Rev. B* **31**, 4403 (1985).
- [114] S. White, D. Scalapino, R. Sugar, E. Loh, J. Gubernatis, and R. Scalettar, Numerical study of the two-dimensional Hubbard model, *Phys. Rev. B* **40**, 506 (1989).
- [115] J. E. Hirsch, Discrete Hubbard-Stratonovich transformation for fermion lattice models, *Phys. Rev. B* **28**, 4059 (1983).
- [116] Z. Y. Meng, T. C. Lang, S. Wessel, F. F. Assaad, and A. Muramatsu, Quantum spin liquid emerging in two-dimensional correlated Dirac fermions, *Nature* **464**, 847 (2010).
- [117] S. Sorella, Y. Otsuka, and S. Yunoki, Absence of a Spin Liquid Phase in the Hubbard Model on the Honeycomb Lattice, *Sci. Rep.* **2**, 992 (2012).
- [118] F. F. Assaad and I. F. Herbut, Pinning the Order: The Nature of Quantum Criticality in the Hubbard Model on Honeycomb Lattice, *Phys. Rev. X* **3**, 031010 (2013).
- [119] F. Assaad, Quantum Monte Carlo Simulations of the Half-Filled Two-Dimensional Kondo Lattice Model, *Phys. Rev. Lett.* **83**, 796 (1999).
- [120] S. Capponi and F. Assaad, Spin and charge dynamics of the ferromagnetic and antiferromagnetic two-dimensional half-filled Kondo lattice model, *Phys. Rev. B* **63**, 155114 (2001).
- [121] Z. Cai, H.-H. Hung, L. Wang, D. Zheng, and C. Wu, Pomeranchuk Cooling of SU(2N) Ultracold Fermions in Optical Lattices, *Phys. Rev. Lett.* **110**, 220401 (2013).
- [122] T. C. Lang, Z. Y. Meng, A. Muramatsu, S. Wessel, and F. F. Assaad, Dimerized solids and resonating plaquette order in SU(N)-Dirac fermions, *Phys. Rev. Lett.* **111**, 066401 (2013).
- [123] D. Wang, Y. Li, Z. Cai, Z. Zhou, Y. Wang, and C. Wu, Competing Orders in the 2D Half-Filled SU(2N) Hubbard Model through the Pinning-Field Quantum Monte Carlo Simulations, *Phys. Rev. Lett.* **112**, 156403 (2014).
- [124] D. Zheng, G. M. Zhang, and C. Wu, Particle-hole symmetry and interaction effects in the Kane-Mele-Hubbard model, *Phys. Rev. B* **84**, 205121 (2011).

- [125] M. Hohenadler, T. C. Lang, and F. F. Assaad, Correlation effects in quantum spin-Hall insulators: A quantum Monte Carlo study, Phys. Rev. Lett. **106**, 100403 (2011).
- [126] A. Messiah, *Quantum Mechanics* (Dover, Mineola, NY, 2014).
- [127] C. Wu, J.-P. Hu, and S.-C. Zhang, Exact SO(5) Symmetry in the Spin-3/2 Fermionic System, Phys. Rev. Lett. **91**, 186402 (2003).
- [128] S. Capponi, C. Wu, and S.-C. Zhang, Current carrying ground state in a bilayer model of strongly correlated systems, Phys. Rev. B **70**, 220505 (2004).
- [129] H.-K. Tang, X. Yang, J. Sun, and H.-Q. Lin, Berezinskii-Kosterlitz-Thouless phase transition of spin-orbit coupled Fermi gas in optical lattice, EPL (Europhys. Lett.) **107**, 40003 (2014).
- [130] S. Chandrasekharan and U.-J. Wiese, Meron-Cluster Solution of Fermion Sign Problems, Phys. Rev. Lett. **83**, 3116 (1999).
- [131] S. Chandrasekharan, Fermion bag approach to lattice field theories, Phys. Rev. D **82**, 025007 (2010).
- [132] S. Chandrasekharan and A. Li, Fermion Bags, Duality, and the Three Dimensional Massless Lattice Thirring Model, Phys. Rev. Lett. **108**, 140404 (2012).
- [133] Z.-X. Li, Y.-F. Jiang, and H. Yao, Solving the fermion sign problem in quantum Monte Carlo simulations by Majorana representation, Phys. Rev. B **91**, 241117(R) (2015).
- [134] L. Wang, Y.-H. Liu, M. Iazzi, M. Troyer, and G. Harcos, Split Orthogonal Group: A Guiding Principle for Sign-Problem-Free Fermionic Simulations, Phys. Rev. Lett. **115**, 250601 (2015).
- [135] Z. C. Wei, C. Wu, Y. Li, S. Zhang, and T. Xiang, Majorana Positivity and the Fermion Sign Problem of Quantum Monte Carlo Simulations, Phys. Rev. Lett. **116**, 250601 (2016).
- [136] Z.-X. Li, Y.-F. Jiang, and H. Yao, Majorana-Time-Reversal Symmetries: A Fundamental Principle for Sign-Problem-Free Quantum Monte Carlo Simulations, Phys. Rev. Lett. **117**, 267002 (2016).
- [137] V. L. Berezinskii, Destruction of long-range order in one-dimensional and two-dimensional systems having a continuous symmetry group I. Classical systems, Sov. Phys. JETP **32**, 493 (1971).
- [138] J. M. Kosterlitz and D. J. Thouless, Ordering, metastability and phase transitions in two-dimensional systems, J. Phys. C Solid State Phys. **6**, 1181 (1973).
- [139] J. M. Kosterlitz, The critical properties of the two-dimensional xy model, J. Phys. C Solid State Phys. **7**, 1046 (1974).
- [140] F. F. Assaad, V. Rousseau, F. Hebert, M. Feldbacher, and G. G. Batrouni, Spin and charge dynamics of stripes in doped Mott insulators, EPL (Europhys. Lett.) **63**, 569 (2003).

- [141] A. Chubukov, Pairing Mechanism in Fe-Based Superconductors, *Annu. Rev. Condens. Matter Phys.* **3**, 57 (2012).
- [142] G. H. Golub and C. F. Van Loan, *Matrix Computations*, 4th ed. (The Johns Hopkins University Press, Baltimore, 2013).
- [143] L. Blum, F. Cucker, M. Shub, and S. Smale, *Complexity and Real Computation* (Springer, New York, 1998).
- [144] E. Y. Loh, J. E. Gubernatis, R. T. Scalettar, R. L. Sugar, and S. R. White, Stable Matrix-Multiplication Algorithms for Low-Temperature Numerical Simulations of Fermions, in *Interacting Electrons in Reduced Dimensions*, NATO ASI Series B: Physics, Vol. 213, edited by D. Baeriswyl and D. K. Campbell (Springer, New York, 1989) pp. 55–60.
- [145] W. H. Press, S. A. Teukolsky, W. T. Vetterling, and B. P. Flannery, *Numerical Recipes*, 3rd ed. (Cambridge University Press, Cambridge, UK, 2007).
- [146] E. Anderson, Z. Bai, C. Bischof, S. Blackford, J. Demmel, J. Dongarra, J. Du Croz, A. Greenbaum, S. Hammarling, A. McKenney, and D. Sorensen, *LAPACK Users' Guide*, 3rd ed. (Society for Industrial and Applied Mathematics, Philadelphia, PA, 1999).
- [147] P. Broecker and S. Trebst, Numerical stabilization of entanglement computation in auxiliary-field quantum Monte Carlo simulations of interacting many-fermion systems, *Phys. Rev. E* **94**, 063306 (2016).
- [148] U. Wolff, Collective Monte Carlo updating for spin systems, *Phys. Rev. Lett.* **62**, 361 (1989).
- [149] C. Geyer, Markov chain Monte Carlo maximum likelihood, in *Computing Science and Statistics: Proceedings of the 23rd Symposium on the Interface*, edited by E. M. Keramidas (Interface Foundation, Fairfax Station, 1991) p. 156.
- [150] K. Hukushima and K. Nemoto, Exchange Monte Carlo method and application to spin glass simulations, *J. Phys. Soc. Jpn.* **65**, 1604 (1996).
- [151] Y. Iba, Extended ensemble Monte Carlo, *Int. J. Mod. Phys. C* **12**, 623 (2001).
- [152] M. H. Gerlach, *Directional Ordering in the Classical Compass Model in Two and Three Dimensions*, Diploma thesis, Leipzig University (2012).
- [153] A. Kone and D. A. Kofke, Selection of temperature intervals for parallel-tempering simulations. *J. Chem. Phys.* **122**, 206101 (2005).
- [154] S. Trebst, D. Huse, and M. Troyer, Optimizing the ensemble for equilibration in broad-histogram Monte Carlo simulations, *Phys. Rev. E* **70**, 046701 (2004).
- [155] H. G. Katzgraber, S. Trebst, D. A. Huse, and M. Troyer, Feedback-optimized parallel tempering Monte Carlo, *J. Stat. Mech. Theor. Exp.* **2006**, P03018 (2006).
- [156] S. Trebst, M. Troyer, and U. H. E. Hansmann, Optimized parallel tempering simulations of proteins. *J. Chem. Phys.* **124**, 174903 (2006).

- [157] G. Alvarez, M. S. Summers, D. E. Maxwell, M. Eisenbach, J. S. Meredith, J. M. Larkin, J. Levesque, T. A. Maier, P. R. C. Kent, E. F. D'Azevedo, and T. C. Schulthess, New algorithm to enable 400+ TFlop/s sustained performance in simulations of disorder effects in high- T_c superconductors, in *Proceedings of the 2008 ACM/IEEE Conference on Supercomputing* (IEEE Press, Piscataway, NJ, USA, 2008) p. 61.
- [158] E. Gull, P. Staar, S. Fuchs, P. Nukala, M. S. Summers, T. Pruschke, T. C. Schulthess, and T. Maier, Submatrix updates for the continuous-time auxiliary-field algorithm, *Phys. Rev. B* **83**, 075122 (2011).
- [159] P. K. V. V. Nukala, T. A. Maier, M. S. Summers, G. Alvarez, and T. C. Schulthess, Fast update algorithm for the quantum Monte Carlo simulation of the Hubbard model, *Phys. Rev. B* **80**, 195111 (2009).
- [160] F. Assaad, Depleted Kondo lattices: Quantum Monte Carlo and mean-field calculations, *Phys. Rev. B* **65**, 115104 (2002).
- [161] D. Poilblanc, Twisted boundary conditions in cluster calculations of the optical conductivity in two-dimensional lattice models, *Phys. Rev. B* **44**, 9562 (1991).
- [162] C. Gros, The boundary condition integration technique: results for the Hubbard model in 1D and 2D, *Z. Phys. B Condens. Matter* **86**, 359 (1992).
- [163] C. Lin, F. H. Zong, and D. M. Ceperley, Twist-averaged boundary conditions in continuum quantum Monte Carlo algorithms, *Phys. Rev. E* **64**, 016702 (2001).
- [164] B. Efron, *The Jackknife, the Bootstrap and Other Resampling Plans* (SIAM, 1982).
- [165] A. M. Ferrenberg and R. H. Swendsen, New Monte Carlo technique for studying phase transitions, *Phys. Rev. Lett.* **61**, 2635 (1988).
- [166] A. M. Ferrenberg and R. H. Swendsen, Optimized Monte Carlo data analysis, *Phys. Rev. Lett.* **63**, 1195 (1989).
- [167] J. D. Chodera, W. C. Swope, J. W. Pitera, C. Seok, and K. A. Dill, Use of the Weighted Histogram Analysis Method for the Analysis of Simulated and Parallel Tempering Simulations, *J. Chem. Theory Comput.* **3**, 26 (2007).
- [168] M. Frigo and S. Johnson, The Design and Implementation of FFTW3, *Proc. IEEE* **93**, 216 (2005).
- [169] A. Cuccoli, V. Tognetti, and R. Vaia, Two-dimensional XXZ model on a square lattice: A Monte Carlo simulation, *Phys. Rev. B* **52**, 10221 (1995).
- [170] G. M. Wysin, A. R. Pereira, I. A. Marques, S. A. Leonel, and P. Z. Coura, Extinction of the Berezinskii-Kosterlitz-Thouless phase transition by nonmagnetic disorder in planar symmetry spin models, *Phys. Rev. B* **72**, 094418 (2005).
- [171] D. J. Scalapino, S. R. White, and S. C. Zhang, Superfluid density and the Drude weight of the Hubbard model, *Phys. Rev. Lett.* **68**, 2830 (1992).

Bibliography

- [172] D. J. Scalapino, S. R. White, and S. Zhang, Insulator, metal, or superconductor: The criteria, Phys. Rev. B **47**, 7995 (1993).
- [173] M. Tinkham, *Introduction to superconductivity*, 2nd ed., International series in pure and applied physics (McGraw-Hill, 1996).
- [174] D. R. Nelson and J. M. Kosterlitz, Universal Jump in the Superfluid Density of Two-Dimensional Superfluids, Phys. Rev. Lett. **39**, 1201 (1977).
- [175] T. Paiva, R. dos Santos, R. Scalettar, and P. Denteneer, Critical temperature for the two-dimensional attractive Hubbard model, Phys. Rev. B **69**, 184501 (2004).
- [176] N. Trivedi and M. Randeria, Deviations from Fermi-Liquid Behavior above T_c in 2D Short Coherence Length Superconductors, Phys. Rev. Lett. **75**, 312 (1995).
- [177] W. Janke, First-Order Phase Transitions, in *Computer Simulations of Surfaces and Interfaces*, NATO Science Series II: Mathematics, Physics and Chemistry, Vol. 114 (Springer Netherlands, Dordrecht, 2003) pp. 111–135.
- [178] R. M. Fernandes and J. Schmalian, Competing order and nature of the pairing state in the iron pnictides, Phys. Rev. B **82**, 014521 (2010).
- [179] J. Schmalian, D. Pines, and B. Stojković, Microscopic theory of weak pseudogap behavior in the underdoped cuprate superconductors: General theory and quasiparticle properties, Phys. Rev. B **60**, 667 (1999).
- [180] L. Li, Y. Wang, M. Naughton, S. Ono, Y. Ando, and N. Ong, Strongly nonlinear magnetization above T_c in $\text{Bi}_2\text{Sr}_2\text{CaCu}_2\text{O}_{8+\delta}$, EPL (Europhysics Lett.) **72**, 451 (2005).
- [181] L. Li, Y. Wang, S. Komiya, S. Ono, Y. Ando, G. D. Gu, and N. P. Ong, Diamagnetism and cooper pairing above T_c in cuprates, Phys. Rev. B **81**, 054510 (2010).
- [182] E. G. Moon and S. Sachdev, Competition between spin density wave order and superconductivity in the underdoped cuprates, Phys. Rev. B **80**, 035117 (2009).
- [183] E. G. Moon and S. Sachdev, Quantum critical point shifts under superconductivity: Pnictides and cuprates, Phys. Rev. B **82**, 104516 (2010).
- [184] N. Ni, A. Thaler, J. Q. Yan, A. Kracher, E. Colombier, S. L. Bud'ko, P. C. Canfield, and S. T. Hannahs, Temperature versus doping phase diagrams for $\text{Ba}(\text{Fe}_{1-x}\text{TM}_x)_2\text{As}_2$ ($\text{TM}=\text{Ni}, \text{Cu}, \text{Cu}/\text{Co}$) single crystals, Phys. Rev. B **82**, 024519 (2010).
- [185] P. M. Chaikin and T. C. Lubensky, *Principles of condensed matter physics* (Cambridge University Press, Cambridge, UK, 2000).
- [186] S. Sachdev and R. La Placa, Bond order in two-dimensional metals with antiferromagnetic exchange interactions, Phys. Rev. Lett. **111**, 027202 (2013).
- [187] J. D. Sau and S. Sachdev, Mean-field theory of competing orders in metals with antiferromagnetic exchange interactions, Phys. Rev. B **89**, 075129 (2014).

- [188] A. Allais, J. Bauer, and S. Sachdev, Density wave instabilities in a correlated two-dimensional metal, Phys. Rev. B **90**, 155114 (2014).
- [189] V. Mishra and M. Norman, Strong coupling critique of spin fluctuation driven charge order in underdoped cuprates, Phys. Rev. B **92**, 60507 (2015).
- [190] A. Levchenko, M. G. Vavilov, M. Khodas, and A. V. Chubukov, Enhancement of the London Penetration Depth in Pnictides at the Onset of Spin-Density-Wave Order under Superconducting Dome, Phys. Rev. Lett. **110**, 177003 (2013).
- [191] K. Hashimoto, K. Cho, T. Shibauchi, S. Kasahara, Y. Mizukami, R. Katsumata, Y. Tsuruhara, T. Terashima, H. Ikeda, M. A. Tanatar, H. Kitano, N. Salovich, R. W. Giannetta, P. Walmsley, A. Carrington, R. Prozorov, and Y. Matsuda, A sharp peak of the zero-temperature penetration depth at optimal composition in $\text{BaFe}_2(\text{As}_{1-x}\text{P}_x)_2$, Science **336**, 1554 (2012).
- [192] D. Chowdhury, B. Swingle, E. Berg, and S. Sachdev, Singularity of the London penetration depth at quantum critical points in superconductors, Phys. Rev. Lett. **111**, 157004 (2013).
- [193] D. Chowdhury, J. Orenstein, S. Sachdev, and T. Senthil, Phase transition beneath the superconducting dome in $\text{BaFe}_2(\text{As}_{1-x}\text{P}_x)_2$, Phys. Rev. B **92**, 081113(R) (2015).
- [194] Y. Schattner, S. Lederer, S. A. Kivelson, and E. Berg, Ising Nematic Quantum Critical Point in a Metal: A Monte Carlo Study, Phys. Rev. X **6**, 031028 (2016).
- [195] Matsui, H. and Terashima, K. and Sato, T. and Takahashi, T. and Fujita, M. and Yamada, K., Direct Observation of a Nonmonotonic $d_{x^2-y^2}$ -Wave Superconducting Gap in the Electron-Doped High- T_c Superconductor $\text{Pr}_{0.89}\text{LaCe}_{0.11}\text{CuO}_4$, Phys. Rev. Lett. **95**, 017003 (2005).
- [196] X. Wang, Y. Schattner, E. Berg, and R. M. Fernandes, Superconductivity mediated by quantum critical antiferromagnetic fluctuations: the rise and fall of hot spots, eprint (2016), arXiv:1609.09568 [cond-mat.supr-con].
- [197] Z.-X. Li, F. Wang, H. Yao, and D.-H. Lee, What makes the T_c of monolayer FeSe on SrTiO_3 so high: a sign-problem-free quantum Monte Carlo study, Sci. Bull. **61**, 925 (2016).
- [198] P. T. Dumitrescu, M. Serbyn, R. T. Scalettar, and A. Vishwanath, Superconductivity and nematic fluctuations in a model of doped FeSe monolayers: Determinant quantum Monte Carlo study, Phys. Rev. B **94**, 155127 (2016).
- [199] S. Sachdev, E. Berg, S. Chatterjee, and Y. Schattner, Spin density wave order, topological order, and Fermi surface reconstruction, Phys. Rev. B **94**, 115147 (2016).
- [200] Z.-X. Li, F. Wang, H. Yao, and D.-H. Lee, The nature of effective interaction in cuprate superconductors: a sign-problem-free quantum Monte-Carlo study, eprint (2015), arXiv:1512.04541 [cond-mat.supr-con].

Bibliography

- [201] Y. Motome and M. Imada, A Quantum Monte Carlo Method and Its Applications to Multi-Orbital Hubbard Models, *J. Phys. Soc. Japan* **66**, 1872 (1997).
- [202] F. Assaad, M. Imada, and D. Scalapino, Charge and spin structures of a $d_{x^2-y^2}$ superconductor in the proximity of an antiferromagnetic Mott insulator, *Phys. Rev. B* **56**, 15001 (1997).
- [203] C. Gattringer and C. B. Lang, *Quantum Chromodynamics on the Lattice: An Introductory Presentation* (Springer, Berlin, 2010).
- [204] R. T. Scalettar, D. J. Scalapino, R. L. Sugar, and D. Toussaint, Hybrid molecular-dynamics algorithm for the numerical simulation of many-electron systems, *Phys. Rev. B* **36**, 8632 (1987).
- [205] S. Beyl and F. Goth, personal communication (2016).

Acknowledgments

First and foremost I thank Simon Trebst for giving me the opportunity to work on a challenging, but very interesting problem. He has always provided support and found the time for patient advise. Next I thank Achim Rosch for agreeing to be the second referee of this thesis. With their research groups Achim and Simon have fostered an exceptional scientific environment that is very conducive to fruitful research. I am also thankful to Markus Braden, who chairs the committee of my examination.

I am very grateful to Erez Berg and Yoni Schattner with whom we have had an exceptionally productive collaboration and from whom I have learned a lot. Our regular, close exchange with often weekly extensive video conferences has really driven forward this project. Last but not least I really enjoyed their hospitality during my seven week visit at the Weizmann institute. I also enjoyed working with Eran Sela, although our joint paper turned out to be orthogonal to the contents of this thesis.

Here in Cologne I have had a wonderful time thanks to all my colleagues at the institute. For many inspiring discussions, good times, and unforgettable conference trips I thank: Benjamin, Carolin, Carsten, Christoph, Emilio, Etienne, Fanny, Finn, Florian, Henry, Jan A., Jan G., Jan M., Johannes H., Johannes W., Jonathan, Kevin, Laura, Lucas, Mario, Mascha, Maximilian, Michael, Peter, Robert, Sarah, Stefan Bi., Stefan Bu., Stefan W., Steffen, Stephanie, Tilman, Tim, Tobias, Wilfried, Yoran, Zala.

Andreas Sindermann deserves a special mention for keeping everything at the institute running at a steady space, not only the IT systems. For further administrative support I thank Mariela Boevska and Yasemin Tieben. For their constant help with issues regarding the Cheops cluster, which has crunched our numbers for millions of CPU hours, I thank the HPC team of the RRZK, in particular Viktor Achter, Stefan Borowski, and Lech Nieroda.

For additional financial support I thank the Bonn-Cologne Graduate School of Physics and Astronomy (BCGS) and the key profile area Quantum Matter & Materials (QM2).

Schließlich: Vielen Dank Ellen, für deine stete Unterstützung und dein Verständnis für manche Abwesenheit in stressigen Zeiten.

Erklärung zur Dissertation

Ich versichere, dass ich die von mir vorgelegte Dissertation selbständig angefertigt, die benutzten Quellen und Hilfsmittel vollständig angegeben und die Stellen der Arbeit — einschließlich Tabellen, Karten und Abbildungen —, die anderen Werken im Wortlaut oder dem Sinn nach entnommen sind, in jedem Einzelfall als Entlehnung kenntlich gemacht habe; dass diese Dissertation noch keiner anderen Fakultät oder Universität zur Prüfung vorgelegen hat; dass sie — abgesehen von unten angegebenen Teilpublikationen — noch nicht veröffentlicht worden ist sowie, dass ich eine solche Veröffentlichung vor Abschluss des Promotionsverfahrens nicht vornehmen werde. Die Bestimmungen der Promotionsordnung sind mir bekannt. Die von mir vorgelegte Dissertation ist von Prof. Dr. Simon Trebst betreut worden.

Publikationen

- E. Sela, H.-C. Jiang, M. H. Gerlach, and S. Trebst, *Order-by-disorder and spin-orbital liquids in a distorted Heisenberg-Kitaev model*, Phys. Rev. B **90**, 035113 (2014).
- M. H. Gerlach and W. Janke, *First-order directional ordering transition in the three-dimensional compass model*, Phys. Rev. B **91**, 045119 (2015).
- Y. Schattner, M. H. Gerlach, S. Trebst, and E. Berg, *Competing Orders in a Nearly Antiferromagnetic Metal*, Phys. Rev. Lett. **117**, 097002 (2016).
- M. H. Gerlach, Y. Schattner, E. Berg, and S. Trebst, *Quantum critical properties of a metallic spin-density-wave transition*, Phys. Rev. B **95**, 035124 (2017).